



The Nature of Extreme X-ray to Optical Ratio Sources (EXOs)

Thesis submitted for the degree of
Doctor of Philosophy
at the University of Leicester
by

Agnese Del Moro

X-ray & Observational Astronomy Group
Department of Physics and Astronomy
University of Leicester

SUPERVISOR: Prof. Mike G. Watson
CO-SUPERVISOR: Dr. Silvia Mateos

February 2010

Declaration

All sentences or passages quoted in this project dissertation from other people's work have been specifically acknowledged by clear cross referencing to author, work and page(s). I understand that failure to do this amounts to plagiarism and will be considered grounds for failure in this module and the degree examination as a whole.

Name: Agnese Del Moro

Signed:

Date: 19-02-2010

The Nature of Extreme X-ray to Optical Ratio Sources (EXOs)

Agnese Del Moro

ABSTRACT

This thesis presents a study of a sample of objects with a high X-ray-to-optical flux ratio, which are believed to be a good tracer of highly obscured, high redshift active galaxies (AGN). Such objects have particular importance since they may account for a significant fraction of the accretion history of the Universe and because of their links with the co-evolution of super-massive black holes and their host galaxies.

In this thesis the results are presented for a new sample of bright, X-ray selected objects with extreme X-ray-to-optical flux ratios (“EXOs”), constructed from a cross-correlation of the 2XMMp X-ray and the SDSS-DR5 optical catalogues. Investigation of the optical/NIR and X-ray colours constrains the fraction of obscured sources to be over half of the sample. Optical and X-ray spectroscopic analysis for a sub-sample of the EXOs confirms these results and reveals the presence of a large number of type-2 QSOs. The discovery of the source with the currently highest X-ray-to-optical flux ratio value is also reported and its properties investigated.

Finally, a population study of a complete sample of bright X-ray selected AGN from the Subaru/XMM-Newton Deep Survey (SXDS) is presented. Through detailed X-ray spectral analysis, the average properties of the sample are investigated and the fraction of absorbed sources and its dependence on the intrinsic X-ray luminosity is studied. The properties of the high X-ray-to-optical flux ratio sources in this SXDS sample is compared with the EXO sample drawn from the the 2XMMp/SDSS catalogue cross-correlation.

Acknowledgements

There are several people I would like to thank for their help throughout my PhD and this thesis work.

Firstly, I would like to thank my supervisor Mike G. Watson, for his consistent guidance during this period and for providing valuable help and assistance when I needed most. Thank you also for believing in my potential and for addressing me in the right way to become a good scientist. I would also like to thank my co-supervisor Silvia Mateos, from whom I learnt a lot: thank you for sharing with me your experience, for the useful discussions and for your patience in explaining things to me. I thank her not only as a “supervisor”, but also as a friend. A big thank you must go also to Valentina Braitto, for teaching me many tricks of XSPEC... Much better than a user guide! Thanks also for her support and help in so many other things, I am grateful for her friendship.

I would also like to thank my family, my Mum, Dad and my brother Stefano, and my best friends, Francy, Valli, Maggi and Gio, who are far away, but with their love and support do not make me feel the distance at all. I feel really lucky to have them in my life. A thank you must also go to Daniele, whose constant presence since the beginning of this journey has been very important to me.

And finally, the most special thanks are for Lorenzo, who is my pillar. Thank you for always being with me and for believing in me.

Contents

1	Introduction	1
1.1	Active Galactic Nuclei	2
1.1.1	Models of AGN	3
1.1.2	Observational phenomena and Spectral Energy Distribution of AGN	4
1.1.3	AGN classification	12
1.2	The Unification scheme	13
1.2.1	Modifications to the unification scheme	15
1.3	General picture	16
1.3.1	X-ray Background	18
1.3.2	Open issues	20
1.4	Extreme X-ray-to-optical sources (EXOs)	21
1.5	Aims of this thesis	24
2	The EXO Sample in 2XMMp	25
2.1	The X-ray data	26
2.1.1	The <i>XMM-Newton</i> Observatory	26
2.1.2	EPIC	27
2.1.3	The 2XMMp and 2XMM catalogues	31
2.2	The SDSS optical data	33
2.2.1	SDSS-DR5	34

2.3	Cross-correlation of the 2XMMp and the SDSS-DR5	36
2.3.1	Likelihood Ratio	37
2.3.2	Cross-identification process	38
2.4	EXO sample selection	40
2.5	Comparison with the Strasbourg cross-correlation method	43
3	The Nature of EXOs	46
3.1	Introduction	47
3.2	General properties of the sample	48
3.2.1	X-ray properties	49
3.2.2	Optical properties	51
3.3	SED model predictions	54
3.3.1	SED templates	54
3.3.2	The SED model	55
3.3.3	The Optical/IR SED analysis	57
3.4	UKIRT NIR data	59
3.4.1	UKIDSS archive data	59
3.4.2	NIR follow-up	61
3.5	Optical spectroscopy	66
3.5.1	Subaru FOCAS data	66
3.5.2	ESO VLT data	67
3.5.3	Other spectroscopic data	68
3.5.4	Optical spectral analysis	69
3.6	The X-ray spectral properties	75
3.6.1	Spectral extraction process	76
3.6.2	Spectral fitting	77
3.6.3	More complex models	81
3.6.4	Spectral constraints from the Hardness Ratios	84
3.6.5	X-ray analysis results	86
3.7	Discussion	87

3.7.1	Comparison between optical and X-ray properties	87
3.7.2	Confrontation of our expectation	90
3.8	Summary and conclusions	94
4	An Extreme EXO: A Type 2 QSO at $z = 1.87$	97
4.1	Introduction	98
4.2	Observations and results	99
4.2.1	X-ray properties of 2XMM J123204	99
4.2.2	Optical/IR properties	101
4.2.3	Near-IR spectrum	102
4.3	Discussion	106
4.4	Summary and conclusions	111
5	The Subaru/XMM Deep Survey: X-ray analysis	113
5.1	Introduction	114
5.2	The Subaru/XMM-Newton Deep Survey	114
5.2.1	Multi-wavelength observations	115
5.2.2	X-ray Data	116
5.3	Our Sample	118
5.4	Spectral analysis	120
5.4.1	Extraction of the X-ray spectra	120
5.4.2	Spectral fitting	122
5.4.3	Soft Excess	124
5.4.4	Iron $K\alpha$ line	126
5.4.5	SXDS 0816	127
5.5	Sample Properties	128
5.5.1	Comparison between optical and X-ray classification	130
5.5.2	Redshift and luminosity distribution	131
5.6	The high f_X/f_{opt} sources	133
5.7	Luminosity dependence of the fraction of type 2 AGN	134

5.8	The mean Fe $K\alpha$ line	136
5.8.1	Averaging method	137
5.9	Conclusions	141
6	Conclusions	144
6.1	Summary of thesis results	145
6.1.1	The EXO sample	145
6.1.2	The most extreme EXO	146
6.1.3	The SXDS sample	147
6.2	Ongoing and future work	148

CHAPTER 1

Introduction

This chapter presents the astrophysical context and the aims of the research described in this thesis. Present knowledge of the structure of Active Galactic Nuclei (AGN) and the physical processes producing their spectrum are summarised, together with their classification and the implications for the well established Unified model (Antonucci 1993); some observed exceptions to the unified scheme of AGN are also described, with the hypotheses put forward to explain them (“modified unification models”).

Our current understanding of AGN population properties and the importance of AGN studies in understanding the origin and evolution of the distant Universe are discussed, focusing on the relevance of obscured (type-2) QSOs amongst the AGN population and their contribution to the X-ray background emission (XRB). A detailed characterisation is presented of those sources with high f_X/f_{opt} (EXOs, extreme X-ray-to-optical ratio sources) amongst the AGN population, which are believed to be the mostly elusive type-2 QSO, and finally, the aims of the thesis are summarised.

1.1 Active Galactic Nuclei

Active galactic nuclei (AGN) are amongst the most powerful persistent objects observed in the sky, emitting radiation throughout the whole electromagnetic spectrum. The enormous power of these objects ($L_{bol} \approx 10^{42} - 10^{48} \text{ erg s}^{-1}$), emitted from a compact (unresolved) region at the centre of a galaxy (active galaxy), is believed to be released from material accreting onto a supermassive black hole ($M_{BH} = 10^6 - 10^9 M_{\odot}$), as no other physical phenomenon is able to produce such large and long-lasting luminosities over such a wide wavelength range.

The first AGN were discovered in the 1940s (NGC 1068, 3C 273; Seyfert 1943, Woltjer 1959, Schmidt 1963) from optical observations and the first radio surveys. Although the physical nature of these objects was not understood at the time, the main characteristics of these sources were already recognised: optical emission lines, strong radio emission, spectral variability, high redshift and high optical luminosity coming from a point-like source, or a compact (unresolved) region at the centre of a galaxy. The origin of such high luminosities was initially attributed to some peculiar stellar process (e.g. a series of supernovae in the galaxy centre, the formation of a supermassive star leading to a super-supernova), but soon the extremely high luminosity of these compact objects was suggested to originate from a massive black hole (e.g. Zel'Dovich 1964; Lynden-Bell 1969).

However, the real breakthrough in understanding the nature of these powerful objects occurred with the advent of space-borne instruments during the 1960s and 1970s (e.g. *Uhuru*, *Ariel-V*, *HEAO-1*, *Einstein*), which opened the new field of X-ray observations and revealed X-ray emission from the sources identified as AGN. It was soon clear that X-ray emission was a common property of AGN (e.g. Giacconi et al. 1974; Elvis et al. 1978). Since then, more and more AGN have been discovered and our knowledge of their properties and the understanding of these objects has increased vastly. It is now clear that the initial population of quasars discovered in radio surveys constitute only a small fraction ($\sim 10\%$) of the AGN population, which is mainly “radio-quiet”.

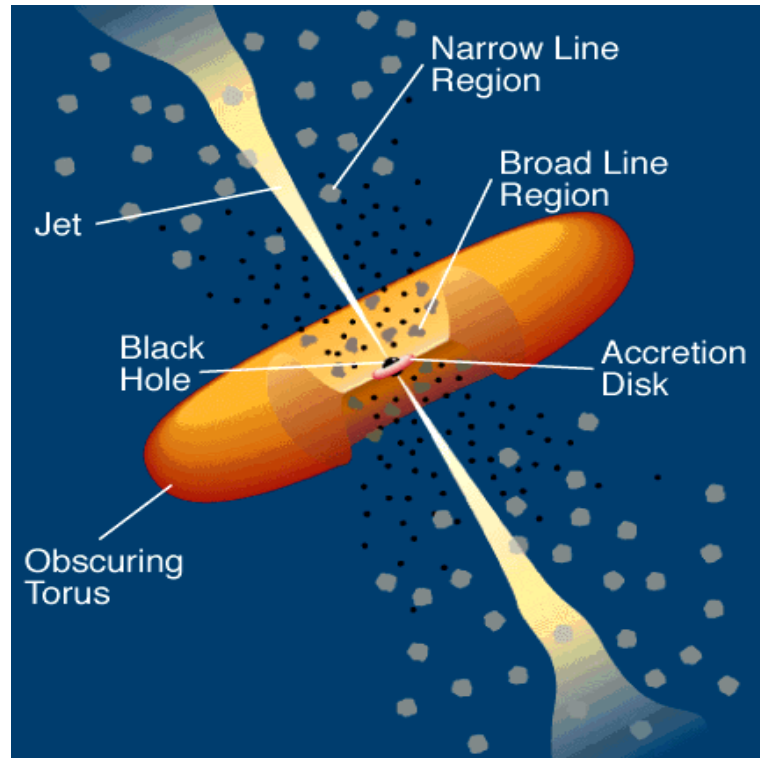


Figure 1.1: Sketch of the structure of an AGN according to the Unified model. The figure is adapted from Urry & Padovani (1995).

1.1.1 Models of AGN

The schematic view of the structure of the AGN, according to our current understanding of the AGN phenomenon and established from 50-60 years of observational studies in different spectral bands and modelling (Antonucci 1993; Urry & Padovani 1995), is shown in Figure 1.1. The central BH-accretion disc system is surrounded by a large amount of gas with different densities and ionisation states: the gas clouds that lie close to the BH are called the Broad Line Region (BLR); these clouds are located within $\sim 10^{-2} - 0.1$ pc from the BH; they have high temperature ($T \sim 10^4$ K; e.g. Kallman & Mushotzky 1985) and density $\rho \sim 10^9 - 10^{11}$ cm $^{-3}$. The gas in these regions, which are assumed to be in Keplerian motion around the central BH, has typically a velocity $v = 2000 - 10000$ km s $^{-1}$ and it is believed to be the origin of the broad emission lines observed in the optical/UV band (see below). The gas clouds that lie further away from the nucleus (at $\sim 10^{18}$ cm; Urry & Padovani 1995) are the Narrow Line Region (NLR), which produce narrow emission lines ($\text{FWHM} \lesssim 1000$ km s $^{-1}$, see below); this is a larger region than the BLR (extending typically up to 100 – 300 pc from the BH, up to a few kpc in bright

quasars; see also Sect. 4.3) of hot gas (and some amount of dust) at temperature $T \sim 10^4$ K and density $\rho \sim 10^3 - 10^6 \text{ cm}^{-3}$. Around the nucleus, at a distance of a few gravitational radii (R_S) from the BH, an accretion disc corona of hot ($T \sim 10^9$ K), relativistic electrons is present, which is responsible for the high energy emission of the AGN (hard X-rays, $E > 2 \text{ keV}$). The nucleus is also surrounded by a region of neutral and ionised gas and dust, which is usually supposed to form a parsec-scale torus around the central region (e.g. Antonucci 1993; Urry & Padovani 1995; Elitzur 2008) and is responsible for the obscuration of the emission coming from the central region and, at some level, for the reprocessed emission observed at different wavelengths (see below). Some sources also show relativistic jets emitted perpendicular to the equatorial plane (where the torus lies), which may extend for several kpc (Fig. 1.1; Urry & Padovani 1995).

1.1.2 Observational phenomena and Spectral Energy Distribution of AGN

The spectra of the AGN are rather complex as they are due to a combination of various physical processes that take place in different regions around the black hole, and the emission produced by each process dominates at different wavebands. Although the spectra can be very different from object to object, the main characteristics observed in the Spectral Energy Distribution (SED) are common for all AGN (Fig. 1.2). Nevertheless, an initial distinction between two classes of objects is necessary, as the physical processes dominating in these two classes are different: i) radio-loud (RL) AGN, which show strong relativistic kpc-scale jets (see Fig. 1.1) and lobes (see below) and produce strong radio emission; ii) radio-quiet (RQ) AGN, where no jets (or in some cases small pc-scale jets; Blundell et al. 1996) are seen and the radio emission is much lower¹. Below, the main spectral properties of AGN are described, although we note that not all these properties are observed in all AGN (see Sect. 1.1.3); they are referred mainly to the RQ AGN, as they constitute $\sim 90\%$ of the AGN population (e.g. Urry & Padovani 1995), however RL

¹Usually the distinction between RL and RQ AGN is made in terms of their radio loudness R , defined as the ratio of the monochromatic radio flux at 5 GHz and the optical flux in the B band: $R = F_{5 \text{ GHz}}/F_B$ (Kellermann et al. 1989); RL AGN have $R > 10$.

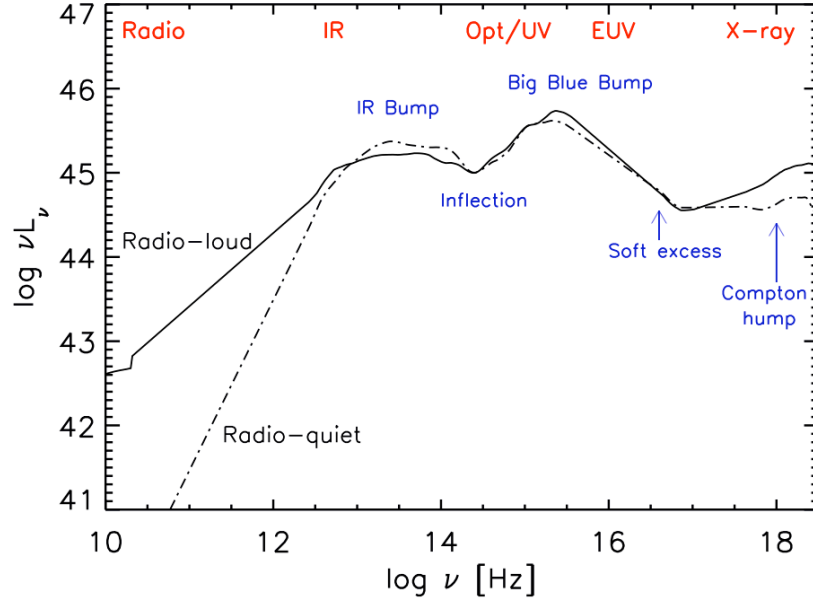


Figure 1.2: Spectral energy distribution (SED) from the radio to the X-ray band for a radio-loud and a radio-quiet AGN (Elvis et al. 1994). The main SED features are indicated in the plot.

AGN characteristics are also mentioned, for completeness.

The accreting gas surrounding the black hole forms a thin, optically thick disc (Shakura & Sunyaev 1973; Shields 1978; Malkan & Sargent 1982); this material, losing angular momentum, tends to fall inward in the disc and eventually onto the BH at a rate \dot{M} . The total energy released by this accretion is given by:

$$L = \eta \dot{M} c^2 \quad (1.1)$$

where c is the speed of light in a vacuum and η is the efficiency of the accretion. The efficiency η depends on the compactness of the central BH (M/R) as:

$$\eta = \frac{GM_{\text{BH}}}{R_{\text{BH}}c^2} = \frac{R_S}{2R_{\text{BH}}} \quad (1.2)$$

where $R_S = 2GM_{\text{BH}}/c^2$ is the Schwarzschild radius. The efficiency is $\eta \approx 0.06$ for non-rotating BHs ($R_{\text{BH}} \approx 3R_S$), while it increases for rotating BHs ($\eta \approx 0.43$ for maximum-rotating BHs, i.e. Kerr BHs, where $R_{\text{BH}} \approx R_S$).

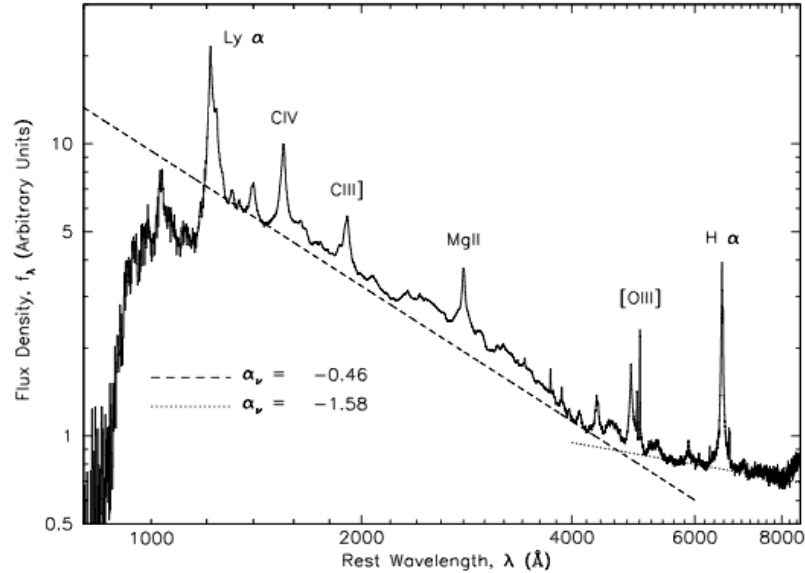


Figure 1.3: Composite quasar spectrum in the optical waveband obtained from Sloan Digital Sky Survey (SDSS) data by Vanden Berk et al. (2001).

The gas in the accretion disc emits thermal radiation, due to gravitational potential energy losses into kinetic rotational energy and through friction due to the viscosity of the disc; this gas emits as a composite black-body radiation with a range of temperatures that depends on the emitting radii and the mass of the central BH (Turner & Miller 2009). The disc emission is responsible for the optical/UV continuum producing the so called “big blue bump” whose peak lies at far-ultraviolet wavelengths (FUV; $\sim 912 - 2000 \text{ \AA}$; e.g. Shang et al. 2005; Fig 1.2). The observed optical/UV continuum can be approximated with a power-law² of the form $f_\lambda \propto \lambda^{\alpha_\lambda}$, where $\alpha_\lambda \approx -0.4$ between $\lambda \sim 300 - 1200 \text{ \AA}$ (e.g. Telfer et al. 2002), $\alpha_\lambda \approx -1.5$ between $\lambda \sim 1200 - 5500 \text{ \AA}$ and $\alpha_\lambda \approx -0.5$ at $\lambda \sim 5500 - 9000 \text{ \AA}$ (Fig. 1.3; Vanden Berk et al. 2001; Risaliti & Elvis 2004; Shang et al. 2005); the flatter spectrum above 5000 \AA is probably due to the contribution of the host galaxy starlight in the AGN spectra (Vanden Berk et al. 2001). Above the continuum, several emission lines characterise the optical/UV emission of AGN (see Fig. 1.3): i) broad, permitted emission lines ($\text{FWHM} \gtrsim 2000 \text{ km s}^{-1}$) are believed to originate from the photoionised gas in the BLR, close to the central BH (see above); the strongest lines commonly seen in the AGN spectra are $\text{Ly}\alpha$ (1216 \AA , rest-frame), CIV (1549 \AA), CIII]

²The power-law is often expressed as a function of the frequency: $f_\nu \propto \nu^{\alpha_\nu}$, where α_ν is related to α_λ as: $(\alpha_\nu + \alpha_\lambda) = -2$.

(1909 Å), MgII (2800 Å), H β (4861 Å) and H α (6563 Å); ii) narrow, high ionisation emission lines (permitted and forbidden, with FWHM $\lesssim 1000 \text{ km s}^{-1}$) originate in the NLR, at a larger distance from the nucleus; the strongest narrow lines characterising AGN spectra are the [OIII] doublet ($\lambda = 4959, 5007 \text{ Å}$). Many weak emission lines are also present in the optical spectrum, making it difficult to properly model the continuum, especially in the wavelength range $\lambda \sim 2200 - 4000 \text{ Å}$, where the FeII emission line forest blends with the Balmer continuum emission, producing the so called “small blue bump” (Vanden Berk et al. 2001, and references therein).

The AGN emission in the IR band, between $2 - 200 \mu\text{m}$, constitutes a large fraction ($\sim 15 - 50\%$) of their bolometric luminosity (e.g. Risaliti & Elvis 2004). Thermal emission from dust with a range of temperature $50 - 1000 \text{ K}$, surrounding the nucleus (namely, the putative torus, extending from $\sim 0.1 \text{ pc}$ up to $\sim 1 \text{ kpc}$), produces the bulk of the radiation from the near-Infrared (NIR) to the sub-millimetre bands; the spectral energy distribution has a maximum typically at $\sim 10 - 30 \mu\text{m}$, forming the so called “IR bump” (e.g. Sanders 1999; see Fig. 1.2). The strength of the IR bump appears to be typically comparable to the big blue bump, although there are variations from object to object (Wilkes 2004). Between $1 - 2 \mu\text{m}$ there is a minimum in the spectrum (“inflection”; see Fig. 1.2) corresponding to the sublimation temperature of the dust grains ($\sim 2000 \text{ K}$; Sanders et al. 1989). In the far-IR/mm band the spectrum declines as a steep power-law $f_\nu \propto \nu^{\alpha_\nu}$, where $\alpha_\nu > 2.5$ (Sanders 1999; Wilkes 2004), generally attributed to grey-body emission from cool dust (e.g. Chini et al. 1989). For radio-loud AGN the spectrum between the IR bump and the sub-mm band declines more smoothly than for RQ AGN: the emission for RL AGN in this band is dominated by synchrotron emission by relativistic electrons and it is well reproduced by a power-law with $\alpha_\nu = 2.5$ (see below), typical for self-synchrotron absorption (Risaliti & Elvis 2004).

In the radio band the emission of the AGN is due to synchrotron radiation from relativistic jets. In this band the SED of RQ and RL AGN differentiate the most as radio-quiet

AGN have typically radio emission $\sim 100 - 1000$ times weaker than the radio-loud AGN. For both classes, however, the radio-emission constitutes only a small fraction of the bolometric luminosity (Fig. 1.2).

- **Radio loud:** In RL objects two different components contribute to the radio emission: an extended component (“lobes”) that can extend for few Mpc and a compact component (“core”), typically smaller than 0.01 pc. The lobes are formed by jets of relativistic electrons and they are almost symmetric on either side of the AGN nucleus; these extended regions produce a steep spectrum. The core is usually coincident with the nucleus of the AGN and produces a flatter spectrum compared to the lobes, which extend to the far-IR band. This is probably due to the compact region being optically thick, which can flatten the synchrotron emission spectrum over a broad range of frequencies.
- **Radio quiet:** in RQ AGN the radio emission is produced by the core, as radio jets are not observed in this class of objects. The origin of the weak radio emission in RQ AGN is not yet clear, but observational evidence shows a strong correlation between the radio and the X-ray emission, which suggest they may come from the same region (a possible origin for the radio emission in RQ AGN may be a magnetically active corona above the accretion disc; Laor & Behar 2007).

A substantial amount of the radiation of AGN (5 – 40% of the bolometric emission; Ward et al. 1987) is known to be emitted in the X-ray band from the accretion disc corona. The UV photons from the innermost edge of the disc are scattered by multiple inverse-Compton interactions with the hot (or relativistic) electrons of the corona (thermal Comptonisation; e.g. Zdziarski et al. 1994), producing the X-ray continuum (direct emission). The coronal spectrum can be well approximated to first order by a power-law with spectral index³ $\alpha_\nu \approx -0.8$ to -1.0 (for radio-quiet AGN⁴), from 1 keV up to a cut-off energy

³The X-ray spectrum is usually represented by a power-law of the form $N(E) \propto E^{-\Gamma}$, where Γ is the “photon index”: $\Gamma = (1 - \alpha_\nu)$.

⁴In RL AGN a different emission mechanism produces the hard X-ray spectrum: synchrotron self-Compton scattering and a flatter spectrum is generally observed for these objects ($\alpha_\nu \approx -0.5$ to -0.7).

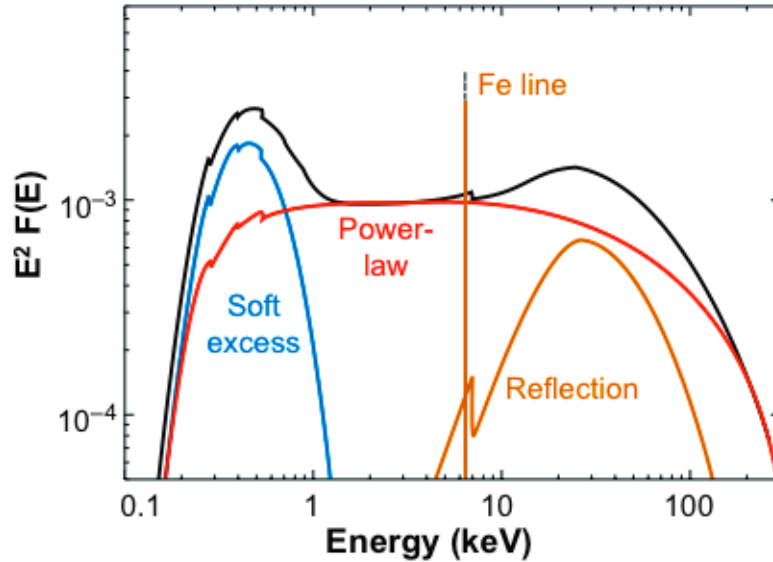


Figure 1.4: Main spectral components representing the X-ray emission from an unabsorbed AGN. Figure adapted from (Fabian 2006).

$E_c \sim kT_e$ ($E_c \sim 100 - 300$ keV; e.g. Risaliti & Elvis 2004), where T_e is the temperature of the electrons). A fraction of these photons are scattered back to illuminate the accretion disc, where they are subject to a number of possible interactions with the cold gas on the surface of the accretion disc: i) Compton scattering by free or bound electrons, which produces a “reflection” component in the X-ray spectrum, ii) photoelectric absorption followed by fluorescent line emission, or iii) photoelectric absorption followed by Auger de-excitation. Also the circumnuclear material (either the BLR or the molecular torus) is involved in producing the reflection component. The observed X-ray continuum is therefore the sum of the direct (primary continuum) and reprocessed (reflection component) emissions (see Figure 1.4).

Additional processes usually take place in AGN and tend to leave significant signatures on the observed X-ray continuum: i) photoelectric absorption by the putative molecular torus that tends to suppress the emission at soft X-ray energies ($E < 2$ keV); ii) a soft emission component (“soft excess”) is often observed in the AGN X-ray spectra below $\lesssim 1$ keV (rest-frame). The components are described in more detail below:

- **The photoelectric absorption:** Absorption in AGN is caused by a mixture of neutral and ionized gas, as well as dust. Absorption causes the suppression of soft X-ray

emission by a factor proportional to $e^{-\tau}$ (where $\tau = N_{\text{H}}\sigma(E)$ is the optical depth of the gas, N_{H} is the equivalent hydrogen column density and $\sigma(E)$ is the photoelectric cross-section). The observed continuum (primary) emission experiences an effective energy cut-off due to the photoelectric absorption that increases with the gas column density, N_{H} (Fig. 1.5; “cold absorber”). When the gas optical depth $\tau < 1$ (optically thin material) the higher energy photons of the continuum are not completely suppressed by the absorption and are directly detectable⁵; when $\tau = 1$, i.e. for $N_{\text{H}} \simeq 1/\sigma_T \geq 1.5 \times 10^{24} \text{ cm}^{-2}$ (where σ_T is the Thomson cross-section), the absorber is Compton-thick and the optical depth even for hard X-ray photons is significant ($E = 2 - 10 \text{ keV}$); hence, the direct emission from the nucleus can be observed only at higher energies ($E > 10 \text{ keV}$, rest-frame; see Figure 1.5). The established model for AGN (see Sect. 1.1.1) assume that this absorbing gas forms a torus around the nuclear region; although, recent observations and measurements on variability in AGN have suggested that the absorbing gas is located closer to the BH, e.g. the BLR (Risaliti et al. 2005, 2007).

- **The reflection component:** Reflection of the primary emission from the X-ray corona is produced by ionised gas lying in the accretion disc and/or at further distance from the BH, e.g. the inner edge of the torus. Due to the energy dependence of photoelectric absorption (see above), the soft X-ray photons illuminating the disc (and the inner torus) are mostly absorbed, whereas hard photons are rarely absorbed and tend to Compton scatter back along the line of sight, producing a reflection component; the strength of this component is strongly dependent on the illuminating angle and on the viewing angle. The reflected continuum has the same slope as the incident emission, but at $E \lesssim 10 \text{ keV}$ it is reduced by a factor of about $\sigma_T/(\sigma_T + \sigma(E))$ from the incident one; at these energies the reflection efficiency is only a few percent of the primary radiation due to photoelectric absorption. Above $\sim 10 \text{ keV}$ (rest-frame) the scattered component dominates over the photoelectric absorption and the reflection component becomes visible (Fig. 1.4 and Fig. 1.5); at

⁵In the energy frame available from the majority of current X-ray observatories (e.g. Chandra and *XMM-Newton*).

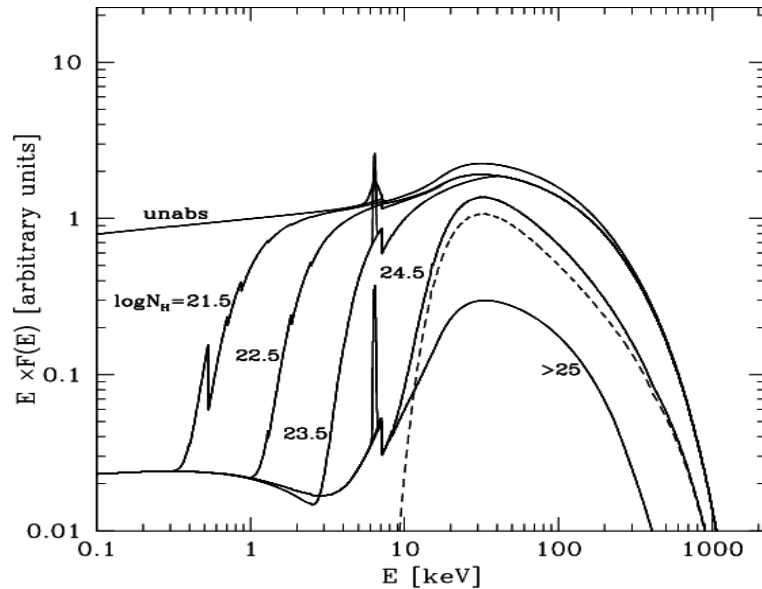


Figure 1.5: Simulation of the effect of the photoelectric absorption with increasing hydrogen column density N_{H} to the unabsorbed AGN spectrum (also shown in Fig. 1.4); a reflection component (dashed line) and a narrow Fe $K\alpha$ line are also included. The energy cut-off moves to higher energies (rest-frame) at higher column densities. Figure adapted from (Gilli et al. 2007).

$E \sim 30$ keV the reflection efficiency reaches its maximum ($\sim 30\%$, and it is higher if the reflecting medium is Compton-thick than in the Compton-thin regime, where part of the incident radiation escapes without interaction; Risaliti & Elvis 2004); at higher energies, the Compton down-scattering becomes important and the reflected spectrum decreases again (“Compton hump”; e.g. Matt et al. 1991). The reflection component due to the disc shows strong variability, following the variations of the primary continuum, while the component produced by the torus varies with longer timescales.

- **The Fe $K\alpha$ line:** $K\alpha$ lines of various heavy elements may be emitted by fluorescence in AGN. Because the probability of emitting photons by fluorescence increases with the atomic number and because Fe has high abundance in AGN, the Fe $K\alpha$ line is the most prominent feature observed in the X-ray spectra, at $E = 6.4$ keV (rest-frame, in neutral material; Turner & Miller 2009). This emission line is thought to be produced in the central region of AGN, such as the accretion disk, the Broad Line Region (BLR) and/or the circumnuclear obscuring torus. When the line is emitted

by the accretion disc close to the BH, a broad asymmetric line profile is produced, due to strong gravitational effects (Fabian et al. 2000; Miller 2007). The Fe $K\alpha$ line also has a narrow core, produced by cold, neutral material; the region where this component is emitted is still uncertain, but it plausibly originates in the outer disc, in the torus or in the BLR (e.g. Yaqoob & Padmanabhan 2004; Nandra 2006; Yaqoob et al. 2010); part of the emission of the narrow Fe $K\alpha$ line is also due to reflection by the inner part of the torus (or the narrow line region), as the line intensity is not depressed when the continuum is affected by photoelectric absorption.

- **The soft excess:** A soft emission component is observed in $\sim 50\%$ of the AGN (RL and RQ; e.g. Wilkes 2004). For a long time this emission was thought to be the high energy tail of the UV big blue bump, and hence to be due to thermal emission from the accretion disc. Although its origin is not yet fully understood, the rather constant temperatures found for the soft excess component ($T \sim 0.1 - 0.2$ keV) suggested it to be due to atomic processes: photoionised emission blurred relativistically by motion in an accretion disc (Crummy et al. 2006), or absorption due to partially ionised, warm gas (“warm absorber”, which produces strong absorption features, but may also produce emission lines) located in the accretion disc or in the circumnuclear region, or outflowing from the nucleus at high velocity (Done & Nayakshin 2007). Indeed, ionised warm absorbers ($T = 10^5 - 10^6$ K) are established to be common in AGN; these absorbers produce a complex absorption line spectrum in the soft X-ray band ($E < 2$ keV), showing variability on relatively short timescales (Turner & Miller 2009). The main absorption features are due to K -shell transitions of heavy elements (e.g. O VII and O VIII, amongst the strongest features; Turner & Miller 2009).

1.1.3 AGN classification

Since their discovery, AGN have been divided into a number of different classes, depending on the properties observed at different wavelengths. Typically the optical (and radio) band is used as a reference band for classification; considering RQ AGN: i) objects which

show a blue optical continuum, with broad lines and narrow emission lines and $M_B > -23$ (where M_B is the absolute magnitude in the optical B band), are classified Seyfert 1 (Sy 1) galaxies; a Seyfert galaxy has a quasar-like (compact) nucleus, but the features of the host galaxy are clearly detected (typically spiral galaxies). When the sources show only narrow lines and a redder optical/UV continuum, they are classified as Seyfert 2 (Sy 2). ii) In the high luminosity regime ($M_B < -23$), the sources are classified as quasars; the quasar spectra are similar to Seyferts, but the galaxy starlight is not seen, as it is overwhelmed by the nuclear emission. Similarly to Seyfert galaxies, the quasars are divided into QSO 1 and QSO 2.

Another class of objects identified amongst the RQ AGN are the LINERS (low-ionisation nuclear emission line region galaxies; Heckman 1980), whose spectra are similar to the Sy 2 galaxies, but with stronger low-ionisation emission lines (such as [OI] $\lambda 6300$ Å and [NII] $\lambda 6548, 6584$ Å).

Similarly to the the Seyfert galaxy classification, when the sources have also strong radio emission (RL; see Sect. 1.1.2), they are classified as broad-line radio galaxies (BLRG) and narrow-line radio galaxies (NLRG), which are the radio-loud analogues of Sy 1 and Sy 2, respectively. These RL AGN appear to be hosted typically in elliptical galaxies, rather than spirals. Amongst the RL AGN, objects with strong variability at all wavelengths have been distinguished⁶, e.g. BL Lacertae (BL Lac) objects, which have a rather flat optical continuum with no strong emission or absorption lines.

1.2 The Unification scheme

Although several classes of objects have been identified through the years amongst the AGN population, it is now clear that they are different manifestations of the same phenomenon (Sect. 1.1.1): according to the Unified model for AGN (Antonucci 1993), the AGN phenomenon is the same in all the various classes and the different properties they show, are due only to inclination effects.

⁶Other sub-classes have been defined amongst the RL AGN, however they are not mentioned here as they are not relevant to the work presented in this thesis.

In this scheme, the angle from which a source is observed plays a key role in its classification and two main classes can be defined, i.e. type-1 AGN and type-2 AGN: i) objects which show a blue optical continuum, with broad and narrow emission lines, are classified as type-1 AGN; they are objects observed at small inclination angle (face on, see Fig. 1.1), the nucleus and the BLR are directly visible and their emission is not hidden by a large amount of obscuring material; ii) sources showing a redder optical/UV continuum, with only narrow emission lines detected in their spectra, are thought to be observed at high inclination angles, through a large amount of absorbing gas and dust (e.g. through the obscuring torus) that hides the central region of the AGN and the BLR, but not the NLR which lies at larger distances from the nucleus; these sources are classified as type-2 (obscured, or narrow line) AGN.

Extending this classification to the X-ray band, type-1 AGN are expected to be sources which show low X-ray absorption in their spectra (typically $N_{\text{H}} \lesssim 10^{22} \text{ cm}^{-2}$; unabsorbed AGN⁷), while type-2 AGN are expected to be absorbed by larger column densities ($N_{\text{H}} \geq 10^{22} \text{ cm}^{-2}$). More specifically, considering radio-quiet sources, in the low X-ray luminosity regime ($L_{2-10 \text{ keV}} \approx 10^{42} - 10^{44} \text{ erg s}^{-1}$), AGN are classified as Sy 1 if they show no obscuration in the optical and low absorption in the X-ray bands, while the obscured and X-ray absorbed ones are Sy 2. In the high luminosity regime ($L_{2-10 \text{ keV}} \geq 10^{44} \text{ erg s}^{-1}$), the sources are classified as type-1 QSO and type-2 QSO, accordingly.

In general the unified scheme is applied also to radio-loud AGN (e.g. Orr & Browne 1982), as the classification of such objects is also based on orientation effects (e.g. BLRG and NLRG are type-1 and type-2 AGN, respectively); in particular, BL Lac objects are observed face-on (through the relativistic jets), in which the jet emission dominates the spectrum (causing the strong variability and a relatively featureless non-thermal spectrum; Urry & Padovani 1995).

⁷We note that this hydrogen column density value, which is generally used to separate between absorbed and unabsorbed AGN, is chosen more for historical reasons than for established physical ones.

1.2.1 Modifications to the unification scheme

Although in general there is good agreement between the optical and X-ray classifications, supporting the unification scheme, some exceptions can be found. A fraction of type-1 AGN with significant absorption in the X-ray band or type-2 AGN unabsorbed in X-rays have been found in survey studies (see Chapters 3, 5; e.g. Page et al. 2001; Panessa & Bassani 2002), suggesting that the classification is not often straightforward. Optical dust reddening is often observed to be lower than expected from the X-ray absorption, considering the standard Galactic gas-to-dust ratio: $A_V/N_H = 1/1.8 \times 10^{21}$ (e.g. Predehl & Schmitt 1995; see e.g. Maccacaro et al. 1982; Maiolino et al. 2001b; Akiyama et al. 2002; Willott et al. 2004). There is also observational evidence that a few sources appear to change type, showing variable X-ray absorption and/or optical reddening (causing the BL to appear or disappear; Matt et al. 2003). In some cases, obscuring material not residing in the circumnuclear torus, but at large distance from the nucleus, such as dust in the NLR (Polletta et al. 2008) or a dust lane in the host galaxy (Rigby et al. 2006; Martínez-Sansigre et al. 2006; Brand et al. 2007), has been invoked to explain the “misclassification” between optical and X-ray bands.

These results indicate that the obscuring molecular torus may in reality be a more complex structure. Current interpretations suggest the presence of a clumpy torus, formed by dusty clouds with a range of optical depths (Nenkova et al. 2008a,b), or obscuring regions of different column densities and different opacity, which may be the BLR clouds themselves, passing through the line of sight and causing the variation in the observed spectra (Elvis et al. 2004; Risaliti et al. 2007; Risaliti 2009). Other scenarios invoke high velocity winds from the accretion disc (e.g. Elvis 2000; Elvis et al. 2004) or warped discs to be the source of obscuration in AGN, not requiring the presence of the molecular torus invoked in the unified model (e.g. Lawrence 2007).

Other situations where the simple unification scheme (Antonucci 1993) may not be sufficient to explain the observational results involve the luminosity dependence of the fraction of type-2 AGN: a decrease in the absorbed fraction with X-ray luminosity has

been found by many authors⁸ (Ueda et al. 2003; Steffen et al. 2003; Hasinger 2004, 2008). A similar decrease was also found in studies based on optically selected AGN (Simpson 2005) and mid-IR selected AGN (Maiolino et al. 2007). If the simple unification model is assumed, the fraction of the absorbed sources, which is a function only of the observation angle (and hence of the covering factor of the molecular torus), should not vary with luminosity. In order to explain the absorbed fraction dependence on luminosity, a “receding torus model” has been suggested, in which the more luminous AGN sublimate the dust in the inner parts of the torus out to larger distances than the less luminous AGN, leading to a larger opening angle for more luminous AGN (e.g. Lawrence 1991).

1.3 General picture

Since they were first discovered, the study of AGN became an important part of astronomical research. With their persistent high luminosity, they could be detected up to higher redshifts than any other object known, therefore their importance in the cosmological context soon became clear.

Over the last two decades, observations in the local Universe have revealed that almost all galaxies host a super-massive black hole (SMBH) in their centre (Kormendy & Richstone 1995; Magorrian et al. 1998; Kormendy & Gebhardt 2001). Moreover, there is increasing observational evidence of a relation between the galaxy bulge properties and the SMBH: this connection is observed, for example, in the $M_{\text{BH}} - \sigma$ relation (see Fig. 1.6; Magorrian et al. 1998; Ferrarese & Merritt 2000; Gebhardt et al. 2000; Marconi & Hunt 2003), which indicates a tight dependence of the mass of the central black hole on the velocity dispersion of the stars in the galaxy bulge (σ); or the relation of M_{BH} with the luminosity of the galaxy spheroid ($M_{\text{BH}} - L_{\text{bulge}}$; Ferrarese & Merritt 2000; Gebhardt et al. 2000; Marconi & Hunt 2003), or with the mass of the galaxy bulge ($M_{\text{BH}} - M_{\text{bulge}}$; Gebhardt et al. 2000; McLure & Dunlop 2002; Marconi & Hunt 2003).

These correlations clearly indicate that the evolution of the galaxies must be strongly

⁸It is not yet clear however if this dependence is real or if it is an observational effect (e.g. Dwelly & Page 2006; Treister & Urry 2006).

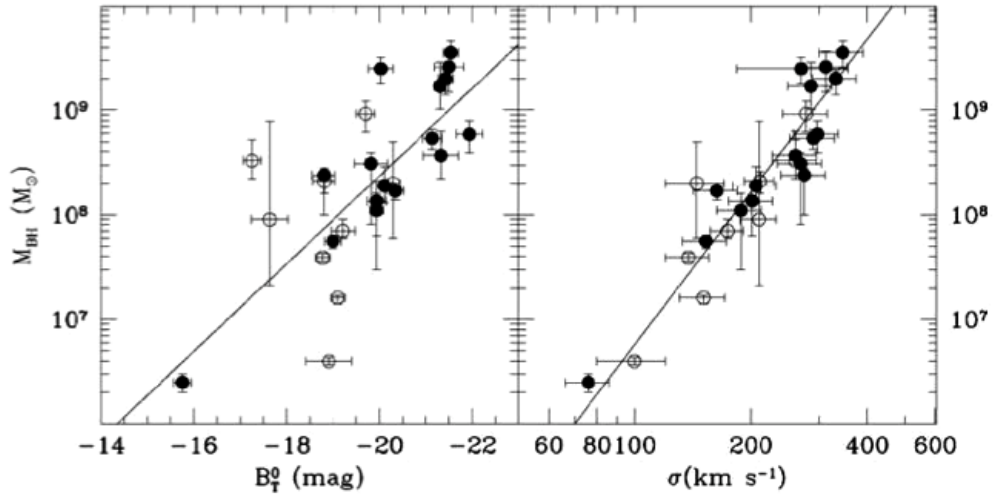


Figure 1.6: BH mass vs. absolute blue luminosity of the host galaxy bulge (left) and M_{BH} vs. the central velocity dispersion of the host galaxy bulge (right). Figure adapted from Ferrarese & Merritt (2000).

linked to the evolution of the BH hosted in their centre. The current proposed scenario is that strong interactions of massive galaxies (e.g. mergers between hot gas-rich spheroids) provide a large amount of gas, which fuels both the star formation (SF) and BH active growth. In this phase, the bulk of the star formation of the galaxy occurs, leading to violent starburst activity which causes the chemical enrichment of the galaxy and the interstellar medium (ISM) around the nuclear region. The central black hole experiences a rapid growth, heavily obscured by a significant amount of circumnuclear gas (“starburst phase”; e.g. Granato et al. 2004; Li et al. 2007). When the merging galaxies coalesce, a large amount of gas is brought into the centre, leading to a peak of the accretion onto the SMBH. At this point, strong galactic winds powered by the BH develop (“AGN feedback”), driving away the obscuring gas and dust, leaving the SMBH optically visible (“quasar phase”). When the BH outshines the galaxy as a bright QSO, the AGN feedback suppresses the star formation in the galaxy and self-regulates the SMBH accretion (e.g. Granato et al. 2001; Di Matteo et al. 2005; Hopkins et al. 2006; Li et al. 2007). Eventually, as the gas is further heated and expelled, the quasar activity can no longer be maintained and both the star formation and the quasar activity die down, leaving a quiescent BH at the centre of a red old galaxy (passive evolution).

Following this scenario, most of the accretion onto the BH must occur in obscured en-

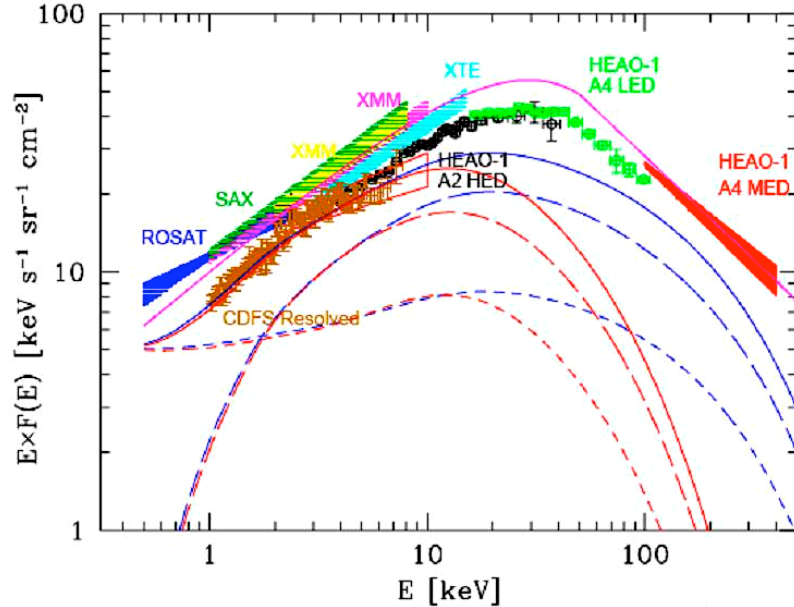


Figure 1.7: X-ray background spectrum measured from the integrated contribution of the X-ray sources found in deep and shallow X-ray surveys to the X-ray background spectrum (different missions are indicated in the plot with different colours); the solid magenta curve represents an analytical fit of the various measurements; the contribution expected from unabsorbed AGN ($N_{\text{H}} < 10^{22} \text{ cm}^{-2}$, short-dashed lines) and from absorbed (Compton-thin) AGN ($N_{\text{H}} = 10^{22} - 10^{24} \text{ cm}^{-2}$, long-dashed line) are shown. Figure adapted from Comastri (2004)

vironments, before the quasar phase (which represents only a brief part of the galaxy life cycle), as implied also by observations (e.g. Fabian & Iwasawa 1999; Brandt & Hasinger 2005, for a review). This is also suggested by the synthesis models of the X-ray background (Setti & Woltjer 1989; Comastri et al. 1995; Comastri 2001; Gilli et al. 2001, 2007), which require a large population of obscured AGN at high redshift ($z > 1$) in order to reproduce the observed hard XRB spectrum (see below).

Therefore, studying the AGN population at different phases of their evolution is essential to probe this scenario and to have a complete understanding of the accretion history of the universe and the evolution of its content across cosmic time.

1.3.1 X-ray Background

The cosmic X-ray background (XRB) was discovered in the 1960s, with the launch of the first X-ray instruments: together with the first X-ray sources, a diffuse background emission from the whole sky was detected. The high degree of isotropy of this radiation

suggested the origin was mainly extra-galactic, however the cause of the XRB emission was not understood. Since its discovery, great effort has been expended both observationally and theoretically, to explain the nature of this background.

At the end of the 1970s, thanks to the various measurements from the available X-ray satellites, the spectrum of the XRB in the 2 – 100 keV band was determined: the data showed that the XRB spectrum has a characteristic “bell” shape, with a peak at $\sim 30 - 40$ keV (Fig. 1.7). It is now clear that the XRB emission is due to the superposition of the emission from discrete sources: at low energies ($E = 0.1 - 0.5$ keV) the contribution to the background emission is mostly of Galactic origin, while at higher energies extragalactic sources (mainly AGN, which constitute the majority of the X-ray source population) are responsible for this emission. However, until the 1990s no more than 50% of the total intensity was resolved (at energies $E < 2$ keV).

AGN population synthesis models, firstly developed in 1989 (e.g. Setti & Woltjer 1989; Comastri et al. 1995; Gilli et al. 2001, 2007), propose that the observed spectrum of the XRB up to 100 keV band is due to a population of obscured AGN and bright unobscured AGN, assuming a wide range of column densities and luminosities.

Impressive results have been obtained with the current X-ray observatories (*Chandra* and *XMM-Newton*), which have carried out a variety of X-ray surveys, sampling complementary populations of objects: i) deep-pencil beam surveys (e.g. the Chandra Deep Field North, CDF-N, and the Chandra Deep Field South, CDF-S; Rosati et al. 2002; Alexander et al. 2003) which probe the X-ray sky at fainter fluxes, both reaching higher redshifts and low luminosity nearby objects; ii) medium-depth wide area surveys (e.g. ASCA MSS/LSS, Ueda et al. 2003; HELLAS2XMM, Baldi et al. 2002; Fiore et al. 2001, 2003; 2XMM Watson et al. 2009, see Chapter 2) which sample the X-ray population at medium redshifts; iii) shallow surveys which allow the characterisation of the bright nearby population. Indeed, the combination of deep surveys and shallower large area surveys resolved $> 90\%$ of the X-ray background below 5 keV as integrated emission from discrete absorbed and unabsorbed X-ray sources (Mushotzky et al. 2000; Hasinger et al. 2001; Alexander et al. 2003; Worsley et al. 2004). However, at higher energies ($E > 5$ keV)

only 50 – 60% of the XRB has been resolved (e.g. Worsley et al. 2004, 2005; see Fig. 1.7).

1.3.2 Open issues

Over the past decades, many studies have focused on the determination of the complete census of the AGN, in particular the bright, obscured objects (type-2 QSOs). Although a large fraction of the XRB has been resolved from the X-ray surveys available to date, the unresolved fraction of the XRB at higher energies ($E > 5$ keV) indicates that a large number of obscured AGN, and heavily obscured AGN (Compton-thick), required to reproduce in particular the peak of the background emission at $E \approx 30$ keV (see Fig. 1.7; Setti & Woltjer 1989; Comastri et al. 1995; Gilli et al. 2001, 2007; Hasinger 2008), are still missing from current flux-limited X-ray surveys.

Moreover, studies of the X-ray AGN luminosity function up to redshift $z \approx 3 - 4$ (Ueda et al. 2003; La Franca et al. 2005; Hasinger et al. 2005; Hasinger 2008; Ebrero et al. 2009) show a strong dependence of the AGN space density evolution on X-ray luminosity (“Luminosity dependent density evolution”, LDDE): at increasing X-ray luminosity, the redshift at which the peak space density occurs increases. This trend means that high luminosity AGN, powered by massive black holes in gas-rich galaxies, form and evolve earlier and more rapidly than lower luminosity AGN, which have a slower growth, probably due to the lack of gas fueling the accretion (Hopkins et al. 2006). A similar trend has been confirmed by studies in the optical and radio bands (Cirasuolo et al. 2005; Bongiorno et al. 2007). Hence, the bulk of the QSO population is expected to peak at high redshift ($z \approx 2 - 2.5$; Gilli et al. 2007).

According to these observational and theoretical results, together with the BH/galaxy co-evolution scenario (see Sect. 1.3), a large population of obscured, high redshift quasars is predicted (although their fraction amongst the QSO population at high redshift is still strongly debated).

Despite the huge progress made so far, which yielded the detection of a large population of obscured (type-2) AGN, mainly in the Seyfert luminosity regime ($L_X = 10^{42} - 10^{44}$

erg s⁻¹; Alexander et al. 2003; Guainazzi et al. 2005; Wang et al. 2007), and an increasing number of type-2 QSO (Zakamska et al. 2003, 2004; Martínez-Sansigre et al. 2006), the number of these bright obscured sources is still small, and the census of the AGN population is still far from complete, especially at high redshift ($z > 3$).

1.4 Extreme X-ray-to-optical sources (EXOs)

A high X-ray-to-optical flux ratio⁹ ($f_X/f_{\text{opt}} \geq 10$, at least ten times higher than typical for X-ray selected AGN) is considered to be a good tracer of highly obscured high redshift AGN (type-2 QSO; e.g. Fiore et al. 2003; Severgnini et al. 2005). Indeed, the f_X/f_{opt} ratio has been largely used as an indicator of the source classification (Maccacaro et al. 1988): normal galaxies have typically $f_X/f_{\text{opt}} \lesssim 0.1$, while the dominant X-ray selected AGN population has $0.1 < f_X/f_{\text{opt}} < 10$, with the obscured AGN having on average $f_X/f_{\text{opt}} \gtrsim 10$ (Figure 1.8; Mignoli et al. 2004).

However understanding the properties of the sources from the f_X/f_{opt} ratio is not straightforward: according to its definition, the f_X/f_{opt} describes the ratio of the observed nuclear X-ray flux to the optical flux, which is due to a combination of nuclear and galaxy emission. In type-1 AGN the ratio is mostly due to nuclear emission in both bands, thus the f_X/f_{opt} ratio depends mainly on the AGN SED. The distribution of the X-ray-to-optical ratio around $f_X/f_{\text{opt}} \approx 1$, therefore, reflects the intrinsic variations of the AGN SEDs (see Sect. 1.1.2). As the source obscuration increases, the contribution from the galaxy light becomes more and more important in the optical band and the f_X/f_{opt} ratio becomes roughly a ratio between the nuclear X-ray emission and the optical host galaxy emission. Since the galaxy R -band luminosity has a relatively small scatter around the mean value $L_R = 10^{11} L_\odot$, while the AGN luminosity spans a much wider range, for high luminosity, obscured AGN the highest f_X/f_{opt} values can be produced (Fiore et al. 2003; Comastri & Fiore 2004).

Sources with $f_X/f_{\text{opt}} \geq 10$, also known as EXOs (Extreme X-ray-to-Optical objects;

⁹Defined as the ratio between the observed X-ray flux in the 2 – 10 keV energy band and the optical R band flux.

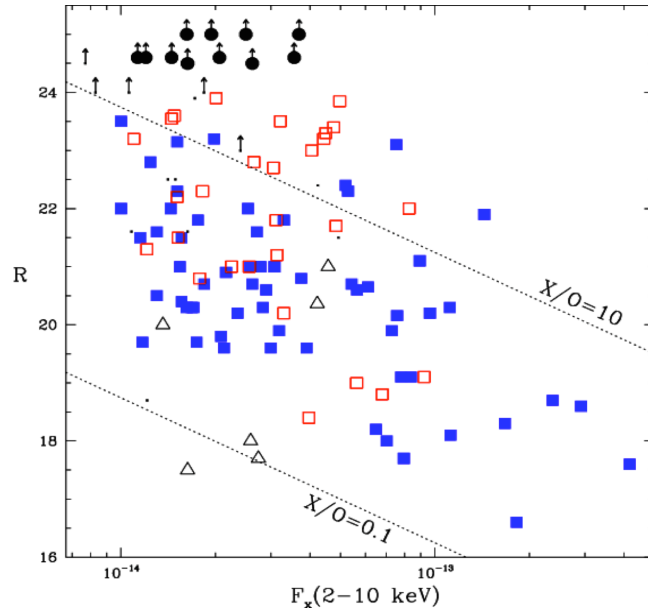


Figure 1.8: X-ray flux (2 – 10 keV) vs. R -band magnitude for a sample of X-ray selected sources from Mignoli et al. (2004). The blue squares represent the type-1 AGN; open red squares are type-2 AGN; black open triangles are normal galaxies; the small black dots are unidentified sources. The black filled circles are the extreme EXOs in the Mignoli et al. (2004) sample.

Koekemoer et al. 2004), constitute a fraction of a few to $\sim 20\%$ of the AGN population (depending on the X-ray energy band used for their selection; Fiore et al. 2003; Barcons et al. 2007); they are believed to be objects where the UV/optical/NIR emission is heavily obscured by dust, whilst the X-ray flux, although strongly absorbed at soft X-ray energies ($E < 2$ keV) is less affected by absorption at higher energies, thus yielding a high f_X/f_{opt} ratio. In order to have extreme f_X/f_{opt} values, sources must also have high luminosity, otherwise the host galaxy starlight contribution to the optical flux may constrain the X-ray-to-optical ratio to lower values. Hence, the EXO population is likely to hide a large fraction of type-2 QSO.

It is worth noting though, that besides the obscured (type-2) AGN, there are other classes of objects characterised by high f_X/f_{opt} ratios. The high ratios for such classes of objects have different origin:

- relatively rare galactic objects like X-ray binaries (XRBs), cataclysmic variables (CVs), isolated neutron stars (INS) or Ultraluminous X-ray sources (ULX) can intrinsically have high f_X/f_{opt} values;

- extreme BL Lac objects, where the spectrum is dominated by non-thermal processes due to the relativistic jets (Sect. 1.1.3);
- high- z unobscured AGN ($z \sim 4 - 5$), where the redshift causes the high f_X/f_{opt} values: the optical emission short-ward of the R band may be completely undetected due to the Lyman break falling into the observed optical band, reducing significantly the observed flux;
- high- z clusters of galaxies, where the X-ray emission comes from the intra-cluster medium and thus does not have an optical counterpart¹⁰.

Nevertheless, these different classes seems to constitute only a small fraction of the EXO population (see Chapter 3)

As expected from the above scenario, the EXOs are usually detected in X-rays and in near-IR, but very difficult to detect in the optical bands. By definition, in fact, sources with such extreme f_X/f_{opt} have faint optical magnitudes and this is even more true for the faint X-ray sources found in the deep, pencil-beam surveys (Koekemoer et al. 2004; Civano et al. 2005). At such faint X-ray fluxes ($f_X = 10^{-15} - 10^{-16} \text{ erg cm}^{-2} \text{ s}^{-1}$), sources with $f_X/f_{\text{opt}} > 10$ have R magnitudes $\sim 25.5 - 28$, so optical follow-up observations are very difficult or impossible. Studies performed at higher X-ray fluxes ($f_X \sim 1 - 40 \times 10^{-14} \text{ erg cm}^{-2} \text{ s}^{-1}$ for the HELLAS2XMM survey; see Fiore et al. 2003; Mignoli et al. 2004), for which optical data are available, have classified more than 50% of their extreme f_X/f_{opt} sources as type-2 QSOs. These studies also found that a significant fraction of the EXO population shows the extremely red colours of the EROs (Extremely Red Objects, with typical values $R - K \geq 5$, Elston et al. 1988; see Fiore et al. 2003; Mignoli et al. 2004). EXOs with optical-NIR colours of EROs are thus amongst the best candidates to be the missing high-redshift type-2 QSO population.

¹⁰Thus this class of objects may be mistakenly included in the EXO population.

1.5 Aims of this thesis

The aims of this thesis are to study the multi-wavelength properties of one of the largest samples of bright X-ray selected EXOs assembled so far (see Sect. 2.4) from one of the largest medium-depth area surveys currently available (2XMM). The main goals in performing this analysis, which involves optical and NIR photometry and optical and X-ray spectroscopy (Chapters 2 and 4), are to constrain the fraction of EXOs powered by AGN focusing on the bright, highly obscured ones (type-2 QSO), testing the effectiveness of our methods in finding this elusive class of objects.

Another aim of this thesis is to place constraints on the evolution of the AGN population across cosmic time, by studying a highly complete and homogeneous sample of bright X-ray sources, selected from a deep small area survey (SXDS; see Chapter 5). The goals of this work are the determination of the X-ray spectral properties of the AGN in this survey and the investigation of the dependence of the absorbed AGN fraction with luminosity. The investigation of the characteristics of the high f_X/f_{opt} sources amongst this sample, in comparison with the properties of the sample extracted from a shallower X-ray catalogue (2XMMp; see Chapter 2) is also a focal point of this work.

CHAPTER 2

The EXO Sample in 2XMMp

This chapter is aimed at giving a background understanding of the data used in this thesis and the analysis and methods that will be employed in the following chapters.

Here the XMM-Newton X-ray data and the Sloan Digital Sky Survey (SDSS) data are described. After a brief introduction to the XMM-Newton satellite, the characteristics of the X-ray data are reported, focusing on the 2nd release of the XMM serendipitous source catalogue (2XMM) and the cross-correlation with the 5th release of the SDSS catalogue. The technique used to perform the cross-match between the two catalogue sources is explained and in particular the process and criteria used to select my sample of Extreme X-ray-to-Optical ratio sources are described in detail.

2.1 The X-ray data

2.1.1 The *XMM-Newton* Observatory

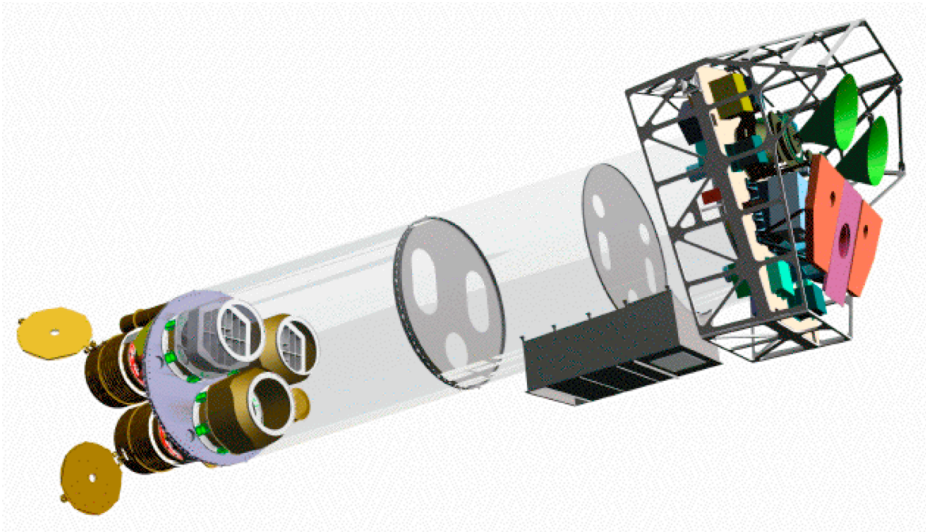


Figure 2.1: Sketch of the *XMM-Newton* observatory payload. On the left the three mirror modules can be seen, while on the right the back-end of the instrument platform (including the EPIC and RGS cameras), with all the radiators is visible. The image is adapted from Jansen et al. (2001).

The X-ray Multi-Mirror Observatory (*XMM-Newton*; Jansen et al. 2001) is the largest satellite developed by the European Space Agency (ESA) and it is part of the ESA’s Horizon 2000 Science Programme. Launched in December 1999, XMM is the most powerful X-ray telescope ever placed in orbit: it carries three advanced grazing-incidence X-ray telescopes, each containing 58 high-precision Wolter I concentric mirrors, highly nested in a co-axial and co-focal configuration, in order to offer the largest collecting area possible. Each mirror shell consists of a paraboloid and an associated hyperboloid surface, designed to utilize a very shallow grazing angle of $30'$ to provide sufficient reflectivity at high energies. The diameter of the mirrors ranges from 30.6 cm for the smallest mirrors to 70 cm for the largest ones and the focal length of the mirror system is 7.5 m. An “open” view of the *XMM-Newton* payload is shown in Fig. 2.1.

In the focal plane of each mirror module is one of the three CCD cameras of the European Photon Imaging Camera (EPIC), the main X-ray instrument of *XMM-Newton*

(see Sect. 2.1.2): one pn CCD imaging camera (Strüder et al. 2001) and two MOS CCD imaging cameras (Turner et al. 2001). However, half of the incoming light from the two telescopes associated with the MOS cameras does not reach the imaging detectors (only $\sim 44\%$ reaches the MOS cameras), but is deflected to a secondary focus, where the Reflection Grating Spectrometer (RGS; den Herder et al. 2001), the other X-ray instrument on board of *XMM-Newton*, is located. The RGS is composed of two spectrometers which operate in the 0.33–2.5 keV energy range and allow X-ray spectroscopy with a resolution of $E/\Delta E = 200\text{--}800$.

Beside the X-ray instruments, *XMM-Newton* is equipped with an optical telescope co-aligned with the X-ray telescopes: the Optical Monitor telescope (OM; Mason et al. 2001). This has a diameter of 30 cm and allows imaging and spectroscopy in a broad-band wavelength range ($\lambda = 1800\text{--}6000 \text{ \AA}$), using three ultra-violet and three optical filters and two low-dispersion UV and optical gratings.

As all the X-ray data used in this thesis are derived from the EPIC cameras, I will focus the description on this particular instrument, in order to better understand the characteristics of the data and the required reduction and analysis performed.

2.1.2 EPIC

The European Photon Imaging Camera (EPIC) is the main focal plane instrument of *XMM-Newton*. The three cameras composing the instrument permit sensitive imaging observations over the telescope's field of view (FOV) of ~ 30 arcmin diameter and in the energy range from 0.15 to 15 keV with moderate spectral resolution ($E/\Delta E \sim 20\text{--}50$) and on-axis spatial resolution of $\sim 5'' - 6''$ (FWHM).

The EPIC cameras consist of charge-coupled devices (CCD) which operate in photon counting mode with a fixed, mode dependent frame read-out frequency. Two of the cameras use Metal Oxide Semi-conductors (MOS) CCDs, developed jointly by Leicester University and English Electric Valve (EEV), in the UK, and the third

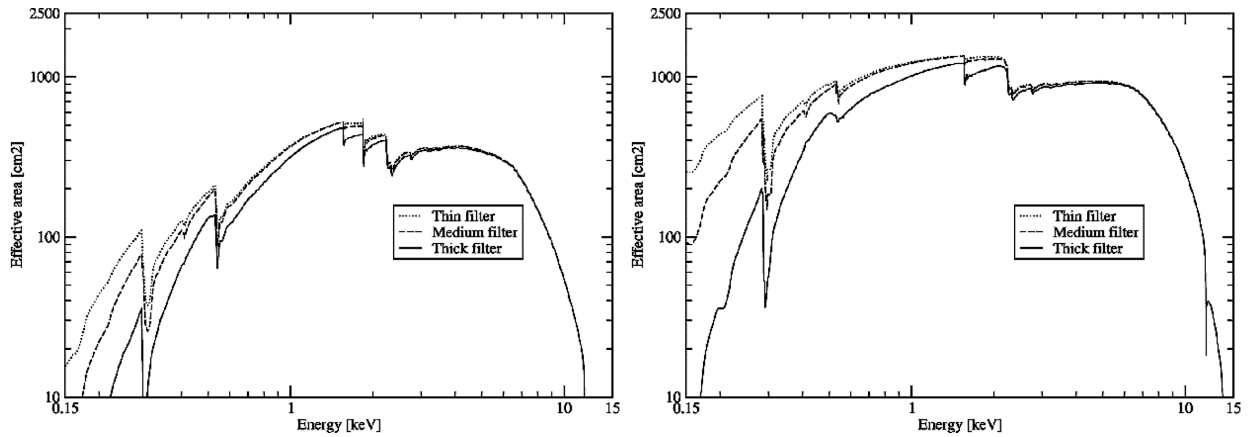


Figure 2.2: Effective areas of the EPIC MOS cameras (left) and the EPIC pn camera (right), with the three different filters: thin, medium and thick. The figures are taken from http://xmm.esa.int/external/xmm_user_support/documentation/uhb/node32.html.

one uses a different type of CCD (pn CCD), developed by the Max Planck Institute for Extraterrestrial Physics in Garching (Germany). The two types of CCDs give different characteristics to the MOS and pn cameras, starting with the geometry of the CCD arrays (the main characteristics of the two types of cameras are reported in table 2.1).

Each EPIC MOS camera consists of seven front-illuminated silicon chips, each made of a matrix of 600×600 pixels ($\sim 40 \mu\text{m}$ square). The central CCDs are located at the focal point of the X-ray telescopes while the external ones are placed 4.5 mm upward, to follow approximately the curvature of the focal plane, improving the focus for off-axis sources. The mosaic of the 7 CCDs has a total imaging area of about 62 mm diameter on the focal plane, corresponding to a FOV of 28.4 arcmin (each pixel covers 1.1×1.1 arcsec). The two detectors are arranged orthogonally so that the CCDs gaps of one camera are covered by the other camera.

The MOS detectors have a thin layer of silicon of $40 \mu\text{m}$ depth and are very sensitive in the lower energy part of the X-ray spectrum with good energy resolution (~ 90 eV at 1.5 keV, FWHM), while the sensitivity and the resolution decrease at high energies (~ 135 eV at 6 keV). The high energy portion of the spectrum is better covered by the pn camera (see below). The on-axis effective areas of the MOS cameras are about 550 cm^2 at 1.5 keV and 100 cm^2 at 8 keV (Fig. 2.2, left).

Table 2.1: Overview of the main EPIC characteristics

Instrument	MOS	pn
Bandpass	0.15-12 keV	0.15-15 keV
FOV	$\approx 30'$	$\approx 30'$
Pixel Size	40 μm (1.1'')	150 μm (4.1'')
PSF (FWHM)	5''	6''
Readout Time	2.5 s	0.08 s
Energy Resolution ^a	~ 90 eV (~ 135 eV)	~ 120 eV (~ 160 eV)

Notes: a) At 1.5 keV and at 6 keV (in parenthesis).

The EPIC pn camera consists of a single back-illuminated high purity silicon wafer, formed by twelve pn CCD chips of 3×1 cm size. The total area of 36 cm^2 contains a matrix of 400×400 pixels, with pixel size of about 4.1 arcsec. Thanks to the 300 μm -thick silicon detectors and the absence of any insensitive layers on its rear side (where the X-rays strike the pn CCDs), the pn camera efficiency is extremely high and homogeneous from the very lowest to the highest *XMM-Newton* energies (over 90% from 0.5 to 10 keV). As the CCDs operate in parallel, the readout time of the 768 independent channels is very small: an image acquisition requires only 80 ms (the MOS readout time is about 2.5 s). The on-axis effective area for the pn camera is about 1400 cm^2 at 1.5 keV and 600 cm^2 at 8 keV (Fig. 2.2, right) and the energy resolution is ~ 120 eV at 1.5 keV and ~ 160 eV at 6 keV (FWHM).

The effective areas of the EPIC detectors are modified, especially in the low energy portion of the spectrum, by the choice of the optical blocking filter, as shown in figure 2.2. These filters are necessary because the EPIC CCDs are not only sensitive to X-ray photons, but also to IR, visible and UV radiation which may contaminate the X-ray signal. All the EPIC cameras are provided with four aluminised optical blocking filters, which help to minimise this contamination: two thin filters, a medium and a thick filter. However, because the use of the blocking filter limits necessarily the softest X-ray energy response, their choice has to be carefully made in order to maximise the scientific return.

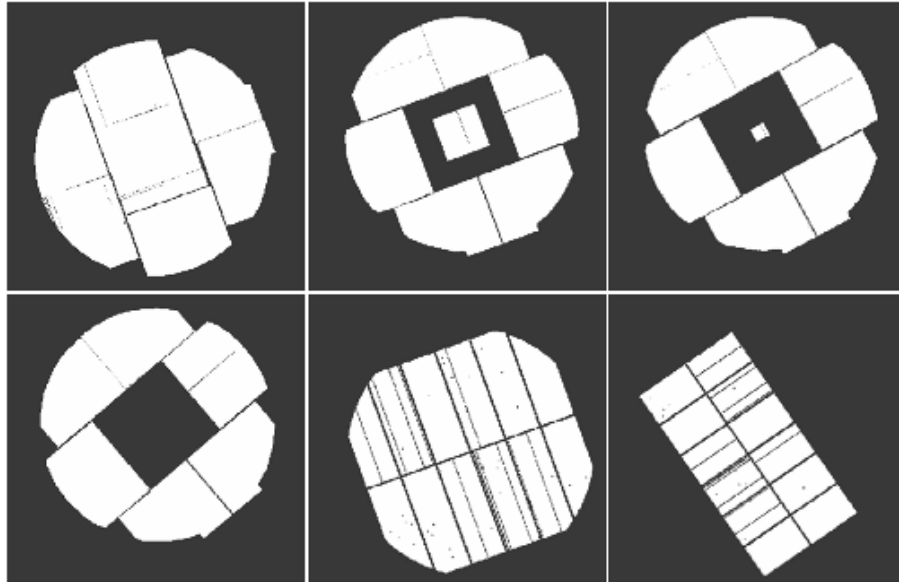


Figure 2.3: Sky footprints of the EPIC MOS and pn observing modes. In the top row, from left to right, there are the MOS full-frame mode and partial windows mode. In the bottom row, there are the MOS fast uncompressed (fast compressed) on the left and the pn full window mode and large window mode (Watson et al. 2009).

Each EPIC camera can operate in several observing modes, shown in Fig. 2.3, which imply different time resolutions and count rate capabilities. In full-frame and extended full-frame (available for pn only) all pixels of all the CCDs are read out and thus the full FOV is covered. In partial window modes, the external 6 CCDs of the MOS cameras are always exposed and remain in standard imaging mode, while the central one can be operated in a different mode of science data acquisition (e.g. in fast uncompressed and compressed modes, the central CCD operates in timing mode¹), reading out only part of the CCD chip; in the pn camera only half of the detector is read out (large window mode) or only part of a CCD is used (small window, timing and burst mode²). For the MOS cameras the maximum count rates (due to telemetry constraints) for full window and partial window imaging modes are about 115 counts/s and 230 counts/s for timing mode. For the pn camera the limit is ~ 600 counts/s for the imaging modes and ~ 450 counts/s for the timing mode.

¹In timing mode imaging is made only in one dimension, along the column axis; along the row direction, data from a predefined area on one CCD chip are collapsed into a one-dimensional row to be read out at high speed.

²Burst mode is a particular type of timing mode of the pn camera, which offers very high time resolution.

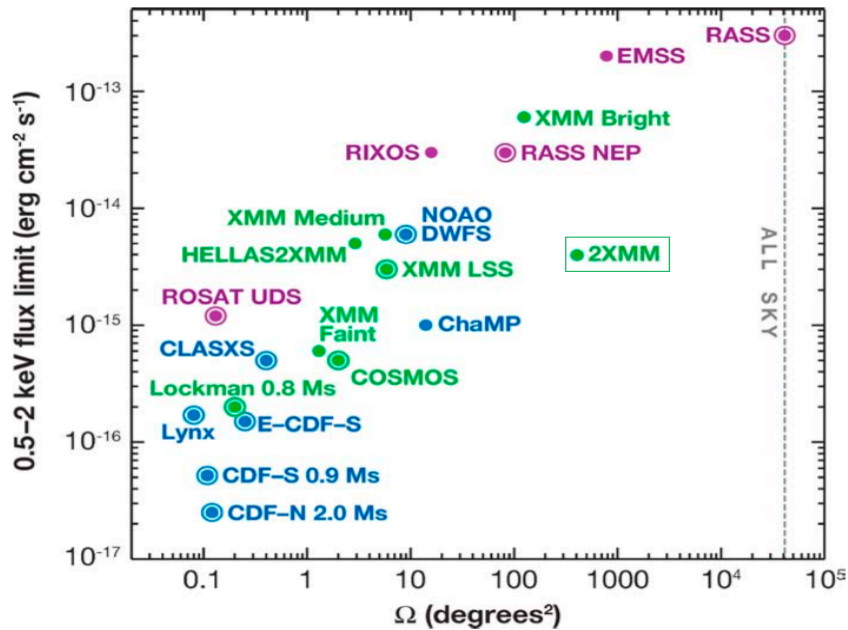


Figure 2.4: Comparison of sky coverage and flux limit (0.5-2 keV) of the main existing X-ray surveys by *XMM-Newton* (green), Chandra (blue) and earlier missions (magenta). Circled dots are the contiguous surveys. The vertical dotted line shows the solid angle of the whole sky. Figure adapted from Brandt & Hasinger (2005).

2.1.3 The 2XMMp and 2XMM catalogues

The 2XMMp catalogue is the pre-release version of the second comprehensive catalogue of serendipitous X-ray sources (2XMM; Watson et al. 2009) detected by the *XMM-Newton* observatory. The 2XMMp catalogue was produced by the *XMM-Newton* Survey Science Centre (SSC) and was released in July 2006. It contains more than 153000 X-ray detections from 2400 EPIC observations made between February 2000 and April 2006. The survey covers a large sky area of $\sim 400 \text{ deg}^2$ ($\sim 285 \text{ deg}^2$ overlap corrected). The 2XMMp catalogue includes $\sim 65\%$ of the fields and $\sim 75\%$ of the sky area covered by 2XMM, while $\sim 88\%$ of all 2XMMp sources appear in the 2XMM catalogue (Watson et al. 2009). The 2XMM catalogue contains source detections from 3491 EPIC observations, covering a total sky area of $\sim 560 \text{ deg}^2$ (360 deg^2 non-overlapping area).

2XMM is the largest X-ray source catalogue ever produced, containing almost twice as many discrete sources as either the ROSAT survey or pointed catalogues. 2XMM complements deeper Chandra and *XMM-Newton* small area surveys (Fig. 2.4), probing a large sky area at the flux limit where the bulk of the objects that contribute to the X-ray

Table 2.2: *XMM-Newton* energy bands used in the data processing of the 2XMM catalogue.

Band Number	Energy (keV)	Notes
1	0.2 – 0.5	
2	0.5 – 1.0	
3	1.0 – 2.0	
4	2.0 – 4.5	
5	4.5 – 12.0	
6	0.5 – 2.0	“soft band”
7	2.0 – 12.0	“hard band”
8	0.2 – 12.0	“full band”
9	0.5 – 4.5	“XID band”

background lie. The median flux in the full energy band (0.2–12 keV) of the catalogue sources is about 2.5×10^{-14} erg cm $^{-2}$ s $^{-1}$; in the soft energy band (0.5–2 keV) the median flux is $\sim 5.8 \times 10^{-15}$ erg cm $^{-2}$ s $^{-1}$, and in the hard band (2–12 keV) it is $\sim 2 \times 10^{-14}$ erg cm $^{-2}$ s $^{-1}$; the flux values from the three EPIC cameras are overall in agreement to $\sim 10\%$ for most energy bands (Mateos et al. 2009). The positional accuracy of the detections is generally $< 5''$ (99% confidence radius), with typical values $\sim 1'' - 2''$.

All the observations included in the 2XMM catalogue were processed through the SSC pipeline (Pipeline Processing System, PPS) which produces the calibrated event files, identifies low-background time intervals (Good-Time intervals, GTI), generates multi-energy band images, exposure maps and background maps for each EPIC camera and performs source detection. Only observations with exposure time > 1000 s were selected for the event-list processing stage and image creation and further selection criteria selected the high quality images used for the detection stage (see Watson et al. 2009 for details). The source detection was performed in simultaneous steps on each image in 5 different energy bands (1-5, see table 2.2) and on the three EPIC cameras (pn, MOS1 and MOS2). As final products of this stage, source positions, detection likelihood, source morphology, fluxes and X-ray colours (*Hardness Ratios*: $HR_n = (R_{n+1} - R_n)/(R_{n+1} + R_n)$, where R_n and R_{n+1} are the count rates in energy bands n and $n + 1$, with $n = 1 - 4$; see table 2.2) were computed. The astrometry was then calibrated by cross-matching the source list with the

USNO B1.0 catalogue (Monet et al. 2003). At high Galactic latitude ($|b| \geq 20^\circ$), about 74% of the fields were successfully corrected (systematic position errors $\sigma_{sys}=0.35''$) while for high object density fields (e.g. low Galactic latitudes, $|b| < 20^\circ$) only 33% were corrected; for all the sources in the remaining fields the σ_{sys} was fixed at $1.0''$ (in the 2XMMp catalogue higher values of the systematic errors were used: $\sigma_{sys}=0.5''$ for corrected frames and $\sigma_{sys}=1.5''$ otherwise).

2.2 The SDSS optical data

The Sloan Digital Sky Survey (SDSS) is an optical imaging and spectroscopic survey and is one of the most ambitious projects undertaken in the past few years. The aim of the project is to map a quarter of the sky obtaining observations of around 200 million objects and spectra for 1 million objects.

The survey, started in 2000, uses a dedicated 2.5 m wide-angle optical telescope (Gunn et al. 2006) based at Apache Point Observatory in New Mexico (Latitude $32^\circ 46' 49.30''$, Longitude $105^\circ 49' 13.50''$ W, Elevation 2788 m). Two instruments are mounted at the telescope: i) a 142 megapixel camera (Gunn et al. 1998), which carries out imaging in drift-scan mode providing observations of 1.5 deg^2 at a time in five broad bands u' , g' , r' , i' and z' (see Fig. 2.5; Fukugita et al. 1996), spanning a wavelength range from 3000 to 10000 Å; ii) a pair of double spectrographs fed by 640 optical fibers, with a diameter of $3''$ each, which allow spectroscopy of more than 600 objects in a single pointing.

The imaging camera operates using an array of 30 CCDs (2048×2048 pixels each) arranged in six columns of five CCDs each, aligned with the pixel columns of the CCDs themselves. The five SDSS filters (r' , i' , u' , z' and g') cover the respective rows of the array, in this order. During drift-scan mode, used for the survey, the telescope moves in great circles on the sky such that the images of objects move along the columns of the CCDs at the same rate the CCDs are being read out. This allows the camera to produce five images, one per each filter, as the objects move along the column of CCDs, with an effective exposure time of 54 s (the time required for an object to move from the beginning

of the CCD to the end) and a time interval from one filter image to another of 71.7 s (time to pass through the gap between the CCDs).

Because there are gaps also between the columns of CCDs, two passes along a great circle are required to obtain complete coverage. The second pass is offset from the first such that the area that fell in the gaps in the first pass is imaged in the centre of the columns in the second pass. An additional 24 CCDs are placed before and after the photometric CCDs in order to collect astrometric data. These CCDs are provided with neutral density filters which allow collection of data on bright reference stars without saturation.

The astrometry of the SDSS data is calibrated using the photometric CCDs in the r filter as reference CCDs. The r -band CCDs are calibrated by matching the bright stars detected by the SDSS with one of the two existing astrometric reference catalogs: i) the US Naval Observatory CCD Astrograph Catalog (UCAC, Zacharias et al. 2000), an all-sky astrometric catalog with a precision of 70 mas at its catalog limit of $r = 16$ mag and systematic errors < 30 mas; ii) Tycho-2 (Høg et al. 2000), an all-sky astrometric catalog with a median precision of 70 mas at its catalog limit of $V_T = 11.5$ mag and systematic errors < 1 mas. The second catalog is used only when a sky scan is not covered by the last version of the UCAC.

The two spectrographs used by the Sloan survey have both a blue channel and a red channel separated by a dichroic filter. A total 640 fibers (320 fibers per spectrograph) feed light from the focal plane into the spectrographs. A total of four 2048×2048 pixels CCDs (one for each channel of each spectrograph) collect the spectra which span the wavelength range 3800-9200 Å with a spectral resolution of $\lambda/\Delta\lambda \approx 2000$.

2.2.1 SDSS-DR5

The SDSS-DR5 (Adelman-McCarthy et al. 2007) is the fifth data release of the Sloan Digital Sky Survey and includes data taken up to June 2005 covering a sky area of 8000 deg². The catalogue, which embodies all the observations from the previous releases (DR1-DR4; Abazajian et al. 2003, 2004, 2005; Adelman-McCarthy et al. 2006), contains photometric

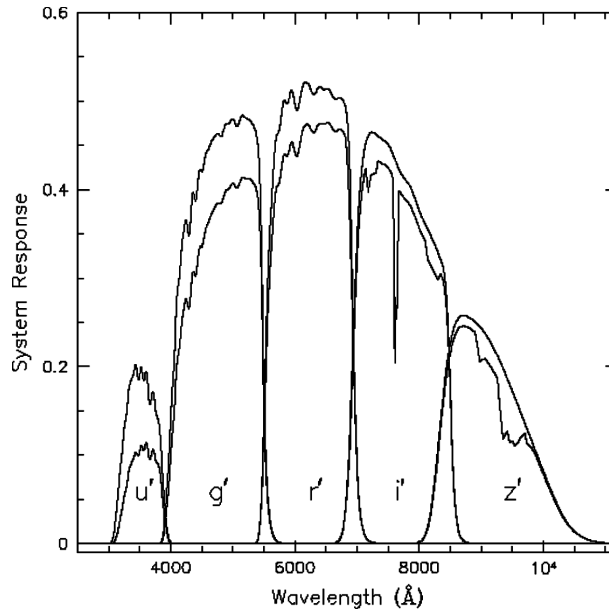


Figure 2.5: SDSS photometric filters u' , g' , r' , i' , z' , centred at 3500 Å, 4800 Å, 6250 Å, 7700 Å, 9100 Å, respectively (Adelman-McCarthy et al. 2007).

data for more than 210 million objects and about 1 million spectra. The imaging available in DR5 covers a contiguous region of the north Galactic cap centred approximately at $\alpha = 185^\circ$ and $\delta = +32.5^\circ$ (with small patches missing, which are now covered in the latest release of the survey catalogue: DR6, DR7; Adelman-McCarthy et al. 2008; Abazajian et al. 2009) and some southern stripes, one along the celestial equator and two centred at $\delta = +15^\circ$ and $\delta = -10^\circ$, respectively (see Fig. 2.6).

The SDSS imaging bands have a wavelength coverage from 3000 to 11000 Å, dividing this range into five essentially non-overlapping pass bands: u' , g' , r' , i' , z' , which peak at 3500 Å, 4800 Å, 6250 Å, 7700 Å, 9100 Å, respectively (Fig. 2.5; Fukugita et al. 1996). The zero point of this photometric scheme is the AB system of Oke & Gunn (1983)³. All the SDSS imaging data are performed under photometric conditions, with seeing better than $2''$ in the r' band (median seeing is $1.4''$). The 95% completeness limit for the detection of point sources in the r' band is 22.2 mag, while the magnitude limits for the other filters are 22.0 mag in the u' , 22.2 mag in the g' , 21.3 mag in the i' and 20.5 mag in z' bands. The photometric calibration is accurate to ~ 0.02 mag in the g' , r' , i' bands and

³This is true for the g' , r' and i' bands (with an uncertainty of 0.01 mag), while the SDSS zero point magnitudes in the u' and z' bands are slightly shifted from the AB zeropoints: $u_{AB} = u_{SDSS} - 0.04$ mag and $z_{AB} = z_{SDSS} + 0.02$ mag

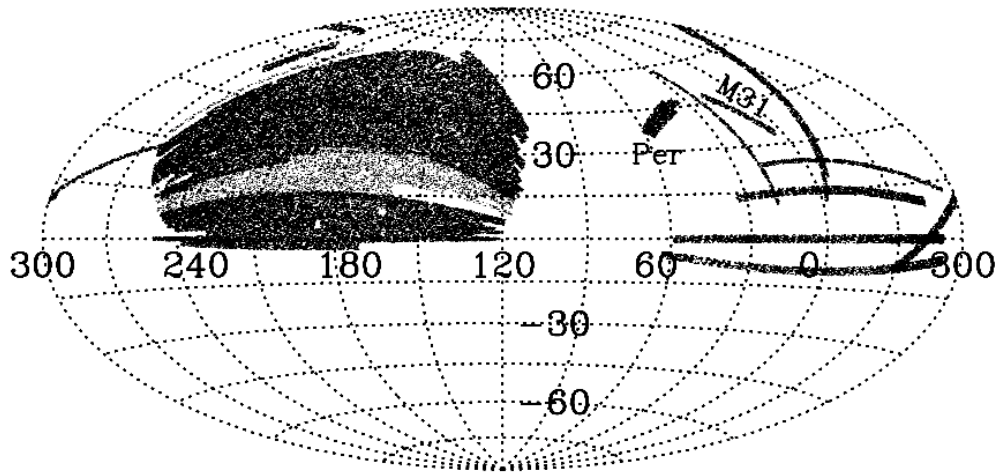


Figure 2.6: Sky coverage of the SDSS-DR5 catalogue in celestial coordinates. The light grey regions are the new photometric data included in the DR5, while the darker regions were also included in the previous catalogue release (DR4). Image adapted from Adelman-McCarthy et al. (2007).

~ 0.03 mag for the u' and z' (Ivezić et al. 2004); the astrometric calibration precision is better than $0.1''$ rms per coordinate (Pier et al. 2003).

The SDSS catalogue also provides object classification based on the morphology⁴: objects are classified as extended (“galaxy”) or point-like (“star”) based on the comparison between their surface brightness profile and the telescope Point Spread Function (PSF). The class “star” includes also quasars and any other unresolved sources, while “galaxy” class includes all resolved objects.

2.3 Cross-correlation of the 2XMMp and the SDSS-DR5

Thanks to their large sky area, the 2XMMp and the SDSS-DR5 catalogues represent an unprecedented resource in order to investigate large and statistically significant samples of objects in the X-ray and optical spectral bands, respectively. However, the greatest advantage in using these two catalogues is the fact that they share a large portion of their sky coverage (~ 75 deg², about 25% of the total area covered by the 2XMMp catalogue; see Fig. 2.7). This is particularly useful in order to build large homogeneous samples of rare and extreme objects, which would be otherwise difficult to find in smaller surveys

⁴<http://www.sdss.org/dr5/algorithms/classify.html#photo.class>

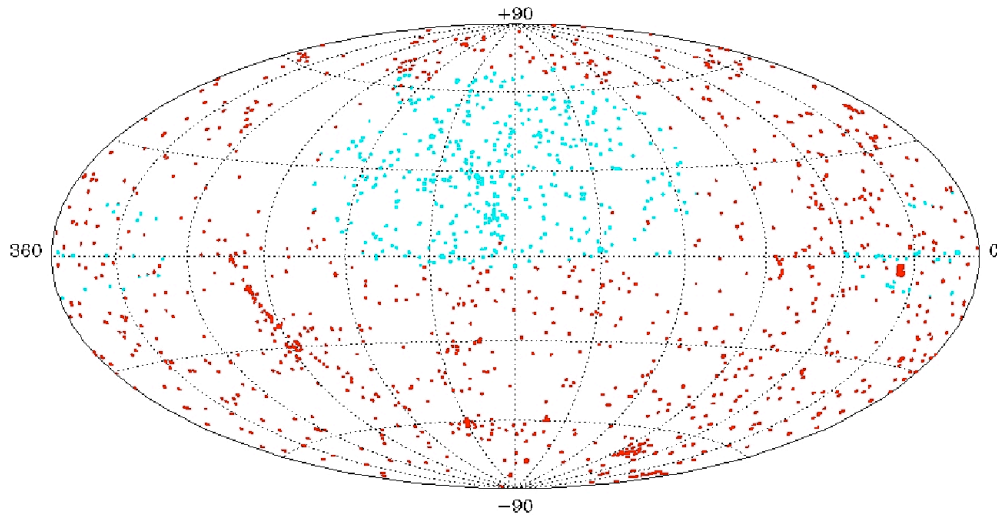


Figure 2.7: Sky map of the 2XMMp coverage (in red). The cyan dots represent the overlapping areas between the 2XMMp catalogue and the SDSS-DR5 catalogue.

because of their low sky density, and to study their multi-wavelength properties. The cross-correlation of the two source catalogues yields, in fact, more than 20000 secure matches, based on the *Likelihood Ratio* (LR) method (Sutherland & Saunders 1992), see below.

2.3.1 Likelihood Ratio

The *XMM-Newton* X-ray positions were initially cross-correlated with the SDSS positions out to a maximum separation of $20''$. Because the sky density in the SDSS data is much higher than that in the *XMM-Newton* data, we expected to find more than one optical source within the search radius. A large initial search radius was, in fact, chosen to identify (and remove) only those fields with no SDSS coverage without losing any “useful” object (the probability that there are no optical sources within $20''$ from the X-ray centroid was estimated to be less than 3%).

In order to obtain an accurate cross-identification between the X-ray and optical sources, the *likelihood ratio* technique (Sutherland & Saunders 1992) has been used, where the likelihood ratio $LR(r, N(< m))$ is defined as:

$$LR(r, N(< m)) = \frac{Q(< m) \exp(-\frac{r^2}{2})}{2\pi\sigma^2 N(< m)} \quad (2.1)$$

where $Q(<m)$ is the probability to have a true optical counterpart, $N(<m)$ is the cumulative number density of optical objects brighter than a magnitude m , r is the separation between the X-ray and the optical position (d) normalised by the positional error (σ). Because the errors on the *XMM-Newton* X-ray coordinates (a few arcsecs) are much larger than those in the SDSS data, only the X-ray position errors were considered in the calculations. This method relates objects detected in two different wavelength bands not only by their positions, but also by their brightness, as it takes into account the sky density of the background sources. The LR is in fact very sensitive to $N(<m)$ and decreases with the increasing sky density at fainter magnitudes. As an approximation, in our calculation $N(<m)$ was estimated considering an average sky density. We are aware that this approximation may introduce some uncertainties in the LR values.

For each counterpart candidate around the X-ray position a reliability (R) was also computed which is defined as the ratio between the LR of the considered candidate j and the total LR of all the possible matches around an X-ray source; this represents the probability that the considered object j is the real counterpart:

$$R_j = \frac{LR_j}{\sum_{i=1}^n LR_i + (1 - Q(< m_{lim}))} \quad (2.2)$$

where LR_i are the likelihood ratios of all the possible matches (n) around the X-ray position, and $Q(<m_{lim})$ is the probability of finding an optical counterpart above the optical sensitivity limit. Objects which are likely to be the true counterpart have usually high reliability.

2.3.2 Cross-identification process

As an initial attempt to distinguish between real and false counterparts amongst the cross-matched catalogue sources, a limit value of $LR = 2.0$ was chosen: all the sources with $LR > 2.0$ and a reliability $R \geq 0.5$ were considered as good candidates. These were arbitrary values, chosen as a good compromise to be small enough to avoid missing many

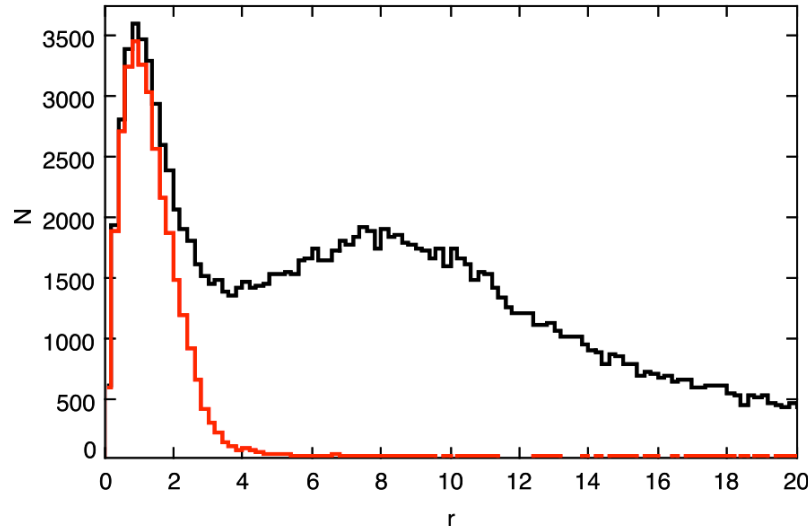


Figure 2.8: Histogram of the offsets between the X-ray and optical positions ($r = d/\sigma$) for all the cross-matched sources (black). Using a large search radius of $20''$ includes in the distribution a large number of spurious sources at high separations ($r > 5''$) due to the high sky density of the SDSS objects. The red histogram represents the sources with high likelihood ratio and reliability (following our selection criteria, see Sect. 2.3.2). This distribution peaks at $r \approx 1''$, with a broad tail to $r \approx 5''$. Only a very small fraction of true matches ($< 0.01\%$) are expected to be found at higher offsets.

real identifications, but large enough to keep the number of spurious identification as low as possible and to increase the reliability of the source identification.

Figure 2.8 shows the distribution for the source positional separation normalised by the errors ($r = d/\sigma$) for the cross-matched catalogue (black histogram) and the one for the sources following our preliminary selection criteria (red histogram). The probability density distribution of the separations is a Rayleigh distribution: the red histogram peaks at $r \approx 1''$, which is the average X-ray position error of the 2XMMp catalogue sources (including the systematic error σ_{sys} , see Sect. 2.1.3) with a broad tail out to $r \approx 5''$ (containing only a small fraction of sources). Up to this separation ($r \approx 5''$) the list of counterpart candidates is 99.99% complete. Above $r \approx 4'' - 5''$ the distribution of all the cross-matched sources (black histogram) rises because of the increasing number of spurious matches at larger search radii.

In order to overcome this problem, a restriction in d was applied: only matches with positional offsets $d \leq 7''$ have been accepted. As stated above, taking into account the positional errors in 2XMMp (Sect. 2.1.3), the large majority of the true counterparts are

expected to lie within a few arcseconds ($r \lesssim 2''$, Fig. 2.8) from the X-ray centroid with a small number of outliers at larger separations (up to $r \approx 5''$, including 99.99% of the counterparts candidates). Hence a negligible fraction of counterparts are expected to have separations above $7''$; we adopted this value as the most conservative upper limit on the possible offset of the true counterparts.

2.4 EXO sample selection

Objects characterised by extreme values of their X-ray-to-optical flux ratios (EXOs, $f_X/f_{\text{opt}} > 10$; Koekemoer et al. 2004; see Sect. 1.4) constitute a small fraction of the X-ray population (about 10–20% of the hard X-ray selected AGN population⁵; e.g. Fiore et al. 2003; Barcons et al. 2007). These rare objects have a low sky density and therefore a large sky area is required to find a sizeable sample of such sources. Moreover, because of their properties (faint optical magnitudes, by definition), the detection and analysis of EXOs is particularly challenging, especially using deep X-ray surveys (the case for most of the previous studies performed on EXOs, e.g. Koekemoer et al. 2004; Civano et al. 2005) which are dominated by faint X-ray sources. This means that their optical counterparts are too faint to allow useful analysis or even to be detected in any of the major optical surveys currently available.

The approach undertaken in this work (described below) overcomes these limitations by using a much wider survey to build-up a sizeable sample of EXOs at much higher X-ray and optical fluxes. Taking full advantage of the fact that 2XMM is the largest X-ray catalogue ever produced with an unprecedented sky coverage at relatively faint X-ray fluxes (Sect. 2.1.3), we created a sample selecting bright X-ray point-like sources ($f_X \geq 10^{-13}$ erg cm⁻² s⁻¹ in the 0.2–12 keV band⁶) with high X-ray-to-optical flux ratio ($f_X/f_{\text{opt}} > 30$, corresponding approximately to $f_X/f_{\text{opt}} > 10$ in the 2.0–10 keV band) from the cross-correlation between the 2XMMp and the SDSS-DR5 catalogues described

⁵The fraction of high f_X/f_{opt} sources is smaller (few percent) in the 0.5–2 keV selected samples (e.g. Barcons et al. 2007).

⁶Total EPIC flux.

above. The f_X/f_{opt} is defined here as:

$$\log(f_X/f_{\text{opt}}) = \log f_{0.2-12 \text{ keV}} + r'/2.5 + 5.5 \quad (2.3)$$

where r' is the SDSS magnitude (AB ; see Sect. 2.2.1; e.g. Civano et al. 2005).

The chosen X-ray flux limit (which selects $\sim 8\%$ of the catalogue sources) guarantees that the SDSS r' -band limit⁷ ($r' = 22.5$ mag) will provide useful constraints with this ratio selection (at our flux limit $f_X \geq 10^{-13}$ erg cm⁻² s⁻¹, a source with $r' = 22.5$ already has $f_X/f_{\text{opt}} > 30$, in the 0.2–12 keV band), whilst also guaranteeing high quality X-ray data.

However, because of their faint optical magnitudes, our EXO sample falls into the range of parameters where the likelihood ratio approach, described above, did not provide in many cases ($\sim 60\%$) a clear identification of the source counterpart. Because of the faintness of the selected objects in the optical, at our sensitivity limits, it was difficult in some cases to differentiate between the possibility that the true match is fainter than the SDSS limit or that the correct counterpart is a faint object with low likelihood ratio (and hence with a higher probability to be a chance match). In these ambiguous cases the brighter object within $7''$ from the X-ray position was chosen as the counterpart candidate. The effect of this ambiguity is that the f_X/f_{opt} values, in these cases, will be underestimated; in fact, although the chosen counterpart may be wrong (i.e. if the true counterpart is a fainter object, with r' below the SDSS limit), our selected high f_X/f_{opt} object sample is robust.

We then complemented the sample with those XMM sources with no SDSS detected counterpart within $7''$ from the X-ray position (36 sources), for which only a lower limit of the f_X/f_{opt} was estimated (calculated with the SDSS magnitude limit $r' > 22.5$ mag). Those sources would otherwise have been lost if the LR method only were taken into account in the sample selection process.

⁷We note that the r' limit reported in the catalogue is $r' = 22.2$ (see Sect. 2.2.1); however at $r' = 22.5$ the uncertainties on the magnitude values and the completeness of source detection are still good enough for the purposes of our analysis. We therefore considered $r' = 22.5$ as the SDSS r' -band sensitivity limit throughout this work.

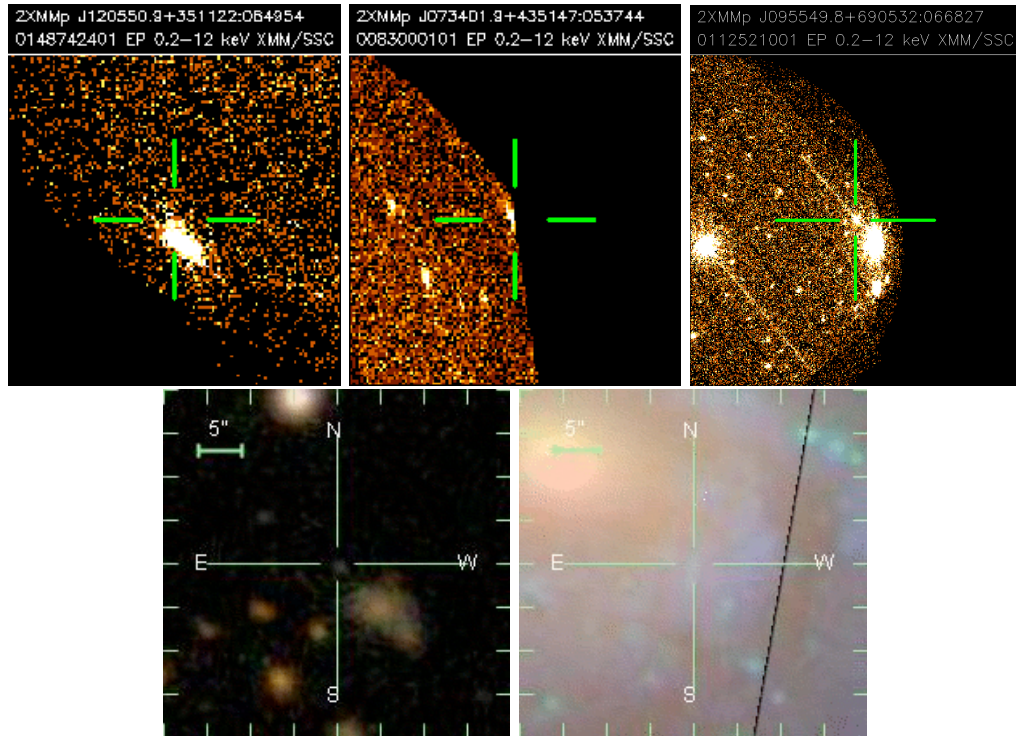


Figure 2.9: Examples of some problematic cases identified in the *XMM-Newton* (top) and in the SDSS (bottom) images, which have been removed from the final EXO sample.

Each *XMM-Newton* and SDSS image of the sample objects has been carefully checked by eye in order to reject all the problematic cases. The main problems identified in the X-ray images were: i) spurious detections (Fig. 2.9, top left) ; ii) cases where the source parameters were highly uncertain, such as objects detected at the edge of the XMM field of view or in a CCD gap in all the three EPIC cameras (Fig. 2.9, top centre) or nearby bright objects (causing flux contamination; Fig. 2.9, top right). In the SDSS images the rejected sources were mainly: i) counterparts likely to be part of a galaxy cluster (Fig. 2.9, bottom left), which are not of interest for the aims of our analysis; ii) counterparts lying in the outskirts of big nearby galaxies (e.g. HII regions; Fig. 2.9, bottom right).

After these processes, with the selection criteria described above, we obtained a final sample of 129 EXOs, which is the largest bright X-ray selected EXO sample compiled so far. Amongst the sample 57% of the objects (74 sources) fulfill the *LR* criteria described above, while the remainder is part of the complementary sample which includes sources with ambiguous counterpart candidates (19 sources, 15% of the sample) and sources with

no detected counterpart in the SDSS imaging data (28% of the sample).

2.5 Comparison with the Strasbourg cross-correlation method

In order to verify the results of the cross-identification performed for our EXO sample, we compared them with the cross-correlation of the 2XMMi (the incremental release of the 2XMM catalogue) with the 7th release of the SDSS catalogue (SDSS DR7; Abazajian et al. 2009), performed by the Strasbourg Survey Science Centre (SSC) group (Pineau et al. 2008; Pineau et al., in preparation). Pineau et al. developed a sophisticated cross-correlation algorithm, which is still based on a likelihood ratio technique (like our approach). Their algorithm takes into account the local sky densities and calculates for each source, not only the probability of finding a good candidate, but also the LR distribution of spurious matches; it also computes the probability of identification for each source counterpart candidate (see Pineau et al., in preparation).

A full description of the details of Pineau et al. approach are beyond the scope of this work, but we note that the reliability (R) calculated for each counterpart candidate given in Pineau et al. is different from our definition of R (eq. 2.2): in Pineau et al. it is defined as the ratio of the number of true counterpart candidates to the total number of candidates (N_{cand}) in a given bin of LR:

$$R(LR) = \frac{N_{cand}(LR) - N_{spur}(LR)}{N_{cand}(LR)} \quad (2.4)$$

where N_{spur} is the number of spurious counterpart candidates in a given LR bin. The reliability and LR are computed for all candidates in each of the SDSS filters, separately. Then using the best reliability obtained amongst the different SDSS filters, the probability

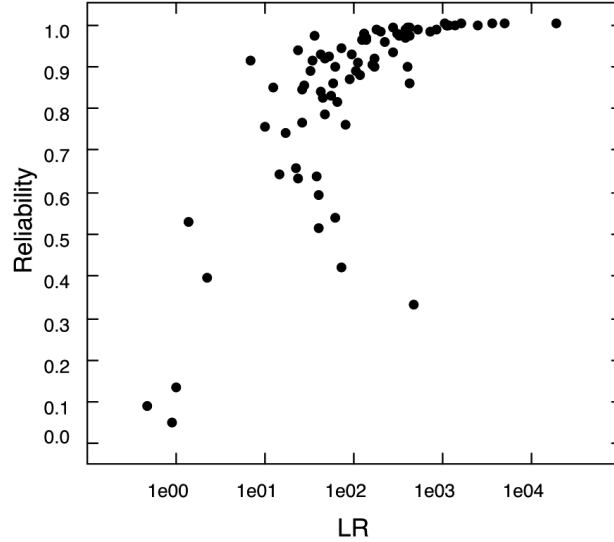


Figure 2.10: Likelihood ratio (LR) vs reliability from Pineau et al. (2008) for 81 of our sample sources included also in the 2XMMi-SDSS DR7 cross-correlated catalogue.

of identification is calculated for each candidate i :

$$P_{id,i} = \frac{\frac{R_i}{1 - R_i}}{\left(1 + \sum_{i=1}^M \frac{R_i}{1 - R_i}\right)} \quad (2.5)$$

where M is the total number of candidates (real and spurious) around an X-ray source (Pineau et al. 2008).

Aiming to compare these results with the counterpart candidates we obtained for our sample objects using the preliminary method described above (Sect. 2.3 and 2.4), we took into account all the sources amongst our sample which are included also in the 2XMMi-SDSS DR7 cross-correlated catalogue produced by Pineau et al. The overlap comprises only 81 sources ($\sim 63\%$ of our sample) because the 2XMMi-SDSS DR7 cross-correlated catalogue does not contain the X-ray sources without an SDSS counterpart (30% of our sample objects, see 2.4) and includes only counterparts with a positional separation between the X-ray and optical centroids up to $5''$, while in our selection we applied a separation limit of $7''$.

We found an agreement of our identified counterpart candidates with those found by

Pineau et al. in 99% of the cases, while a different optical match has been identified only for one source. However, not all the counterpart candidates identified have a high reliability⁸ (Fig. 2.10); this means that the true counterparts might instead be a fainter object, not detected in the SDSS image.

From the reliability distribution plotted in Figure 2.10, we can separate our counterpart candidates into different groups: about 80% (64 objects, 50% amongst the whole EXO sample) of the sources compared with the Pineau et al. catalogue have a reliability above 70% and hence a high probability to be the true counterpart; we considered these sources to be “good matches”. The sources with lower reliability values (about 12% of the whole EXO sample) were considered as “possible matches”. All the sources not included in the 2XMMi-SDSS DR7 cross-correlated catalogue (the undetected objects in the SDSS are 30% of our sample) were treated as “upperlimits” ($\sim 38\%$). We want to stress that a low reliability may imply that the real counterpart is in fact a fainter object than the one identified; therefore in these cases the f_X/f_{opt} values are *underestimated*: in this sense our EXO sample is robust.

⁸We took into account the LR of our sources, according to our definition (Sect. 2.3.1) and the reliability computed by Pineau et al. in the SDSS r' band, as it is the optical band we used to define the f_X/f_{opt} .

CHAPTER 3

The Nature of EXOs

In this chapter the properties of our EXO sample are presented. The global properties of the sample in the X-ray and in the optical bands are firstly investigated through the colours of the sources and then through a spectral energy distribution (SED) model, used to constrain the expected spectral parameters. For a fraction of the sample for which follow-up near-IR photometric data and optical spectroscopic data were obtained, the multi-wavelength analysis is also described.

The second part of the chapter focuses on the EXOs with optical identification amongst our sample (25%); detailed optical and X-ray spectral analysis of this sub-sample are presented and the results obtained are discussed.

3.1 Introduction

The ratio between the X-ray and optical fluxes is believed to be a good tracer of obscuration amongst the AGN population. The high f_X/f_{opt} ratio is expected for obscured sources because while the nuclear UV/optical/NIR emission is heavily obscured by dust, the X-ray flux, although strongly depressed by the photoelectric absorption at low energies (below ~ 2 keV), is less attenuated overall. In order to have the most extreme f_X/f_{opt} values, the AGN must be very luminous, otherwise the dilution of the optical flux of the host galaxy constrains the ratio to lower values. In this context, the high f_X/f_{opt} population is expected to be dominated by type-2 QSOs. Indeed previous studies on EXOs (e.g. Fiore et al. 2003; Mignoli et al. 2004; Koekemoer et al. 2004) found that the majority of such sources are high luminosity, highly obscured AGN, hence the mostly elusive type-2 QSO.

As described in Chapter 2 (see Sect. 2.4), our EXO sample was created selecting X-ray bright point-like sources with $f_X \geq 10^{-13}$ erg cm $^{-2}$ s $^{-1}$ (in the 0.2–12 keV band) and high X-ray-to-optical flux ratio ($f_X/f_{\text{opt}} > 30$, corresponding approximately to $f_X/f_{\text{opt}} > 10$ in the 2.0–10 keV band) from the cross-correlation between the 2XMM and the SDSS-DR5 catalogues. The sample obtained comprises 129 EXOs (Fig. 3.1), which constitutes the largest such sample compiled to date.

The advantages of our approach are: i) a large sky area (see Sect. 2.3), which allows the selection of bright sources, whilst still producing a large sample for statistical analysis; ii) bright sample sources (Sect. 2.4), which implies both good X-ray data to perform detailed X-ray analysis for most of the sources, as well as making the optical and IR band analysis accessible (see below). With our analysis we aim to constrain the fraction of EXOs powered by AGN (see Sect. 1.4) and in particular, the fraction of obscured, high redshift quasars in our sample.

3.2 General properties of the sample

Considering the whole 2XMM catalogue, the sky density¹ (at high galactic latitudes, $|b| > 20^\circ$) of the bright X-ray point-like sources ($f_X \geq 10^{-13}$ erg cm⁻² s⁻¹, 0.2–12 keV energy band) was estimated to be 38 ± 0.7 deg⁻². These objects constitute $\sim 8\%$ of the total X-ray catalogue sources (see Sect. 2.1.3). Although it is expected the majority of these X-ray selected sources are AGN, the estimated sky density will include some non-AGN objects, like stars or galaxy clusters, which constitute a non-negligible fraction of the X-ray population especially in the soft band (< 2 keV). Indeed, using the $\log N - \log S$ function computed by Mateos et al. (2008) for stars in the *XMM-Newton* data and by Rosati et al. (1998) for clusters using the *ROSAT* Deep Cluster Survey data, the density of such objects at $f_X \geq 10^{-13}$ erg cm⁻² s⁻¹ was estimated to be: 1.14 ± 0.20 deg⁻² for stars and 1.09 ± 0.19 deg² for clusters of galaxies². Correcting the initial sky density for these two values gives an estimation of the AGN sky density of 36.1 ± 0.8 deg⁻².

As the fraction of EXOs amongst the AGN population varies from a few percent up to $\sim 20\%$ (depending on energy band selection; Barcons et al. 2007), we estimated the sky density of the EXOs at our bright flux selection to be 1.1, 1.8, 3.6 deg⁻² (for a fraction of 3%, 5%, 10%, respectively), which yields an expected number of high f_X/f_{opt} sources in the whole 2XMMp/SDSS-DR5 cross-matched catalogue (~ 75 deg²; see Sect. 2.3) of 81, 136, 271, respectively.

Therefore, the number of our sample EXOs (129 sources) is broadly consistent with expectation. We note that our EXO sample will include a small fraction of non-AGN sources (see Sect. 1.4), although their impact on the sample is expected to be small.

The distribution of the f_X/f_{opt} of our sample objects is shown in Figure 3.1. The large majority of our sources (70%) have X-ray-to-optical flux ratios in the range $f_X/f_{\text{opt}} =$

¹Calculated directly from the number of detected sources, divided by the sky coverage of the 2XMM catalogue at high galactic latitudes, which is ~ 234 deg² (Watson et al. 2009). We note that the sky area of the catalogue is a function of the flux, as it includes only the areas that are sensitive to a given flux, inferred from the sensitivity maps; at bright fluxes, such as $f_X \geq 10^{-13}$ erg cm⁻² s⁻¹, the sky coverage correction for the sensitivity is negligible (see Watson et al. 2009).

²Our EXO selection excluded extended sources; however, galaxy clusters at high redshift may appear as point-like objects in the X-ray data at low signal-to-noise.

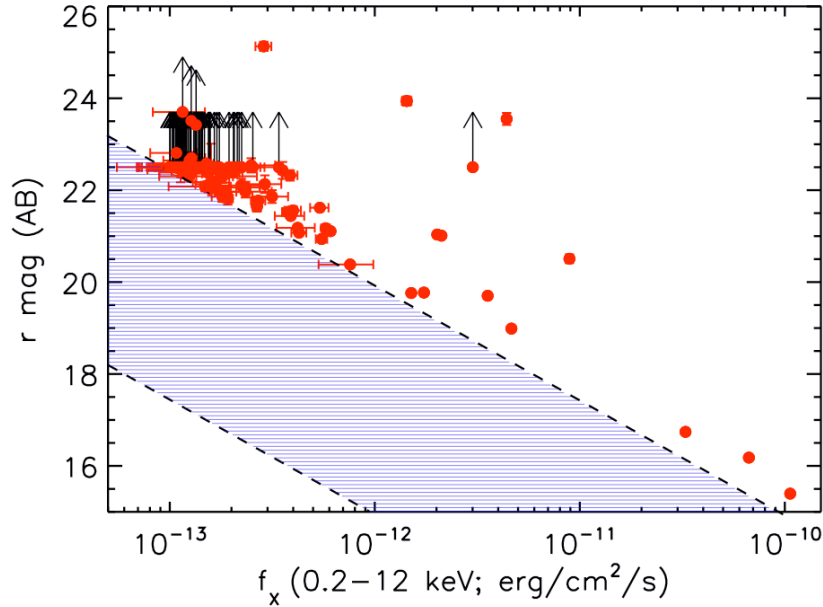


Figure 3.1: X-ray flux in the 0.2 – 12 keV energy band vs the SDSS r' magnitude (used to define the f_X/f_{opt} in our sample). The upperlimit for the faint optical sources (or the undetected sources) was fixed at $r' = 22.5$ mag. The dashed lines indicates the limits $f_X/f_{\text{opt}} = 0.3$ and $f_X/f_{\text{opt}} = 30$ (0.2 – 12 keV); the shaded area represents the typical location of AGN.

30 – 50 (in the 0.2 – 12 keV band), which is already up to 20 times higher than the typical values for optically selected AGN (see Sect. 1.4). The remaining 30% have $f_X/f_{\text{opt}} > 50$, reaching also very extreme values up to $f_X/f_{\text{opt}} > 5000$ (0.2 – 12 keV; see Chapter 4).

In order to constrain the fraction of known (and possibly) non-AGN sources amongst our sample the objects were searched for in the literature and in online databases (e.g. NED, SIMBAD) to find a classification. Seventeen objects (13% of the sample) were found with known identifications in the literature: ten are AGN (five BL Lacs, one QSO, two BL AGN, two NL AGN), while seven are non-AGN (two INS, two ULXs, two CVs, one XRB; see Sect. 1.4). The remaining sources (112, i.e. 87% of the sample) are not identified from previous studies.

3.2.1 X-ray properties

The flux distribution of the sample is shown in Figure 3.2. The red histogram represents the EPIC X-ray flux in the 2–10 keV band, the black dashed histogram is the flux in the 0.5–2 keV band and the blue long-dashed histogram is the flux in the total energy band

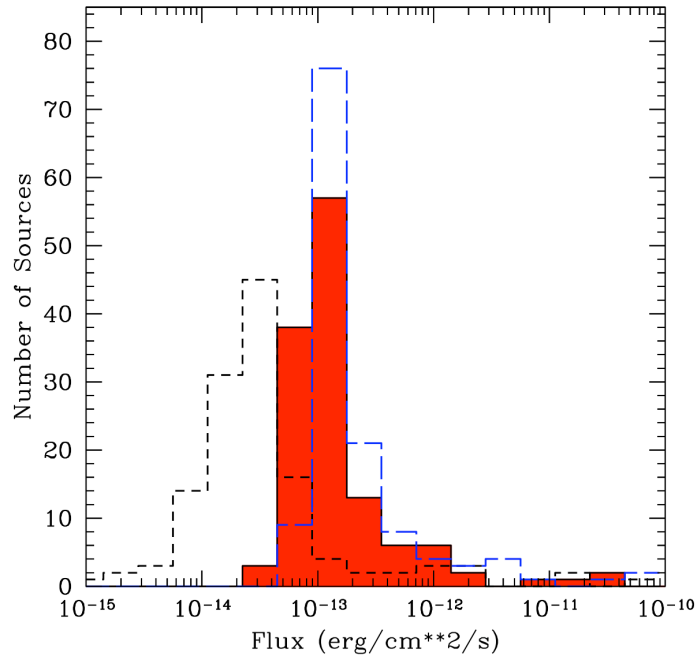


Figure 3.2: X-ray flux distribution of our sample objects: the black dashed histogram is the distribution for the soft-band fluxes (0.5 – 2 keV); the red histogram is for the hard-band fluxes (2 – 10 keV) and the blue long-dashed histogram is the distribution for the total-band flux (0.2 – 12 keV).

(0.2–12 keV). The hard-band flux distribution for our sample sources peaks at $f_X \approx 10^{-13}$ erg cm $^{-2}$ s $^{-1}$ (2–10 keV) and tends to be higher than the soft-band fluxes (peak at $f_X \approx 3 \times 10^{-14}$ erg cm $^{-2}$ s $^{-1}$, 0.5–2 keV). The X-ray parameters for the whole EXO sample are summarised in Table A1.1 (Appendix 1).

The global X-ray spectral properties of our sample sources were investigated using the X-ray colours (Hardness Ratio, HR; see Sect. 2.1.3), as the redshift is unknown for many of the sources (the redshift was available only for eight sources from the literature). Indeed, the redshift is essential to constrain the intrinsic (rest-frame) spectral parameters such as the hydrogen column density, which scales with redshift as: $N_{H,z} \approx (1 + z)^{2.6} N_{H,z=0}$ (where $N_{H,z}$ is the rest-frame column, while the $N_{H,z=0}$ is the column density at $z = 0$; Barger et al. 2002; Alexander et al. 2003).

If a simple absorbed power-law is assumed, it is possible to estimate the N_H from the HR, as the X-ray colours are very sensitive to the hydrogen column density. In order to do that, some assumption on the spectral slopes is needed, however we note that the HR is weakly sensitive to the changes in Γ (e.g. Fiore et al. 2003). Figure 3.3 shows the X-ray

colour-colour plot for our EXO sample: the colours HR2 (defined in the bands 2 and 3; see Table 2.2) and HR3 (bands 3 and 4) were used to investigate the hardness of the spectra. The tracks³ in the plot represent the evolution of the HR for an absorbed power-law ($\Gamma = 1.9$) with redshift ($z = 0 - 6$, step size $\Delta z = 0.5$); the different tracks represent different hydrogen column density values ($N_{\text{H}} = 3 \times 10^{20}, 4 \times 10^{21}, 10^{22}, 5 \times 10^{22}, 10^{23}, 5 \times 10^{23} \text{ cm}^{-2}$). From the tracks in the plot, it is evident that, for a given N_{H} the sources would have softer colours as the redshift increases and tend to lie on the left end of the HR distribution in the plot. The colour-colour distribution for our EXOs has a tail toward hard colours⁴ (right-top end of the plot): using the spectral tracks as a guide, we can argue that the sources with $\text{HR2} \gtrsim 0.3$ (51% of the sample) should have spectra absorbed by high column density $N_{\text{H}} > 10^{22} \text{ cm}^{-2}$ up to high redshift ($N_{\text{H}} \geq 4 \times 10^{21} \text{ cm}^{-2}$, if $z < 1$); at $\text{HR2} = 0 - 0.3$ the X-ray colour distribution comprises a mixture of unabsorbed objects and high- z absorbed objects ($N_{\text{H}} > 4 \times 10^{21} \text{ cm}^{-2}$), thus the fraction of absorbed AGN amongst our sample is likely to be higher than 51%, which is consistent with the fraction found in previous studies (e.g. Fiore et al. 2003; Civano et al. 2005; Perola et al. 2004; Comastri & Fiore 2004).

3.2.2 Optical properties

As stated in the previous Chapter (see Sect. 2.5), our EXO sample comprises: 50% of sources whose counterparts detected in the optical SDSS r' band are “good matches”, 12% with “probable matches” and the remaining 38% source counterparts are upperlimits, with 30% of the sources (amongst the whole sample) not detected in any of the SDSS photometric bands.

For the sources with a detected counterpart in the SDSS data (62%, i.e. 79 sources, comprising the “good” and “probable” matches) it was possible to constrain the brightness and the morphology from the SDSS data: 59 out of 79 sources have magnitudes brighter than the SDSS r' -band upperlimit ($r' = 22.5$ mag), ranging between $r' = 15.4 - 22.5$; we

³The tracks in the plot were computed from simulation performed for the EPIC pn camera only, assuming a thin filter.

⁴We note that the three sources on the left, with $\text{HR2} \approx -1$ are all non-AGN objects (see Sect. 3.2).

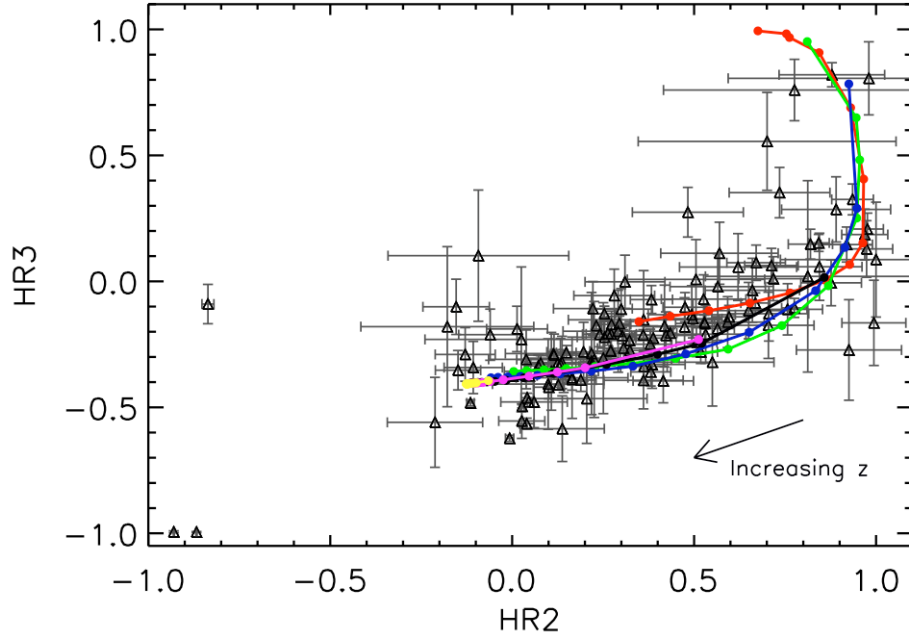


Figure 3.3: X-ray *Hardness Ratio* distribution for our EXO sample. The tracks in the plot represent the X-ray colours of a simulated absorbed power-law with $\Gamma = 1.9$ (assuming thin filter, for EPIC pn data only) at different redshift ($z = 0 - 6$, $\Delta z = 0.5$). The different tracks are computed for different hydrogen column densities: $N_{\text{H}} = 3 \times 10^{20} \text{ cm}^{-2}$ (yellow), $N_{\text{H}} = 4 \times 10^{21} \text{ cm}^{-2}$ (magenta), $N_{\text{H}} = 10^{22} \text{ cm}^{-2}$ (black), $N_{\text{H}} = 5 \times 10^{22} \text{ cm}^{-2}$ (blue), $N_{\text{H}} = 10^{23} \text{ cm}^{-2}$ (green), $N_{\text{H}} = 5 \times 10^{23} \text{ cm}^{-2}$ (red).

note that all the sources with $r' < 21.0$ are sources found in the literature. The remainder are fainter objects; as the magnitudes provided by the SDSS catalogue in these cases have large uncertainties, the r' magnitude for these objects was set to $r' > 22.5$. This upperlimit was also used for all the sources with no detected counterpart⁵ (38% of the sample).

Aiming to obtain a lower fraction of upperlimit sources, the *Isaac Newton Telescope* (INT) *Wide Field Camera* Survey (WFS) data archive was searched⁶ in order to look for detections of our EXOs. The WFC survey consists of a rather heterogeneous collection of multi-colour data with observations taken in several filters from U to Z (centred at $\lambda = 3560 \text{ \AA}$ and $\lambda = 9100 \text{ \AA}$, respectively); many of these observations include also three filters which correspond approximately to the SDSS g' , r' and i' . The typical depth in

⁵In the other filters the upperlimits were set to $g' = 22.5$, $i' = 21.5$, $z' = 20.5$ mag. We did not take into account the u' -band magnitudes in our analysis, as we expect our sources to have on average red colours, and thus the u' band is of limited interest.

⁶Through the Cambridge Astronomical Survey Unit (CASU), which is responsible for the processing and archiving of the WFS dataset.

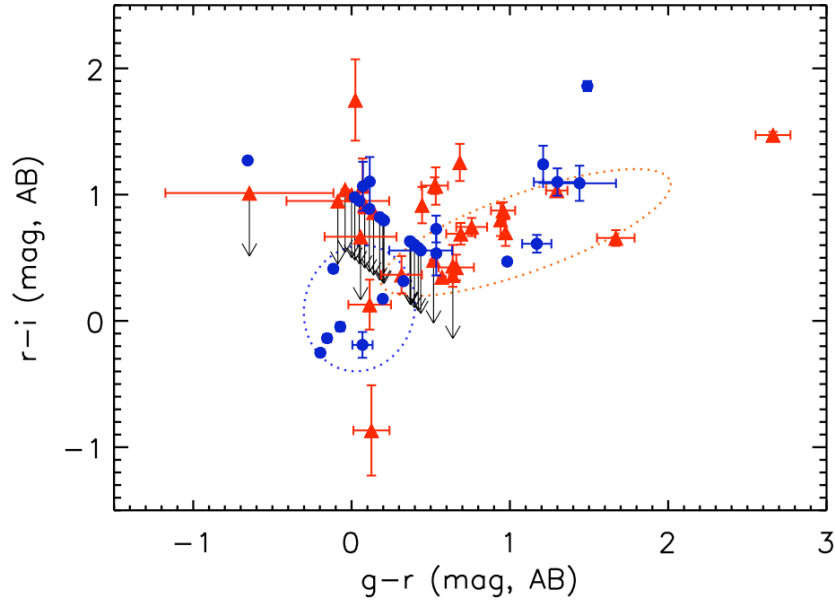


Figure 3.4: Optical colour-colour plot: $(g' - r')$ vs $(r' - i')$. The morphology of the sources is also shown: objects classified as “stellar” (blue circles) and objects classified as “galaxy” (red triangles); the typical location of galaxies and QSOs in the SDSS catalogue is also shown, represented by the orange and blue ellipses, respectively (Newberg et al. 1999; Hatziminaoglou et al. 2005).

these three filters in the WFS is $g' = 25.1$, $r' = 24.7$ and $i' = 24.1$ mag (5σ , $1''$ seeing), which is more than a magnitude deeper than the SDSS data.

WFC data coverage was found for 14 of our sample EXOs⁷, although four of them are not detected in the WFC images; the optical photometric information for the ten objects detected was updated with the WFC magnitude values (see Table A1.1, Appendix 1).

In Figure 3.4 the optical colours $(g' - r')$ and $(r' - i')$ for the detected sources are plotted. The morphology of the objects, according to the SDSS catalogue classification (see Sect. 2.2.1) or to the WFC data (where available), are also shown: 34% of the sample sources have galaxy morphology, presumably because the nuclear emission in these sources is obscured in the optical band and the host galaxy light becomes dominant; 28% have a stellar morphology in the SDSS r' band, hence in these objects the nuclear emission dominates above the starlight of the host galaxy. It is important to point out, however, that because the magnitudes of our objects are typically faint (considering the sensitivity limits

⁷Many of the WFS fields were in fact observed as part of the XMM XID program and as such were targeted on XMM fields.

of the optical data available) the morphology given for these objects is not fully reliable⁸.

3.3 SED model predictions

In order to constrain the expected parameters for obscured high-redshift QSOs and to constrain their fraction amongst our EXO sample, a simple model to reproduce the Spectral Energy Distribution (SED) of a typical QSO in the optical and IR bands was created. With this toy model we aim to study the expected optical colours and f_X/f_{opt} with increasing obscuration of the nuclear emission and the evolution of these parameters with redshift.

3.3.1 SED templates

To build the model a library of SEDs for quasars and different galaxy types (Polletta et al. 2007) was used. The quasar template adopted is a composite quasar spectrum for type-1 QSOs from the Large Bright Quasar Survey (Brotherton et al. 2001) complemented at the IR wavelengths using the average rest-frame IR spectra of a sample of 35 quasars (Hatziminaoglou et al. 2005) from the SDSS/SWIRE (Spitzer Wide-Area Infrared Extragalactic survey; Lonsdale et al. 2004); the SED with the highest IR/optical flux ratio was selected amongst the three type-1 QSO SED available⁹ from Polletta et al. (2007), as luminous X-ray selected sources have typically high IR-to-optical flux ratios (e.g. Polletta et al. 2008; Lanzuisi et al. 2009; see also Chapter 1).

As QSOs are typically found to be hosted in massive spheroids (McLeod & Rieke 1995; Aretxaga et al. 1998; Dunlop et al. 2003), the SED of a 13 Gyr dust-free elliptical galaxy generated with the GRASIL code (Silva et al. 1998) was used to reproduce the host galaxy spectral emission in our model. We note that in the wavelength range considered for our SED model, the difference between the various galaxy type templates is small, therefore the choice of one template amongst the others does not significantly affect the results obtained (see below). We note that in the case of starburst galaxies the template

⁸The SDSS stellar-galaxy separation is reliable at least to $r' = 21.5$ (to a confidence level of 95%) and it is quite good up to $r' \approx 22$ (Lupton et al. 2001).

⁹The three type-1 QSO templates derived by Polletta et al. (2007) differ for their IR SEDs: one has the highest IR average flux and one has the lowest.

may change considerably from a normal galaxy because of the enhanced emission due to the star formation; however the major variations in the template occur in the IR band, hence not affecting significantly the results in the optical band.

3.3.2 The SED model

The host galaxy contribution to the total emission observed in AGN is still a debated issue. Many authors have addressed the study of composite SEDs of X-ray selected active galaxies (see e.g. Alexander et al. 2001a,b, 2002; Perola et al. 2004; Franceschini et al. 2005; Polletta et al. 2006, 2007), but they found the SEDs show a wide variety of properties and the parameters do not have tight constraints. In particular, the galaxy contribution in the optical band can range from a few percent to more than 50% of the total emission, depending on the object type: in Seyfert galaxies, for example, the host galaxy contribution can be high, as the galaxy features are often observed in the optical spectra of these objects; while in unobscured quasars it is expected to be only a few percent of the total flux, as the nucleus dominates the overall emission.

To reproduce the spectrum of a realistic quasar and parameterise this contribution we used the definition of galaxy fraction (F_g) from Vanden Berk et al. (2006):

$$F_g = \frac{f_{gal}}{f_{gal+qso}}$$

where f_{gal} and $f_{gal+qso}$ are the host galaxy flux and the total flux, respectively, over a small range of rest-frame wavelengths (4160 – 4210 Å), chosen because it avoids major galaxy and quasar emission features. As a starting point of this analysis the galaxy fraction F_g was fixed to an arbitrary value of 5% of the total flux. We stress that our aim is not to perform a sophisticated SED analysis of our sources, but to investigate the expected properties of a quasar in the simplest possible scenario.

In order to properly reproduce the emission of a typical quasar, the extinction from our Galaxy, which affects both the nucleus and the host galaxy emissions, and the extinction of the nuclear emission, due to gas and dust in the circumnuclear regions of the AGN

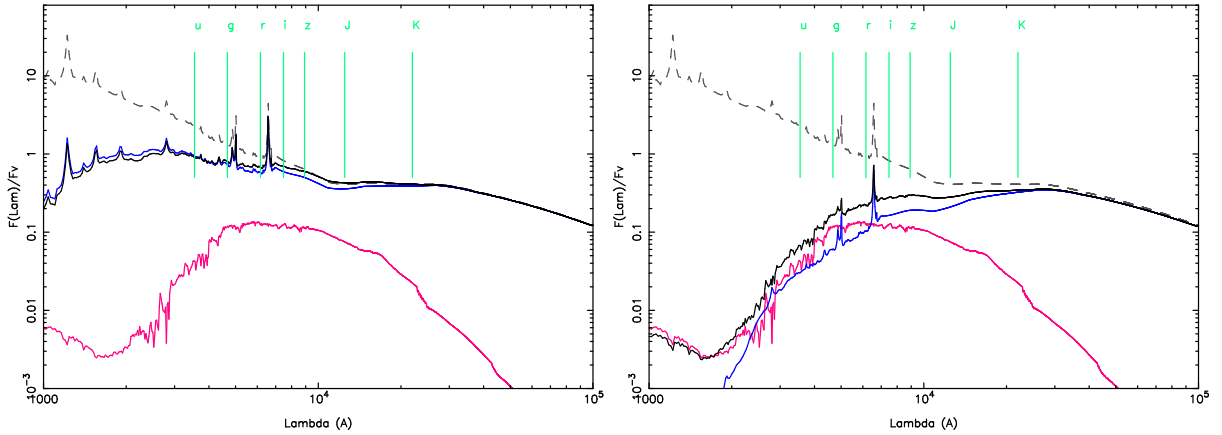


Figure 3.5: SED models obtained for $N_{\text{H}} = 10^{21} \text{ cm}^{-2}$ (left) and $N_{\text{H}} = 5 \times 10^{21} \text{ cm}^{-2}$ (right), assuming $z = 0$ (the fluxes are in arbitrary units); the grey dashed line is the unabsorbed QSO template, the blue line is the absorbed nucleus, the red line is the galaxy SED and the black line is the resulting SED; the galaxy fraction was fixed to $F = 0.05$. Selected optical and near-IR photometric bands are marked with green vertical lines.

(e.g. the putative torus; see Chapter 1), were taken into account. The optical extinction (A_V) was parameterised assuming a dust-to-gas ratio fixed to the canonical Galactic value $N_{\text{H}} = 1.813 \times 10^{21} A_V$ (e.g. Predehl & Schmitt 1995). The effect of the obscuring material is particularly important in type-2 QSO SEDs, where the absorbing gas has typically high column densities, of the order of $N_{\text{H}} > 10^{22} \text{ cm}^{-2}$, which yields highly reddened optical continua.

To account for the effects of the obscuration in the SEDs, we incorporated in the model: i) the Galactic extinction using the Milky Way extinction law from Pei (1992), with a column density fixed to a typical value for our Galaxy ($N_{\text{H}}^{\text{Gal}} = 2 \times 10^{20} \text{ cm}^{-2}$, corresponding to $A_V = 0.11 \text{ mag}$); ii) the intrinsic absorption of the quasar, modelled using the Small Magellanic Cloud (SMC) extinction curve (Pei 1992): as the Magellanic Clouds have lower metal abundances than the Milky Way, their extinction law is likely to be more similar to those of high redshift galaxies, which are presumably in the early stages of their chemical evolution (Pei 1992). Different N_{H} values were then applied to reproduce the SEDs of obscured and unobscured QSOs (see below). Two examples of the resulting SED model are shown in Fig. 3.5.

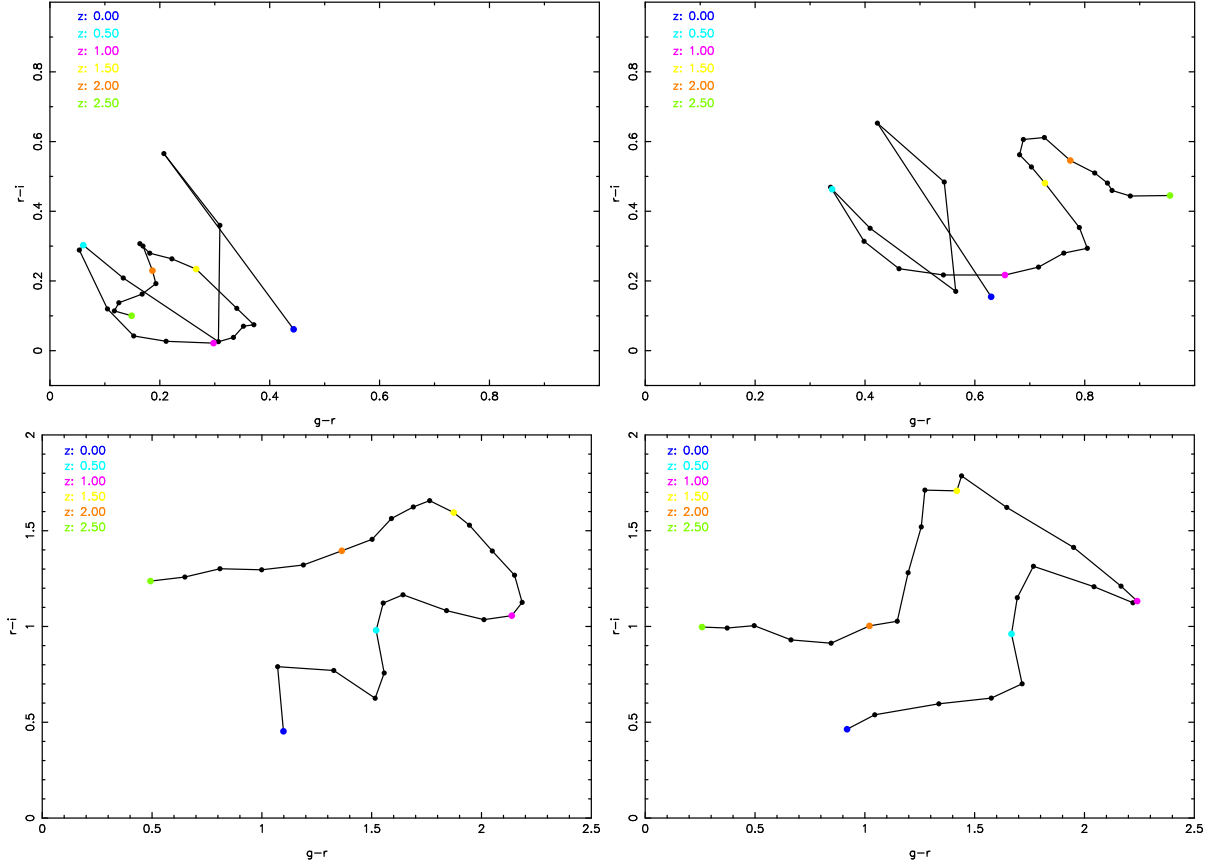


Figure 3.6: Optical colour tracks ($g' - r'$) vs ($r' - i'$) with redshift from $z=0$ to $z=2.5$ obtained for the SED model with different absorption: $N_H = 10^{20} \text{ cm}^{-2}$ (top left), $N_H = 10^{21} \text{ cm}^{-2}$ (top right), $N_H = 5 \times 10^{21} \text{ cm}^{-2}$ (bottom left), $N_H = 10^{22} \text{ cm}^{-2}$ (bottom right).

3.3.3 The Optical/IR SED analysis

The SED model described above was then used to predict the properties expected for highly obscured, high- z objects in the observed optical/NIR bands (the green lines in Fig. 3.5). Using the transmission curves of the SDSS photometric filters, the magnitudes g' , r' and i' were computed from various SEDs with increasing absorption ($N_H = 10^{20}, 10^{21}, 5 \times 10^{21}, 10^{22} \text{ cm}^{-2}$) and progressively increasing redshift ($z = 0 - 2.5$, with step size of $\Delta z = 0.1$). The optical synthetic colours $g' - r'$ and $r' - i'$ were then derived. In Figure 3.6 the colour tracks obtained from each SED with different N_H are shown. The top plots represent the colours of the unobscured QSOs (low absorption, $N_H = 10^{20} \text{ cm}^{-2}$ and $N_H = 10^{21} \text{ cm}^{-2}$), while the bottom plots represent the colours of the obscured QSOs ($N_H = 5 \times 10^{21} \text{ cm}^{-2}$ and $N_H = 10^{22} \text{ cm}^{-2}$) where the host galaxy emission becomes important (see Fig. 3.5, right) and produces redder colours than those characteristic of the

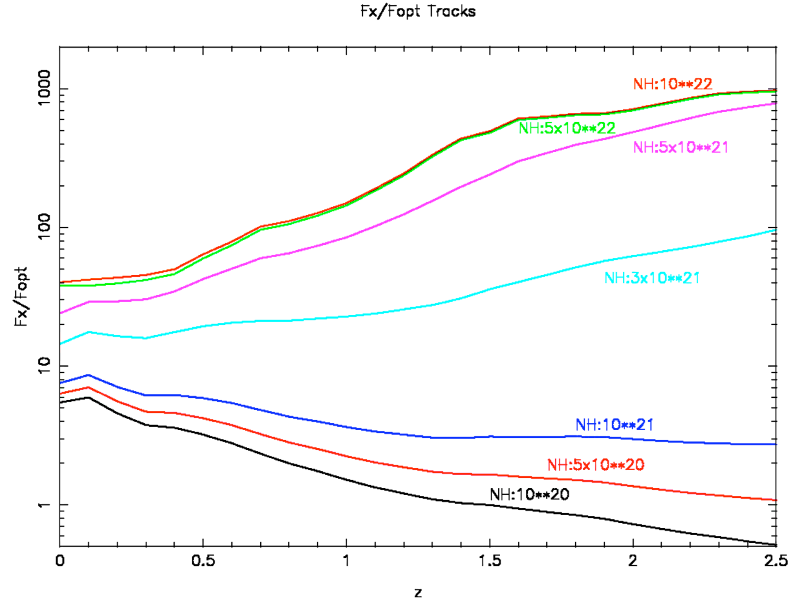


Figure 3.7: f_X/f_{opt} tracks for increasing X-ray column densities (and hence increasing A_V , $N_{\text{H}} = 1.813 \times 10^{21} A_V$), over a redshift range $0 \leq z \leq 2.5$. The normalisation is such that an unabsorbed AGN at redshift $z = 1.5$ has $f_X/f_{\text{opt}} = 1$.

nuclear emission.

Comparing the synthetic colours obtained from the SED models with the $g' - r'$ and $r' - i'$ colours of our sample sources, we note that the two tracks obtained for obscured QSOs ($5 \times 10^{21} \text{ cm}^{-2}$ and $N_{\text{H}} = 10^{22} \text{ cm}^{-2}$, Fig. 3.6, bottom) reproduce the colours of our sources lying on the top right end of the plot (which are outside the galaxy and quasar loci; Fig 3.4). This suggests that our toy model, although very simplistic, can give useful constraints on the source properties.

In an attempt to place constraints on the redshift of our EXOs, the evolution of the f_X/f_{opt} with redshift was also investigated, using the same method as above: the r' magnitude was computed for different model SEDs with increasing N_{H} , in the redshift range $z = 0 - 2.5$ (see above).

In order to model the X-ray emission, a simple power-law with a photon index $\Gamma = 1.8$ (e.g. Nandra & Pounds 1994) including Galactic and the intrinsic (nuclear) absorption (with the same intrinsic N_{H} used to parameterise the extinction in the optical/IR SED) was used. The X-ray flux in the 2–10 keV energy band was computed and the f_X/f_{opt} derived ($\log(f_X/f_{\text{opt}}) = \log f_{2-10 \text{ keV}} + r'/2.5 + 5.5$; e.g. Civano et al. 2005). In Figure 3.7 the

resulting f_X/f_{opt} tracks for increasing N_{H} and increasing redshift are shown. The tracks have been normalised to $f_X/f_{\text{opt}} = 1$ for a typical unabsorbed (and unobscured) QSO at $z = 1.5$.

According to the f_X/f_{opt} tracks obtained, a strong dependence of the X-ray-to-optical flux ratio with the redshift was found: for obscured objects the f_X/f_{opt} increases with the redshift, indicating that the more extreme EXOs are likely to be the highest redshift objects (see also Fiore et al. 2003); furthermore, the f_X/f_{opt} decreases for unobscured sources, thus no such objects at high redshift should be included in our EXO sample. However, as the normalisation of the curves was arbitrarily chosen, no tight constraints on the results can be placed.

3.4 UKIRT NIR data

As many EXOs are found to have very red colours, even typical for extremely red objects (EROs; see Chapter 1), they are expected to be bright in the NIR band. Indeed, in order to further investigate the properties of our EXOs, in particular those with no detection in the optical bands, the NIR band was explored. As the dust obscuration effects are much lower in this band, the NIR can provide important information on the brightness and colours of the sources.

3.4.1 UKIDSS archive data

The United Kingdom Infrared Telescope (UKIRT) Deep Sky Survey (UKIDSS; Lawrence et al. 2007) is a combination of five surveys started in May 2005, with complementary area, depth and Galactic latitude coverage. The surveys use up to five photometric filters (Z, Y, J, H, K ; Hewett et al. 2006) covering the wavelengths from 0.83 to 2.37 μm . These broad-band filters are Mauna Kea Observatory Near-IR (MKO-NIR) filters, which are designed to match the atmospheric windows in order to obtain optimal signal-to-noise (see Fig. 3.8; Simons & Tokunaga 2002).

The survey data are taken using the Wide Field Camera (WFCAM; Casali et al. 2007)

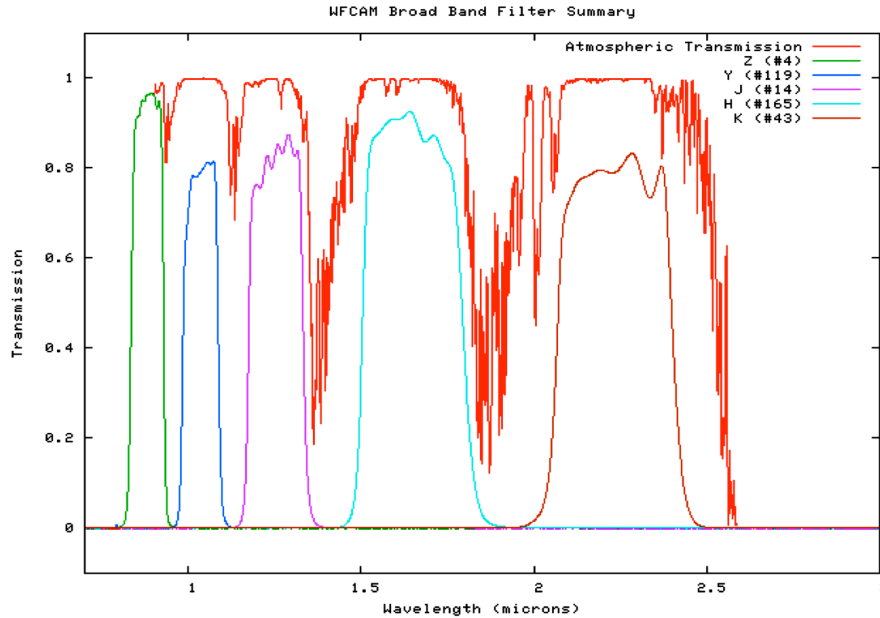


Figure 3.8: UKIRT-WFCAM NIR broad-band filters Z , Y , J , H , K (left to right); the red line represents the atmospheric transmission curve. The Figure is adapted from: http://www.jach.hawaii.edu/UKIRT/instruments/wfcam/user_guide/description.html

instrument on the 3.8 m telescope UKIRT, in Mauna Kea, Hawaii. The camera consists of 4 Rockwell Hawaii-II (2048×2048 pixels) detector arrays, with a field of view (FoV) of 0.21 deg^2 each. The four arrays are arranged in a square pattern, separated by a central gap of $12.9'$, covering a total sky area of 0.75 deg^2 .

Two of the five surveys composing the UKIDSS are targeted on Galactic fields, while the other three are targeted on extragalactic fields: the Large area Survey (LAS) is planned to cover 4000 deg^2 of the SDSS survey in four bands (Y , J , H , K , Vega), with a typical depth $K = 18.2$; the Deep Extragalactic Survey (DXS) is a medium deep survey performed using the J and K filters (typical depth $K = 21.0$), covering about 35 deg^2 ; the Ultra Deep Survey (UDS) is the deepest of the UKIDSS surveys and covers a smaller sky area of 0.78 deg^2 , centred in the central region of the Subaru/*XMM-Newton* Deep Survey (SXDS; see Chapter 5).

Our sources were initially searched for in the UKIDSS-LAS DR3 data archive, released in December 2007, which contains observations for about 36 million objects with depth $Y \approx 20.2$, $J \approx 19.6$, $H \approx 18.8$, $K \approx 18.2$. Ten sources were found to have IR

imaging in the archive, although all four filters were not available for all the source observations (see Table 3.1). These sources have been complemented later on with four more detections obtained at the release of UKIDSS-LAS DR5 data archive, in April 2009.

3.4.2 NIR follow-up

In order to enlarge the fraction of sources with NIR data, we have also embarked on a program of NIR follow-up imaging of the sample: UKIRT NIR data were obtained through service time proposals with the WFCAM (J and K) and with UFTI (J , H and K ; see below) for 30 of our EXOs (23% of the whole sample).

The WFCAM data were obtained in February and May 2007 for six of our sample sources. The WFCAM data were processed in Cambridge with a pipeline developed by CASU (Cambridge Astronomical Survey Unit): this pipeline performs a complete data reduction, including flat fielding, microstep processing and mosaicing. Afterwards, it carries out object detection and creates a source catalogue for each image, followed by astrometric and photometric calibration.

From the source catalogue obtained for our source images, the magnitude in the J and K bands were computed with the following formula:

$$m_i = -2.5 \log (f_i/t_{exp}) + ZP_i - AC \quad (3.1)$$

where f_i is the flux¹⁰ in the NIR band i (in our case, $i = J, K$) reported in the catalogue, t_{exp} is the exposure time of the image, ZP_i is the zero point magnitude for each image and the AC is the aperture correction. The errors were estimated accordingly propagating the errors of the parameters reported in the image catalogue. When a source was not detected in the field, the magnitude upperlimit of the image (reported in the observation log) was used. All the resulting values are reported in Table 3.1.

¹⁰In the calculation the aperture flux within a radius 1.0'' ("rcore"; catalogue entry APER_FLUX_3) was used; in $\approx 1.0''$ seeing an rcore-radius aperture contains $\sim 2/3$ of the total flux of stellar images.

The UKIRT Fast-Track Imager (UFTI; Roche et al. 2003) data were obtained for 24 sample sources between December 2007 and January 2008. The UFTI is one of the instruments operating at UKIRT until recently; its imaging camera consists of a 1024×1024 pixel detector array with a field of view of $92''$ ($0.09''/\text{pixel}$). The UFTI uses a set of standard broad and narrow-band filters in the wavelength range $1 - 2.5 \mu\text{m}$ (Simons & Tokunaga 2002; see also Fig. 3.8).

For our sources, the photometric data in the J, H, K bands (covering the wavelengths $\lambda = 1.17 - 1.33 \mu\text{m}$, $\lambda = 1.49 - 1.78 \mu\text{m}$, $\lambda = 2.03 - 2.37 \mu\text{m}$, respectively) were obtained: 2×9 -point jitter frames of $50 - 60$ sec exposure were taken for each source in the three filters, with photometric conditions and seeing better than $1.0''$ (typical seeing $0.7''$). During one night only the seeing was bad, $\sim 1.5 - 2''$; we note that for the six sources observed that night, the uncertainties on the photometry are larger (see Table 3.1).

The data obtained each night were processed using the ORAC-DR pipeline (Currie et al. 1999). The pipeline is created to perform the standard photometric data reduction: i) it subtracts the darks taken during the night, ii) applies a bad-pixel mask, iii) combines the nine frames from each group and creates the flat field, masking out the central region where the target should lie, iv) then it performs the flat-fielding for each observation of the group, and finally v) it shifts and averages the observations to produce a mosaic image; for each source, two mosaic images result from this process (one image for each grid of 9 pointings); they are then stacked together to produce the final image.

Astrometry calibration was then performed on each image by comparing the coordinates of the sources in the field with those reported in the 2MASS (where available) or in the USNO-B catalogues.

Aperture photometry was performed on each final image for all the sources using the GAIA software¹¹. The standard stars observed each night were used to calibrate the images; in order to minimise the uncertainties due to the sky and seeing variations during the night, the standard star observed closer in time to the source was used for the calibration of the relative source image.

¹¹<http://astro.dur.ac.uk/~pdraper/gaia/gaia.html>

A circular aperture with a radius of 5 times the FWHM (typically $r_* = 35 - 40$ pixels, corresponding to $\sim 3.2 - 3.6''$, for good seeing; $r_* = 80$ pixels for bad seeing) was adopted to extract the instrumental magnitude for the standard stars, where the FWHM was estimated for each image. The zero point magnitude (ZP) for the observation was calculated as the difference between the magnitude of the standard star reported in the literature and the instrumental magnitude, corrected for the extinction.

The magnitude of the EXOs was extracted from an elliptical region, chosen to include the total emission of the source and minimise the background counts inside the extraction region. Typically the semimajor axis¹² adopted was $r_{EXO} = 10 - 15$ pixels (corresponding to $1 - 1.35''$, in good seeing conditions). The background was estimated from an annular region centred on the source coordinate.

Due to variable seeing and the variable extraction region used in our calculations, an aperture correction was determined individually for each image: a bright star in the source field was selected as reference object; the difference between the instrumental magnitudes measured within r_* of the standard star selected for the calibration and r_{EXO} of the source to be calibrated was taken as the aperture correction AC (e.g. Kuhn 2004).

The magnitude of our sources was then determined from their instrumental magnitude with the following formula:

$$m_i = m_i(r_{EXO}) + ZP_i - AC_i - k_i(\chi - 1) \quad (3.2)$$

where m_i is the source magnitude in the band i ($i = J, H, K$) and $m_i(r_{EXO})$ is the instrumental magnitude within the radius r_{EXO} ; the parameter $k_i(\chi - 1)$ is the extinction correction, where k_i is the extinction coefficient in the relative NIR band and χ is the air-mass; the extinction coefficients were taken from Hodgkin et al. (2009). The errors were calculated as the quadrature sums of the errors in the instrumental magnitude, aperture correction and zero point (see Table 3.1).

We note that four of our EXOs observed with UFTI now also have WFCAM archival

¹²The typical radius adopted corresponds to $1.5 - 2 \times \text{FWHM PSF}$; in the cases where the source looked extended or in bad seeing conditions larger radii were used.

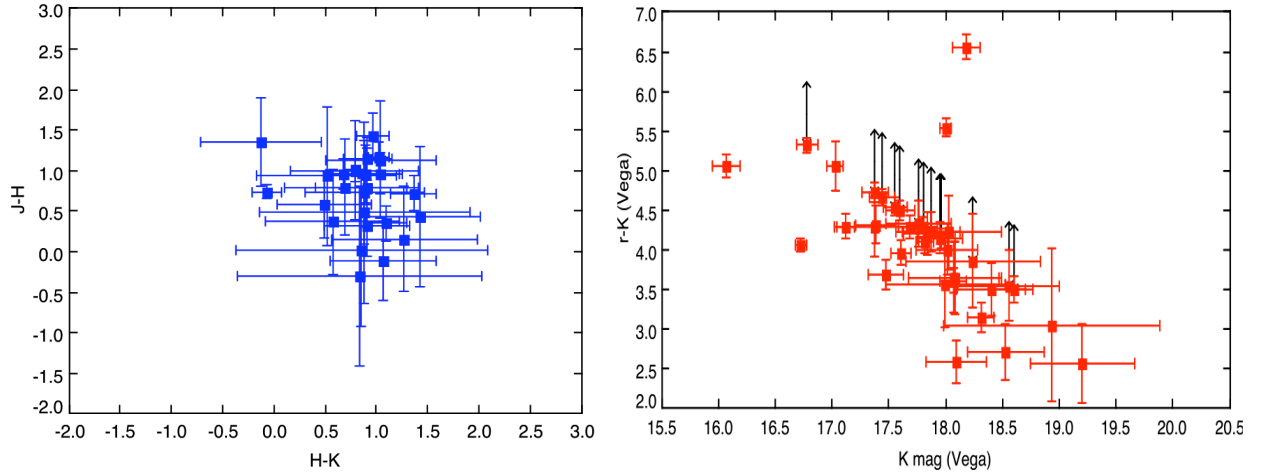


Figure 3.9: Left: NIR colour-colour plot for the subsample of objects with UKIRT data (31% of the sample). Right: UKIRT K magnitude vs. $(r - K)$ colour (Vega) for all the sources detected in the NIR band; the $(r - K)$ colour of our EXOs is typically red, and at least five sources have values typical for EROs ($r - K > 5$; the fraction of sources with ERO colours is probably higher, taking into account the upperlimits in the r -band).

data from the UKIDSS (DR5). In order to verify the results obtained through the aperture photometry, the magnitudes obtained from the UFTI data for these four sources were compared with the values reported in the UKIDSS catalogue: in all the cases the magnitudes were consistent within the errors.

The NIR follow-up observations performed for our sources allowed the magnitude determination in at least one of the three NIR bands used, and in the majority of the cases, in all three bands. These observations provided also the detection and hence the likely counterpart identification of fourteen sources defined as “upperlimits” in the optical (see Sect. 2.5), four of which were undetected in any of the SDSS bands.

In Figure 3.9 (left) the NIR $H - K$ and $J - H$ colours are shown; the colour distribution of our sources is consistent with the typical NIR colours of quasars (see e.g. Kouzuma & Yamaoka 2009), suggesting that amongst these sources the sample should not have large contamination by non-AGN sources (see Sect. 1.4). The optical/NIR colour $r - K$ is also shown (Fig. 3.9, right); the $r - K$ colour is typically red for the majority of the sources, in at least five cases reaching the extreme values typical of EROs ($r - K \geq 5$; e.g. Severgnini et al. 2005). However, fourteen of the sources shown in the plot only

Table 3.1: UKIRT NIR magnitudes

ID	J mag	H mag	K mag	Instrument	Comments
2XMM J004109.1-092606	19.00 ± 0.41	18.65 ± 0.51	18.07 ± 0.40	UFTI	
2XMM J015603.7+002738	–	18.57 ± 0.20	17.95 ± 0.20	WFCAM	UKIDSS
2XMM J020957.9-100301	19.23 ± 0.65	18.81 ± 0.56	17.38 ± 0.18	UFTI	seeing $\approx 1.8 - 2.0''$
2XMM J023028.9-010222	18.25 ± 0.06	17.53 ± 0.06	17.60 ± 0.13	WFCAM	UKIDSS
2XMM J023125.3-073135	> 19.18	19.04 ± 0.65	17.76 ± 0.29	UFTI	seeing $\approx 1.8 - 2.0''$
2XMM J030228.5-000601	19.77 ± 0.50	18.78 ± 0.35	18.00 ± 0.53	UFTI	
2XMM J035430.5+003616	–	–	17.96 ± 0.13	WFCAM	UKIDSS
2XMM J035453.8+002536	19.50 ± 0.14	19.16 ± 0.17	18.07 ± 0.11	WFCAM	UKIDSS
2XMM J073536.6+314620	19.23 ± 0.22	18.93 ± 0.32	18.02 ± 0.27	UFTI	
2XMM J075050.0+143528	19.15 ± 0.27	17.74 ± 0.13	16.78 ± 0.10	UFTI	
2XMM J080605.8+152734	19.46 ± 0.25	18.90 ± 0.34	18.40 ± 0.31	UFTI	
2XMM J082053.8+210735	20.03 ± 0.55	18.92 ± 0.47	17.87 ± 0.25	UFTI	
2XMM J084630.0+345858	19.03 ± 0.22	19.16 ± 0.44	18.09 ± 0.27	UFTI	
2XMM J091946.4+302953	19.68 ± 0.24	18.73 ± 0.26	17.84 ± 0.21	UFTI	
2XMM J092043.5+303701	19.45 ± 0.10	18.75 ± 0.19	17.38 ± 0.12	UFTI	J band from WFCAM (UKIDSS)
2XMM J092201.2+301412	19.52 ± 0.19	18.39 ± 0.18	17.48 ± 0.16	UFTI	
2XMM J093911.2+354537	19.24 ± 0.41	17.90 ± 0.37	18.03 ± 0.46	UFTI	
2XMM J094204.6+480448	19.52 ± 0.66	18.60 ± 0.55	18.08 ± 0.41	UFTI	
2XMM J094352.4+465506	> 19.08	19.39 ± 1.11	18.56 ± 0.45	UFTI	seeing $\approx 1.8 - 2.0''$
2XMM J100058.1+014559	18.91 ± 0.124	17.92 ± 0.08	17.12 ± 0.08	WFCAM	UKIDSS, also observed with UFTI
2XMM J101317.2-001907	18.91 ± 0.16	17.75 ± 0.09	16.73 ± 0.05	WFCAM	UKIDSS, also observed with UFTI
2XMM J101659.8+213316	19.30 ± 0.13	–	17.82 ± 0.08	WFCAM	
2XMM J102016.0+082142	18.98 ± 0.44	18.26 ± 0.46	17.38 ± 0.35	UFTI	
2XMM J102336.7+005152	19.80 ± 0.55	19.79 ± 0.77	18.93 ± 0.95	UFTI	
2XMM J103451.0+393836	19.60 ± 0.74	19.13 ± 0.84	18.24 ± 0.59	UFTI	seeing $\approx 1.8 - 2.0''$
2XMM J111121.2+482332	18.05 ± 0.18	17.10 ± 0.18	16.07 ± 0.12	UFTI	seeing $\approx 1.8 - 2.0''$
2XMM J112305.8+014912	> 19.19	–	18.18 ± 0.12	WFCAM	
2XMM J112604.1+423950	20.68 ± 0.44	19.90 ± 0.39	19.21 ± 0.46	UFTI	
2XMM J115446.8+232917	> 20.50	–	18.60 ± 0.17	WFCAM	
2XMM J121919.0+295326	19.95 ± 0.17	–	18.31 ± 0.12	WFCAM	
2XMM J122437.8+131327	19.43 ± 0.15	18.48 ± 0.10	17.81 ± 0.12	WFCAM	UKIDSS, also observed with UFTI
2XMM J123204.9+215255	> 21.27	–	18.00 ± 0.05	WFCAM	
2XMM J123242.9-000455	–	–	17.55 ± 0.10	WFCAM	UKIDSS
2XMM J125357.1+154314	–	18.25 ± 0.13	17.03 ± 0.07	WFCAM	UKIDSS
2XMM J125906.6-015057	20.22 ± 0.32	19.44 ± 0.38	18.53 ± 0.34	UFTI	
2XMM J151755.9+062232	–	18.78 ± 0.14	17.61 ± 0.09	WFCAM	UKIDSS
2XMM J154930.6+213422	–	–	17.69 ± 0.10	WFCAM	
2XMM J160545.9+255145	19.74 ± 0.12	–	–	WFCAM	UKIDSS
2XMM J231731.6+001032	–	–	17.44 ± 0.11	WFCAM	UKIDSS
2XMM J231740.8+001052	–	18.83 ± 0.25	–	WFCAM	UKIDSS

Notes: All the magnitudes are in Vega magnitude system.

have r -band magnitude upperlimits, therefore the number of sources with extremely red colours may be as high as seventeen ($\sim 43\%$ of the NIR subsample and 13% of the total EXO sample). These results confirm our EXOs are likely to be highly obscured objects, with highly reddened continua.

3.5 Optical spectroscopy

An optical spectroscopic follow-up campaign was started in order to identify and investigate the sources in our sample and to characterise the high f_X/f_{opt} population in more detail. Dedicated observing runs were obtained at the 8-m Subaru telescope, on Mauna Kea (Hawaii) and the ESO Very Large Telescope (VLT), in Cerro Paranal (Chile) for 26 of our sample objects. The observations were performed between February and August 2008.

3.5.1 Subaru FOCAS data

Optical long-slit spectroscopy was performed using the Faint Object Camera and Spectrograph (FOCAS) on the Subaru Telescope for sixteen objects on the 9th and 10th of February 2008. The sources were observed with a 300/mm grating (B300 grism) without any order cut filter and a $0.8''$ slit, with a spectral resolution $\lambda/\Delta\lambda \approx 700$. The seeing during the observations ranged between $1.0 - 2.0''$. The spectra obtained cover a wavelength range of $\lambda \approx 5800 - 9800 \text{ \AA}$.

For each source 2-3 frames of 1200 s exposure each were obtained, shifting the source position along the slit ($3.0''$ dithering observations). Standard stars were also observed at the beginning and at the end of each night (using a $2.0''$ slit width), as well as flat field, bias and comparison frames.

The spectral reduction was performed with IRAF, using a task specifically implemented for Subaru-FOCAS data (`focasred`). The source spectral frames were calibrated separately and then combined together. After bias subtraction and flat fielding, the wavelength calibration for the source spectra was obtained using the sky emission lines, which are rather constant at the wavelengths covered by our observations; the calibration of the standard stars was done using the ThAr lamps.

After sky-subtraction, the standard stars observed during the nights (GD71 and GRW+78D5824) were used to perform the flux calibration (it is worth noting that because the weather conditions were not photometric during the whole observing run, the absolute flux calibration cannot be guaranteed). The flux-calibrated frames were then corrected for

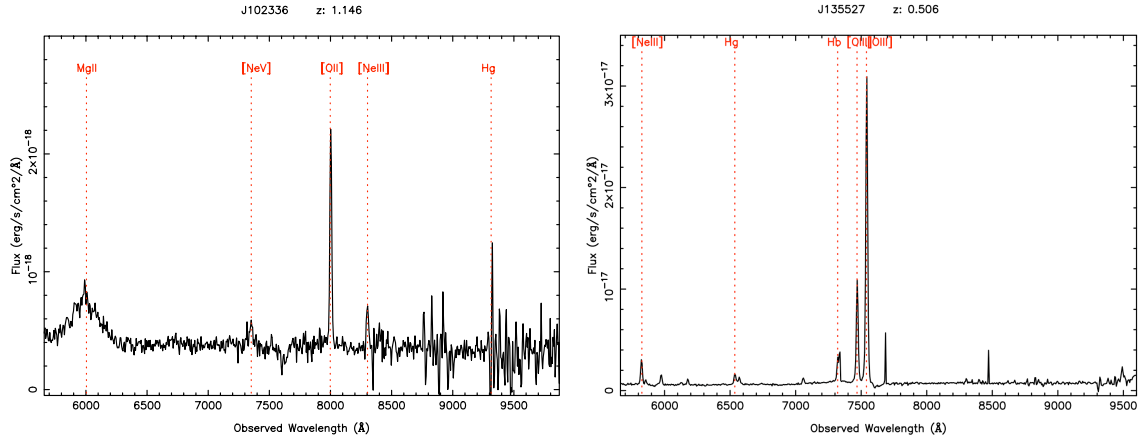


Figure 3.10: Examples of two optical spectra of our EXOs, obtained at the Subaru Telescope: a broad emission line (BL) AGN on the left and a narrow emission line (NL) AGN on the right. The spectra have been renormalised to the SDSS i' – band magnitude for each source (see text). The “spikes” (narrowest emission features) in the spectra are not real emission lines, but they are due to cosmic rays.

the atmospheric extinction measured at the summit of Mauna Kea, shifted and combined together in order to improve the signal-to-noise (S/N) of the spectra. Figure 3.10 shows two examples of the reduced spectra¹³ obtained from the Subaru Telescope.

3.5.2 ESO VLT data

The ESO-VLT optical spectra were obtained with the FORS2 spectrograph for ten of our EXOs between April and August 2008. The long-slit spectroscopy was performed with the GRIS 300I+21 grism and $1.0''$ slit width: this configuration provided a spectral resolution $\lambda/\Delta\lambda \approx 700$, equivalent to a line velocity width $\Delta v \approx 400 \text{ km s}^{-1}$, and wavelength coverage $\lambda \sim 6000 - 11000 \text{ \AA}$. The typical seeing of the observations was $\sim 1''$.

The objects were observed with 2 – 4 frames with exposures ranging from 900 s to 1350 s, depending on the source r' magnitude. The usual calibration frames were also taken during the observing run, in order to perform the data reduction, which was performed by a standard ESO pipeline. We took the bias-subtracted, flat-fielded, wavelength calibrated data to perform the sky-subtraction and the flux calibration. The different

¹³We note that the narrowest emission features in the spectra are not real emission lines, but they are due to cosmic rays, which in some cases, were not properly corrected (see also Fig. 3.11 and Fig. A1.1, Appendix 1).

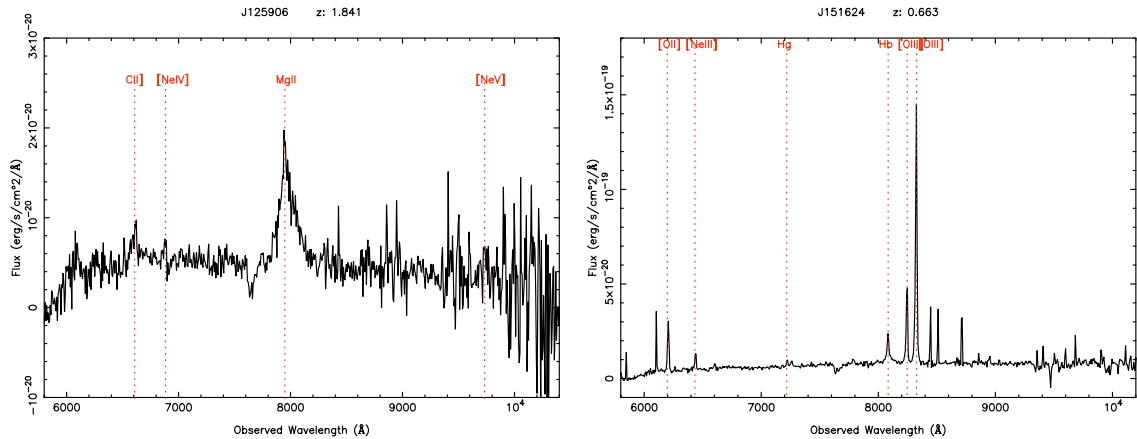


Figure 3.11: Examples of two of the ten optical spectra obtained with the VLT-FORS2: a broad emission line (BL) AGN on the left and a narrow emission line (NL) AGN on the right. The spectra have been renormalised to the SDSS i' -band magnitude for each source (see text).

frames obtained for each source were processed separately and combined at the end of the calibration process.

In order to produce the flux calibrated spectra several standard stars were used, choosing for each source, the star observed closer in time, to reduce the uncertainties due to atmospheric variations. The calibrated frames were then corrected for the atmospheric extinction and finally shifted and combined. We stress that the absolute flux calibration of the spectra is not reliable, as the observing conditions were not photometric during the whole observing run. Two of the ESO-VLT spectra are shown in Figure 3.11.

3.5.3 Other spectroscopic data

Follow-up spectroscopic observations were obtained for two additional sources amongst our EXOs from other ground based facilities. Targeted NIR spectroscopy with the Multi-Object Infrared Camera and Spectrograph (MOIRCS) at the Subaru telescope was performed on the most extreme f_X/f_{opt} object of our sample (2XMM J123204; Del Moro et al. 2009); the spectroscopy allowed the classification of this source as a type-2 QSO (more precisely type 1.9, following the typical classification used for Seyfert galaxies) at redshift $z = 1.83$. For an extensive description on the analysis and the properties of this source we refer to Chapter 4.

Another of our sample sources, 2XMM J143623, was observed at the 10-m Gran Telescopio Canarias (GTC) in April 2009, as part of a spectroscopy identification campaign on a different sample of high f_X/f_{opt} sources ($f_X/f_{\text{opt}} > 20$ in the 2 – 10 keV energy band) assembled by merging three different samples of X-ray selected sources. Some further objects in our EXO sample are included in this on-going campaign.

The optical spectrum of 2XMM J143623, the only one amongst our sample obtained at the GTC to date, is characterised by low signal-to-noise but a single narrow emission line was reliably detected (and possibly a second weak line). The spectral analysis of the GTC data for 2XMM J143623, performed elsewhere (kindly provided by Dr Francisco J. Carrera¹⁴, private communication), follows the standard reduction technique. Two identifications are possible for the detected emission line: i) MgII, with redshift $z = 1.522$ or ii) [OII], with redshift $z = 0.892$. As in the optical image the source looks extended (galaxy morphology), we assumed the second hypothesis is more likely, therefore the source was classified as a type-2 AGN at redshift $z = 0.892$.

Neither of these sources are included in the optical spectral analysis described in the following section, but will be taken into account in the final consideration of our EXO sample.

3.5.4 Optical spectral analysis

Comparing the reduced Subaru and the ESO-VLT spectra, a systematic depression in flux was noted in the latter data. This effect is unlikely to be intrinsic as the optical magnitudes of the sources observed at Subaru and at VLT are comparable; it is reasonable to think that this effect was produced during the ESO pipeline data reduction, and probably related to a coding error. In order to overcome this problem and to make the spectra obtained with different instruments as uniform as possible, we renormalised all the source spectral fluxes to their SDSS i' -band magnitude. All the spectra are shown in Fig. A1.1 (Appendix 1).

We also note that there are some features that are common for all our source spectra, hence they are not characteristics of the objects, but have different origins: i) the strong

¹⁴Instituto de Física de Cantabria (CSIC-UC), Santander, Spain.

absorption line at $\lambda \approx 7600 \text{ \AA}$ is a feature produced by the atmosphere; ii) the significant spectral noise at $\lambda \gtrsim 9500 \text{ \AA}$ is due to a complex of sky lines, which is difficult to properly correct in the sky-subtraction process.

All but two of our source spectra (24 objects) show several strong emission lines above the continuum, which allowed the source classification and the redshift measurement¹⁵. The sources 2XMM J101659 and 2XMM J123242 show a rather red continuum with no significant emission or absorption lines. Therefore for these two objects, the redshift could not be measured from the current data and no further analysis was performed on them. We note that the red continuum and the very red $r - K$ colour of these sources ($r - K > 4.4$, see Fig. 3.9, right) suggest that they may be highly obscured, high redshift objects ($z \sim 2$), whose broad lines (e.g. MgII would be observed at $\lambda \approx 8400 \text{ \AA}$, at $z = 2$) are heavily reddened and the strong narrow emission lines fall out of the optical band observed¹⁶.

Using spectral templates of different emission and absorption line objects as a reference (QSOs, Seyfert galaxies, normal galaxies, starburst galaxies) we were able to identify the emission lines detected in the spectra (for 24 objects) and estimate the redshifts. In addition to the emission lines, some absorption lines are also detected in some spectra (2XMM J090729, 2XMM J100058, 2XMM J122437, 2XMM J231731, 2XMM J233817); these lines were identified as absorption features typical of normal galaxies. The presence of these galaxy absorption lines indicates that for these sources the host galaxy emission makes a significant contribution to the spectrum; this is typical of Seyfert galaxy spectra, or of obscured AGN, where the nuclear emission does not outshine the host galaxy.

In order to measure the emission line parameters (line width and flux) and have an accurate classification of our EXOs, the spectra were then analysed using the task `specfit` within IRAF. As the majority of the sources show a rather flat (and red) continuum, the underlying emission was fitted with a power-law, with slope and normalisation as free

¹⁵We point out that one of the sources observed at the ESO-VLT telescope (2XMM J204043) was already spectroscopically identified by other authors (Caccianiga et al. 2004); we used this source as a comparison object to test the quality of our optical spectral analysis.

¹⁶Following this hypothesis, we included these two sources amongst the targets for NIR spectroscopy at Subaru telescope (to be performed in April 2010; see Chapter 6).

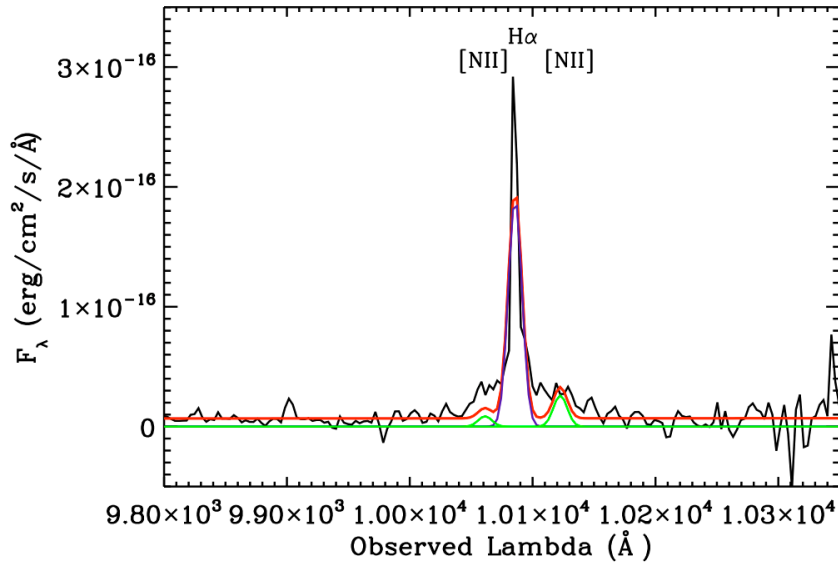


Figure 3.12: Example of emission line fitting with multiple Gaussian components; this is the narrow $H\alpha$ line detected in the source 2XMM J151755 (black line), which was fitted with a narrow Gaussian profile (blue) and two narrow profiles (green) to reproduce the $[NII]$ emission lines; the red line represents the resulting model.

parameters. In some cases however, a single power-law does not provide a good representation of the continuum, which appears to have a “bump”; this occurred especially in the spectra showing galaxy signatures, thus the “curved” continuum is very probably due to the starlight emission (see Fig. 3.5). For these sources the continuum was parameterised with a broken power-law. We note that our aim was not to obtain the best-fit of the spectra, but to have a representation of the underlying continuum that is good enough to allow the analysis of the emission lines.

A Gaussian profile was included in the spectral model at the observed wavelength expected for each emission line (considering the estimated z) in the wavelength range covered by the spectra (Fig. 3.12); for the permitted lines (MgII and Balmer lines), two Gaussian profiles were used in order to characterise the broad and narrow components of the line. When a line was not significantly detected above the continuum, a 3σ upperlimit of the flux was estimated. The FWHM of the lines was left free to vary, but it was constrained to be the same for all the broad lines (and the narrow lines) in a spectrum, as we supposed all the broad lines to have a common origin (in the BLR) and all the narrow lines to originate in the NLR (Sect. 1.1.2)

From the results of our spectral analysis, following the classification criteria adopted by Caccianiga et al. (2004), based on the line width and the $[\text{OIII}]\lambda 5007\text{\AA}/\text{H}\beta$ line flux ratio¹⁷ (see also Véron-Cetty & Véron 2001), we were able to classify all 24 sources. As noted in several previous works (e.g. Caccianiga et al. 2008, and references therein), the $[\text{OIII}]\lambda 5007\text{\AA}/\text{H}\beta$ flux ratio is, in fact, a good indicator of the source spectral type: objects with significant reddening in the optical spectra (e.g. Seyfert 2, 1.9, 1.8¹⁸) have typically high line ratios ($[\text{OIII}]\lambda 5007\text{\AA}/\text{H}\beta > 3$), as the broad component of $\text{H}\beta$ is reddened, while unobscured (or moderately obscured) objects, namely the Seyfert 1, to 1.5, have usually lower values, $[\text{OIII}]\lambda 5007\text{\AA}/\text{H}\beta = 0.2 - 3$; narrow line objects with $[\text{OIII}]\lambda 5007\text{\AA}/\text{H}\beta < 3$ are usually HII region galaxies or starburst galaxies, where the $\text{H}\beta$ emission is enhanced by the star formation activity (Caccianiga et al. 2008).

Amongst our sample sources we found:

- 8 objects showing broad permitted emission lines ($\text{FWHM} \gtrsim 2000 \text{ km s}^{-1}$) in their spectra: these were classified as broad emission line (BL) AGN;
- 1 object (2XMM J090729) with several narrow emission lines ($\text{FWHM} \lesssim 1000 \text{ km s}^{-1}$) except for a broad $\text{H}\alpha$ line; this was classified as Seyfert 1.9 (Sy 1.9). Although the $\text{H}\beta$ line is not detected in this object, the $[\text{OIII}]\lambda 5007\text{\AA}/\text{H}\beta$ flux ratio given by the $\text{H}\beta$ flux upperlimit is rather high (> 2.6), which supports this classification;
- 14 sources showing only narrow emission lines ($\text{FWHM} \lesssim 1000 \text{ km s}^{-1}$) and a high $[\text{OIII}]\lambda 5007\text{\AA}/\text{H}\beta$ flux ratio (> 3 , for all sources where these two lines were covered); these were classified as narrow emission line AGN (NL AGN). One of these sources (2XMM J101317, whose spectrum does not cover $[\text{OIII}]$ and $\text{H}\beta$) presents a narrow MgII line core ($\text{FWHM} \approx 520 \text{ km s}^{-1}$) with weak broad wings (detected at the 5σ level); nonetheless, we included this source in the NL AGN group as the equivalent width of the broad MgII component is significantly smaller than the

¹⁷The ratio is defined by the flux of the forbidden $[\text{OIII}]\lambda 5007\text{\AA}$ (narrow) emission line and the total flux (broad + narrow components) of the $\text{H}\beta$ emission line.

¹⁸Seyfert 1.9 and 1.8s are intermediate types of objects where mainly narrow emission lines are seen in the spectra, but one or two broad Balmer lines, respectively are present as well. These objects are usually associated with the type-2 category as the extinction measured for them is still high ($A_V \gtrsim 2 \text{ mag}$).

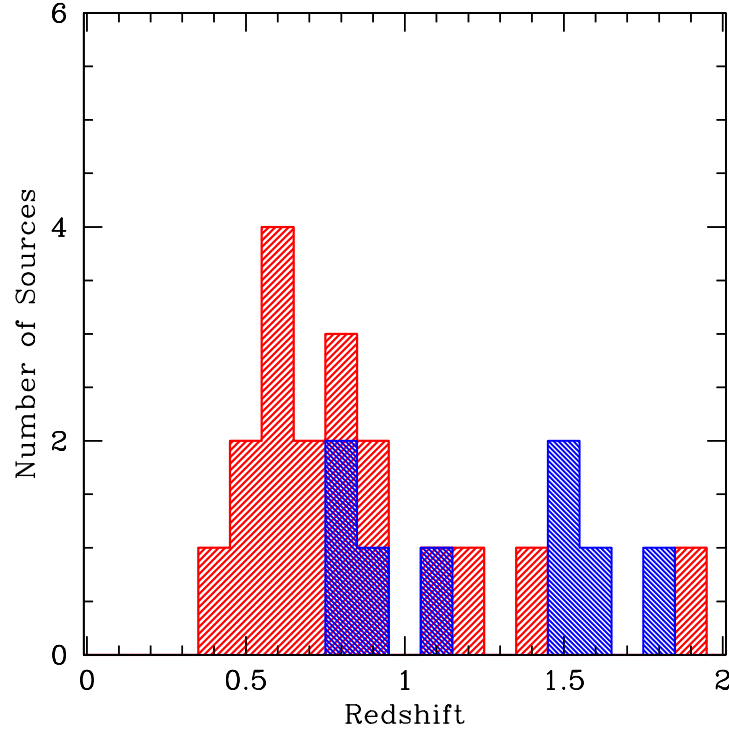


Figure 3.13: Redshift distribution for all the spectroscopically identified EXOs in our sample. The type-2 AGN (as defined in the text) are represented in red and the type-1 AGN in blue. The distribution for the type-2 objects peaks at $z \sim 0.6 - 0.7$, while most of the type-1 objects have redshifts > 1 .

sources classified as BL AGN and the spectral continuum is red, suggesting some level of obscuration in this object. Moreover, we note that the FeII emission line complex at $\lambda \approx 2200 - 4000 \text{ \AA}$ (rest-frame, see Sect. 1.1.2) may cause significant uncertainties in the definition of the underlying continuum as it is difficult to deblend this complex from the MgII emission.

- 1 source (2XMM J233819) whose spectrum shows narrow emission lines only, but with $[\text{OIII}]\lambda 5007\text{\AA} / \text{H}\beta \sim 1.3$ was classified as a narrow emission line galaxy (NELG); nevertheless, the oxygen line flux ratio $[\text{OII}]\lambda 3727\text{\AA} / [\text{OIII}]\lambda 5007\text{\AA} \sim 1.8$ is lower than the typical values for starburst or HII-region galaxies (~ 3 ; Veilleux & Osterbrock 1987), which suggests that the emission in this source could be a combination of AGN and starburst components.

The spectral properties and classification of the sources are summarised in Table 3.2. According to the standard classification for AGN, we considered all the BL AGN as type-

Table 3.2: Optical spectral parameters and classification

ID	r' mag	z	FWHM (broad)	FWHM (narrow)	Class	Type
			(km s^{-1})	(km s^{-1})		
2XMM J004109	22.12±0.17	1.385	–	800	NL AGN	2
2XMM J015603	>22.5	1.115	–	510	NL AGN	2
2XMM J030228	21.96±0.13	1.515	8000	500	BL AGN	1
2XMM J035453	22.08±0.10	0.914	6010	500	BL AGN	1
2XMM J090729	20.38±0.05	0.387	8010	560	AGN 1.9	2
2XMM J092201	21.56±0.09	0.567	–	560	NL AGN	2
2XMM J100058	21.82±0.13	0.622	–	640	NL AGN	2
2XMM J101317	21.18±0.07	1.174	4990	520	NL AGN	2
2XMM J101659	22.32±0.11	0.0	–	–	–	–
2XMM J102336	22.38±0.13	1.147	8100	520	BL AGN	1
2XMM J111121	21.53±0.08	0.847	5980	500	BL AGN	1
2XMM J121919	21.86±0.14	1.587	8000	500	BL AGN	1
2XMM J122437	>22.5	0.827	–	510	NL AGN	2
2XMM J123242	>22.5	0.0	–	–	–	–
2XMM J125357	22.48±0.30	0.941	–	490	NL AGN	2
2XMM J125906	21.64±0.11	1.840	7970	720	BL AGN	1
2XMM J135402	21.97±0.08	1.517	5090	500	BL AGN	1
2XMM J135527	21.17±0.06	0.506	–	650	NL AGN	2
2XMM J145030	21.86±0.12	0.760	5540	790	BL AGN	1
2XMM J151624	22.05±0.12	0.663	–	850	NL AGN	2
2XMM J151755	21.97±0.13	0.538	–	330	NL AGN	2
2XMM J154930	22.38±0.10	0.633	–	590	NL AGN	2
2XMM J204043	21.44±0.04	0.621	–	740	NL AGN	2
2XMM J230503	>22.5	0.654	–	570	NL AGN	2
2XMM J231731	>22.5	0.813	–	670	NL AGN	2
2XMM J233819	22.81±0.07	0.770	–	480	NELG	2

Notes: The errors on the line widths are typically $\sim 10\%$, estimated at 1σ confidence level.

1 and all the NL AGN, Sy 1.9 and NELG as type-2 AGN (e.g. Caccianiga et al. 2004). In summary, amongst the 24 spectroscopically identified EXOs in our sample, 8 objects are type-1 (33%) while 16 objects are type-2 (67%). We note that considering the two sources mentioned above (2XMM J123204 and 2XMM J143623, see Sect. 3.5.3), which are included in the type-2 class, the fraction of type-1 and type-2 AGN amongst the spectroscopically identified sources become 69% of type-2 AGN and 31% of type-1 AGN.

The redshift distribution for all the spectroscopically identified sources is shown in Figure 3.13. Our sources span a rather wide range of redshift ($z = 0.39 - 1.84$), with $\sim 35\%$ of the sources lying at high redshift ($z > 1$). The distribution for type-2 AGN

peaks at $z \sim 0.7$ while most of the type-1 AGN have higher redshift ($z > 1$). This result is in agreement with those obtained from several population studies of X-ray selected AGN (e.g. Cowie et al. 2003; Steffen et al. 2003; Hasinger 2003; Mateos et al. 2005b). The type-2 fraction amongst our sample however is higher than that usually found in the bright X-ray selected AGN population (e.g. Caccianiga et al. 2004; see also Chapter 5).

As stated above, almost all the spectra obtained show flat and/or red continuum, indicating that some amount of reddening is present in our objects, indeed this is also confirmed by the line ratio diagnostic $[\text{OIII}]\lambda 5007\text{\AA} / \text{H}\beta$. In order to have tighter constraints on the reddening of the sources, the Balmer line decrement was investigated. As the redshift range of our sources is large, different sets of Balmer lines were used in different spectra; moreover, for some spectra the observed frame do not include any of the Balmer lines. The most reliable measurement of the Balmer decrement is provided by the $\text{H}\alpha/\text{H}\beta$ ratio, as they are the strongest broad lines in the optical spectra. Unfortunately the $\text{H}\alpha$ line was detected in only two spectra (2XMM J090729 and 2XMM J151755), a type 1.9 AGN (hence with a broad $\text{H}\alpha$ line) and a NL AGN. For the other sources the $\text{H}\gamma/\text{H}\beta$ ratio was used. However, as the majority of our sources are NL AGN and the $\text{H}\gamma$ is a rather weak line, a reliable detection of the broad component of the $\text{H}\beta$ and $\text{H}\gamma$ lines was found only for a few sources. Therefore the analysis of the Balmer line ratios did not provide useful constraints on the reddening A_V for our sources.

3.6 The X-ray spectral properties

Having obtained the redshifts from the optical spectra for 20% of the sample (25 sources), the X-ray spectral analysis was performed focusing on this sub-sample of EXOs in order to compare their optical and X-ray properties and to have a clearer understanding of their SEDs.

The X-ray spectral analysis has been performed on those objects with > 100 counts (0.2 – 12 keV) in at least one of the three EPIC cameras (see Sect. 2.1.2), according to the values reported in the 2XMM catalogue (Watson et al. 2009). Amongst the 25 optically identified objects, 17 have sufficient counts to allow detailed spectral analysis, while the

remainder have too low signal to noise; consideration of their X-ray spectral properties will be made below, using their X-ray colours (HR; Figure 3.3).

We note that the sources whose redshift was obtained from the literature (eight objects; see Sect. 3.2) are not included in this X-ray spectral analysis. Nevertheless, they will be taken into account in the final consideration of the properties of the EXO sample.

3.6.1 Spectral extraction process

The spectral extraction was performed using the Pipeline Processing System (PPS) products, which are a collection of standard processed high-quality products generated by the Survey Science Centre (SSC; see Chapters 2), and the version 8.0.0 of the *Science Analysis Software* (SAS 8.0.0¹⁹).

The source spectra were extracted (for the three EPIC cameras separately) using a circular region whose radius was optimised with the SAS task `eregionanalyse` and defined not to exceed 40". The background spectra were extracted using a circular region with radius 3 times that used for the source extraction. The background regions were placed offset from the source and other nearby sources. Any possible contaminant sources were excluded from the background area using circular regions, with radii determined by their total counts and off-axis angles. In order to select and optimise the location of the background regions an automated code, which examines the detector images masking out all the possible sources, was used.

As the response of the two MOS cameras is very similar (see Sect. 2.1.2), the spectra obtained from MOS1 and MOS2 have been co-added in order to obtain a better signal-to-noise (S/N): the source and the background spectra were combined using the task `mathpha`²⁰, rescaling the final extraction area as the weighted mean of the two original areas, while the response matrices were combined using “weightings” based on the effective exposure time on the extraction region on each MOS camera ($w_1 = t_1/(t_1 + t_2)$ and $w_2 = t_2/(t_1 + t_2)$, where t_1 and t_2 are the exposure times in the MOS1 and MOS2 images, respectively).

¹⁹<http://xmm.esac.esa.int/sas/8.0.0/>

²⁰<http://heasarc.gsfc.nasa.gov/lheasoft/ftools/fhelp/mathpha.txt>.

3.6.2 Spectral fitting

The XSPEC software package, version v.11.3.2 (Arnaud 1996), was used in the spectral fitting process. The spectra were grouped in order to have a minimum of 20 net counts/bin and analysed in the energy range $E = 0.3 - 10$ keV; χ^2 statistics were adopted to evaluate the goodness of the fit.

Amongst the 17 objects considered in this analysis, five have total net counts (pn + MOS) in the 0.3-10 keV energy band below 180. In these cases, particular care was taken in fitting the spectra (see below).

To obtain the best-fit model for each source, we started the fitting process adopting two basic models: i) a simple power-law model (MOD0), including a photoelectric absorption component due to our Galaxy and ii) a power-law model with intrinsic absorption (MOD1) and Galactic absorption (Fig. 3.14):

$$F(E) = e^{-\sigma(E)N_{\text{H}}^{\text{Gal}}} AE(1+z)^{-\Gamma} \quad (\text{MOD0}) \quad (3.3)$$

$$F(E) = e^{-\sigma(E)N_{\text{H}}^{\text{Gal}}} [Ae^{-\sigma(E(1+z))N_{\text{H}}} E(1+z)^{-\Gamma}] \quad (\text{MOD1}) \quad (3.4)$$

The MOD0 model, was represented by the XSPEC components: `wabs×zpowerlw`, where the `wabs` component describes the photoelectric absorption using Wisconsin cross-section (Morrison & McCammon 1983) and is parameterised by the hydrogen column density $N_{\text{H}}^{\text{Gal}}$. Accordingly, in the MOD1 (`wabs×zwabs×zpowerlw`) the intrinsic absorption is parameterised by N_{H} . In the spectral fitting performed for our sources, the Galactic column density was fixed to $N_{\text{H}}^{\text{Gal}} = 3 \times 10^{20} \text{ cm}^{-2}$, which is an average value for the galactic latitudes²¹ of our sources (e.g. Dickey & Lockman 1990). The other parameters of the two models, respectively the photon index Γ (see Sect 1.1.2) in both the MOD0 and MOD1, and N_{H} in MOD1, were left free to vary. The F -test with a confidence level of 95% was used to evaluate the significance of any additional components used in the models.

²¹Our sources lie at $|b| > 20^\circ$, as the sample is constructed from the cross-matching with the SDSS-DR5 catalogue, whose coverage is focused at high Galactic latitudes (Sect.2.2.1). The actual Galactic column density ranges between $N_{\text{H}}^{\text{Gal}} = (1.0 - 7.2) \times 10^{20} \text{ cm}^{-2}$.

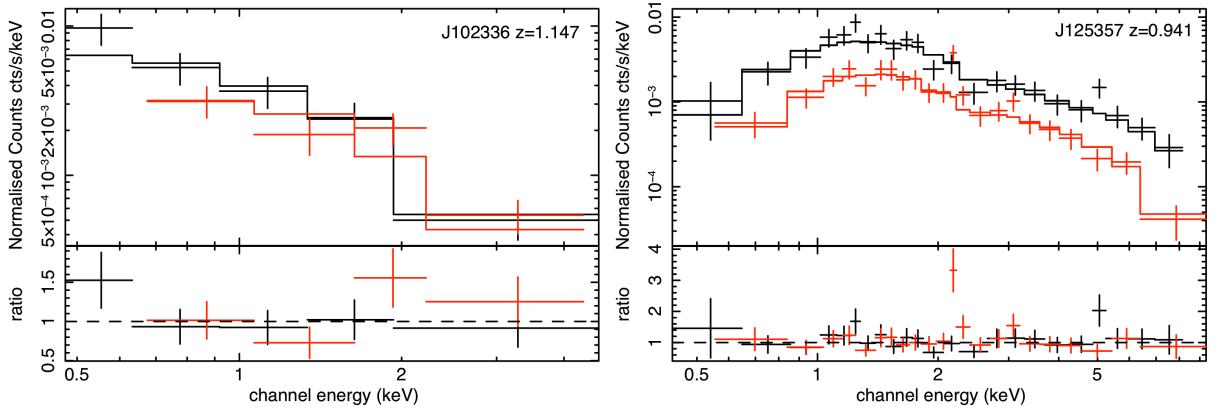


Figure 3.14: Examples of two X-ray spectra of our EXOs with different best-fit models: on the left the unabsorbed power-law (MOD0) and on the right the absorbed power-law (MOD1) with an hydrogen column density $N_{\text{H}} = 1.9 \times 10^{22} \text{ cm}^{-2}$. For both the spectra the pn (black) and the MOS (red) dataset are plotted; in the bottom panels the ratio between the data and the model is shown.

The results of the spectral fitting are summarised in Table 3.3. Six objects (35%) are well represented by the MOD0 model, indicating that these sources are unabsorbed in the X-ray band; for the remaining eleven sources (65%), adding an intrinsic absorption component significantly improved the spectrum, hence the MOD1 produced a better fit.

Leaving the spectral index Γ as a free parameter resulted, in some cases, in a very flat spectrum ($\Gamma \sim 1.0$), which is an improbable value considering the typical photon index expected for AGN ($\Gamma = 1.9$; e.g. Mainieri et al. 2002; Caccianiga et al. 2004; Mateos et al. 2005b). This was the case, in particular, for spectra that showed the signature of absorption, but due to the low S/N, the data did not properly constrain the spectral parameters. For these sources the spectral index was fixed at $\Gamma = 1.9$ (see Table 3.3). With a spectral index fixed at $\Gamma = 1.9$, these sources (three cases: 2XMM J004109, 2XMM J092201, 2XMM J204043) have significant absorption $N_{\text{H}} > 10^{22} \text{ cm}^{-2}$, thus they are best-fitted by the MOD1; however, for the source 2XMM J004109, which has a limited count statistics (total net counts = 81, 0.3–10 keV), the MOD1 model did not pass the F -test confidence threshold (95% confidence level), hence the MOD0 was assumed for this source (see Table 3.3).

We note that not all the sources where the MOD1 provided a better fit can be classified as absorbed objects: we chose $N_{\text{H}} = 4 \times 10^{21} \text{ cm}^{-2}$ as a threshold to separate the X-

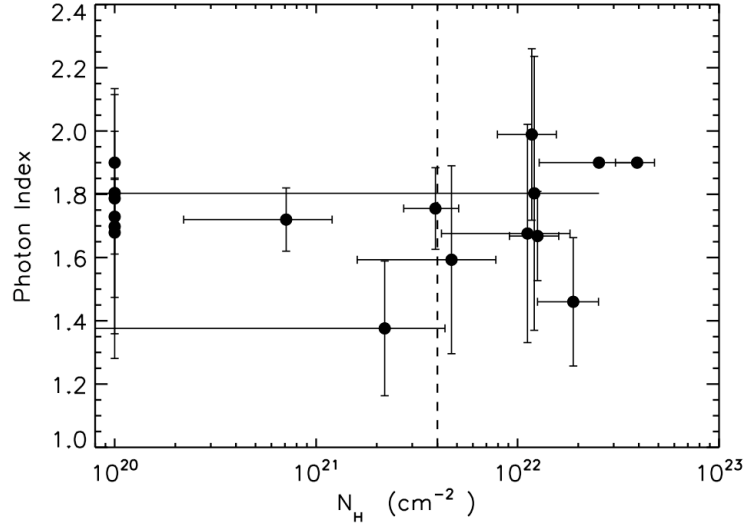


Figure 3.15: Hydrogen column density N_{H} vs the photon index Γ obtained from the spectral fitting performed on our sample sources. The source photon indices are distributed around $\Gamma \approx 1.8$, with the absorbed objects having a larger spread around this value than the unabsorbed objects. The vertical dashed line indicates the separation between absorbed and unabsorbed sources ($N_{\text{H}} = 4 \times 10^{21} \text{ cm}^{-2}$).

ray absorbed and unabsorbed AGN amongst our sample. This column density threshold is below the value usually adopted to classify the AGN as X-ray absorbed ($N_{\text{H}} = 10^{22} \text{ cm}^{-2}$), which is generally used more for historical reasons than for established physical ones. Assuming a standard Galactic dust-to-gas ratio $A_{\text{V}}/N_{\text{H}} = 1/(1.8 \times 10^{21})$ (e.g. Predehl & Schmitt 1995), $N_{\text{H}} = 4 \times 10^{21} \text{ cm}^{-2}$ corresponds to an optical reddening $A_{\text{V}} \approx 2$ mag. It has been observed that such an amount of obscuration in the optical spectra, is in general sufficient to extinguish the blue continuum and the broad emission lines typical of type-1 objects (see Sects. 1.1.3 and 3.5.4), i.e. they would be classified as optically type-2 AGN (e.g. Caccianiga et al. 2008); hence, in relation to the optical classification, our chosen N_{H} is a reasonable separation value to allow the X-ray classification.

The intrinsic hydrogen column densities estimated from the fit of our EXOs ranges between $N_{\text{H}} \approx 7 \times 10^{20} \text{ cm}^{-2}$ and $N_{\text{H}} = 4 \times 10^{22} \text{ cm}^{-2}$, and two of the sources best-fitted by the MOD1 model have $N_{\text{H}} < 4 \times 10^{21} \text{ cm}^{-2}$. Thus, amongst the seventeen EXOs analysed, a total of nine objects are absorbed (type-2 AGN) by column densities $N_{\text{H}} \geq 4 \times 10^{21} \text{ cm}^{-2}$ and eight are unabsorbed (type-1 AGN). In Figure 3.15 the spectral index and the intrinsic column density resulting from the fitting of the two basic models are shown. For

Table 3.3: Best-fit spectral parameters from models MOD0 and MOD1.

ID	z	pn cts	MOS cts	Model	Γ	N_{H} (10^{22} cm^{-2})	$\chi^2/d.o.f.$	f_{2-10}^a ($10^{-13} \text{ erg/cm}^2/\text{s}$)	$L_{0.5-2}^a$ (10^{44} erg/s)	L_{2-10}^a (10^{44} erg/s)	Type ^b
2XMM J004109	1.385	81	0	MOD0	1.9	< 0.01	12.7/3	0.96	0.004	10.61	2
2XMM J030228	1.515	0	287	MOD1	$1.80^{+0.43}_{-0.37}$	$1.21^{+1.33}_{-1.01}$	14.0/11	0.62	2.99	7.65	1
2XMM J092201	0.567	140	203	MOD1	1.9	$3.92^{+0.86}_{-0.71}$	18.8/14	1.90	0.83	2.68	2
2XMM J100058	0.622	320	243	MOD1	$1.38^{+0.21}_{-0.20}$	$0.22^{+0.22}_{-0.17}$	18.0/23	1.68	0.52	2.01	2
2XMM J102336	1.147	100	80	MOD0	$1.68^{+0.33}_{-0.30}$	< 0.01	7.3/6	0.55	1.27	4.05	1
2XMM J111121	0.847	983	774	MOD1	$1.76^{+0.13}_{-0.12}$	$0.39^{+0.12}_{-0.10}$	77.0/77	1.96	2.60	6.02	1
2XMM J121919	1.587	0	143	MOD0	$1.80^{+0.33}_{-0.30}$	< 0.01	5.0/5	0.99	5.34	13.80	1
2XMM J122437	0.827	100	0	MOD0	$1.70^{+0.42}_{-0.37}$	< 0.01	3.3/3	0.38	0.36	1.05	2
2XMM J125357	0.941	463	458	MOD1	$1.46^{+0.20}_{-0.19}$	$1.89^{+0.63}_{-0.53}$	40.0/41	0.93	0.82	2.98	2
2XMM J125906	1.840	1439	1056	MOD0	$1.79^{+0.06}_{-0.06}$	< 0.01	67.9/103	1.21	8.22	23.60	1
2XMM J135402	1.500	367	242	MOD0	$1.73^{+0.12}_{-0.11}$	< 0.01	31.5/27	0.85	4.47	10.75	1
2XMM J135527	0.506	1337	1070	MOD1	$1.72^{+0.10}_{-0.10}$	$0.07^{+0.05}_{-0.05}$	111.0/101	2.74	1.10	2.43	2
2XMM J143623	0.892	910	450	MOD1	$1.67^{+0.14}_{-0.13}$	$1.26^{+0.35}_{-0.29}$	63.0/62	2.44	3.88	8.57	2
2XMM J145030	0.760	202	185	MOD1	$1.68^{+0.35}_{-0.29}$	$1.12^{+0.70}_{-0.50}$	15.4/15	0.90	0.81	2.00	1
2XMM J151624	0.663	406	307	MOD1	$1.99^{+0.27}_{-0.24}$	$1.18^{+0.38}_{-0.31}$	30.1/31	0.91	1.16	1.75	2
2XMM J154930	0.633	222	207	MOD1	$1.59^{+0.30}_{-0.26}$	$0.47^{+0.31}_{-0.24}$	23.6/17	1.02	0.55	1.44	2
2XMM J204043	0.620	120	0	MOD1	1.9	$2.54^{+1.26}_{-0.82}$	3.6/4	1.62	1.37	2.54	2

Notes: a) Fluxes and luminosities are unabsorbed and they are calculated from the best-fit model for each source; b) Optical classification.

the sources modelled with the MOD0 model, the intrinsic N_{H} was fixed to an upperlimit value of $N_{\text{H}} = 10^{20} \text{ cm}^{-2}$ for plotting purposes. The spectral indices Γ are distributed around the value $\Gamma \approx 1.8$, in agreement with the typical values expected for AGN (e.g. Mainieri et al. 2002; Caccianiga et al. 2004; Mateos et al. 2005b), although some of the absorbed sources show flatter spectral slopes: this effect may be due to the presence of an absorption component, which in limited statistics spectra tends to be underestimated, causing a flattening of the spectral index.

3.6.3 More complex models

Although the two basic models provided rather good spectral fits for the majority of the sources, in some cases the results obtained and the residuals of the fit suggested that additional components may be required to properly model the spectra. Where significant residuals were present in the spectra, more complex models were tested, using again the F -test and a confidence level of 95% to evaluate the significance of the new model adopted. This hypothesis of a more complex spectrum was tested also for those sources showing a flat power-law spectrum ($\Gamma < 1.6$); as in fact, a flat spectral index may result from the presence of a scattered component in the soft band ($E \lesssim 2 \text{ keV}$; rest-frame) and/or a reflection component (at energies $E > 10 \text{ keV}$, rest-frame) in low S/N spectra, where the model parameters cannot be constrained. Indeed, fixing the spectral index to $\Gamma = 1.9$, in these cases (three sources: 2XMM J092201, 2XMM J100058, 2XMM J125357) revealed an excess of counts in the soft and/or in the hard band.

In the spectra of three sources (2XMM J125906, 2XMM J135527, 2XMM J143623) a **soft excess** at energies $E < 2 \text{ keV}$ was clearly noted (see Chapter 1). In order to model this excess at low energies, two components were tested (each of them added to the basic model MOD1): i) a second unabsorbed power-law (MOD1+pl: $\text{wabs} \times (\text{zpowerlw} + \text{zwabs} \times \text{zpowerlw})$), with the same spectral index of the primary power-law ($\Gamma_1 = \Gamma_2$), in order to parameterise the data if the soft emission is due to the Thomson scattering of the nuclear radiation by the circumnuclear material; ii) a

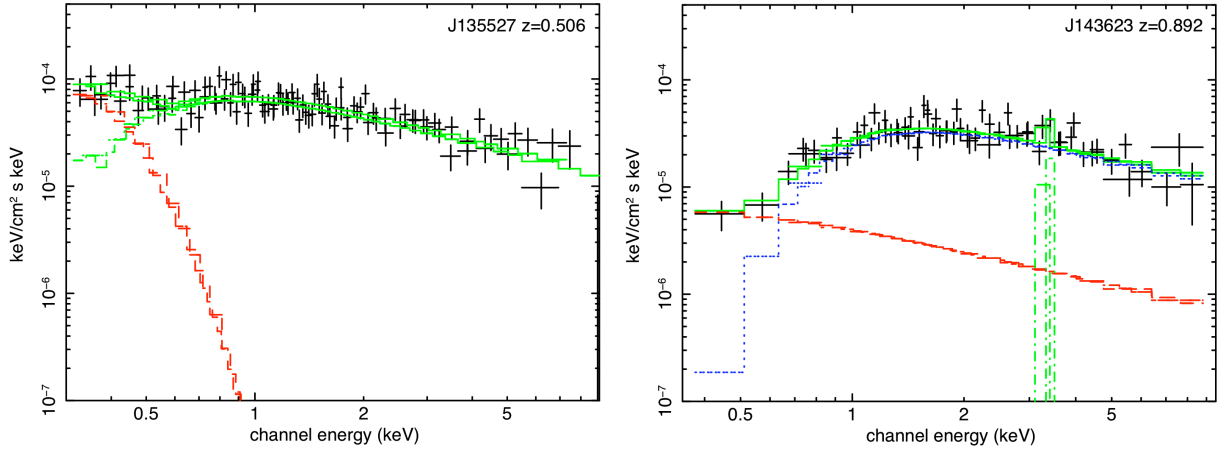


Figure 3.16: X-ray spectra of two of our sample sources requiring extra components in addition to the basic models: on the left a black-body component, added to model MOD1; on the right a power-law (added to MOD1), with the same spectral index of the primary power-law. In the second spectrum a narrow Gaussian component ($\sigma = 10$ eV) to fit the Fe $K\alpha$ emission line at $E = 6.4$ keV (rest-frame) was also added.

black-body component (MOD1+bb: $wabs \times (zbody + zwabs \times zpowerlw)$); see Sect 1.1.2).

These two models significantly improved the fit of the source spectra: the sources 2XMM J125906, 2XMM J135527 were better modelled by the black-body component (MOD1+bb), while for 2XMM J143623 the MOD1+pl model provided a better-fit (Figure 3.16). The black-body temperatures obtained for the sources 2XMM J125906, 2XMM J135527 are too high to be produced by thermal emission from the accretion disc (e.g. Mateos et al. 2005b), therefore the soft excess must have a different origin (e.g. atomic processes in partially ionised material, disc reflection; see Sect 1.1.2). On the other hand, as the source 2XMM J143623 is absorbed by high column density, the soft emission is most probably due to scattering: the scattered emission in 2XMM J143623 was estimated to be $\sim 7\%$ of the primary continuum. The parameters resulting from the spectral fitting of the two soft excess components are summarised in Table 3.4.

For the three sources with flat spectral index, the two soft excess models seemed to improve the spectral fit, however the confidence level was below the 95% threshold; hence, in these cases the new models were rejected.

The spectra of the EXOs 2XMM J030228 and 2XMM J111121 showed an excess of

Table 3.4: Soft Excess spectral parameters

ID	z	Model	Γ	N_{H} (10^{22} cm^{-2})	kT (eV)	$\chi^2/d.o.f$	Type ^a
2XMM J125906	1.840	MOD0+bb	$1.83^{+0.17}_{-0.13}$	< 0.01	$133.0^{+134.0}_{-79.9}$	64.8/100	1
2XMM J135527	0.506	MOD1+bb	$1.85^{+0.19}_{-0.13}$	$0.23^{+0.53}_{-0.11}$	$84.4^{+9.6}_{-9.5}$	102.3/99	2
2XMM J143623	0.892	MOD1+pl	$1.78^{+0.17}_{-0.16}$	$1.83^{+0.58}_{-0.52}$	–	54.6/ 60	2

Notes: a) Optical classification.

counts in the hard energy band, compared to the adopted basic model (MOD1 for both the objects). As these are high redshift objects ($z = 0.847$ and $z = 1.515$, respectively) the observed rise of the spectrum at energies $E \gtrsim 5$ keV (observed-frame) may be related to a **reflection component**. This possibility was tested adding to the simple absorbed power-law model (MOD1) a reflected power-law component with exponential high energy cut-off (pexrav; Magdziarz & Zdziarski 1995) fixed at $E_c = 100$ keV.

The χ^2 resulting from the spectral fit using this new model improved slightly compared to the previous model used (MOD1), but for both the sources the improvement was not significant (according to the F -test statistics). It is clear that with the current count statistics of our data it is not possible to constrain the reflection parameters, hence this component was rejected for both the sources.

The presence of the **Fe K α emission line** in the X-ray spectra of our EXOs was also investigated. For this purpose, a Gaussian component was added to the basic models (MOD0 or MOD1) with energy fixed at $E = 6.4$ keV (rest-frame) and line width²² fixed at $\sigma = 10$ eV to represent the narrow component of the Fe K α line (typical values measured for the narrow iron line from high-resolution spectroscopy are $\sigma = 30 - 50$ eV; e.g. Yaqoob & Padmanabhan 2004). The emission line was significantly detected in two of our source spectra (2XMM J111121 and 2XMM J143623; see Figures 3.16, right, and 3.17) with equivalent widths $\text{EW} = 274.0^{+155.0}_{-154.0}$ eV and $\text{EW} = 138.0^{+116.0}_{-115.6}$ eV, respectively; for the remaining sources an upperlimit of the EW was estimated. The strength of the line we detected in our spectra (and the upperlimit estimated) is consistent with the equivalent

²²We note that narrow lines with $\sigma < 90$ eV are unresolved in the *XMM-Newton* EPIC data (see Sect. 2.1.2).

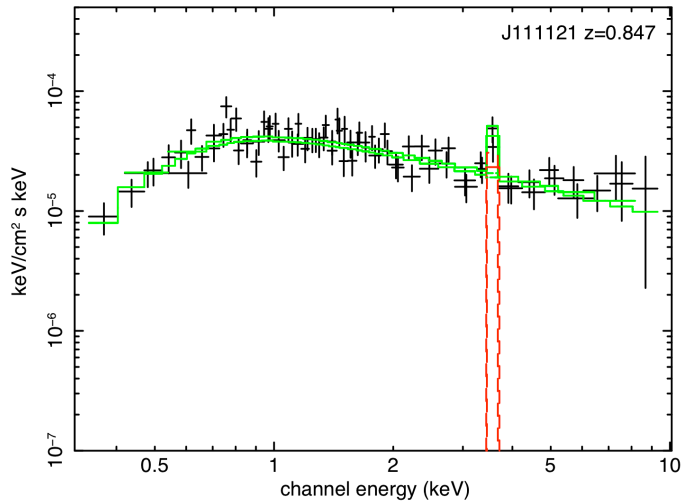


Figure 3.17: Spectrum of one of our EXOs where a narrow Fe $K\alpha$ emission line was detected; the source best-fit model is given by an absorbed power-law plus a Gaussian component with $\sigma = 10$ eV, fixed at $E = 6.4$ keV (rest-frame).

width expected from a uniform shell of Compton-thin material surrounding the nucleus (e.g. Turner et al. 1998).

3.6.4 Spectral constraints from the Hardness Ratios

As noted above, amongst the optically identified sources (25 objects), only seventeen had enough counts (in the 0.2-12 keV energy band) to allow a detailed spectral analysis, while for the remainder (eight objects) the signal-to-noise was too low to perform useful spectral extraction. For these sources we were able to place constraints on the intrinsic absorption from their X-ray colours HR2 and HR3 (Fig. 3.18). We assumed that these sources could be represented by a simple absorbed power-law model with $\Gamma = 1.9$; this assumption seems reasonable considering that this model provided the best-fit for the majority of the X-ray spectra analysed in the previous section (MOD1). We then compared²³ the HR of our sources with the values expected at the source redshift from the HR evolution tracks shown in Figure 3.3 (see Sect. 3.2.1 and Watson et al. 2009).

The column density estimated from the comparison are reported in Table 3.5; the location of these sources in the colour-colour plot is typical for absorbed objects, with

²³We note that this is a rough estimation, as spectral simulations are necessary to obtain a proper estimation of the N_{H} from the HR colours.

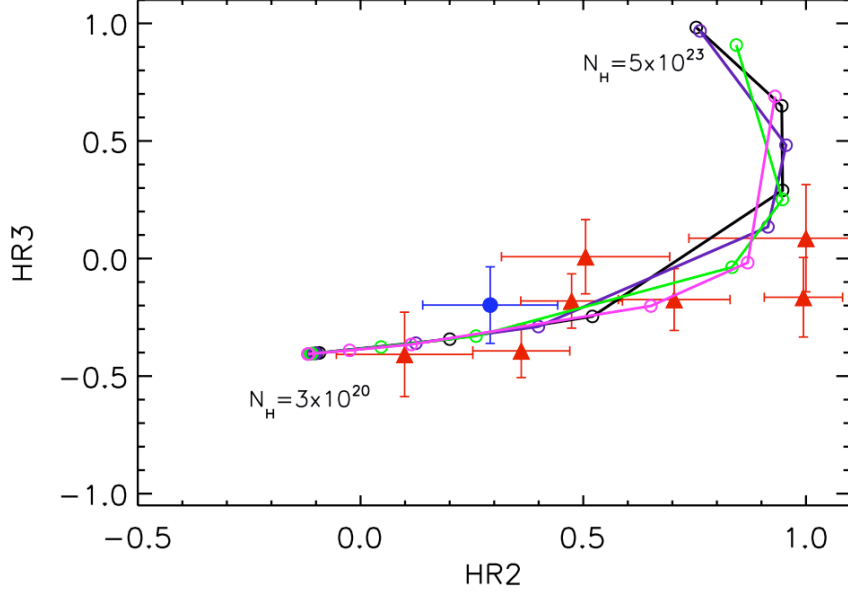


Figure 3.18: Hardness ratios HR2 vs HR3 for sources with low net counts in the 0.2 – 12 keV energy band (< 100 , in each of the three EPIC cameras); the sources are divided into type-1 AGN (blue circles) and type-2 AGN (red triangles) according to the optical spectroscopic classification. The tracks represent the variation of the X-ray colours with increasing N_{H} at a given redshift: $z = 0.5$ (black), $z = 0.7$ (purple), $z = 1$ (green), $z = 1.5$ (magenta). The open circles indicate the different column density values (in the range $N_{\text{H}} = 3 \times 10^{20} - 5 \times 10^{23} \text{ cm}^{-2}$).

column densities in the range $N_{\text{H}} = 4 \times 10^{21} - 5 \times 10^{22} \text{ cm}^{-2}$. Moreover, we note that the majority of these low-counts sources (six out of eight) are classified as NL AGN in the optical, hence they are likely to be absorbed in the X-ray band.

Table 3.5: X-ray properties of the optically identified sources with low X-ray counts.

ID	$f_{\text{X}}/f_{\text{opt}}$	z	Type ^a	$f_{2-10 \text{ keV}}^b$ ($10^{-13} \text{ erg/cm}^2/\text{s}$)	$L_{2-10 \text{ keV}}^c$ (10^{44} erg/s)	HR2	HR3	N_{H}^d (10^{22} cm^{-2})
2XMM J015603	1.59	1.115	2	0.91	6.48	0.10 ± 0.15	-0.41 ± 0.18	0.4-1.0
2XMM J035453	1.50	0.914	1	1.02	4.43	0.29 ± 0.15	-0.20 ± 0.16	1.0-5.0
2XMM J090729	1.53	0.387	2	6.51	3.46	0.99 ± 0.09	-0.16 ± 0.17	0.4-1.0
2XMM J101317	1.60	1.174	2	3.45	27.93	0.47 ± 0.11	-0.18 ± 0.12	1.0-5.0
2XMM J151755	1.66	0.538	2	1.01	1.18	0.51 ± 0.19	0.01 ± 0.16	1.0-5.0
2XMM J230503	1.55	0.654	2	1.01	1.90	1.00 ± 0.26	0.09 ± 0.23	1.0-5.0
2XMM J231731	1.74	0.813	2	1.91	6.17	0.36 ± 0.11	-0.39 ± 0.11	0.4-1.0
2XMM J233819	1.66	0.770	2	0.82	2.32	0.70 ± 0.13	-0.17 ± 0.13	1.0-5.0

Notes: a) Optical classification; b) Flux reported in the 2XMMp catalogue (not corrected for absorption) shifted to the rest-frame assuming a simple power-law with $\Gamma = 1.9$; c) Rest-frame luminosity (not corrected for absorption), calculated from the catalogue flux values; d) Column density range estimated from the HR.

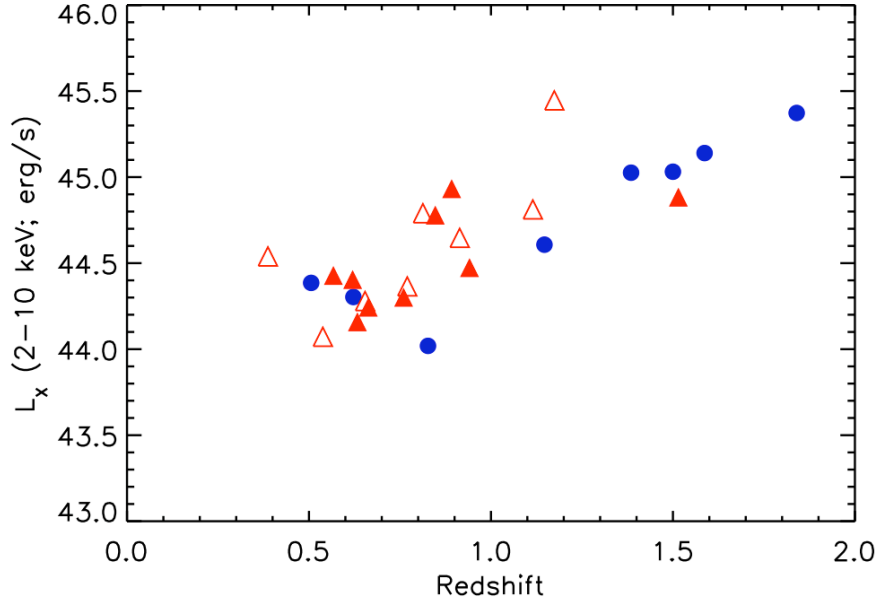


Figure 3.19: X-ray luminosity in the 2 – 10 keV energy band (corrected for absorption) as a function of redshift for the optically identified sources. The unabsorbed objects are represented by blue circles and the absorbed objects are represented by red triangles. The low-count sources are represented with open symbols: for them the luminosity (2 – 10 keV) has not been corrected for absorption.

3.6.5 X-ray analysis results

Considering the results obtained from the X-ray spectral analysis and the HR colours for all the optically identified sources (25 of our EXOs) we found that 68% of them are absorbed in the X-ray by column densities $N_{\text{H}} \geq 4 \times 10^{21} \text{ cm}^{-2}$, while the remainder are unabsorbed. Moreover, we note that amongst the apparently unabsorbed objects, there are many of the sources with the lowest S/N spectra, hence in some cases an absorption component may be present, but it cannot be significantly constrained with the current data (as in the case of the source 2XMM J004109, see above).

In Figure 3.19 the unabsorbed X-ray luminosity²⁴ in the 2 – 10 keV energy band for our sources is shown. The unabsorbed objects are distributed up to higher redshifts ($z \sim 1.8$) compared to the absorbed objects, while the absorbed objects are sampled up to $z \sim 1.5$. This result is probably due to the biases affecting the flux limited samples toward the unabsorbed objects, which are detectable up to larger volumes compared to the

²⁴For the low-count sources the luminosity was not corrected for absorption, as the N_{H} in these cases was not derived from a proper modelling of the spectra; the corrections due to photoelectric absorption on the hard band luminosity however, are expected to be small ($\leq 10 - 20\%$; e.g. Fiore et al. 2003).

absorbed objects, since the latter have luminosities depressed by photoelectric absorption (e.g. Della Ceca et al. 2008). We note, however, that all our sources have high X-ray luminosities, typical of the quasar regime ($L_{2-10 \text{ keV}} > 10^{44} \text{ erg s}^{-1}$). In particular, taking into account the X-ray classification only, amongst the 25 EXOs analysed here, 68% are absorbed QSOs (48% considering only the objects with $N_{\text{H}} > 10^{22} \text{ cm}^{-2}$; see Chapter 1). These fractions are consistent with those found for X-ray absorbed AGN in previous studies on relatively bright X-ray selected EXOs (Perola et al. 2004; Comastri & Fiore 2004). Nevertheless, to classify these objects as real type-2 QSOs, the optical properties also need to be taken into account (see below).

3.7 Discussion

3.7.1 Comparison between optical and X-ray properties

The Unification models for AGN (Antonucci 1993, see Chapter 1) predict that the X-ray absorption and the optical obscuration in AGN are coupled. This relation is seen overall in AGN, where low N_{H} values are usually found for type-1 objects and higher absorption is observed in type-2 AGN. Nevertheless, a number of exceptions to this behaviour are known, such as type-2 AGN with no evidence of absorption in the X-rays (e.g. Bassani et al. 1999; Page et al. 2001; Panessa & Bassani 2002; Mateos et al. 2005b, see also Chapter 5), or vice versa type-1 AGN with high X-ray column densities (e.g. Perola et al. 2004; Tozzi et al. 2006). The fraction of AGN not following the unification scheme predictions is rather uncertain, but values estimated from previous studies based on medium and deep X-ray surveys are $\sim 10 - 30\%$ (Panessa & Bassani 2002; Perola et al. 2004; Tozzi et al. 2006).

In order to verify whether our EXO population is different from the AGN population (with no particular cut in $f_{\text{X}}/f_{\text{opt}}$) found in these medium and deep surveys, we compared the properties resulting from the optical spectroscopy and X-ray spectral analyses. Amongst our EXO sample, the redshift distribution obtained for optically obscured and unobscured objects is rather similar to those resulting for X-ray absorbed and unabsorbed

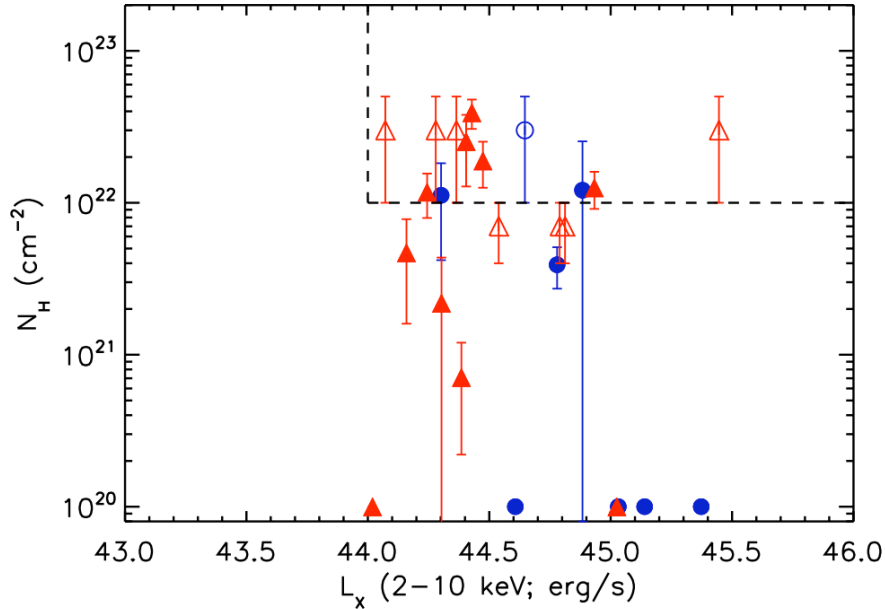


Figure 3.20: Hydrogen column density N_{H} as a function of the X-ray unabsorbed luminosity in the 2 – 10 keV for the type-1 AGN (blue) and the type-2 AGN (red). The open symbols represent the objects for which the N_{H} was estimated from the HR, for which the plotted luminosity is not corrected for absorption. The region of the plot occupied by type-2 QSO is also marked (top right corner).

sources, suggesting that in general our sources can be interpreted in the context of the simple AGN unification scheme.

The N_{H} distribution as a function of the intrinsic X-ray luminosity (2 – 10 keV) for the type-1 and type-2 objects is shown in Figure 3.20. The sources with N_{H} estimated from the HR are also reported, although the luminosity plotted in these cases is not corrected for the absorption. As already stated in the previous section, all our optically identified sources have X-ray luminosity typical of QSOs; from the comparison between the optical and X-ray properties we were able to classify $44 \pm 8\%$ of these sources as real type-2 QSOs²⁵. This fraction is below the values found in some of the previous studies on EXOs (Fiore et al. 2003; Mignoli et al. 2004), however it must not be considered representative of the whole EXO sample. Indeed, some biases were introduced in selecting the optical spectroscopy sub-sample: these sources are part of the brighter end of the r' magnitude distribution (besides the objects identified from the literature, which are the brightest ones). This means that the remaining unidentified objects, which are the optically faintest

²⁵Including the source 2XMM J123204 (analysed in Chapter 4) the fraction of type-2 QSOs becomes $46 \pm 8\%$, amongst 26 sources.

sources, are likely to hide the bulk of the highly-obscured (type-2) QSO population.

Amongst the EXOs with optical and X-ray classifications (25 objects), we also found 8 sources with “mis-matching” classification (32%): four type-1 objects have X-ray column densities $N_{\text{H}} > 4 \times 10^{22} \text{ cm}^{-2}$ and four type-2 objects have low X-ray absorption. We note that amongst the unabsorbed type-2 AGN two sources (2XMM J004109 and 2XMM J100058) have some indication of high photoelectric absorption in the X-ray spectra, but this cannot be parameterised due to limited statistics; for the other two sources (2XMM J122437 and 2XMM J135527) the low signal-to-noise cannot explain the absence of absorption in the X-ray spectrum. A possible explanation for the properties observed in these sources is the spectral variability: as the X-ray and optical data are not simultaneous, a variation in the X-ray column density may have occurred (e.g. Elvis et al. 2004; Risaliti 2009). Other interpretations have been given by several authors to explain the observed mis-match between optical and X-ray classification, e.g.: i) the absence of broad line regions: in this case the presence of obscuration is not required to explain the observed properties of these objects (“naked Seyfert 2” galaxies; Panessa & Bassani 2002); ii) the presence of dust not associated with the absorbing torus, but residing at larger distance from the nucleus, such as the NLR (Sturm et al. 2005; Polletta et al. 2008) or in the host galaxy (e.g. Rigby et al. 2006; Martínez-Sansigre et al. 2006; Brand et al. 2007), affecting more the optical emission than the X-rays (see also Sects.1.2.1 and 4.3); iii) a different dust-to-gas ratio compared to Galactic values (see Sect. 3.3.2) or a different line of sight for the X-ray and the optical emissions (e.g. Maiolino et al. 2001b); iv) the presence of hot mostly dust-free material (above the dust sublimation temperature) that absorbs the X-ray emission (Risaliti et al. 2001).

We note that one of the absorbed type-1 QSOs found in our sample (2XMM J111121), shows extremely red optical/NIR colours ($r - K > 5$ and $J - K \sim 2$; Fig. 3.9), which are the characteristics typical of *red* QSOs (Cutri et al. 2002; Piconcelli et al. 2010). This class of objects is mainly composed of BL AGN with a reddened continuum ($A_V \sim 1 - 5 \text{ mag}$) and absorbed X-ray spectra (with $N_{\text{H}} \leq \text{few} \times 10^{22} \text{ cm}^{-2}$; Kuraszkiewicz et al. 2009).

Although this class of sources are not yet well explored, the studies to date suggest that *red* QSOs are objects viewed at intermediate inclination angles (e.g. through the edge or the atmosphere of the torus, or through a clumpy disc wind), hence the observed emission is likely to be a combination of direct, reprocessed and scattered light (Wilkes et al. 2008); in these sources the obscuration and emission from the circumnuclear gas as well as from the host galaxy play an important role. The majority of *red* QSOs seem to be hosted in galaxies with “disturbed” morphology, i.e. interacting or merging galaxies (Urrutia et al. 2008), thus these objects, at high redshift, are believed to represent a particular phase of the BH-galaxy evolution, where the nucleus is still embedded in gas and dust (provided by the merging galaxies) and will become more and more visible as the AGN feedback expels the obscuring material (leading to the “quasar phase”; see Sect. 1.3).

Although not all the type-1 QSOs found in our EXO sample (8 sources) show the typical red optical/NIR colours²⁶ of *red* QSOs (see Fig. 3.9), their optical continuum tends to be redder than typical type-1 QSOs selected in the optical bands (e.g. Risaliti & Elvis 2004). The fact that half of them show also absorption in the X-ray band suggests, in fact, that these objects are observed through some amount of obscuring material (either circumnuclear or at large distance from the nucleus), but not enough to suppress the broad emission lines in the optical spectra. These sources with “intermediate” properties are not unexpected, even according to the simple unification scheme of AGN (Antonucci 1993): if the inclination angle is the differentiating element between type-1 and type-2 AGN (viewed face-on and edge-on, respectively), at intermediate angles a large variety of properties in between these two classes should be, and are indeed, observed. Therefore, labeling these sources simply as type-1 or type-2 AGN is limiting, as a distribution of sources with “intermediate” properties should be present amongst the AGN population.

3.7.2 Confrontation of our expectation

Taking into account the working hypothesis on the origin of the extreme f_X/f_{opt} values in AGN, i.e. that the high f_X/f_{opt} in AGN is an effect of the obscuration affecting more the

²⁶UKIRT NIR data are available for six of the eight type-1 QSOs in our sample.

UV/optical/NIR bands than the X-ray band and that this effect is enhanced i) by the high luminosity, which reduces the dilution from the host galaxy and ii) by the high redshift, as the ratio between the optical and X-ray optical depth increases with increasing redshifts (e.g. Fiore et al. 2003), we want to critically discuss the results obtained from our analysis. According to the arguments presented in Chapters 1 and 2 (see Sections 1.4 and 2.4), the majority of EXOs are expected to be highly obscured, high redshift objects ($z > 1$). *Is that what we found?*

- **Obscuration:** In total, considering strictly the optical classification only, the fraction of type-2 objects found in our sub-sample of optically identified EXOs is 69% (amongst 26 sources²⁷); this fraction is already considerably higher than those found in population studies of X-ray selected AGN at similar fluxes (without any selection in f_X/f_{opt}) which normally find only $\sim 30\%$ of type-2 AGN (e.g. Fiore et al. 2003; Caccianiga et al. 2004). Considering that all our type-2 sources have luminosities typical of QSOs, the excess of such objects in our sample compared to X-ray selected AGN samples is even higher. On the other hand, deep X-ray surveys are more effective in finding type-2 objects (e.g. Mainieri et al. 2002; Tozzi et al. 2006) as they sample the X-ray sky down to fainter fluxes; however, these surveys are dominated by lower luminosity objects and include only few sources with the high luminosity typical of QSOs, hence the number of such objects in deep surveys is low (this is even more true considering that usually deep surveys have also small sky coverage).

Taking into account the X-ray band, similar conclusions can be drawn. Several studies performed on X-ray selected samples of AGN at different flux limits seem to find that the fraction of absorbed AGN decreases at high luminosity²⁸ (e.g. Ueda et al. 2003; Steffen et al. 2003; Hasinger 2004, 2008). The fraction of absorbed objects (F) predicted by Della Ceca et al. (2008), for high X-ray luminosities

²⁷Here we considered all the spectroscopically identified sources: 25 identified from optical spectroscopy at the Subaru, ESO-VLT and GTC telescopes plus the source identified through NIR spectroscopy (2XMM J123204, analysed in Chapter 4). These include: 25 sources for which the X-ray spectral analysis has been performed in this Chapter, plus the source 2XMM J123204 (see Chapter 4).

²⁸It is still unclear whether this correlation is real or is due to observational effects (e.g. Dwelly & Page 2006; Treister & Urry 2006; Tozzi et al. 2006).

($L_X > 10^{44}$ erg s $^{-1}$) is expected to be $F = 0.38 \pm 0.1$. Although a direct comparison of our results with this prediction is not possible, as our (sub-) sample is not complete and is affected by selection biases (see Sect. 3.7.1), it is worth noting that the fraction of absorbed QSO ($L_X > 10^{44}$ erg s $^{-1}$) amongst our sample is much higher ($F = 0.68$). These considerations can be extended to the whole EXO sample, for which a large fraction ($> 51\%$) of absorbed sources was estimated using the X-ray colours (Sect. 3.2.1). These results are a valuable confirmation that the high X-ray flux, high f_X/f_{opt} selection used to build up our EXO sample (Sect. 2.4), constitutes a powerful tool for the type-2 QSO quest.

Nevertheless, we note that the fraction of confirmed type-2 QSOs (fulfilling the optical and X-ray classification criteria) found in our sub-sample of optically identified EXOs ($46 \pm 8\%$, amongst 26 sources) is below those found in previous studies of high f_X/f_{opt} , selected at similar X-ray fluxes ($\sim 60\%$, e.g. Fiore et al. 2003; Mignoli et al. 2004; Comastri & Fiore 2004). We stress that the sub-sample of spectroscopically identified sources amongst our sample is biased toward bright optical sources, thus it may include a larger number of unobscured sources (constraining the fraction of type-2 QSO identified so far to lower values). From the estimates obtained from the X-ray and optical/NIR colours, we are confident that more than a half of our sample objects are obscured, hence confirming broadly our prediction on the nature of the high f_X/f_{opt} sources.

- **Redshift distribution:** By selecting high f_X/f_{opt} sources our expectation was that we would find a large population of high- z ($z > 1$) obscured objects (Fiore et al. 2003; Comastri & Fiore 2004). The redshift distribution obtained so far for such sources amongst our sample, however, peaks at $z \sim 0.7$; this is the value typically found for low luminosity X-ray selected AGN in deep surveys (e.g. Cowie et al. 2003; Hasinger 2003, 2008; see Sect. 3.5.4). Comparing the redshift of the type-2 QSO identified in our EXO sample to those found by Fiore et al. (2003); Mignoli et al. (2004) for their high f_X/f_{opt} objects ($z \approx 0.7 - 2$), our sources are typically at lower redshift; although we found some objects at $z > 1$, up to $z = 1.9$ (see Chap-

ter 4), their number is far below the expectations. We point out however, that the redshift distribution obtained so far is in fact affected by the biases introduced by selecting the optical spectroscopic sub-sample (Sect. 3.7.1): selecting this sub-sample to include objects with bright optical magnitudes amongst our sample constrained the redshift of the obscured objects to lower values. Indeed, if the nucleus is obscured, the detected magnitude is in fact a measure of the host galaxy emission, limiting us to lower redshift than for unobscured AGN. Hence, the unidentified objects in our sample, which are the faintest optical sources, are likely to constitute the bulk of the high- z type-2 QSO population.

Some other conclusions can be made from the population of objects identified amongst our EXO sample, in particular on the type-1 QSO included in our high f_X/f_{opt} selection criteria. While the presence of obscured (type-2) objects in our sample is straightforward, according to our hypothesis on the origin of the high f_X/f_{opt} values, the population of type-1 QSO found amongst our sources raises some questions: *Why are they included in our sample? What produces the high f_X/f_{opt} ratios in these sources?*

Indeed, if the obscuration is the major factor responsible for the high f_X/f_{opt} ratios observed in EXOs, it seems surprising that a relatively large fraction of type-1 QSO are found in our sample (31% of the optically identified sources). A number of type-1 AGN are also found in previous studies on EXOs (Fiore et al. 2003; Mignoli et al. 2004), however their nature is not discussed anywhere. A possible explanation for the type-1 QSOs in our sample is purely statistical: although the f_X/f_{opt} for type-1 objects are typically distributed between the values $f_X/f_{\text{opt}} = 0.1 - 10$, the tail of the distribution reaches higher values. Selecting our EXO sample in the full X-ray energy band (0.2 – 12 keV, while the typical f_X/f_{opt} selection is usually made in the 2 – 10 keV energy band) may have included the tail of the distribution, leading to a relatively large fraction of type-1 objects in our selected sample. Another possibility relates to the properties of the objects themselves (and observational effects): as discussed earlier (Sect. 3.7.1), the optical spectra of our identified type-1 AGN show a rather red continuum, indicating the spectra are reddened, at some level; some of them also show a signature of absorption in the X-ray band. Al-

though the objects are not highly obscured, they all lie at high redshift ($z \gtrsim 0.9$), meaning that the amount of reddening they have, may be enough to reduce the optical flux in the observed frame to produce the high f_X/f_{opt} values.

3.8 Summary and conclusions

In this chapter we presented the multi-wavelength analysis of a sample of 129 bright X-ray selected high f_X/f_{opt} sources ($f_X/f_{\text{opt}} > 30$ and $f_X \geq 10^{-13}$ erg cm $^{-2}$ s $^{-1}$; 0.2 – 12 keV) drawn from the cross-match between the *XMM-Newton* 2XMMp serendipitous X-ray source catalogue (Watson et al. 2009), and the SDSS-DR5 photometric catalogue. This sample constitutes the largest X-ray selected EXO sample compiled to date. The main results obtained from this analysis can be summarised as follows:

1. We obtained identifications for 17 of our sample sources from the literature: ten are AGN (3 type-1 AGN, 2 type-2 AGN and 5 BL Lacs) and seven are non-AGN sources (including X-ray binaries, isolated neutron stars and ULXs); these 17 objects have the brightest X-ray and optical fluxes in our sample.
2. We investigated the X-ray spectral properties of our EXO sample using the hardness ratios (HR). The sources have X-ray colours distributed from normal (HR2 \sim 0) to hard (HR2 \sim 1 and HR3 $>$ 0.5) and we placed constraints on the fraction of absorbed objects ($N_{\text{H}} > 4 \times 10^{21}$ cm $^{-2}$) to be more than 50% by comparing the HR with simulated colours. The X-ray colours of the identified non-AGN sources lie at the softer end of the colour distribution, suggesting that they should be only a small fraction (few percent) of the whole sample.
3. A simple SED model was produced in order to investigate the expected properties for an obscured QSO in the X-ray/optical/NIR bands at different redshifts ($z = 0 - 2.5$); we found that the expected optical colours are consistent with those of our sample objects; moreover, a strong correlation between f_X/f_{opt} and redshift was found, indicating that the highest f_X/f_{opt} ratios are expected to be produced by the most obscured and high redshift QSOs.

4. The analysis of the optical/NIR colours ($r - K$) was performed for 31% of the sample (40 sources) for which UKIRT NIR follow-up imaging data and UKIDSS archival data were obtained; we found that the colours of our sources are typically red, as expected for obscured objects, reaching the extreme values typical of EROs ($r - K > 5$) in at least five cases.
5. We have identified 26 EXOs in our sample (20%) through optical spectroscopy obtained at Subaru and ESO-VLT telescopes and classified them as type-1 AGN (8 sources) and type-2 AGN (18 sources), thanks to a detailed spectroscopic analysis and line ratio diagnostics; we also found indication of reddening in the type-1 AGN spectra, with one of them having the properties of a *red* QSO. Our sources are distributed in the range $z = 0.39 - 1.84$ with the type-1 AGN peaking at higher redshift ($z \sim 1.5$) compared to the type-2 AGN ($z \sim 0.7$).
6. Detailed X-ray spectral analysis was performed on the optically identified sub-sample and for the sources with a low number of counts, constraints on the spectral properties were inferred from the X-ray colours. We found a large fraction of absorbed sources (68%, with $N_{\text{H}} > 4 \times 10^{21} \text{ cm}^{-2}$), larger than those found in typical X-ray selected AGN samples.
7. All the sources for which the spectroscopic identification was obtained have very high X-ray luminosity typical of QSOs ($L_{\text{X}} \geq 10^{44} \text{ erg s}^{-1}$); in particular we found that $46 \pm 8\%$ of them are in fact type-2 QSOs (12 ± 2 sources). Noting that the sub-sample of spectroscopically identified sources at present is biased towards the brightest optical magnitudes, it is likely that the fraction of type-2 QSOs found to date in our sample is just a lower limit.
8. The redshift distribution found for the type-2 QSO in our sample peaks at lower redshift compared to our expectations; this could be explained considering that the faintest objects in our sample, which are not yet identified, are likely to hide the bulk of the obscured, high redshift population we expected to find in our EXO sample.

9. Finally, taking into account all the results obtained from our multi-wavelength analysis we conclude that our selection criteria are indeed very effective in finding the elusive population of type-2 QSO.

CHAPTER 4

An Extreme EXO: A Type 2 QSO at $z = 1.87$

This chapter reports the discovery of 2XMM J123204, the source with the most extreme X-ray-to-optical flux ratio ($f_X/f_{\text{opt}} > 3300$) recorded to date outside the Galaxy, found amongst our sample of bright X-ray selected EXOs drawn from a cross-correlation of the 2XMMp catalogue with the SDSS-DR5 catalogue. We used 2XMMp X-ray data, SDSS-DR5, NOT and UKIRT optical/near-IR photometric data and Subaru MOIRCS IR spectroscopy to study the properties of this source. We also adopted a simple SED model including an obscured QSO and a host galaxy component in order to constrain the optical/near-IR extinction and the AGN/galaxy relative contributions to the total emission.

This Chapter is largely based on my published paper:

Del Moro, A., Watson, M. G., Mateos, S., et al. 2009, A&A, 493, 445.

4.1 Introduction

As largely discussed in Sect. 1.4 and in Chapter 3, the high X-ray-to-optical flux ratio population ($f_X/f_{\text{opt}} > 10$, 2 – 10 keV energy band), especially those sources with the reddest optical/NIR colours (typical of EROs; Mignoli et al. e.g. 2004, is expected to hide a large fraction of the highly obscured, high redshift sources, i.e. the mostly elusive type-2 QSO.

The analysis of our bright X-ray selected EXO sample drawn from the cross-correlation between the 2XMMp and the SDSS-DR5 catalogues (see Sect. 2.4 and Chapter 3), indeed confirmed that a large fraction of these sources have properties typical of obscured AGN. Moreover, the majority of the sources with optical spectroscopic identifications, turned out to be, in fact, obscured and high luminosity AGN, hence type-2 QSOs (Sects. 3.5.4 and 3.7.1). Our results suggest that the faintest optical sources, thus those with the highest f_X/f_{opt} ratios in our sample (which are not spectroscopically identified) are likely to hide the bulk of the type-2 QSO population at high redshift ($z > 1$), in agreement with the findings obtained in previous studies performed on EXOs (e.g. Fiore et al. 2003; Comastri & Fiore 2004; Mignoli et al. 2004).

However, if it is true that the sources with $f_X/f_{\text{opt}} > 10$ (2 – 10 keV) account for 10 – 20% of the AGN population (Fiore et al. 2003; Barcons et al. 2007), sources with higher f_X/f_{opt} ratios constitute a much smaller fraction (e.g. $f_X/f_{\text{opt}} > 50$ are estimated to be 1 – 2% of the AGN population at $f_X \gtrsim 10^{-13} \text{ erg cm}^{-2} \text{ s}^{-1}$; 2 – 10 keV; Della Ceca et al., in preparation); such extreme sources are rare and only a few cases have been found and studied to date (e.g. see Figure 7 in Gandhi et al. 2006; Severgnini et al. 2006).

Here we present the multi-wavelength analysis of 2XMM J123204, the most extreme source amongst our sample of 129 bright EXOs (Del Moro et al. 2009; see Chapters 2 and 3), with the highest f_X/f_{opt} ratio recorded so far for any extragalactic object. 2XMM J123204 is a bright X-ray source with $f_X \approx 10^{-12} \text{ erg cm}^{-2} \text{ s}^{-1}$ (2 – 10 keV energy band) which has no detection in any of the SDSS optical bands, already constraining the X-ray-to-optical ratio to be very high ($f_X/f_{\text{opt}} > 278$); additional photometric data (see below)

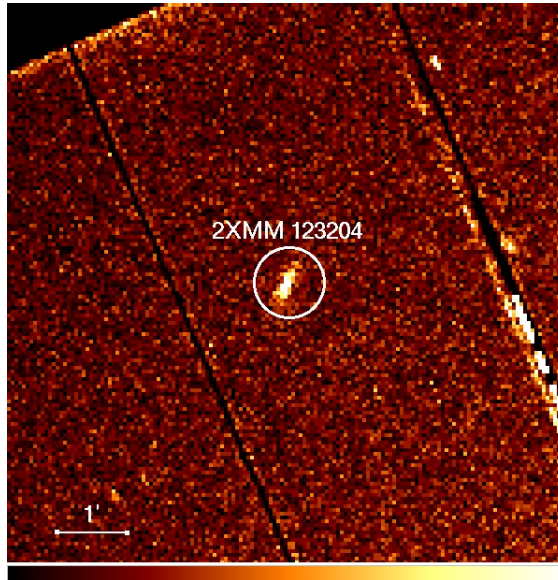


Figure 4.1: 2XMMp EPIC pn image of 2XMM J123204 in the 0.2 – 12 keV band with the size of 8 arcmin square; the circle is centred at the source X-ray position and has 30'' radius.

constrained its ratio to the extreme value $f_X/f_{\text{opt}} > 3300$.

4.2 Observations and results

4.2.1 X-ray properties of 2XMM J123204

The source 2XMM J123204 is the most extreme object amongst our EXO sample. It is a bright X-ray source with $f_X = 8.8_{-2.6}^{+0.7} \times 10^{-13} \text{ erg cm}^{-2} \text{ s}^{-1}$ (in the 2 – 10 keV energy band). On the basis of the lack of an SDSS counterpart it has $f_X/f_{\text{opt}} > 278$, already one of the highest ratios recorded so far, whilst as we show below, more recent data demonstrated the ratio to be $f_X/f_{\text{opt}} > 3300$, making it the highest known X-ray-to-optical flux ratio source outside the Galaxy. The source was detected in an *XMM-Newton* observation with target “NGP Rift 3”, which was made in July 2001 (Fig.4.1), at about 14.3 arcmin off-axis in the pn image ($\approx 13.4'$ in MOS1 and $\approx 13.8'$ in MOS2 images). The exposure time is ~ 15 ks with pn and ~ 20 ks with MOS1 and MOS2.

The statistical position error for 2XMM J123204 is 0.3''. Taking into account the expected systematic error component for the 2XMM catalogue of 0.35'' (see Sect 2.1.2), the counterpart is expected to lie within $\approx 1.4''$ (99% confidence). However, following

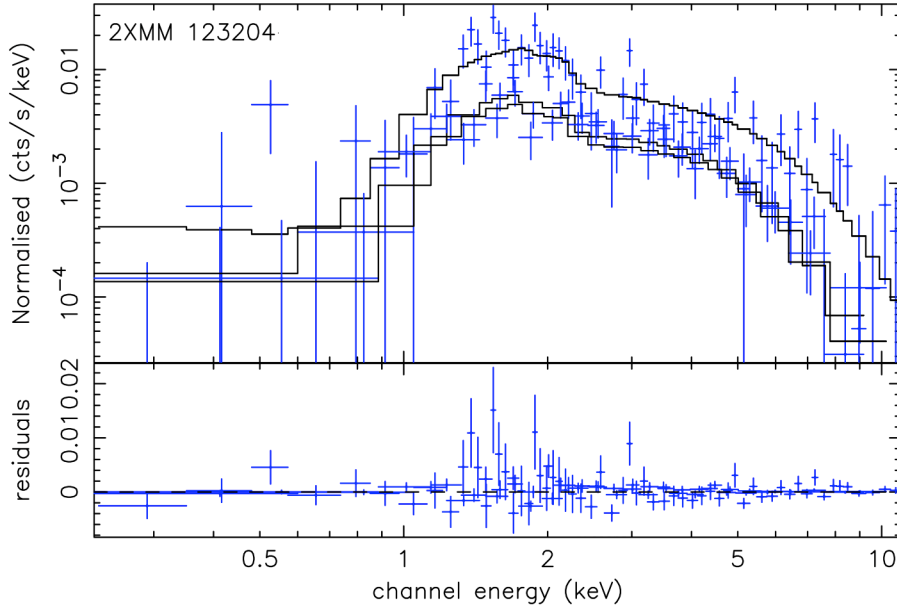


Figure 4.2: 2XMMp EPIC pn, MOS1 and MOS2 X-ray spectra of 2XMM J123204+215255 (top panel): the model is represented by the black lines; residuals are also shown (lower panel). The data are well represented by an absorbed power-law with a photon index $\Gamma = 1.5 \pm 0.1$ and a hydrogen column density $N_{\text{H}} = 1.8 \times 10^{23} \text{ cm}^{-2}$ at $z = 1.87$.

the arguments presented in Chapter 2 (Sect. 2.3.1), we adopted a radius of $7''$ as the most conservative upper limit on the possible separation of the true counterpart (see Chapter 2).

To study the X-ray spectrum of 2XMM J123204, the data were processed using the standard SAS v.7.1.0 tasks (*XMM-Newton* Science Analysis System, Gabriel et al. 2004). The spectrum of the source was extracted using an elliptical region to reproduce the shape of the Point Spread Function (PSF) of the *XMM-Newton* telescopes at the source position. The corresponding background spectrum was extracted using an annular region with radii $30''$ and $90''$, centred on the source position, removing any other detected nearby sources. The data were then filtered for high background intervals. The total number of EPIC counts in the 0.2–12 keV energy band after the filtering was 2234 cts. The spectral analysis was performed with XSPEC v.11.3.2 (Arnaud 1996), grouping the number of counts to a minimum of 10 counts per bin, and the χ^2 statistics was used. We found an acceptable fit to a simple model composed of a power-law plus Galactic and intrinsic absorptions; fixing $N_{\text{H}}^{\text{Gal}} = 2 \times 10^{20} \text{ cm}^{-2}$, the best fit parameters are: photon index $\Gamma = 1.7 \pm 0.2$ and hydrogen column density $N_{\text{H}} = (1.2 \pm 0.2) \times 10^{22} \text{ cm}^{-2}$ (assuming $z = 0$), with

$$\chi^2/\text{d.o.f.} = 118.0/106.$$

Repeating the X-ray spectral analysis for $z = 1.87$, anticipating the result presented below (Sect. 4.2.3), we obtained a best fit to the data with a photon index $\Gamma = 1.5 \pm 0.1$ and a column density $N_{\text{H}} = (1.8 \pm 0.3) \times 10^{23} \text{ cm}^{-2}$ ($\chi^2/\text{d.o.f.} = 115.7/106$; Fig. 4.2). We note the presence of marginally significant structure in the spectrum residuals at energy $\sim 1.5 - 3 \text{ keV}$ which might be related to red-shifted line or edge features. The reality of these features clearly requires confirmation at higher signal-to-noise.

4.2.2 Optical/IR properties

As noted above (Sect. 4.1), no counterpart has been found for 2XMM J123204 within $7''$ (Sect. 4.2.1) from the X-ray position in any of the SDSS bands (u' , g' , r' , i' , z' ; Fukugita et al. 1996), indeed the nearest SDSS object lies $\sim 30''$ away.

We obtained deeper optical imaging of the field on February 2007 on the 2.5m *Nordic Optical Telescope* (NOT). Four separate i' -band images were taken with the NOT AL-FOSC camera with integration times of 1800 seconds each. Conditions were photometric with $\sim 1''$ seeing, but unfortunately the images are affected by bad fringing. As there were no sky flats available to correct properly for the fringing, an empirical approach was adopted in which a smoothed version of each image (with bright objects removed) was used to estimate the effective sky background plus fringing effects. The resultant background-subtracted images were then stacked to make the final image (Fig. 4.3). This technique does not fully remove the fringing effects, but reduces them to a modest level, significantly improving the sensitivity for faint objects.

We found no detection of any counterpart within $7''$ of the position of 2XMM J123204 with an estimated 5σ limit $i' > 25.2 \text{ mag.}$, based on the amplitude of the residual background fluctuations. The photometric calibration was established by comparing the count rates of a sample of objects detected in the NOT image with the SDSS-DR5 photometric catalogue.

As the object is likely to be heavily obscured in the optical, the obvious next step was IR observations, where the effective dust obscuration will be lower. Follow-up J -band

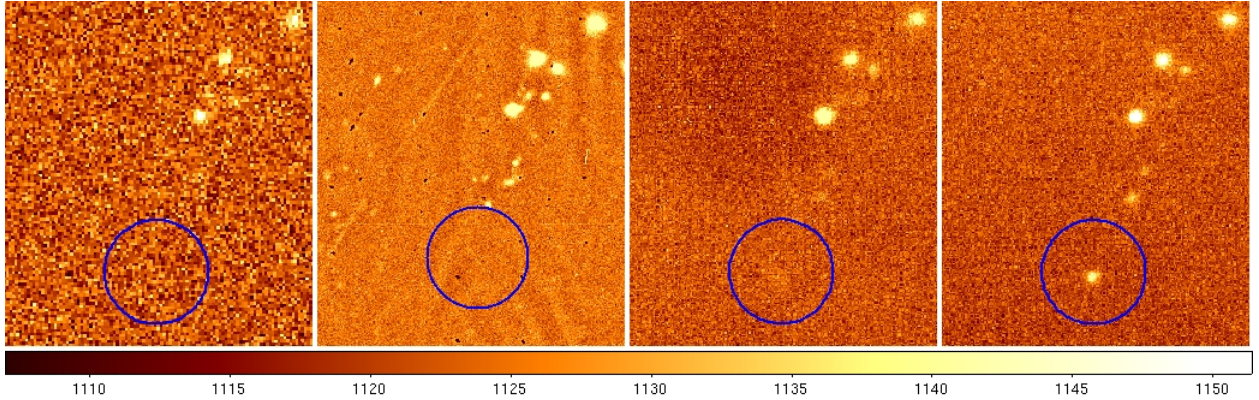


Figure 4.3: Optical/NIR finding charts for the source 2XMM J123204. From left to right: SDSS r' -band image, NOT i' -band stacked image, UKIRT-WFCAM J and K bands. The K -band image shows an apparent stellar counterpart ($K = 19.9 \pm 0.05$, AB). The circles have a radius of $7''$ and are centred on the X-ray position.

and K -band observations of 2XMM J123204 were obtained with the UKIRT-WFCAM (see Sect. 3.4.1) on the 12th of February 2007 with an exposure time of 1200 s in the J -band and 2×1200 s in the K -band. The NIR images (Fig. 4.3) show an apparently stellar counterpart in the K -band with a magnitude $K = 18.0 \pm 0.05$ (Vega, $K = 19.9 \pm 0.05$ in the AB magnitude system, Oke & Gunn 1983; see Hewett et al. 2006) and a very marginal detection in the J -band ($J \gtrsim 21.3$, Vega). All these values are reported in Table 4.1. The IR counterpart lies $\approx 1''$ from the X-ray centroid, consistent with the position errors discussed in Sect. 4.2.1. The IR detection allowed us to place limits on the optical/IR colours of the source: $r' - K > 2.6$ and $i' - K > 5.3$ (AB). As the optical emission is likely to be dominated by a high redshift galaxy, as discussed below (Sect. 4.3), it is likely that $r' - i' > 0$ which means that the r' magnitude should be of the order of $r' \gtrsim 25.2$. If that is true, the $r' - K$ colour becomes greater than 5.3 (AB), corresponding to $r' - K > 7$ in the Vega system, which is extremely red even for EROs.

4.2.3 Near-IR spectrum

2XMM J123204 was observed in the $H + K$ bands with the *Multi-Object Infrared Camera and Spectrograph* (MOIRCS, Ichikawa et al. 2006) at the Subaru Telescope in March 2007. The observation was performed in long-slit spectroscopy mode using the $HK500$ grism and $0.8''$ slit width, under a seeing of $0.6''$. The spectrum covers a wavelength range

Table 4.1: Photometric data for the source 2XMM J123204.

Magnitude	Wavelength Range [\AA]	Observed ^a	Predicted ^b
r'	5220-7220	> 22.5	27.7
i'	6520-8800	> 25.2	26.3
J	10510-14495	$\gtrsim 22.2$	22.6
K	19019-24995	19.9 ± 0.05	19.9

Notes: a) Photometric measurements and upperlimits from SDSS (r'), NOT (i') and UKIRT (J and K) data in AB magnitude system; b) magnitudes predicted from the best-fit model (see Sect. 4.3).

of 13000–23000 \AA , with a spectral resolution of $\approx 40 \text{\AA}$ (~ 5 pix) FWHM estimated from the width of OH airglow lines.

We took 6 target frames with 7 minutes exposure each, thus the total on-source integration time is 42 minutes. The telescope was dithered after every single exposure and the target was observed at different positions along the slit (1.5'' or 3'' from the slit centre). After sky subtraction, carried out by subtracting adjacent object frames from each other, flat-fielding was performed using dome-flat frames. These sky-subtracted and flat-fielded frames were then shifted, mirrored and combined to determine the average intensity value at each pixel with a 3σ clipping algorithm. Atmospheric absorption correction and flux calibration have been performed using the spectrum of a bright star (HD 119496, spectral type of A2V). The standard star spectrum was taken at the end of the night at a similar airmass to the target and with the same instrumental setup.

The observed spectrum (Fig. 4.4) reveals a red continuum emission, which is well represented by $f_\lambda \propto \lambda$. Using this form and extrapolating it out to the wavelengths longer than 23000 \AA , the K -band magnitude of this source was estimated to be 19.7 ± 0.1 mag in the AB system without any corrections (the emission line is at the edge of the K -band and its effect on this estimate can be ignored). This is consistent with the UKIRT-WFCAM photometry ($K = 19.9 \pm 0.05$, see Sect. 4.2.2 and Table 4.1) within the uncertainties. An estimated $\sim 10\%$ of the total flux from the object falls outside the slit width in the 0.6'' seeing conditions of the observation. As the slit losses are uncertain and the magnitude estimates from the spectroscopy are consistent with the UKIRT imaging, we therefore did

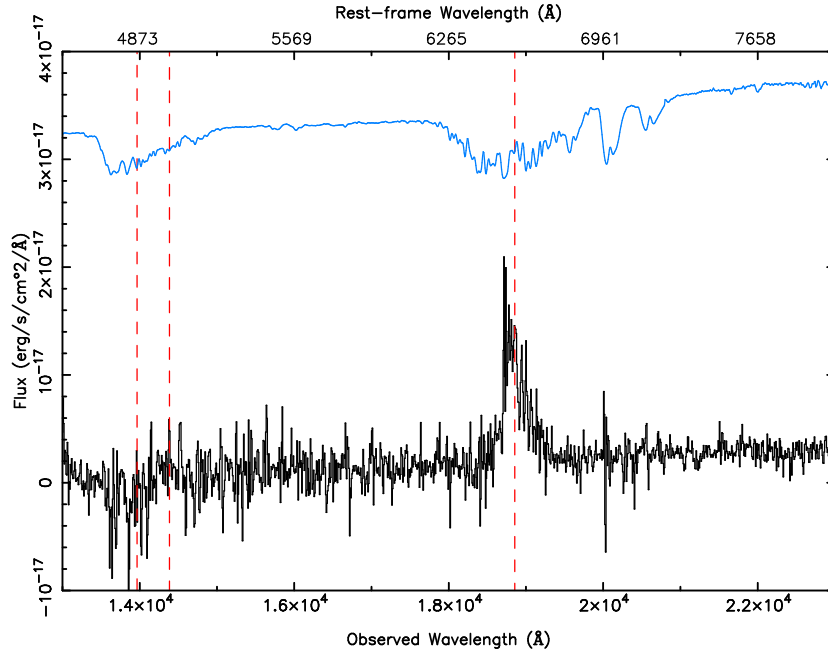


Figure 4.4: Subaru MOIRCS IR spectrum of 2XMM J123204 showing a single broad emission line (FWHM ~ 5300 km/s) likely to be $H\alpha$ at $z = 1.87$. The atmospheric absorption features are also reported, in arbitrary units (cyan). The dashed vertical lines indicate the central wavelengths of $H\alpha$ (Sect. 4.2.3 and Table 4.2) and the expected $H\beta$ and [OIII] emission lines for this redshift. On the top axis the rest-frame wavelengths are plotted.

not apply any slit-loss corrections to the emission line fluxes estimated below, but note that they have $\sim 10\text{-}20\%$ systematic uncertainty.

As shown in Fig. 4.4, a single broad emission line (FWHM = 5280 ± 331 km s $^{-1}$) is clearly visible on the red continuum in the observed spectrum at 18837 ± 7 Å (line centroid). The line flux is $f_{line} = (5 \pm 0.2) \times 10^{-16}$ erg cm $^{-2}$ s $^{-1}$ (uncorrected for absorption; Table 4.2). The emission line centre and line width were estimated by fitting a Gaussian to the spectrum in the vicinity of the line after the continuum was subtracted, whilst the line flux was estimated by directly integrating the continuum-subtracted line profile. The derived *Equivalent Width* (EW) is $EW = 2500 \pm 140$ Å; this is much higher than the EW of the $H\alpha$ line typically found in broad line QSO ($EW \approx 300$ Å; e.g. Brotherton et al. 2001; Akiyama et al. 2002). All the uncertainties were estimated from the 1σ errors in the Gaussian fitting process.

Although there are no other significant emission or absorption lines visible in the spectrum, the most likely interpretation is that the line detected is $H\alpha$. We also considered other

possible interpretations for this line:

- i) if it were one of the Paschen series the implied redshift would be $z < 1$ which seems unlikely as the host galaxy is not detected in the optical (and would thus be a very low luminosity object) and the detected line flux would be much higher than expected;
- ii) if it were MgII the redshift would be $z \sim 5.7$ which would make the X-ray absorption $N_{\text{H}} \approx 1.5 \times 10^{24} \text{ cm}^{-2}$ (Compton-thick). However, no strong Fe $K\alpha$ line is detected in the X-ray spectrum and the derived luminosity at this redshift would be extremely high ($L_{\text{X}} \approx 1.8 \times 10^{47} \text{ erg s}^{-1}$), so we considered also this hypothesis is unlikely.

Assuming the $\text{H}\alpha$ identification is correct, the estimated redshift for the source is $z = 1.87$. Even though the emission line is just at the wavelength range where the spectrum is seriously affected by the atmospheric absorption lines between H and K bands (Fig. 4.4), this can not explain the total absence of the [OIII] (expected from the narrow line region) and the $\text{H}\beta$ emission lines. For those lines we estimate flux upper limits from our MOIRCS spectrum (see Table 4.2): $f_{[\text{OIII}]} < 3 \times 10^{-17} \text{ erg cm}^{-2} \text{ s}^{-1}$ (assuming an FWHM $\leq 500 \text{ km s}^{-1}$) and $f_{\text{H}\beta} < 1 \times 10^{-16} \text{ erg cm}^{-2} \text{ s}^{-1}$ (assuming the same FWHM as $\text{H}\alpha$). These limits are conservative values estimated at several times higher than the formal 3σ level (derived from empirical estimates of the noise in the vicinity of these lines) to allow for the systematic deviations from the expected smooth continuum which occur in this part of the spectrum. The estimated line ratio $\text{H}\alpha/\text{H}\beta$ is > 5 , which is higher than the typical intrinsic unreddened value for AGN ($\text{H}\alpha/\text{H}\beta \approx 3.5$, e.g. Ward et al. 1988). Noting that the $\text{H}\beta$ flux is a conservative upper limit, this already indicates significant extinction in this object. In fact, the observed Balmer line ratio scales with the extinction as:

$$E(B - V) = a \log \frac{(\text{H}\alpha/\text{H}\beta)_{\text{obs}}}{(\text{H}\alpha/\text{H}\beta)_{\text{int}}} \quad (4.1)$$

where $E(B - V)$ is the reddening ($A_V = R_V \times E(B - V)$, with $R_V \simeq 3.0$; e.g. Ward et al. 1988; Pei 1992), $(\text{H}\alpha/\text{H}\beta)_{\text{obs}}$ and $(\text{H}\alpha/\text{H}\beta)_{\text{int}}$ are the observed and the intrinsic Balmer

decrement, respectively, and a is a constant (see e.g. Reynolds et al. 1997).

We also note the clear asymmetry in the $H\alpha$ line profile for which we have no obvious explanation, although an incomplete correction for the severe atmospheric absorption may be a possible reason. A narrow [NII] $\lambda 6583$ line may also be present in the spectrum and contribute to the asymmetry of the $H\alpha$ profile. The presence of this line, assuming it has $\text{FWHM} \leq 500 \text{ km s}^{-1}$, cannot however explain all the observed red wing, given the $H\alpha$ line width.

4.3 Discussion

For a redshift $z = 1.87$, the intrinsic X-ray luminosity of the source is $L_X = 1.6 \times 10^{46} \text{ erg s}^{-1}$ (2–10 keV rest-frame) and the X-ray spectrum has a large column density ($N_H \approx 2 \times 10^{23} \text{ cm}^{-2}$; see Sect. 4.2.1). The X-ray properties of 2XMM J123204 thus make it a very luminous, heavily absorbed AGN, with spectral parameters typical for a type-2 QSO (in X-ray).

In contrast the IR spectrum shows a broad $H\alpha$ emission line and the IR counterpart detected in the K -band has a probable stellar morphology, characteristics of a type-1 object (see also Sects. 1.1.2 and 3.5.4). To further complicate the story the predicted emission line fluxes are much higher than those observed (Table 4.2): using the correlations between hard X-ray luminosity and $H\alpha$ and [OIII] luminosities from Panessa et al. (2006):

$$\log L_X = (1.06 \pm 0.04) \log L_{H\alpha} + (-1.14 \pm 1.78) \quad (4.2)$$

$$\log L_X = (1.22 \pm 0.06) \log L_{[\text{OIII}]} + (-7.34 \pm 2.53) \quad (4.3)$$

the predicted flux for $H\alpha$ is $f_{H\alpha} \approx 1.7 \times 10^{-14} \text{ erg cm}^{-2} \text{ s}^{-1}$, which is about 30 times brighter than the detected line flux (uncorrected for absorption) and the predicted fluxes for [OIII] and $H\beta$ are: $f_{[\text{OIII}]} \approx 2.9 \times 10^{-15} \text{ erg cm}^{-2} \text{ s}^{-1}$ and $f_{H\beta} \approx 4.8 \times 10^{-15} \text{ erg cm}^{-2} \text{ s}^{-1}$ (assuming the standard $H\alpha/H\beta$ ratio, e.g. Ward et al. 1988), whereas these lines are not detected at all.

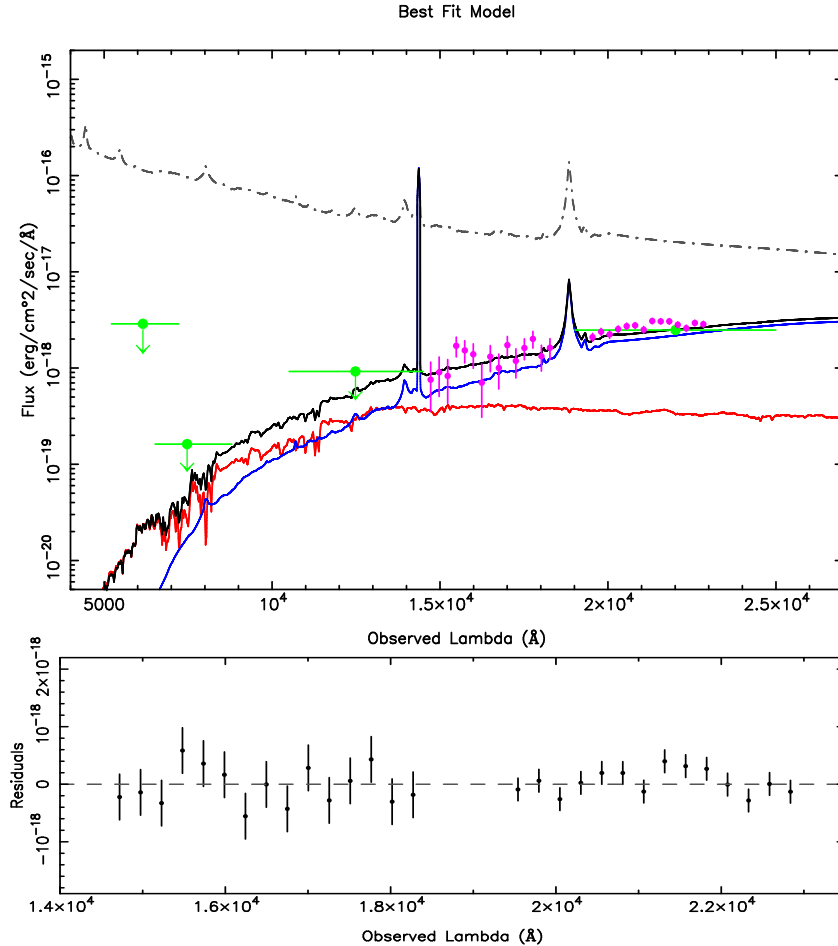


Figure 4.5: *Top*: Best-fit model of the NIR spectrum (magenta points); green circles: photometric measurements and upperlimits of the r' , i' , J and K –band magnitude; red line: galaxy SED template; blue line: absorbed QSO SED; grey dash-dotted line: unabsorbed QSO SED template; black line: resulting SED (QSO + host galaxy). *Bottom*: Residuals of the fitting in the 14500–23000 Å wavelength range.

In order to see whether it was possible to reconcile the X-ray, optical and near-IR characteristics of this object, we carried out simple modelling of the observed IR spectral continuum using an adaptation of the composite SED model described in Chapter 3 (Sect. 3.3; see Fig. 4.5). In this case, to represent the host galaxy of 2XMM J123204, we adopted a 5 Gyr early-type galaxy template¹ generated with the GRASIL code (Silva et al. 1998). To reproduce the QSO we adopted a composite spectrum of a type-1 QSO with the highest IR/optical ratio (from Polletta et al. 2007). In the model the QSO SED component had intrinsic absorption, i.e. nuclear extinction, parameterised by a rest-frame equivalent

¹We followed the assumption that QSOs are typically found to be hosted in massive elliptical galaxies (McLeod & Rieke 1995; Aretxaga et al. 1998; Dunlop et al. 2003) and selected the elliptical galaxy template at the closest epoch to the object ($z = 1.87$).

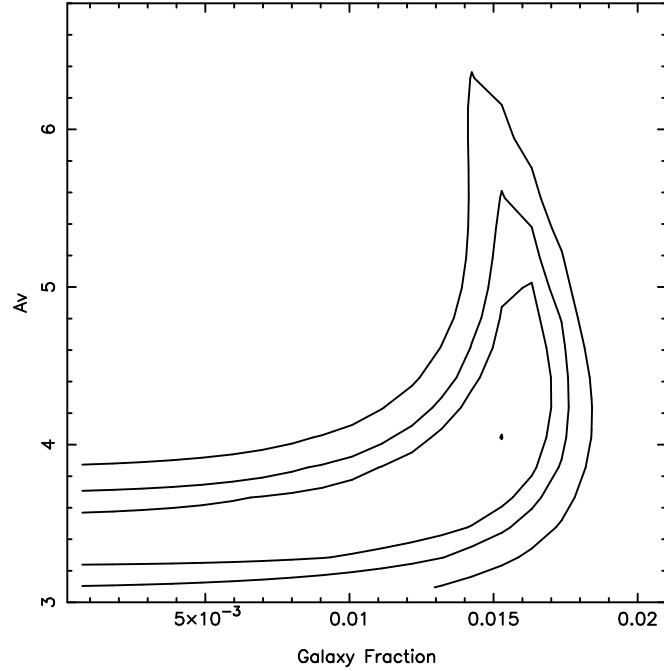


Figure 4.6: χ^2 contours at 68, 90 and 99% confidence obtained from modelling of the IR spectrum for a grid of *Galaxy Fraction* and A_V values, as defined in the text.

A_V and represented by the Small Magellanic Cloud (SMC) extinction curve from Pei (1992), whilst both the QSO and galaxy SEDs had fixed Galactic absorption ($N_{\text{H}}^{\text{Gal}} = 2 \times 10^{20} \text{ cm}^{-2}$, with a dust-to-gas ratio $A_V/N_{\text{H}} = 1/1.8 \times 10^{21}$; e.g. Predehl & Schmitt 1995), using the Milky Way extinction curve (Pei 1992; see Sect. 3.3). The other free parameter in the model is the *Galaxy Fraction*² (g), which we define here as the ratio between the host galaxy and the intrinsic QSO fluxes in the rest-frame wavelength range $\lambda_1 = 4160 \text{ \AA} < \lambda < \lambda_2 = 4210 \text{ \AA}$ (see Sect. 3.3):

$$g = \frac{\int_{\lambda_1}^{\lambda_2} f_{\lambda, \text{gal}} d\lambda}{\int_{\lambda_1}^{\lambda_2} f_{\lambda, \text{QSO}} d\lambda}. \quad (4.4)$$

We used this SED model to fit the IR continuum (Fig. 4.4) in the wavelength range 14500-23000 \AA . As we aimed to reproduce only the spectral continuum, we excluded the emission line from the fitting; we excluded also the wavelengths below 14500 \AA because of the lower S/N in this part of the spectrum and to avoid the wavelengths of the expected [OIII] and the $\text{H}\beta$ emission lines. After binning the spectrum, we computed χ^2 values for a grid

²We note that the definition of the galaxy fraction adopted here is slightly different from that expressed in Chapter 3, called F_g .

of possible nuclear extinction and *Galaxy Fraction* (g) parameters and we determined confidence intervals for the two free parameters using the usual $\Delta\chi^2$ prescription (Fig. 4.6). Our modelling provides strong constraints on the rest-frame equivalent $A_V = 3.2\text{--}5.0$ (1σ confidence) and a reasonably robust upper limit on the galaxy contribution $g \lesssim 1.7\%$. The best-fit of the near IR spectrum and the residuals of the fitting are shown in Fig. 4.5. We can also use the model fit results to constrain the expected r' , i' and J -band magnitudes. Our best-fit model predicts $r' \approx 27.7$, $i' \approx 26.3$ and $J \approx 22.6$, values consistent with the upper limits discussed in Sect. 4.2.2 (Table 4.1). We note that the general properties of 2XMM J123204 are rather similar to the object presented by Severgnini et al. (2006), although our source has higher extinction and has not yet been detected in the optical band. Our constraints on the host galaxy mass are comparable to, or somewhat lower than, that inferred by Severgnini et al. (2006) for their object.

Our modelling cannot be considered as definitive, as it is limited by the restricted wavelength coverage of our data, by the fact that we cannot be sure of the intrinsic SEDs for the galaxy and AGN components and by the assumption that just two components will adequately represent the data. We can however examine how our result depends on the choice of the SED components in the spectral range we are investigating, by using different QSO templates (from Polletta et al. 2007; see Sect. 3.3) in the fitting process. For this range of templates we found variations of $\lesssim 10\%$ in the derived rest-frame equivalent A_V . As in all the models we tested the contribution of the galaxy appeared to be only few percent of the total emission, there is clearly little sensitivity to the precise shape of the galaxy SED adopted.

With the model parameters obtained from our analysis, the extinction for the QSO component in the J -band (close to $H\beta$ and $[OIII]$) corresponds to ≈ 5.3 mag and ≈ 2.4 mag in the K -band, in the vicinity of the redshifted $H\alpha$ line. Correcting the observed $H\alpha$ flux for this extinction (A_K) gives a value $f_{H\alpha} \approx 4.6 \times 10^{-15}$ erg cm $^{-2}$ s $^{-1}$, which is lower than the flux expected from the L_X - $L_{H\alpha}$ correlation of Panessa et al. 2006 (see Table 4.2), but well within the scatter of the correlation. The much higher extinction ($A_J \approx 5.3$) at the $H\beta$ line is fully consistent with its non-detection.

Table 4.2: Optical emission line fluxes.

Line	λ_{rest}^a Å	Observed Flux ^b [erg cm ⁻² s ⁻¹]	Predicted Flux ^c [erg cm ⁻² s ⁻¹]	Corrected Flux ^d [erg cm ⁻² s ⁻¹]	A_λ^e [mag]
H α	6563	$(5 \pm 0.2) \times 10^{-16}$	1.7×10^{-14}	4.6×10^{-15}	2.4
H β	4861	$< 1 \times 10^{-16}$	4.8×10^{-15}	—	5.3
[OIII]	5007	$< 3 \times 10^{-17}$	2.9×10^{-15}	—	5.3

Notes: a) central wavelength of the line (rest-frame); b) flux and upperlimits measured from the IR spectrum; c) flux predicted from the correlations of Panessa et al. (2006); d) flux corrected for extinction; e) extinction of the QSO component in the vicinity of the line, estimated from the model.

The lack of any detection of the [OIII] line is not explained in the model, as this line is expected to originate in the narrow line region (NLR) which should not be affected by the large extinction of the nuclear region. However, the weakness or disappearance of the [OIII] emission line has already been reported for high-luminosity AGN (see Yuan & Wills 2003; Netzer et al. 2004; Sulentic et al. 2004). A possible explanation may be related to the fact that the simple scaling law: $R_{NLR} \propto L_{ion}^{1/2}$ (where R_{NLR} is the radius of the narrow line region and L_{ion} is the ionising source luminosity; Netzer et al. 2004), which may explain the correlation between the X-ray and the [OIII] luminosities at lower values, must break down when the NLR radius becomes comparable with the size of the galaxy.

Another possible explanation may be the presence of obscuring dust outside the torus, at larger distances from the nucleus (see Sects. 1.2.1 and 3.7.1; Rigby et al. 2006; Martínez-Sansigre et al. 2006; Brand et al. 2007; Polletta et al. 2008) and could thus absorb the emission coming from the narrow line region. This interpretation is equally consistent with the observed red continuum and the extinction of the broad lines whilst also providing an explanation for the absence of any narrow lines in the IR spectrum. However, as it is not possible to constrain the location of the obscuring dust with the present data, neither the interpretations can be rejected.

Alternative explanations for the lack of narrow emission lines in the spectrum may be i) the total absence of the NLR: at such high luminosity, enormous NLRs should be expected

($R_{NLR} \sim 10 - 100$ kpc); however, to produce the typical narrow lines observed in lower luminosity AGN, the gas would have velocities exceeding the escape velocity of the system and may not form the “canonical” NLR clouds; or ii) a NLR with different properties from those typically observed in lower luminosity AGN: e.g. if the NLR were formed by very high density gas, the forbidden transitions that produce the narrow emission lines would be collisionally de-excited (as in the BLR) and no narrow line would appear in the spectrum; or if the gas ionization were too high the typical narrow lines observed in AGN would not be produced.

Finally we note that the values obtained for the optical extinction from our modeling are significantly lower than expected from the measured X-ray column density. This can most easily be parameterised by a dust-to-gas ratio which is about 20 – 25 times lower than the standard Galactic value ($A_V/N_H = 1/1.8 \times 10^{21}$, e.g., Predehl & Schmitt 1995). Such low ratios have been reported in several previous studies of AGN (Maccacaro et al. 1982; Maiolino et al. 2001b; Akiyama et al. 2002; Willott et al. 2004). In this comparison, as is the case in the other papers cited, we are assuming the simplest possible geometry where the dust and gas are co-spatial and lie in a uniform foreground screen³. One possible explanation for the high ratio is a different dust grain size distribution dominated by large grains, whose formation is naturally expected in the high density environments, like those characterising the circumnuclear region of AGNs. This dust grain distribution can produce a flatter extinction curve than the Galactic one and yield a lower A_V/N_H ratio (Maiolino et al. 2001a; Maiolino 2002). This would not be a valid explanation if the absorption is on kpc-scales as discussed above.

4.4 Summary and conclusions

On the basis of its X-ray and optical properties, 2XMM J123204 has the highest recorded f_X/f_{opt} of any extragalactic X-ray source. IR spectroscopy confirms this object is an AGN

³This assumption may lead to an underestimation of the effective extinction of the source (e.g. MacKenty et al. 2000). More realistic dust and gas distributions can of course lead to different conclusions about the dust-to-gas ratio; however, as it is not possible to constrain the gas and dust distribution with the present data, considering more sophisticated models is beyond the purpose of our analysis.

at $z = 1.87$. In X-rays it is a very luminous object with large absorption, making it a type-2 QSO candidate. Its optical/NIR properties show a strongly reddened continuum, but stellar appearance in the K band and broad $H\alpha$, more consistent with a type-1 classification (type 1.9 in the classification used for low redshift AGN). We have shown that these apparently discrepant properties can be reconciled with a model consisting of a heavily reddened AGN nucleus (rest-frame equivalent $A_V = 3.2 - 5.0$) and fainter host galaxy. According to the classification criteria adopted for the whole EXO sample (see Sect. 3.5.4), this object can be classified as a type-2 QSO. Our results also provide tight constraints on the X-ray column density and optical/IR extinction which demand a dust-to-gas ratio for this object ~ 25 times lower than the standard Galactic value. The non-detection of a narrow [OIII] emission line at anything like the expected flux in this object may be related to its very high luminosity $L_X = 1.6 \times 10^{46}$ erg s $^{-1}$ (2–10 keV rest-frame).

Alternatively 2XMM J123204 might be a member of a population of AGN with absorption on kpc-scales, sometimes described as “host-obscured” AGN (e.g. Brand et al. 2007), which may be an important ingredient in resolving the discrepancy between the predicted and observed ratios of type-1 and type-2 AGN, which exists in some models of AGN obscuration (e.g. Martínez-Sansigre et al. 2006; Brand et al. 2007).

We have shown that f_X/f_{opt} selection using the large samples afforded by the 2XMM catalogue provides an effective way of discovering extreme objects like 2XMM J123204, which are a rare but important part of the obscured AGN population. Our analysis has demonstrated that the extreme properties of this object are a natural consequence of its very high luminosity and large obscuration. It is interesting to note that a high luminosity object of this type with only a factor two higher absorption would appear as an entirely “normal” galaxy in that it would have no detectable broad lines in its spectrum and presumably no narrow lines either, given the apparent strong suppression of the narrow emission lines evident at these high luminosities.

CHAPTER 5

The Subaru/XMM Deep Survey: X-ray analysis

In this chapter a detailed X-ray spectral analysis of the Subaru/ XMM-Newton Deep Survey is presented. The analysis is restricted to a sample of 68 sources with a flux limit of $f_X \geq 2.4 \times 10^{-14} \text{ erg cm}^{-2} \text{ s}^{-1}$ (2 – 10 keV), which have high spectroscopic identification completeness ($\sim 90\%$ of the sources), with redshifts up to $z = 2.8$. Different spectral models have been tested in order to obtain the best fit and the spectral properties for each individual source. In addition a stacking technique has been applied in order to analyse the average Fe K α line profile of the type-1 AGN.

The estimation of the fraction (F) of the absorbed AGN in the sample and the dependence of F with the X-ray luminosity are reported and compared to literature results. Moreover, the properties of the high X-ray-to-optical flux ratio sources ($f_X/f_{\text{opt}} > 10$) found amongst this sample are described and compared to the sample presented in previous Chapters.

5.1 Introduction

One of the major goals of extragalactic astronomy is to understand the SMBH and galaxy evolution and how this relates to their environment (see Sect. 1.3). Although optical surveys are extremely important for source population studies, as they can provide accurate positions and identifications, they are biased toward luminous and unobscured objects. On the other hand, X-ray surveys are a key means to detect and study the AGN population, but they need to be complemented by other wavelength data in order to have a clear characterisation of the sources. Moreover, deep pencil-beam surveys are limited by the area that can be covered to very faint fluxes (typically of the order of 0.1 deg^2) and are affected by cosmic variance (Somerville et al. 2004).

In order to overcome these problems, in the past few years a number of deep imaging multi-wavelength programs have been undertaken, such as the Cosmic Evolution Survey (COSMOS; Scoville et al. 2007; Hasinger et al. 2007) and the Subaru/*XMM-Newton* Deep Survey (SXDS; Sekiguchi et al. 2009, in preparation). Thanks to their high sensitivity over a wide wavelength range and a relatively large contiguous sky area ($\sim 1 \text{ deg}^2$), these surveys constitute an unprecedented resource in order to study the distant Universe and the origin and evolution of its content.

5.2 The Subaru/*XMM-Newton* Deep Survey

The Subaru/*XMM-Newton* Deep Survey (SXDS) is one of the major multi-wavelength surveys carried out in the past few years (see above): it covers a contiguous sky region of $\sim 1.3 \text{ deg}^2$. This survey represents a unique combination of depth and sky area coverage: it is founded on a combination of deep, wide-area imaging in the X-rays with *XMM-Newton* and in the optical with Subaru/Suprime-Cam. A wide range of companion surveys at longer wavelengths (IR, submillimeter and radio bands) are also part of the SXDS project, using most of the major observing facilities currently available (see below).

The SXDS field is centred at R.A. = $02^h 18^m 00^s$ and dec = $-05^\circ 00' 00''$, chosen to be accessible from the main ground based telescopes in the northern and in the southern

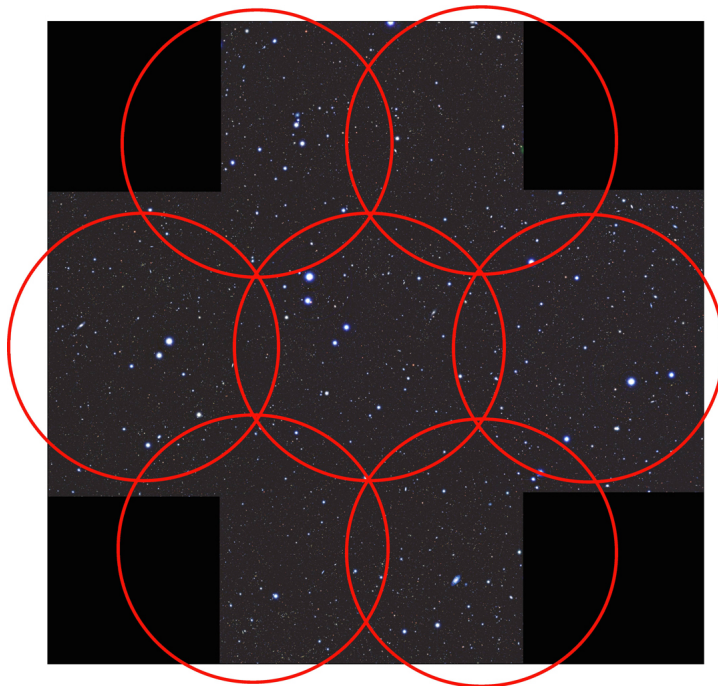


Figure 5.1: B , i' and z' colour image of the Subaru/*XMM-Newton* Deep Survey field. The red circles indicate the 7 pointings of *XMM-Newton*. Image taken from <http://www.naoj.org/Science/SubaruProject/SDS>.

hemispheres.

5.2.1 Multi-wavelength observations

The optical imaging observations were performed at the Subaru Telescope, at Mauna Kea (Hawaii), with the prime focus camera Suprime-Cam (Miyazaki et al. 2002), in the period between September 2002 and September 2005. The field of view of the Suprime-Cam covers $\sim 34' \times 27'$, in five different broad-band filters: B , V , R_c , i' and z' , down to a magnitude limit of $B = 28.4$, $V = 27.8$, $R_c = 27.7$, $i' = 27.7$ and $z' = 26.6$ (AB magnitudes, 3σ ; Furusawa et al. 2008). The SXDS field has been observed with 5 contiguous pointings (Fig. 5.1), covering a total sky area of 1.22 deg^2 . The optical sensitivity achieved by this survey is more than a magnitude deeper than any other surveys of comparable area.

A campaign of optical spectroscopic follow-up of the sources detected in the field is ongoing. To date over 10000 optical spectra have been obtained from some of the larger ground-based telescopes available (Subaru, Gemini, VLT, AAT, Magellan).

The SXDS region is also the target field of the deepest wide-area near-infrared survey

to date: the Ultra Deep Survey (UDS; Foucaud et al. 2007), performed with the Wide Field Camera (WFCAM) on the United Kingdom Infrared Telescope (UKIRT) as part of the United Kingdom Infrared Deep Sky Survey (UKIDSS; Lawrence et al. 2007). The NIR observations are focused on the central field of the SXDS, covering 0.8 deg^2 to a depth of $J = 24.0$, $H = 23.7$, and $K = 23.9$ (5σ , for point sources; AB magnitudes).

In the mid- and far-infrared bands the SXDS has been observed by the *Spitzer Space Telescope*. Observations of almost the entire area ($\sim 1 \text{ deg}^2$) were performed with the Infrared Array Camera (IRAC; Fazio et al. 2004) in the 3.6, 4.5, 5.8 and $8.0 \mu\text{m}$ bands, reaching a magnitude $m_{3.6 \mu\text{m}} = 24.5$, and in the 24, 70 and $160 \mu\text{m}$ bands with the Multiband Imaging Photometer for Spitzer (MIPS; Rieke et al. 2004) as part of the *Spitzer* Wide-area Infrared Extragalactic legacy survey project (SWIRE; Lonsdale et al. 2004).

About 0.25 deg^2 of the SXDS also have submillimeter mapping at $850 \mu\text{m}$ to a median depth of about 2.2 mJy/beam (1σ) from the SCUBA Half Degree Extragalactic survey (SHADES; Mortier et al. 2005) at the James Clerk Maxwell Telescope (JCMT) and a larger area of 0.81 deg^2 has been covered at 1.1 mm by the Astronomical Thermal Emission Camera (AzTEC) at the JCMT.

A fraction of the SXDS region also has ultra-violet imaging data obtained with the Galaxy Evolution Explorer (GALEX) as part of its Deep Imaging Survey and Medium-Deep Spectroscopic Survey.

Radio observations were carried out with the National Radio Astronomy Observatory's Very Large Array (VLA) between August and September 2002. Fourteen overlapping pointings in B-array have been undertaken at 1.4 GHz for a total of 64 hours, providing a uniform sensitivity of $\sim 60 \mu\text{Jy/beam}$ (5σ) over virtually the entire field. The radio catalogue produced from these observations contains 505 sources at a peak flux limit of $100 \mu\text{Jy}$, covering a sky area of 0.8 deg^2 (Simpson et al. 2006).

5.2.2 X-ray Data

The X-ray data, together with the Subaru optical photometric data, are the foundations of the SXDS. The X-ray observations were performed by the EPIC cameras on board of the

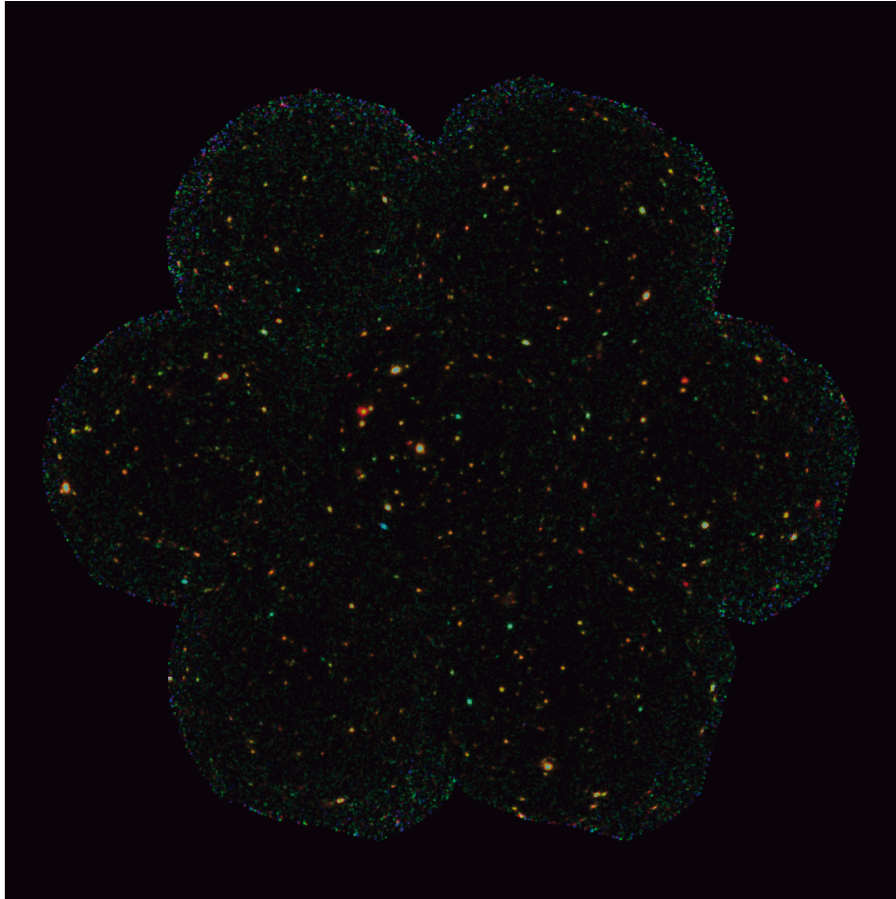


Figure 5.2: Smoothed X-ray image of the 7 pointings of the SXDS field, obtained from 3 different energy bands: 0.5 – 2 keV (red), 2 – 4.5 keV (green), and 4.5 – 10 keV (blue). Image adapted from Ueda et al. (2008).

XMM-Newton Space Observatory (see Chapter 2) in 3 separate epochs between July 2000 and January 2003. The survey covers a continuous area of 1.14 deg^2 covered by 7 different pointings: a central pointing of 100 ks (SDS-1) and six around it with 50 ks exposure each (named SDS-2 to SDS-7, Fig. 5.2).

In the field a total of 1245 sources were detected with a likelihood $ML \geq 7$ (Ueda et al. 2008) with an estimated spurious detection rate below 5%, depending on the energy band considered (and hence on the sensitivity). The mean flux of the survey in the hard X-ray band (2 – 10 keV) is $f_X \sim 1 \times 10^{-14} \text{ erg cm}^{-2} \text{ s}^{-1}$ (Fig. 5.3), while at softer energies, in the 0.5 – 4.5 keV energy band (XID band), the mean flux is $f_X \sim 2.5 \times 10^{-15} \text{ erg cm}^{-2} \text{ s}^{-1}$. The SXDS field is at least a factor 2 deeper than the typical sensitivity of the 2XMM catalogue (Sect. 2.1.3; Watson et al. 2009).

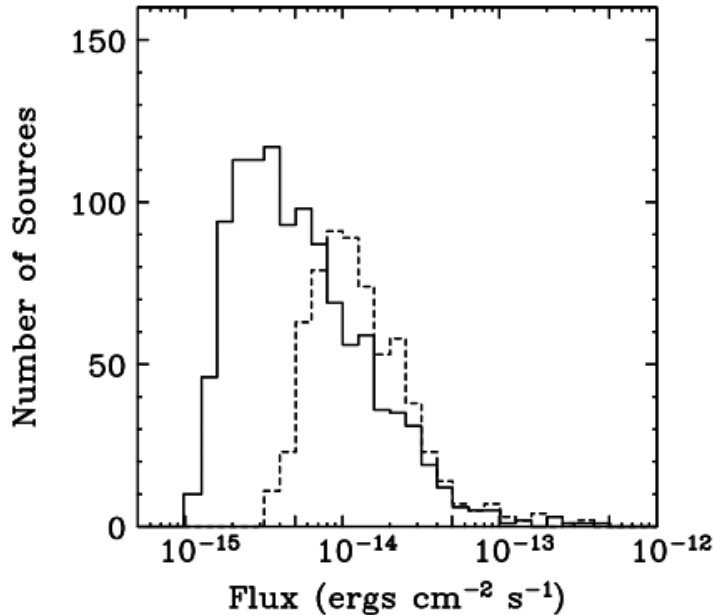


Figure 5.3: X-ray flux distribution of the SXDS sources in the 0.5-4.5 keV band (XID band, solid line) and in the 2 – 10 keV band (hard band, dashed line). Image adapted from Ueda et al. (2008)

The cross-correlation of the X-ray sources with the optical sources in the SXDS fields was performed by Akiyama et al. (paper in preparation) using the likelihood ratio technique (de Ruiter et al. 1977; Sutherland & Saunders 1992) supported by Monte Carlo simulations in order to compute the fraction of mis-identifications in the field. This method was applied to the Subaru photometric data (covering 738 of the X-ray sources detected in the 0.3-10 keV energy band; Ueda et al. 2008) and to the *Spitzer* MIR data (3.6 μm band), in order to improve the completeness of the identifications; the number of mis-identifications is estimated to be $\sim 4.5\%$ (Akiyama et al., in preparation).

5.3 Our Sample

Amongst the X-ray sources detected in the SXDS field, within the field of view observed with Suprime-Cam (see Sect. 5.2.1 and Fig. 5.1), we selected a sample of 68 sources from the source catalogue presented in Ueda et al. (2008), with a detection likelihood $ML \geq 9$ (2 – 10 keV) and a hard band count-rate (2 – 10 keV) above 0.003 cts/s (EPIC combined

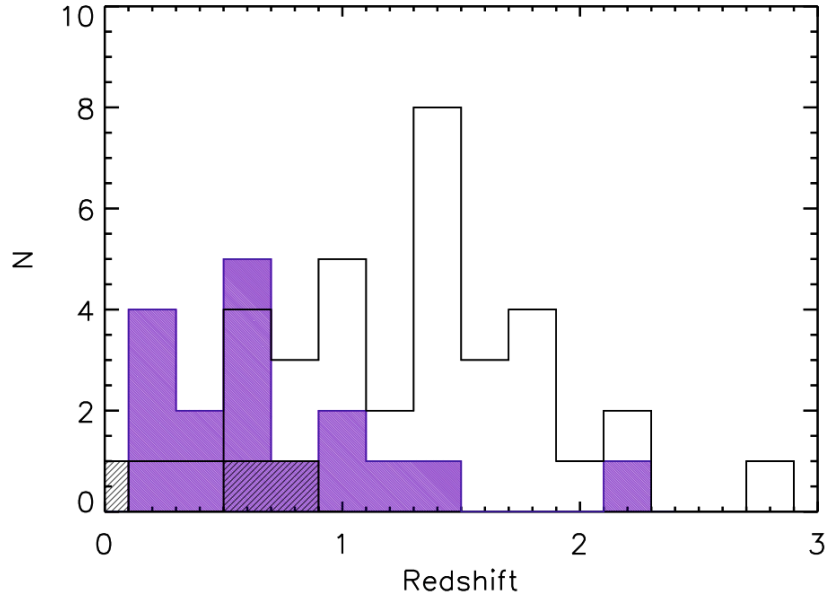


Figure 5.4: Redshift distribution of the optical identified sample sources. Black open histogram: BL AGN; purple histogram: NL AGN; black shaded histogram: absorption line sources.

data; see Ueda et al. 2008). Using the conversion factors¹ reported in Ueda et al. (2008), this limit corresponds to a flux $f_X \geq 2.4 \times 10^{-14} \text{ erg cm}^{-2} \text{ s}^{-1}$. With this selection we are able to sample the X-ray sources in the flux regime that provides the major contribution to the X-ray background below 10 keV (see Chapter 1).

This sample was chosen in particular also for its high completeness: spectroscopic redshifts (from Subaru/FOCAS and ESO-VLT/VIMOS, AAT/AAOmega² optical data) are available for 87% of the objects and optical identifications have been obtained for 82% of the sources³. About half of the sample (35 objects) was identified as broad emission line galaxies (BL AGN) and 25% (17 objects) as narrow emission line galaxies (NL AGN; Akiyama et al., in preparation); amongst the identified objects there are also three absorption line galaxies (ABS) and a star. In Figure 5.4 the redshift distribution for the sample sources is shown. The BL AGN redshift distribution peaks at $z \approx 1.4$; while the NL AGN are typically detected at lower redshift, with the peak of the distribution at $z \approx 0.6$.

¹In order to convert from count rate to flux the conversion factor obtained by Ueda et al. (2008) assuming a single power-law with spectral index $\Gamma = 1.9$ in the 2 – 10 keV band was used.

²AAOmega is the multi-object and integral field spectrograph mounted at the Anglo-Australian Telescope.

³Three sources were observed at the AAT and VLT telescopes as part of a different ID program: the data are not public, therefore the spectra could not be analysed, however, the redshift information was available.

Selecting an homogeneous sample of objects in a wide redshift range as in our case ($z = 0 - 3$), is the most powerful tool in order to investigate the properties of the AGN population and their evolution at different epochs.

5.4 Spectral analysis

5.4.1 Extraction of the X-ray spectra

The *XMM-Newton* X-ray data were downloaded from the *XMM-Newton* Science Archive (XSA⁴) interface: the 7 SXDS fields (SDS-1 to SDS-7) were covered by 10 different observations, as SDS-1, SDS-3 and SDS-4 were observed twice (the exposure time of these pointings, stated in Sect. 5.2.2, is the sum of the exposure of the two observations).

The spectral analysis of the 68 sample sources was performed for the 3 *XMM-Newton* EPIC cameras (pn, MOS1, MOS2) separately. We used the PPS products (see Chapters 2 and 3), and the version 8.0.0 of the *Science Analysis Software* (SAS 8.0.0⁵), released in July 2008.

After filtering the event files for high background intervals⁶, we extracted the source spectra from a circular region produced by the SAS task `region` with a radius enclosing 80% of the total flux under the Point Spread Function (PSF) at the source position; the region radius has been then optimised for each source by the task `eregionanalyse`. The background spectra were extracted from annular regions centred on the source position, masking out all the objects falling in the extraction region. The background regions have been then carefully checked by eye: in the cases where they lay partially outside the field of view of the EPIC cameras or they were contaminated by emission from a nearby bright source, they have been replaced by a circular source-free region in the vicinity of the corresponding source (and preferably in the same CCD of the source). Using the tasks `rmfgen` and `arfgen` we also extracted the response matrices for each individual source, camera and observation.

⁴<http://xmm.esac.esa.int/xsa/>

⁵<http://xmm.esac.esa.int/sas/8.0.0/>

⁶The time intervals when the count rate was > 0.35 cts/s in the MOS camera images and > 0.40 cts/s in pn camera images were removed.

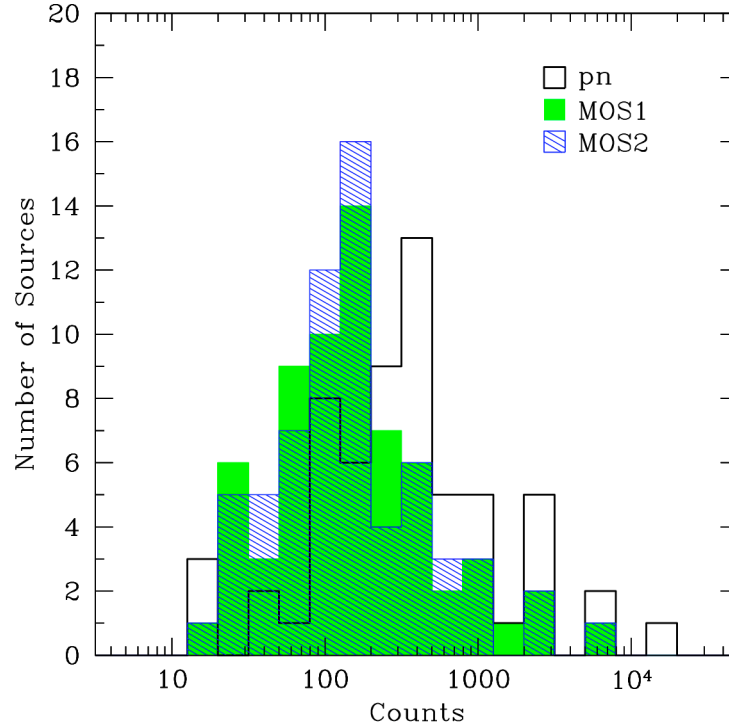


Figure 5.5: Count distribution of the 3 EPIC cameras for our sample objects in the 0.2-12 keV energy band: pn (black), MOS1 (green), MOS2 (blue). The 3 distributions peak between 100-400 counts; about 13% of the objects have pn counts below 70.

For the objects detected in the SDS-1, SDS-3 and SDS-4 fields, which have two observations per field, and for the sources lying in the overlapping areas between two fields (see Sect. 5.2.2), multiple spectra have been extracted. In order to obtain better signal to noise spectra, we co-added the multiple spectra of the same source, the corresponding background spectra and response matrices, for each EPIC camera separately, using appropriate weightings (see Sect. 3.6.1). It was possible to apply this procedure to half of the sample sources. The count distribution of the sample objects is shown in Fig. 5.5. Despite the stacking process applied, two of the sources were detected with only 30 total net counts (0.2 – 12 keV) and therefore the spectral fit was not possible for these objects.

The spectra were then binned with a minimum of 15 net (background-subtracted) counts per bin and the χ^2 statistic was used during the fitting process. For the sources detected with less than 100 total counts, the spectra were grouped with a minimum of 10 cts/bin and both the χ^2 and the C statistics were used in order to test the goodness of the fit and to obtain the best-fit parameters.

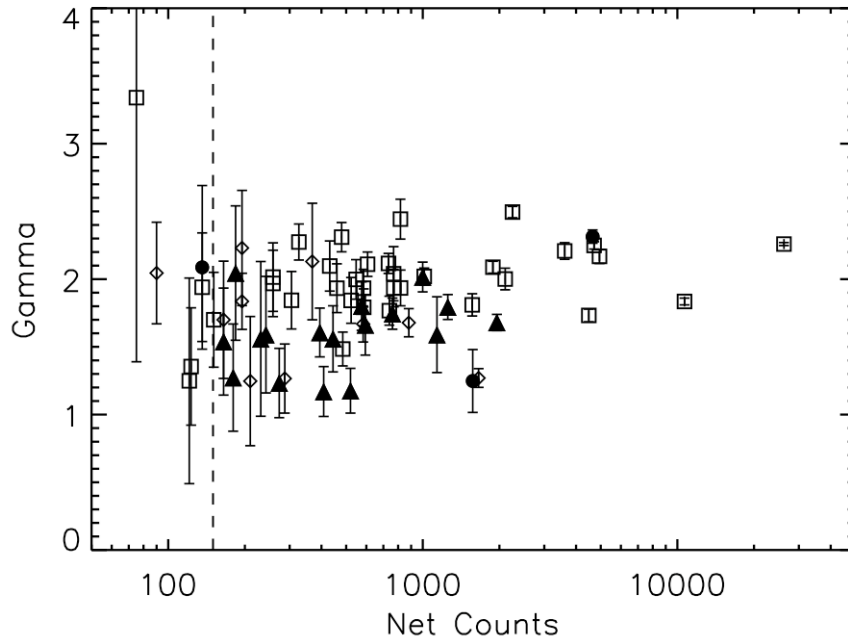


Figure 5.6: Spectral slope Γ obtained from the initial spectral fit of MOD1 as a function of the net counts (0.2 – 12 keV, pn + MOS1 + MOS2). In the plot the optical classification of the objects is indicated: broad line AGN (open squares), narrow line AGN (filled triangles), absorption line galaxies (filled circles). The unidentified sources are represented by open diamonds. The dashed line indicates the limit of 150 counts, below which the source spectral index was subsequently fixed at $\Gamma = 1.9$ (see text).

5.4.2 Spectral fitting

The spectral fitting analysis was performed using XSPEC v11.3.2⁷. We started with a baseline model (MOD1) composed of a power-law modified by photoelectric absorption due to Galactic and intrinsic hydrogen column densities ($N_{\text{H}}^{\text{Gal}}$ and N_{H} respectively), of the form:

$$F(E) = e^{-\sigma(E)N_{\text{H}}^{\text{Gal}}} [Ae^{-\sigma(E(1+z))N_{\text{H},z}} E(1+z)^{-\Gamma}] \quad (5.1)$$

The XSPEC components used to describe this model are `wabs` \times `zwabs` \times `zpowerlw`. The Galactic absorption was fixed to an average value for the SXDS field of $N_{\text{H}}^{\text{Gal}} = 3 \times 10^{20} \text{ cm}^{-2}$ (e.g. Dickey & Lockman 1990), while all the other parameters were left free. The spectral fit was performed in the observed energy range 0.3-10 keV. For each source the redshift was fixed to the value obtained from the optical spectra and for the 12 sources with no optical identification the model was tested with redshift $z = 0$. We note

⁷<http://xspec.gsfc.nasa.gov/>

that the estimated N_{H} in these cases is, in fact, a lower limit as higher redshifts for the absorbed power-law will lead to higher absorption: indeed, the rest-frame column density is related to the observed $N_{\text{H}}(z = 0)$ as $N_{\text{H},z} \approx (1 + z)^{2.6} N_{\text{H},z=0}$ (Alexander et al. 2003).

In Figure 5.6 the power-law slopes (Γ) obtained from the fitting of MOD1 are reported as a function of the net counts. We note that the uncertainties in the spectral slope (estimated at a 90% confidence level) increase significantly when the count statistics decreases, therefore for spectra with the number of counts below 150 we fixed the spectral index to $\Gamma = 1.9$, a typical value for AGN (Reeves & Turner 2000; Mainieri et al. 2002; Caccianiga et al. 2004; Mateos et al. 2005b). In some cases though, the large errors on Γ may indicate the need of additional components to correctly reproduce the source spectrum. In fact, although the average spectral index for the sample appears to be $\Gamma = 1.9 - 2.0$, as expected for typical unabsorbed AGN, there is a large scatter in the Γ distribution. In particular, objects classified as NL AGN in the optical have typically flatter spectra compared to the BL AGN. This effect may be due to the presence of a scattering component at low energies, or to absorption that is not properly modelled (see Sect. 3.6.2), and/or the Compton reflection component (at energies above 10 keV, rest-frame; see Sects. 1.1.2 and 3.6.2).

About 79% of the sample sources show an acceptable fit to the absorbed power-law model (MOD1); in many cases the intrinsic column density converged to $N_{\text{H}} = 0$ during the fit, showing no need of the intrinsic absorption component. For these unabsorbed objects, an upperlimit for the intrinsic column density was estimated. We considered an object to be X-ray absorbed when $N_{\text{H}} \geq 4 \times 10^{21} \text{ cm}^{-2}$ (see Sect. 3.6.2; e.g. Caccianiga et al. 2008). We note that the column density upperlimits estimated for some sources exceed the chosen N_{H} threshold; these sources are considered unabsorbed, as the N_{H} is unconstrained.

We note that some of the fitting results obtained from MOD1 have low null hypothesis probability (below 1%). For each source the results obtained were carefully checked and further models were tested, in order to obtain the best-fit model of the source spectra. The significance of each component added to the baseline model was tested using the F -test and a confidence level of 95%. In Table A2.1 (Appendix 2) the best-fit model parameters

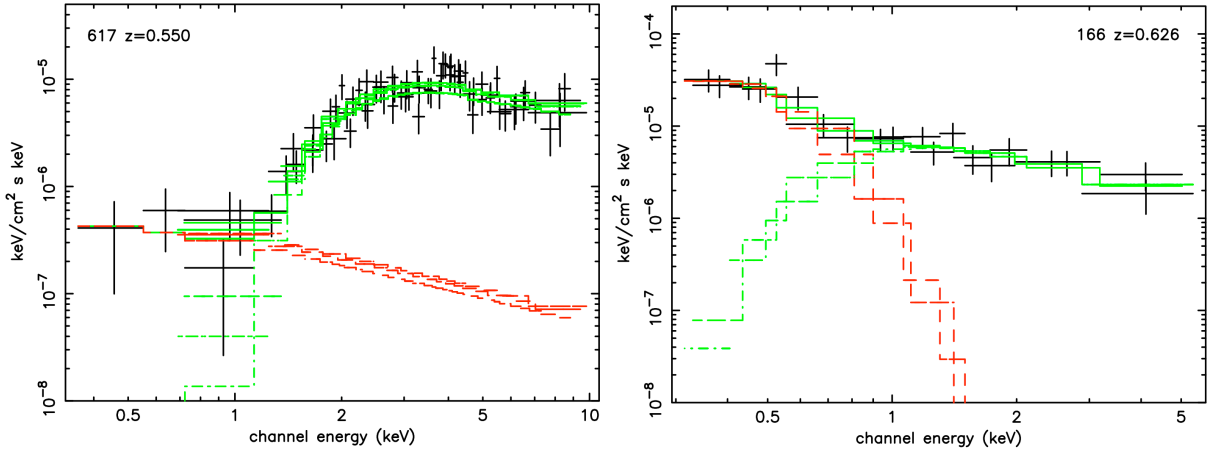


Figure 5.7: Unfolded spectra of two of the sources showing a soft excess below 2 keV: the source SXDS 0617 is modelled with the MOD2 model (left); SXDS 0166 is modelled with an absorbed power-law and a black-body component (MOD3, right).

for each source are reported; the errors were estimated at 90% confidence level.

For the sources with flat spectral index ($\Gamma < 1.5$) the MOD1 has been tested also fixing the spectral index to $\Gamma = 1.9$ (Mainieri et al. 2002; Caccianiga et al. 2004; Mateos et al. 2005b) in order to verify whether an additional component was needed; all the sources showed significant excess of counts compared to the model in the soft band (below 2 keV), therefore further spectral components were tested to obtain the best-fit of the spectra.

5.4.3 Soft Excess

To verify the presence of the soft excess in our source spectra, especially in those showing significant residuals below 2 keV, we defined a new model adding to the MOD1 components a second power-law with the same spectral index as the primary power-law (MOD2: $wabs \times (zpowerlw + zwabs \times zpowerlw)$). This model will provide a good parameterisation if the observed residuals are due to reprocessed emission scattered along the line of sight by photoionised gas.

The same model was tested also with the two power-law slopes free to vary ($\Gamma_1 \neq \Gamma_2$): this test was done to investigate whether the observed soft excess required a steeper component to be modelled; in this case, the soft excess may be due to atomic processes from relativistic, partially ionised material in the circumnuclear region (warm absorber), or photoionised emission in the accretion disc (see Sect. 1.1.2).

Table 5.1: Spectral parameters of the black-body component (MOD3).

ID	Γ	N_{H} (10^{21} cm^{-2})	kT (eV)	Redshift	Class
SXDS 0707	$1.95^{+0.05}_{-0.04}$	<0.16	177^{+12}_{-17}	0.714	BL
SXDS 0817	$2.11^{+0.13}_{-0.14}$	<19.10	211^{+45}_{-44}	1.400	BL
SXDS 1240	$1.90^{+0.15}_{-0.12}$	<2.63	134^{+22}_{-19}	0.252	BL
SXDS 0166	$2.17^{+0.99}_{-0.69}$	<20.70	145^{+37}_{-28}	0.626	BL
SXDS 0185	$1.83^{+0.09}_{-0.10}$	<0.10	199^{+25}_{-22}	0.875	BL

MOD2 provided a better fit for 19% of the sources (13 objects), based on F -test probability results, both with $\Gamma_1 = \Gamma_2$ and with $\Gamma_1 \neq \Gamma_2$. However, it was difficult to distinguish between the two models based on the statistics obtained, which gave similar results in the two cases. Nevertheless, four of the 13 sources (SXDS 0774, SXDS 0617, SXDS 0457 and SXDS 1156) show evidence of significant photoelectric absorption and therefore we consider scattering is more likely to be responsible for the soft excess in these cases (Fig 5.7, left). The spectral parameters are reported in Table A2.1, in Appendix 2. The other nine sources are unabsorbed, thus for them, the soft excess is more likely to be due to the emission from the accretion disc, or to a warm absorber.

We tested the spectral fit of the latter group of sources (nine unabsorbed objects) with a new model (MOD3) which includes a redshifted black-body component added to the baseline model: the XSPEC models used for the fitting are `wabs*(zbody+zwabs*zpowerlw)`. MOD3 improved significantly the χ^2 in five cases so this model was accepted as the best-fit model (Fig. 5.7, right), while in the remaining four spectra MOD3 was rejected and MOD1 (the baseline model) was accepted as best-fit model. The results of the fitting of MOD3 are summarised in Table 5.1 (the power-law parameters together with the χ^2 are reported also in Table A2.1, in Appendix 2).

The average black-body temperature obtained for our sources is $\langle kT \rangle = 173 \pm 13$ eV. This value is higher than the typical temperatures found for the black-body component in similar samples ($kT \approx 100$ eV; e.g. Mainieri et al. 2007; Mateos et al. 2005b); never-

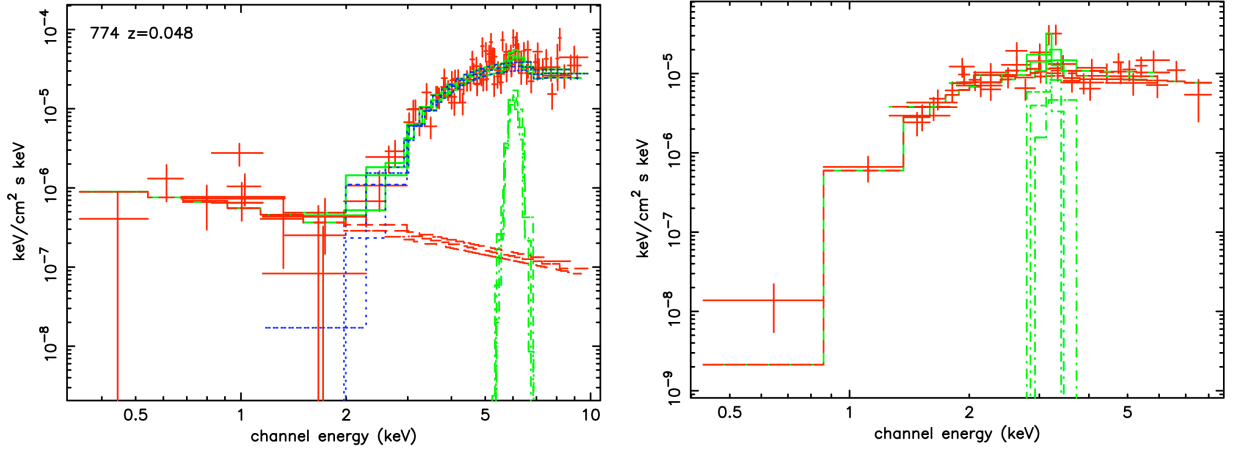


Figure 5.8: Unfolded spectra of two of the sources (four in total) where the Fe $K\alpha$ emission line at 6.4 keV (rest-frame) was observed. Here the parameters of the Gaussian component (central energy and width of the line) are left free to vary.

theless it is consistent with the typical values found for the AGN soft excess component ($T \sim 0.1 - 0.2$ keV; e.g. Crummy et al. 2006; Done & Nayakshin 2007), supporting the hypothesis that atomic processes are involved in producing this soft emission. We note however that more complex processes may be involved in producing the soft excess (e.g. a combination of scattering and thermal emission, partial covering, etc.). However, testing more complex models is not realistic considering the quality of our data and it would be difficult to choose between the different interpretations.

5.4.4 Iron $K\alpha$ line

A significant feature in the residuals of four source spectra (SXDS 0774, SXDS 0617, SXDS 0590 and SXDS 0338) was observed at energies corresponding to the redshifted Fe $K\alpha$ emission line (6.4 keV rest-frame). For these sources a Gaussian component (`zgauss`) was added to their best-fit models in order to reproduce the emission feature. For all the sources the fit was performed: i) fixing the energy at 6.4 keV with the line width left free to vary and ii) with both energy and line width as free parameters (Fig. 5.8). The results of the line fitting are reported in Table 5.2. In parentheses we give the parameters obtained with the energy $E = 6.4$ keV (rest-frame) fixed. From the spectral analysis we obtained line widths which are rather broader compared to the typical values measured for the Fe $K\alpha$ line from high-resolution spectroscopy ($\sigma = 30 - 50$ eV, e.g. Yaqoob &

Table 5.2: Parameters of the Fe $K\alpha$ emission line obtained from the spectral fitting of a Gaussian component added to the best-fit model of each spectrum.

ID	z	Energy (keV)	σ (keV)	EW (eV)	Model	N_{H}^a	Class
SXDS 0774	0.048	$6.34^{+0.13}_{-0.16}$	$0.18^{+0.24}_{-0.14}$ ($0.10^{+0.24}_{-0.10}$) ^b	235^{+157}_{-157} (175^{+194}_{-107})	MOD2	$22.44^{+3.95}_{-3.62}$	ABS
SXDS 0617	0.550	$6.29^{+0.21}_{-0.20}$	$0.33^{+0.23}_{-0.19}$ ($0.34^{+0.24}_{-0.14}$)	415^{+231}_{-210} (413^{+229}_{-214})	MOD2	$9.64^{+2.23}_{-1.99}$	NL
SXDS 0590	0.986	$6.32^{+0.10}_{-0.10}$	$0.09^{+0.18}_{-0.09}$ ($0.08^{+0.30}_{-0.08}$)	333^{+179}_{-170} (272^{+163}_{-146})	MOD1	$11.34^{+3.52}_{-1.92}$	NL
SXDS 0338	1.739	$6.01^{+0.57}_{-0.47}$	$0.23^{+0.73}_{-0.23}$ ($0.50^{+1.26}_{-0.50}$)	257^{+318}_{-174} (315^{+456}_{-157})	MOD1	$0.57^{+0.52}_{-0.40}$	BL

Notes: a) Expressed in unit of 10^{22} cm^{-2} ; b) The values in parenthesis were obtained fixing the line centroid to $E = 6.4$ keV (rest-frame).

Padmanabhan 2004). This was not unexpected as such narrow lines are unresolved in the EPIC camera data. The equivalent width of the lines (reported in table 5.2) are higher than expected for the measured N_{H} of the sources (Turner et al. 1998). Therefore in order to measure the actual strength of the narrow Fe line, we fixed the line width to $\sigma = 50$ eV. We obtained $\text{EW} = 191^{+56}_{-143}$ eV for SXDS 0774, $\text{EW} = 276^{+63}_{-202}$ eV for SXDS 0617, $\text{EW} = 215^{+136}_{-163}$ eV for SXDS 0590, $\text{EW} = 271^{+163}_{-208}$ eV for SXDS 0338 (rest-frame); these values are in agreement with the expectations for absorbed (Compton thin) objects (e.g. Turner et al. 1998).

We note that for SXDS 0338, which has the lowest signal-to-noise spectrum amongst the four (586 net counts, 0.2-12 keV), the line parameters are still not well constrained and the line centroid moved to $E \approx 5.9$ keV. Fixing the energy at $E = 6.4$ keV gives a rather high EW upperlimit ($\text{EW} < 583$ eV), meaning that with the current data the line parameters cannot be properly constrained.

5.4.5 SXDS 0816

The source SXDS 0816, identified from the optical spectrum as a star, was not fitted with the same models used for the rest of the sample, as the emission in this case is presumably due to thermal processes. In order to fit the source spectrum we used a model composed of two thermal emission components and a power-law ($\text{wabs} \times (\text{apec} + \text{apec} + \text{power-law})$). The two temperatures obtained from the fitting are $kT_1 = 0.37 \pm 0.02$ keV and $kT_2 = 0.93 \pm 0.05$ keV respectively; the power-law slope

$\Gamma = 2.86_{-0.05}^{+0.06}$ (reported also in table A2.1). This $2T$ model is a good representation of the data ($\chi^2/d.o.f. = 285.8/263$), with the two temperatures obtained in good agreement with the values found in the literature (e.g. López-Santiago et al. 2007, and references therein).

As the aims of our analysis are studying the properties of the AGN population in the SXDS field, this object was excluded from further consideration.

5.5 Sample Properties

In summary, at the end of the detailed spectral analysis, we found that an absorbed power-law model (MOD1) represents the best-fit model for 82% of the source spectra, with hydrogen column density in the range $N_{\text{H}} = 10^{20} - 2 \times 10^{23} \text{ cm}^{-2}$; 6% of the sample spectra are better reproduced by an absorbed power-law with a scattering component (MOD2) and in 7% of the spectra a black-body component provided a better fit of the soft spectrum (MOD3, Table 5.1).

In all the models used in this analysis, the spectral index (Γ) and the hydrogen column density (N_{H}) were free parameters (except for the six sources with number of net counts below 150, see Sect. 5.4.2). The results of the spectral analysis are shown in Figure 5.9. The spectral slopes of the sample are distributed around the value $\Gamma \approx 1.9$, with a large dispersion at high N_{H} . The weighted mean of the spectral index is $\langle \Gamma \rangle = 1.92 \pm 0.02$, which is consistent with the values found in similar surveys and in deeper surveys (e.g. Perola et al. 2004; Page et al. 2006; Mainieri et al. 2007). We calculated also the weighted mean of the spectral index taking into account the optical classification of the sources, i.e. for BL AGN (type-1 objects) and for NL AGN (type-2 objects; see Sect. 3.5.4) separately; we obtained $\langle \Gamma \rangle = 1.94 \pm 0.02$ and $\langle \Gamma \rangle = 1.71 \pm 0.07$, respectively. The $\langle \Gamma \rangle$ measured for type-2 AGN is flatter than that of type-1 AGN. We note that this is probably not an intrinsic property of obscured AGN, but is likely to be an observational effect: if the signature of absorption is not very significant in the X-ray spectra, the measured N_{H} will tend to be underestimated (see Mateos et al. 2005a) and the resulting Γ will be flatter. This effect is more evident in NL AGN as the fraction of X-ray absorbed objects is higher than in

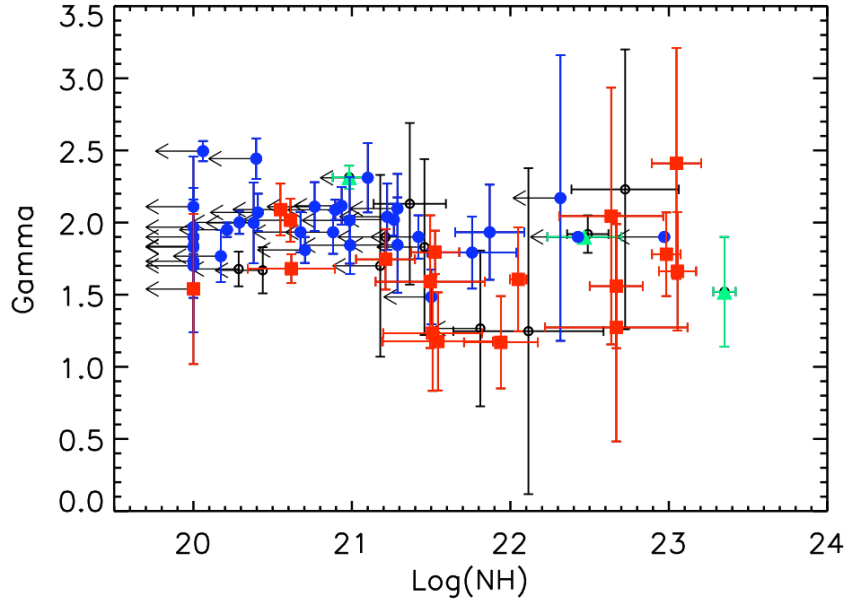


Figure 5.9: Intrinsic absorption $\log(N_{\text{H}})$ vs. Γ resulting from the best-fit model for all the sources. The optical classification of the sources is also shown: BL AGN (blue circles); NL AGN (red squares); absorption line galaxies (green triangles); the black open circles are the unidentified sources; for these sources the observed N_{H} ($z = 0$) was plotted.

BL AGN (see below). In fact, flatter values of Γ for type-2 objects are reported also in previous studies (e.g. Mateos et al. 2005b; Mainieri et al. 2007).

Objects showing significant X-ray absorption ($N_{\text{H}} \geq 4 \times 10^{21} \text{ cm}^{-2}$) are about 22% of the sample (15 objects; Fig. 5.9). The hydrogen column density measured for these sources ranges between $N_{\text{H}} = 4 \times 10^{21} - 2 \times 10^{23} \text{ cm}^{-2}$, indicating that all the absorbed objects in our sample are Compton-thin AGN⁸. Three sources showing column densities very close to our “separation” value ($N_{\text{H}} = 4 \times 10^{21} \text{ cm}^{-2}$) have been considered as absorbed AGN; this increased their fraction to 26%.

The majority of the sources with significant X-ray absorption also show obscuration in the optical band (NL AGN): amongst the absorbed objects, eleven are classified as NL AGN, two as BL AGN, two are absorption line galaxies and the remainder (3 sources) are unidentified.

Amongst the optically unidentified sources (18% of the sample) the range of column

⁸We found no cases where the X-ray absorption was $N_{\text{H}} \geq 10^{24} \text{ cm}^{-2}$, typical for Compton-thick objects.

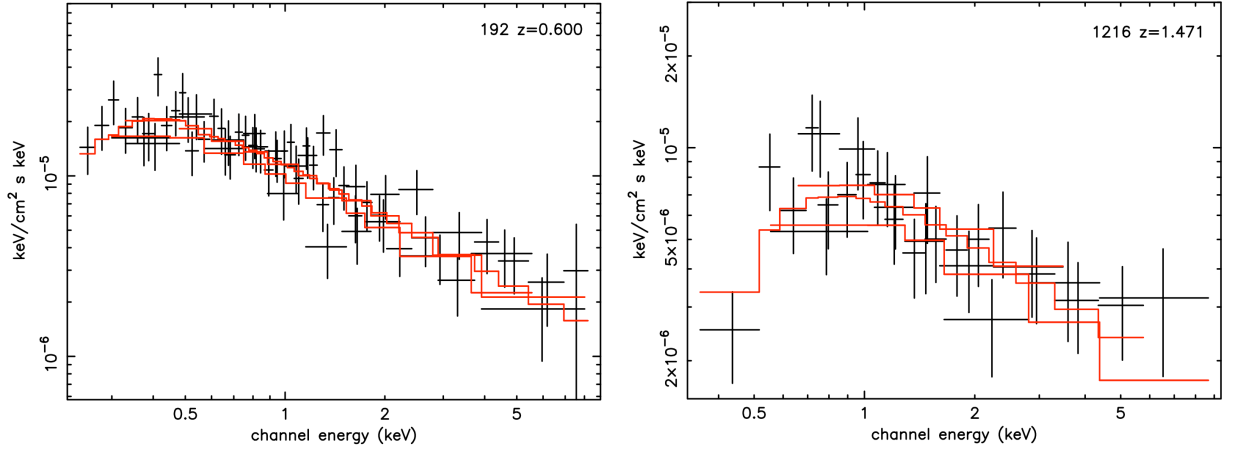


Figure 5.10: Unfolded spectra of two objects with conflicting classification between the optical and X-ray band: a NL AGN with low hydrogen column density $N_{\text{H}} < 4.1 \times 10^{20} \text{ cm}^{-2}$ (left) and a BL AGN which shows the signature of significant absorption $N_{\text{H}} = 7.4_{-3.8}^{+4.8} \times 10^{21} \text{ cm}^{-2}$ (right).

density measured is rather wide. However, for these sources the N_{H} is underestimated since their redshift is unknown (we considered $z = 0$ in the fitting process, see Sect. 5.4.2); we note that if all the sources were at high redshift ($z \gtrsim 1$), their column density may reach the $N_{\text{H}} > 4 \times 10^{21} \text{ cm}^{-2}$ threshold for absorbed AGN (see Sect. 5.4.2), therefore the fraction of unidentified sources is very likely to introduce some bias toward unabsorbed objects in the current spectroscopically identified sample.

5.5.1 Comparison between optical and X-ray classification

According to the unification scheme (Antonucci 1993; see Sect. 1.2), where the differences observed in type-1 and type-2 AGN are only due to the inclination of the objects with respect to the line of sight (see Chapter 1), we may expect obscured objects in the optical band to be also absorbed in the X-rays and the unobscured objects (BL AGN) not to show absorption in the X-ray band. Overall this scenario appears to be correct for a large fraction of the AGN population, although a number of outliers ($\sim 10\text{-}30\%$) have typically been observed in AGN population studies (e.g. Panessa & Bassani 2002; Mateos et al. 2005b; Mainieri et al. 2007; see also Sect. 3.7.1).

In our sample we found 9% (6 objects) of the sources identified as NL AGN with no evidence of significant X-ray absorption (Fig. 5.10, left). Considering the upperlimit of the

column density measured for these sources, only one is close to the range of the absorbed AGN (see above). A possible explanation for these results is that the spectra have not enough signal to noise to allow the correct parameterisation of the spectral slope (e.g. the presence of a soft excess) and hence to detect the signature of X-ray absorption. This may be the case for one of our sources, which has a low count spectrum (total net counts = 165); the other sources, however, have sufficient statistics to provide a satisfactory measurement of the spectral parameters.

Other possibilities to explain the low column density and the lack of broad lines in the optical spectra are: i) spectral variability (see Sect. 3.7.1); ii) obscuration not due to the putative pc-scale molecular torus predicted by the unification models (Antonucci 1993), but residing at larger scales: in this scenario, the broad line regions may be obscured by clouds of dusty material that affect more efficiently the optical emission than the X-ray emission (high dust-to-gas ratio, e.g. dust lanes or HII regions; Panessa & Bassani 2002); iii) weak or absent BLR in these objects (Hawkins 2004; Panessa et al. 2009): in this case no absorbing material is required and the sources are truly not absorbed (see Sect. 3.7.1).

In our sample we also found two broad line AGN (optically unobscured) with high X-ray absorption (3%; see Fig. 5.10, right), although we note that the N_{H} estimated for these sources is lower than in type-2 AGN. In these cases the disagreement between the optical and the X-ray classification may be due to a lower dust-to-gas ratio compared to the typical Galactic value ($A_V/N_{\text{H}} = 1/1.8 \times 10^{21}$; e.g., Predehl & Schmitt 1995), which has often been observed in AGN (see Sects. 3.7.1 and 4.3).

5.5.2 Redshift and luminosity distribution

Using the best-fit parameters obtained, we corrected the X-ray luminosity of each source for intrinsic absorption. The corrected X-ray luminosity in the 2 – 10 keV energy band (rest-frame) as a function of the redshift is plotted in Figure 5.11 (left). At each redshift, the luminosity distributions of unabsorbed and absorbed AGN are very similar, with no evidence for the absorbed sources to be intrinsically less luminous than the unabsorbed

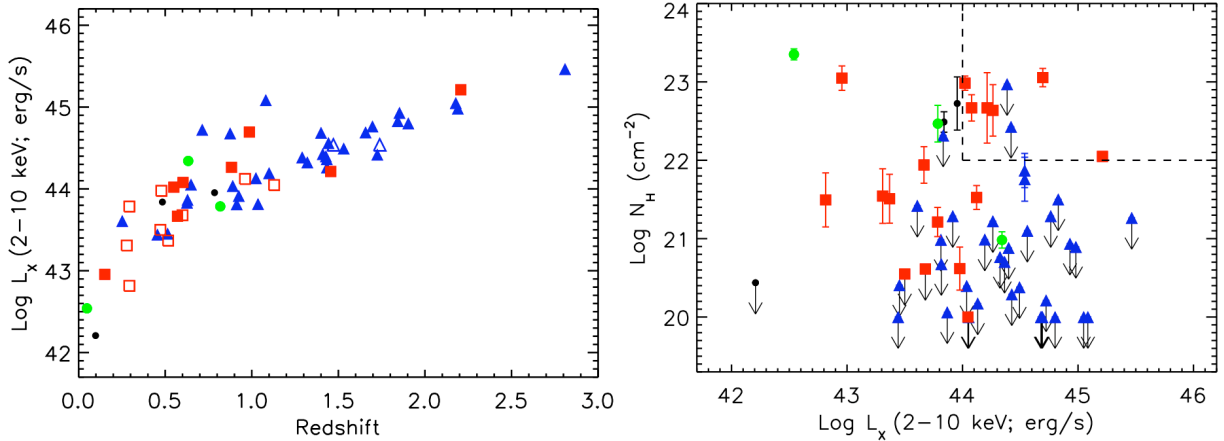


Figure 5.11: Left: X-ray luminosity (2–10 keV, unabsorbed) as a function of redshift for our sample sources (87% with known redshift). The different classification of the sources is shown: BL unabsorbed AGN (type-1 AGN; filled triangles); BL absorbed AGN (open triangles); NL absorbed AGN (type-2 AGN; filled squares); NL unabsorbed AGN (open squares); absorption line galaxies (filled green circles); unclassified objects (black dots). Right: X-ray luminosity vs intrinsic hydrogen column density for all the sample objects; the symbols used are the same as in the figure on the left. On the upper right corner of the plot the parameter space occupied by the type-2 QSO is marked ($L_X \geq 10^{44}$ erg s $^{-1}$ and $N_H \geq 10^{22}$ cm $^{-2}$).

ones. However, the unabsorbed type-1 AGN are sampled up to higher redshift ($z = 2.8$, see Sect. 5.3) than the absorbed ones ($z = 2.2$). For all sources the luminosities range from $L_X = 10^{42} - 5 \times 10^{45}$ erg s $^{-1}$, which are typical for AGN ($L_X > 10^{42}$ erg s $^{-1}$). In particular, the three sources identified in the optical as absorption line galaxies also have $L_X > 10^{42}$ erg s $^{-1}$, clearly indicating the presence of nuclear activity; therefore we considered them as AGN. We note that two of them have high column densities in their X-ray spectra (Fig. 5.11, right) and therefore the lack of AGN signatures in the optical spectra (broad or narrow emission lines) may be due to high obscuration of the nucleus, whose emission is diluted by a bright (large) host galaxy (with $M_R \leq M^*$, where M is the absolute magnitude; Severgnini et al. 2003). Indeed, this is the case for SXDS 0774 (one of the “absorption line galaxies” in our sample; see also Fig. 5.7), which is identified in the literature as a Sy 2 galaxy (Severgnini et al. 2003). Another possibility for the lack of nuclear features in the optical spectra is that these sources may in fact be BL Lacs, where the non-thermal emission from the relativistic jets dominates the spectrum (see Sects. 1.1.2 and 1.1.3).

More than a half of our sample sources (53%) have luminosity $L_X > 10^{44}$ erg s⁻¹, typical for QSOs. Six of the sources (9% of the total sample) with such high luminosity show also significant intrinsic absorption ($N_H > 10^{22}$ cm⁻²; Fig. 5.11, right). In the optical they are identified as narrow line AGN and therefore they can be classified as type-2 QSOs, with redshift $z = 0.55 - 2.21$.

5.6 The high f_X/f_{opt} sources

Another important diagnostic to understand the properties of the sample is the f_X/f_{opt} ratio. A non-negligible fraction ($\sim 10 - 20\%$; e.g. Fiore et al. 2003; Barcons et al. 2007) of the AGN population is found to have $f_X/f_{\text{opt}} > 10$ (2 – 10 keV; see Sects. 1.4, 2.4, 3.2) and the majority of them are expected to be type-2 QSO at high redshift ($z > 1$; e.g. Fiore et al. 2003; Comastri & Fiore 2004). The f_X/f_{opt} here is defined as the ratio between the observed 2 – 10 keV flux and the Subaru R band flux (see Chapter 1). The f_X/f_{opt} distribution of our sample objects is shown in Figure 5.12 (left). The majority of the sources have $0.1 < f_X/f_{\text{opt}} < 10$ as expected for typical X-ray selected AGN (Akiyama et al. 2000; Mainieri et al. 2002), with the obscured (narrow line) AGN having on average higher values than the unobscured (BL) objects. Nine objects (13%) have high X-ray-to-optical flux ratio ($f_X/f_{\text{opt}} > 10$). This fraction is in agreement with the expectations from previous population studies of AGN (e.g. Fiore et al. 2003; Civano et al. 2005; Barcons et al. 2007). Amongst the high f_X/f_{opt} sources, there are four type-2 AGN, a type-1 AGN and the remainder are unidentified sources. We note that all the sources with high X-ray-to-optical flux ratio show the signature of large photoelectric absorption in their X-ray spectra: the BL AGN with high f_X/f_{opt} is, in fact, one of the two sources with significant absorption (see Sect. 5.5.1), confirming that the f_X/f_{opt} is an effective way to select bright absorbed objects and hence type-2 QSO candidates. The four high X-ray-to-optical flux ratio sources classified as NL AGN are indeed type-2 QSO.

We also analysed the optical/NIR colour ($R - K$) of the sample, shown in Figure 5.12 (right). The computation of the colour was possible only for 69% of the sample, as the

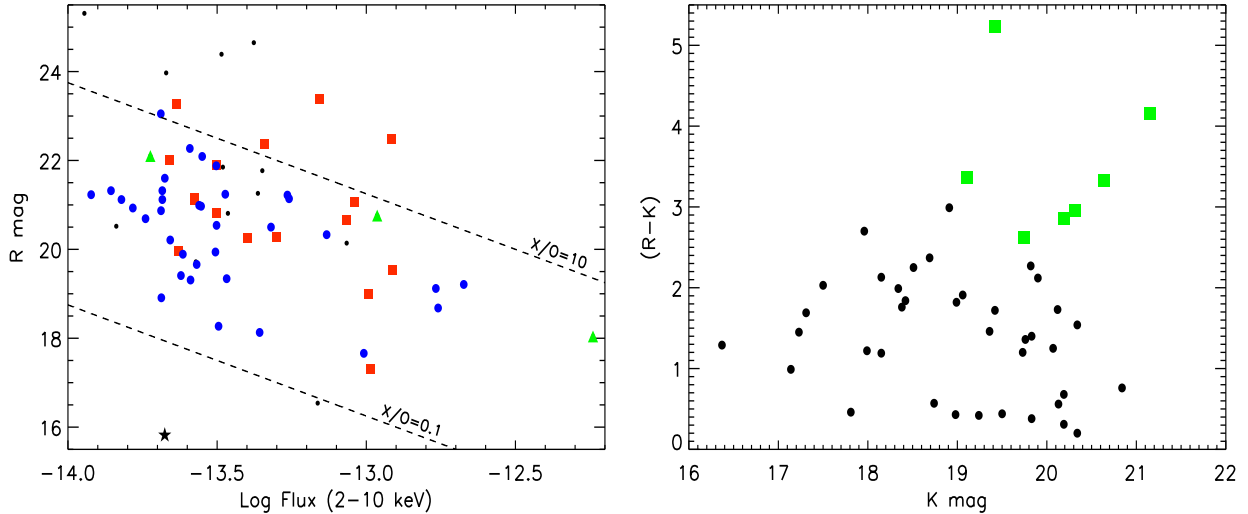


Figure 5.12: (Left): X-ray flux (2 – 10 keV) vs R magnitude plot. The blue circles are the BL AGN, the red squares are the NL AGN and the green triangles are the absorption line sources. The black dots are the sources without an optical spectroscopic identification and the black star is the source classified as star. (Right): K magnitude vs. $R - K$. The green squares are the sources with high f_X/f_{opt} amongst the sample. They show redder optical/NIR colours than the rest of the sample and the $(R - K)$ value for the high f_X/f_{opt} sources is typical of EROs ($R - K > 3.2$, AB).

K -band magnitude was not available for all the sample sources (the NIR data cover 0.77 deg² of the whole SXDS field; see Sect. 5.2). The objects with high f_X/f_{opt} have also the reddest $R-K$ colours of the rest of the sample, with values typical for EROs ($R-K > 3.2$, AB magnitude) in most of the cases. This result confirms there is a connection between X-ray absorption and optical obscuration, although this connection is not straightforward as in the X-ray we observe the nuclear emission of the AGN, while in the optical band we observe a combination of AGN and host galaxy light (see Sect. 1.4).

5.7 Luminosity dependence of the fraction of type 2 AGN

Understanding the contribution of the absorbed AGN to the AGN population and how their fraction⁹ (F) varies with luminosity and redshift is a very important issue, in order to understand the cosmological evolution of AGN. Current results on this matter are controversial. An anti-correlation between the fraction of absorbed sources and the X-ray lumi-

⁹ F is defined as the number of absorbed AGN over the total, absorbed and unabsorbed, population.

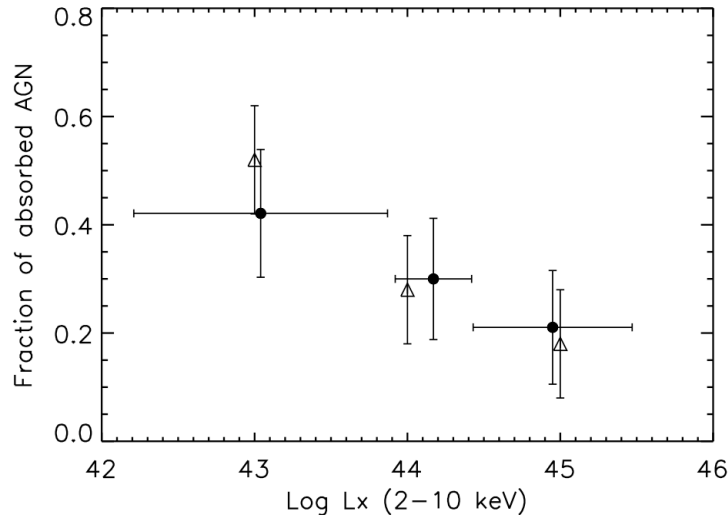


Figure 5.13: Fraction of absorbed AGN as a function of luminosity in the 2 – 10 keV band. The filled circles are the fraction estimated from our sample. The open triangles are the fraction of absorbed AGN obtained integrating the luminosity function of the HBSS by Della Ceca et al. (2008), plotted for comparison.

osity was initially suggested by Lawrence & Elvis (1982) and at present, several studies have found this correlation (e.g. Ueda et al. 2003; Gilli et al. 2007; Hasinger 2008; Della Ceca et al. 2008), while other studies seem to find also that F increases with redshift (e.g. La Franca et al. 2005; Treister & Urry 2006). It is not yet clear however, whether these correlations are real or due to observational and selection effects (Dwelly & Page 2006). Nevertheless, these findings suggest that the simple unified model (Antonucci 1993) for AGN is not sufficient to explain the observed fraction of absorbed AGN and that a different evolution is expected for objects at different luminosities (see Chapter 1).

Here we investigate the relation between F and L_X in our SXDS sample sources. Figure 5.13 shows the X-ray absorbed source fraction versus the X-ray luminosity (unabsorbed, in the 2 – 10 keV rest-frame). We grouped the sources in three different luminosity bins, each bin having approximately the same number of total sources (absorbed + unabsorbed) so that they have the same statistical significance. The three bins are centred at $L_X = 1.1 \times 10^{43} \text{ erg s}^{-1}$, $L_X = 1.5 \times 10^{44} \text{ erg s}^{-1}$ and $L_X = 8.9 \times 10^{44} \text{ erg s}^{-1}$ and the fraction of absorbed AGN in each bin is 8/19, 6/20 and 4/19, respectively.

In agreement with several previous studies, we found that the fraction of absorbed AGN decreases with increasing luminosity. Although our correlation appears to be slightly

flatter than that found e.g. in Della Ceca et al. (2008) (in particular, in our sample we detected a lower number of absorbed AGN in the lower luminosity bin), the results are consistent within the uncertainties. We note that amongst our sample sources lying in the lower luminosity bin, there are a larger number of low signal to noise spectra. A possible explanation for the lack of absorbed AGN in the low luminosity bin is that for these objects the spectral analysis may have failed to constrain the real slope of the spectrum (e.g. the presence of a soft component) and hence to constrain the intrinsic absorption, yielding to an incorrect classification as unabsorbed objects.

It is important to note that our values are not corrected for the selection effects due to intrinsic absorption: since the luminosity of the absorbed sources is depressed by the photoelectric absorption, we are able to detect absorbed sources within a smaller volume compared to unabsorbed AGN. In fact, as shown also in Fig. 5.11, our sample is biased toward unabsorbed AGN at high redshift (and hence at high luminosity). However, as the luminosity dependence of the absorbed fraction observed for our sources is in good agreement with the one found by Della Ceca et al. (2008), which is corrected for the selection biases due to intrinsic absorption, we expect these bias corrections to be small. Our results support the scenario of a different evolution of AGN at different luminosities.

5.8 The mean Fe $K\alpha$ line

The Fe $K\alpha$ emission line is the most prominent feature in the X-ray spectra of AGN and it appears to be a common characteristic for all AGN (Yaqoob & Padmanabhan 2004; Nandra 2006; Fabian 2006). This emission line is produced in the central region of AGN, plausibly in the accretion disc, the broad line region (BLR) and/or the circumnuclear obscuring torus. A straightforward way to unambiguously determine the origin of this emission line is measuring the line profile, which is strongly dependent on the distance from the central BH, inclination and properties of the emitter (ionisation state, velocity, etc.; Nandra 2006; Yaqoob et al. 2010). However, recent observations have revealed that the Fe $K\alpha$ line is likely formed by two different components: i) a narrow “core”, which is ubiquitous in all AGN, whose centroid is always observed at $E \sim 6.4$ keV, implying an origin in cold, neu-

tral matter (e.g. Sulentic et al. 1998; Yaqoob & Padmanabhan 2004; Nandra 2006) and ii) a broad redshifted component, presumably originating in a relativistic accretion disc (e.g. Fabian et al. 2002; Fabian 2006). However, the presence of this second component in all AGN has been largely debated (e.g. Reeves et al. 2004; Turner et al. 2005), as its detection is difficult and sometimes ambiguous (e.g. Bianchi et al. 2004; Nandra et al. 2005).

Many studies have addressed the properties of the Fe $K\alpha$ emission line and its origin, especially focusing on bright local objects (e.g. Yaqoob & Padmanabhan 2004; Fabian 2006; Nandra et al. 2007), where the available data quality often allow a good characterisation of the line profiles. On the other hand, this emission feature is poorly constrained in fainter, high redshift objects, due to the limited statistics of the data and only a few studies have been attempted to date in order to properly measure the average line properties, understand the importance of the line amongst the AGN population (Streblyanska et al. 2005; Corral et al. 2008; Krumpke et al. 2008) and the average contribution of the Fe line to the X-ray background (e.g. Brusa et al. 2005).

We attempted here to perform an analysis of the average Fe $K\alpha$ line profile in our sample. As our sample has a high spectroscopic identification fraction ($\sim 90\%$), we were able to analyse the spectra in their rest-frame in order to produce the average spectrum for AGN. For this analysis we took into account only the BL AGN, as they constitute a larger fraction of our sample and the data quality for them is better than that of the type-2 AGN. Moreover, from the spectral analysis performed, we are confident that none of the sources are affected by significant X-ray absorption in the energy range considered during the analysis (see below).

5.8.1 Averaging method

In order to obtain a mean spectrum for our AGN, the averaging method described in Corral et al. (2008) was used. As the main aim of this analysis is to characterise the Fe $K\alpha$ line, this method uses a simple arithmetic mean, which preserves the relative flux of the emission features; we note that a geometric mean would have been the appropriate choice if our main interest were to characterise the global continuum shape, as it preserves the

power-law like nature of AGN continua (e.g. Vanden Berk et al. 2001).

For our analysis, we used the spectra extracted from the pn camera only (see Sec. 5.4.1), which typically have a larger number of counts, given the pn larger effective area. Moreover, merging the pn and MOS data is a complex process, which yields to large uncertainties on the resulting spectra. In total 28 sources with pn counts above 100 were used.

As we aimed to create the average *intrinsic* spectrum for type-1 AGN, the unfolded spectra of each source, i.e. the incident spectrum before reaching the detector, were obtained. For this purpose, the source spectra (grouped with a minimum of 15 counts per bin, see Sect. 5.4.1) were fitted with the baseline model described in the previous section (MOD1, see Sect. 5.4.2) using XSPEC v11.3.2. To avoid the contribution from any possible soft excess component, only energies above 1 keV rest-frame were considered (Corral et al. 2008). The model was then saved for each source and then applied to the ungrouped spectra, without fitting. The spectra thus obtained are in units of $\text{keV cm}^{-2} \text{s}^{-1} \text{keV}^{-1}$.

The second step of the process was to correct the spectra for Galactic absorption, in order to eliminate the effect of the Galactic column density ($N_{\text{H}}^{\text{Gal}}$) on the intrinsic spectra, and then to shift them to the rest-frame. The extinction model was obtained by dividing an absorbed power-law model (`wabs×powerlw`, with $N_{\text{H}} = 3 \times 10^{20} \text{ cm}^{-2}$) by a power-law. All the spectra were corrected using this extinction curve and then shifted to the rest-frame, by multiplying the energy bins in each spectrum by the factor $(1 + z)$, where z is the redshift obtained from the optical spectra (Table A2.1, in Appendix 2).

Before the stacking process, the spectra were renormalised to the flux in the 2 – 5 keV (rest-frame) energy range, as this band avoids the distortions due to the intrinsic absorption¹⁰ and any emission features (Corral et al. 2008), in order for each spectrum to

¹⁰Although only type-1 AGN, which in general have low intrinsic column density, were selected for this analysis amongst our sample, some of them may still be affected by some small amount of absorption.

have the same weight on the final average spectrum. We note that the resulting rescaled spectra preserved their spectral slopes and features, but they were normalised to have the same rest-frame flux in the 2 – 5 keV energy range.

It is important to note that shifting the spectra to the rest-frame modified the width of the energy bins, which changes with redshift. Therefore it was necessary to produce a common energy grid for all the spectra to allow the stacking process. In order to create the new energy grid, the real number of counts in each bin must be taken into account, as the newly defined bins must have enough counts to be statistically significant: in fact, if the number of counts per new bin were too low the statistics would be dominated by the errors. Since the unfolded spectra (in physical units) used up to this point did not have the information on the real counts of the sources, the spectra in counts versus energy for each source were obtained. The spectra in counts were then shifted to the rest-frame, rebinned to a common grid of narrow bins with width = 20 eV and summed all together. The narrow bins were then grouped to have a minimum of 300 real counts per each new bin, in order to obtain a more uniform distribution of the counts. With these operations we defined the new energy grid, which was then used to rebin the spectra in flux.

We defined slightly different bins compared to those used in Corral et al. (2008) because of the much smaller number of spectra available in our sample and hence the lower number of total counts; however we note the selected bins contain enough counts to still be statistically significant.

In order to create the average spectrum (in physical units) the new energy grid was applied to all the rest-framed, renormalised spectra (resulting from the first 3 steps of the process), adding them together and finally using a simple un-weighted standard mean to obtain the average. The spectra were rebinned using the following formulas from (Corral et al. 2008), which calculate the flux density in each new energy bin for each spectrum:

$$S'_j = \sum_{i \subset j} \frac{S_i \Delta \epsilon_i f_{ij}}{\Delta' \epsilon_j} \quad (5.2)$$

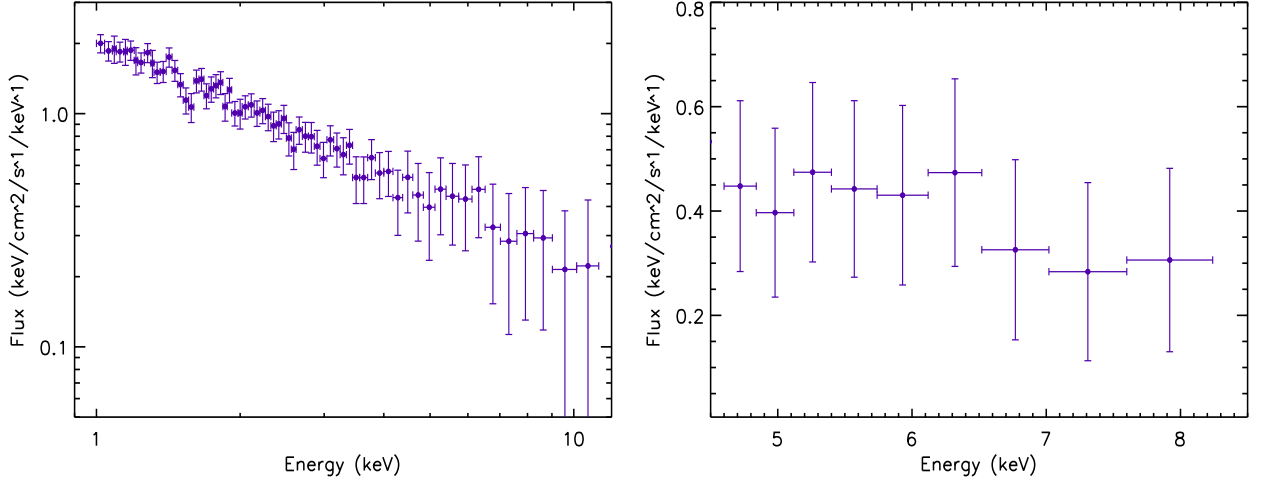


Figure 5.14: Average spectrum for the type 1 AGN in the sample (left). Zoom of the mean spectrum in the 4.5-8.5 keV energy range to show where the Fe line should be (right).

$$f_{ij} = \frac{\min(\epsilon_{imax}, \epsilon'_{jmax}) - \max(\epsilon_{imin}, \epsilon'_{jmin})}{\Delta\epsilon_i} \quad (5.3)$$

where S'_j and S_i are the flux density values expressed in $\text{keV cm}^{-2} \text{s}^{-1} \text{keV}^{-1}$ and $\Delta'\epsilon_j$ and $\Delta\epsilon_i$ are the widths (in keV) of the new and the old bins, respectively; f_{ij} is a correction factor for the possible overlap of the old bin i and the new bin j .

Finally the average spectrum was produced by adding the new flux density values S'_j of all the spectra and dividing the total by the number of spectra contributing to each bin (N_j):

$$S_j = \frac{\sum_{n=1}^N S'_j}{N_j} \quad (5.4)$$

where S_j is the average flux density value in bin j , with error (Err_j):

$$\text{Err}_j = \frac{\sqrt{\sum_{n=1}^N \sigma_j^2}}{N_j} \quad (5.5)$$

where σ_j is the error of each n spectrum in bin j .

The mean spectrum resulting from the described process is shown in Figure 5.14. Unfortunately, in our average spectrum we found no significant evidence of the Fe line emis-

sion at $E \approx 6.4$ keV; only a marginal excess of data can be seen at the energy expected for the Fe $K\alpha$ line (6.4 keV). The non-detection of the Fe $K\alpha$ line is due to the small number of spectra available for this analysis, which clearly requires much better statistics in order to be effective.

Following the analysis performed by (Corral et al. 2008), spectral simulations should be applied to construct the underlying continuum and then to characterise the emission line; nevertheless, no further analysis was performed on our average spectrum as the line feature is not significantly detected.

As the number of type-2 (NL AGN) in the sample is lower than the number of type-1, the process was not tested for this class of objects.

5.9 Conclusions

We presented in this chapter the detailed spectral analysis of a sample of 68 X-ray selected sources from the SXDS field, with $f_X \geq 2.4 \times 10^{-14}$ erg cm $^{-2}$ s $^{-1}$. The sample has spectroscopic redshift measurements for 87% of the sources; two sources have total net counts below 50, which did not allow a detailed spectral analysis, therefore the spectral fit was performed on 97% of the sample sources (66 objects). The main results of this analysis are summarised below:

- Amongst our sample we found that an absorbed power-law model gives the best-fit for 82% of the source spectra, with hydrogen column density in the range $N_H = 10^{20} - 2 \times 10^{23}$ cm $^{-2}$; 13% of the sample spectra required more complex models; 47 AGN (69%) do not show significant signature of photoelectric absorption, while 18 sources (26%) have $N_H \geq 4 \times 10^{21}$ cm $^{-2}$;
- The average spectral index for the sample is $\langle \Gamma \rangle = 1.92 \pm 0.02$, with the type-2 objects (NL AGN) having a flatter spectrum ($\langle \Gamma \rangle = 1.71 \pm 0.07$) than the type-1 (BL) AGN $\langle \Gamma \rangle = 1.94 \pm 0.02$; the lower $\langle \Gamma \rangle$ value for type-2 AGN is probably not an intrinsic property of obscured AGN, but is likely to be an observational effect: a flatter spectral index can result from an absorbed power-law spectrum when the

absorption component is not well constrained (e.g. in limited S/N spectra) and N_{H} tends to be underestimated. This affects the type-2 AGN more than the type-1 AGN as the fraction of absorbed AGN is larger than for type-1 AGN;

- There is a general correspondence between the optical and the X-ray classification of the sources, however we find 12% of conflicting classifications: these can be explained in some cases by the poor quality of the data, but other possible explanations can be offered: i) a dust-to-gas ratio different from the typical Galactic value; ii) dust obscuration residing not in the putative molecular torus, but at larger distances (e.g. in the NLR or in the host galaxy); iii) spectral variability.
- The Iron $K\alpha$ emission line at 6.4 keV (rest-frame) has been significantly detected in three sources and some indication of this emission line was found in a fourth object; the measured equivalent widths of the lines are typical for objects with the continuum depressed by high column densities $N_{\text{H}} > 6 \times 10^{21} \text{ cm}^{-2}$.
- Amongst the sample we found 6 type-2 QSOs (9% of the sample), with redshift up to $z = 2.2$; comparing this fraction with that found in the EXO sample described in Chapter 3, which has a similar flux selection to this SXDS sample, we note that the number of type-2 QSO found amongst the EXO sample is much higher ($46 \pm 8\%$, amongst the spectroscopically identified sub-sample, see Sect. 3.7.1), highlighting that the high $f_{\text{X}}/f_{\text{opt}}$ criteria is important in order to select type-2 QSO.
- 13% of the sample sources have high $f_{\text{X}}/f_{\text{opt}}$ values ($f_{\text{X}}/f_{\text{opt}} > 10$, 2 – 10 keV) and these objects also show the reddest optical/NIR colour, typical of EROs; amongst these sources there are four of the six type-2 QSOs found in our sample, confirming again that $f_{\text{X}}/f_{\text{opt}}$ is a good indicator of obscuration; we note that the fraction of high $f_{\text{X}}/f_{\text{opt}}$ sources in this sample (selected in the 2 – 10 keV energy band) is consistent with those found in other work (e.g. Fiore et al. 2003; Civano et al. 2005), which is higher than the fraction of EXOs we obtained from the 2XMMp/SDSS-DR5 cross-matched catalogue (selected in the 0.2-12 keV band). These results also indicate that the band selection is very important in efficiently selecting high $f_{\text{X}}/f_{\text{opt}}$

sources. Moreover, we note that the optical/NIR colours of the high f_X/f_{opt} sources amongst the SXDS sample are *all* very red, while for our EXOs with NIR data (40 sources; see Sect. 3.4.2) we estimated a fraction of $\sim 40\%$ to have extremely red colours. This suggests that the different bands used for the selection of the two samples, select slightly different populations of objects and the 2 – 10 keV band selection is more efficient in finding the obscured population.

- As in several previous studies we found an anti-correlation between the fraction of absorbed sources and the intrinsic X-ray luminosity (2-10 keV), which is more consistent with a “modified unified scheme”, such as the receding torus model (Lawrence 1991);
- An analysis of the average AGN spectrum was carried out in order to study the average properties of the Fe $K\alpha$ line profile, however the statistics available were not sufficient to provide useful results.

CHAPTER 6

Conclusions

This Chapter summarises the analyses presented in this thesis and the main results obtained. Subsequently, a description of the work currently ongoing to further progress with this study is given and possible future developments of this work are also described.

6.1 Summary of thesis results

6.1.1 The EXO sample

In this thesis the multi-wavelength analysis of a sample of bright X-ray selected high f_X/f_{opt} sources (EXOs) has been presented. The sample was drawn from the cross correlation of the *XMM-Newton* 2XMMp and the SDSS-DR5 catalogues by selecting sources with $f_X/f_{\text{opt}} > 30$ (0.2–12 keV energy band) and $f_X \geq 10^{-13}$ erg cm⁻² s⁻¹ (0.2–12 keV) and constitutes the largest X-ray selected EXO sample assembled so far (129 sources). This sample represents $\sim 5\%$ of the X-ray population in the whole cross-matched catalogue at the chosen bright flux selection.

Reliable optical counterparts were obtained from the SDSS photometric data for 50% of the objects, while for $\sim 12\%$ a tentative match was identified and for the remainder (38% of the sample) an optical upperlimit was set ($r' > 22.5$ mag) where no optical counterpart was detected in the SDSS images (30% of the total sample) or where a low reliability counterpart was identified (remaining 8%); for these sources the f_X/f_{opt} value obtained is only a lower limit.

Starting with the working hypothesis that the EXO population is likely to hide the bulk of the obscured, high luminosity AGN, i.e. type-2 QSO, at high redshifts ($z > 1$), the properties of the sample were investigated in the optical, NIR and X-ray bands in order to test our hypothesis and to constrain the fraction of type-2 QSO amongst the selected sample, exploring the effectiveness of the selection criteria adopted.

The X-ray source colour (HR2 and HR3) analysis, performed using the *XMM-Newton* EPIC data in the 2XMMp catalogue, constrained the fraction of absorbed AGN ($N_{\text{H}} \geq 4 \times 10^{21}$ cm⁻²) amongst the sample to be $> 51\%$. The optical colours and morphology of the sources, investigated for 62% of the sample (as the remainder are only upperlimits in the optical band) using optical SDSS photometric data and the deeper INT-WFC data (available for 14 sources), revealed that the majority of the sources have typically redder colours than those expected for unobscured QSOs and 34% of the sample also has galaxy morphology, suggesting that in these sources the nuclear emission is obscured. However it

is worth noting that most of the “upperlimit” sources (38% of the sample) are likely to be highly obscured high- z objects, where the galaxy is too faint to be detected at the SDSS sensitivity limits. As a result, the fraction of obscured objects amongst the sample is likely to be much higher. These considerations are also supported by the results obtained from a simple model of a QSO spectral energy distribution (SED), created to investigate the effects of high obscuration and high redshift on the optical colours and the f_X/f_{opt} ratio.

NIR photometric follow-up carried out with UKIRT-WFCAM and UFTI, together with UKIDSS archival data, provided IR colour information for 40 sample EXOs: the optical/NIR colours ($r - K$) again confirmed that a significant fraction (up to $\sim 43\%$ of the 40 sources) have very red colours, with values typical of EROs.

For a sub-sample of 26 EXOs (20% of the total sample), optical spectroscopic follow-up data from Subaru ESO-VLT and GTC telescopes were obtained and a detailed optical and X-ray spectroscopic analysis was performed in order to constrain the spectral parameters of these EXOs and better understand their nature. Through optical emission line diagnostics the sources were classified as type-1 AGN (31% of the sub-sample) with redshift in the range $z = 0.8 - 1.8$ and type-2 AGN (69%) with redshift $z = 0.4 - 1.9$ (peaking at $z \sim 0.7$).

The X-ray analysis of this sub-sample provided constraints on the fraction of absorbed AGN ($N_{\text{H}} \geq 4 \times 10^{21} \text{ cm}^{-2}$) to be 68% (17 sources) while the remainder are unabsorbed; all these sources have high X-ray luminosity, typical for QSO ($L_X > 10^{44} \text{ erg s}^{-1}$; 2 – 10 keV), leading to a fraction of type-2 QSO amongst the analysed sub-sample of $44 \pm 8\%$. About 32% of the spectroscopically identified sub-sample presents “conflicting” classification in the optical and X-ray bands, suggesting that some modification to the classical unification scheme may be required to explain the characteristics of these sources.

6.1.2 The most extreme EXO

Amongst the sample of 129 bright EXOs, the source with the currently most extreme f_X/f_{opt} value (outside the Galaxy) was found. The non-detection of this bright X-ray source ($f_X = 9 \times 10^{-13} \text{ erg cm}^{-2} \text{ s}^{-1}$; 2 – 10 keV) in any of the SDSS photometric bands

constrained the X-ray-to-optical ratio to a very high value ($f_X/f_{\text{opt}} > 278$); deeper optical data subsequently obtained at the NOT telescope constrained the ratio to the extreme value of $f_X/f_{\text{opt}} > 3300$, estimated from the non-detection in the NOT i -band image ($i' > 25.2$; AB magnitude system). A detection in the UKIRT-WFCAM K -band provided an extremely red $i' - K$ colour limit ($i' - K > 5.3$), indicating the presence of high obscuration. NIR Subaru-MOIRCS spectroscopy however, revealed the presence of a single broad line ($\text{FWHM} \approx 5300 \text{ km s}^{-1}$), identified as $\text{H}\alpha$ at $z = 1.87$, suggesting a type-1 classification, in apparent disagreement with the X-ray classification of the source as an absorbed, very luminous QSO ($N_{\text{H}} \approx 2 \times 10^{23} \text{ cm}^{-2}$; $L_X > 1.6 \times 10^{46} \text{ erg s}^{-1}$; 2 – 10 keV). Simple modelling of the optical/NIR SED of this object explained the apparently discrepant properties of the object, providing a reasonable understanding of its extreme nature. The absence of the expected [OIII] narrow emission lines may be related to the very high luminosity of the source, while a lower dust-to-gas ratio value than Galactic can explain the high X-ray absorption as well as the detection of the broad $\text{H}\alpha$ line.

6.1.3 The SXDS sample

The last part of the thesis presents a detailed X-ray analysis of a sample of X-ray sources selected from the Subaru/*XMM-Newton* Deep Survey to have $f_X \geq 2.4 \times 10^{-14} \text{ erg cm}^{-2} \text{ s}^{-1}$ (2 – 10 keV) and with high optical spectroscopic identification ($\sim 90\%$). The X-ray spectral analysis results show that the majority of the source spectra (82%) can be well reproduced by an absorbed power-law, with a wide range of N_{H} , whilst 13% of the sources required additional components. The fraction of unabsorbed AGN ($N_{\text{H}} < 4 \times 10^{21} \text{ cm}^{-2}$) was constrained to be 69% of the sample (47 sources) and the absorbed AGN fraction to be 26% (18 sources); the remainder are not spectroscopically identified.

The spectral parameters obtained are in agreement with the typical properties of AGN and are consistent with the results from previous studies of the AGN population. A slightly flatter average spectral index ($\langle \Gamma \rangle = 1.71 \pm 0.07$) was obtained for sources classified as type-2 AGN compared to the type-1 AGN ($\langle \Gamma \rangle = 1.94 \pm 0.02$), but this is likely to be an effect related to the spectral fitting rather than an intrinsic effect. Typically type-1 AGN

have higher luminosities and higher redshifts than the type-2 AGN. Amongst the sample 53% of the sources have luminosities in the QSO regime and amongst them, six sources are type-2 QSO.

The fraction of high f_X/f_{opt} sources in this sample was also investigated: nine sources (13% of the sample) have $f_X/f_{\text{opt}} > 10$ (2 – 10 keV), these turned out to be the objects with the reddest optical/NIR colours in the sample and to comprise four of the six type-2 QSO identified.

The dependence of the fraction of absorbed objects with the X-ray luminosity, which is still a debated issue, was also investigated. In agreement with many previous works (e.g. Ueda et al. 2003; Gilli et al. 2007; Hasinger 2008; Della Ceca et al. 2008), a decrease of the absorbed fraction with increasing luminosity was found, which supports the idea of a different evolution for AGN at different luminosities.

An attempt was made to study the properties of the average Fe $K\alpha$ emission line, however, after the stacking of the type-1 AGN spectra, no iron line was significantly detected in the average spectrum because of the low S/N, preventing any further analysis.

6.2 Ongoing and future work

Further development of the work presented in this thesis is already ongoing. In fact, the analysis performed so far on the EXO population in the 2XMM/SDSS-DR5 cross-matched catalogue is not yet conclusive. The fraction of the spectroscopically identified sources in the sample is still too low to draw firm statistical conclusions on the properties of the sample and on the fraction of type-2 AGN it contains, although the analysis performed so far has produced interesting results. Moreover, the fraction of spectroscopically identified sources to date is biased towards brighter optical objects, which may constrain the redshift distribution of the sources to lower values. It is also worth noting that the fainter objects in the sample are likely to be the most obscured and high redshift examples, therefore the current sub-sample of spectroscopically identified sources may not be representative of the properties of the whole sample.

To overcome these issues, deep optical R -band imaging has been requested at the

Telescopio Nazionale Galileo (TNG) for those X-ray sources with no optical detection in the SDSS photometric data (30% of the sample); the observations will be performed this Spring. The aim of these observations is to obtain a reliable optical counterpart and, in the future, perform detailed optical spectroscopy with 8-m and 10-m class telescopes in order to address the biases in the current sub-sample of identified objects, pushing the peak of our type-2 QSO redshift distribution to higher values (possibly up to redshift $z \approx 2$).

In addition, observing time at the Subaru telescope has been obtained to perform NIR spectroscopy (with MOIRCS) for additional sources in the EXO sample. The NIR spectroscopy was proposed with the aim of identifying the optically fainter objects, and increasing the redshift distribution peak for the type-2 QSOs in the sample to higher values.

The optical spectroscopic follow-up campaign at the GTC telescope, started two years ago, is also ongoing and other spectroscopic observations are scheduled at the ESO-VLT telescope for the upcoming semester, promising to produce more redshift measurements and to increase the completeness of the EXO sample.

The analysis performed on the EXO sample presented in this thesis showed an interesting set of properties of these objects, not only because of its effectiveness in finding obscured objects, but also in revealing “puzzling” sources such as type-1 AGN with red colours and in some cases X-ray absorption as well. The origin of the high f_X/f_{opt} value in this type of object is not at all clear. Indeed type-1 AGN with high f_X/f_{opt} values have never been studied in any detail to date.

One promising approach to investigate further the properties of the EXO sample would be to perform a detailed SED analysis on the EXOs (both type-1 and type-2), using the current (and future) optical, NIR and X-ray data available: this kind of analysis can place constraints on the different components contributing to the total SED and therefore may be able to explain the origin of the high f_X/f_{opt} values in type-1 QSO. In type-2 QSOs this analysis is equally important as it will allow the study of the relationship between the optical reddening (A_V) and the intrinsic X-ray absorption, providing tight constraints on the nuclear gas-to-dust ratio, a parameter which has barely been explored in the high

redshift regime.

Appendix 1: EXO sample properties and optical spectra

Table A1.1:

X-ray and optical parameters in the 2XMMp/SDSS-DR5 cross-matched catalogue for the EXO sample described in Chapter 3. The Table is arranged as follows:

Col. 1: 2XMM ID; **Col. 2:** X-ray coordinates (J2000.0); **Col. 3:** Optical coordinates on the identified counterpart (J2000.0); **Col. 4:** Logarithm of the f_X/f_{opt} values calculated using the 0.2 – 12 keV X-ray band flux and r' optical band magnitude; **Col. 5:** Optical magnitudes from the SDSS-DR5 catalogue and in some cases from the INT-WFC photometric data; the upperlimit $r' > 22.5$ was set for all the X-ray sources with undetected counterparts and for those with a detected counterpart fainter than the SDSS sensitivity limit; **Col. 6:** Logarithm of the X-ray flux in the 0.2-12 keV energy band (EPIC; in units of $\text{erg cm}^{-2} \text{s}^{-1}$); **Col. 7:** X-ray Hardness Ratio HR2 (see Sect. 3.2.1); **Col. 8:** X-ray Hardness Ratio HR3.

X-ray and optical properties of the EXO sample

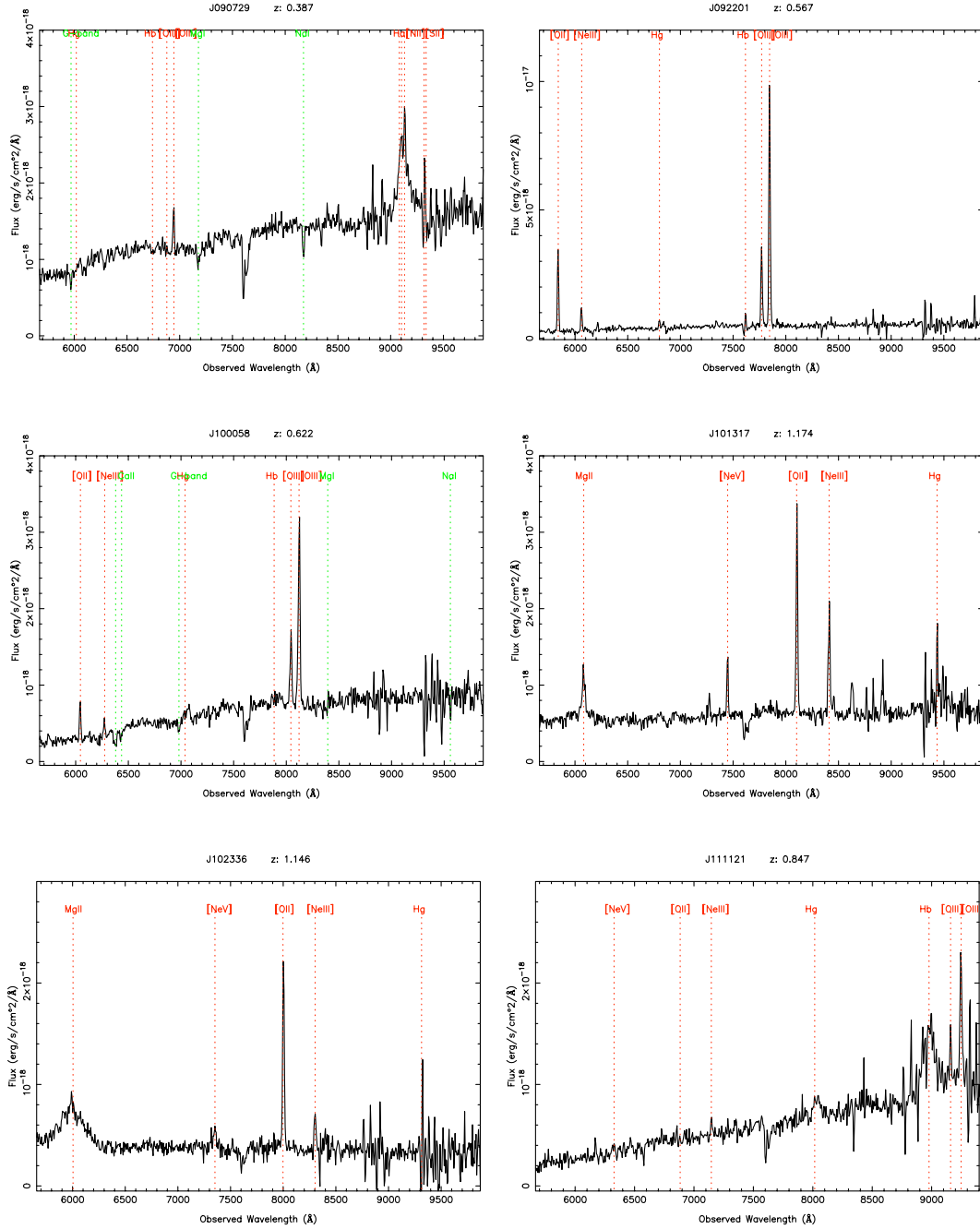
2XMM ID	X-ray RA dec	Optical RA dec	$\log(f_X/f_{opt})$	r mag	$\log f_{0.2-12}$	HR2	HR3
2XMM J004109.2-092606.9	00:41:09.22 -09:26:06.9	00:41:09.15 -09:26:06.6	1.54	22.13±0.17	-12.81	0.72±0.10	0.01±0.09
2XMM J004350.2+005750.2	00:43:50.26 +00:57:50.2	00:43:50.26 +00:57:50.7	1.62	20.94±0.01	-12.26	0.11±0.03	-0.35±0.03
2XMM J015603.7+002738.9	01:56:03.75 +00:27:38.9	01:56:03.76 +00:27:38.0	1.59	> 22.5	-12.91	0.10±0.15	-0.41±0.18
2XMM J020957.9-100300.8	02:09:57.94 -10:03:00.8	02:09:57.99 -10:03:00.4	1.69	22.10±0.15	-12.65	0.06±0.09	-0.48±0.10
2XMM J023028.9-010222.4	02:30:28.93 -01:02:22.4	--	1.84	> 22.5	-12.66	0.38±0.06	-0.07±0.06
2XMM J023125.4-073135.5	02:31:25.40 -07:31:35.5	02:31:25.42 -07:31:35.3	1.58	> 22.5	-12.92	0.78±0.03	-0.11±0.04
2XMM J023507.3-083719.9	02:35:07.31 -08:37:20.0	02:35:07.25 -08:37:18.6	1.50	> 22.5	-13.00	0.70±0.35	0.56±0.19
2XMM J030228.5-000601.1	03:02:28.52 -00:06:01.1	03:02:28.52 -00:06:02.4	1.55	21.96±0.13	-12.74	0.30±0.07	-0.27±0.07
2XMM J035430.5+003616.4	03:54:30.60 +00:36:16.4	--	1.52	> 22.5	-12.98	0.66±0.13	-0.04±0.13
2XMM J035453.9+002537.3	03:54:53.96 +00:25:37.3	03:54:53.94 +00:25:38.8	1.50	22.08±0.10	-12.83	0.29±0.15	-0.20±0.16
2XMM J072918.5+364956.3	07:29:18.54 +36:49:56.3	--	1.83	> 22.5	-12.67	0.36±0.20	-0.15±0.20
2XMM J073412.1+313841.9	07:34:12.11 +31:38:41.9	07:34:11.96 +31:38:42.3	1.69	> 22.5	-12.81	0.53±0.11	-0.21±0.12
2XMM J073536.6+314621.4	07:35:36.65 +31:46:21.4	07:35:36.68 +31:46:20.9	1.57	22.42±0.17	-12.90	0.32±0.07	-0.23±0.07
2XMM J075050.1+143530.5	07:50:50.15 +14:35:30.5	07:50:50.02 +14:35:29.5	1.81	> 22.5	-12.69	0.49±0.12	-0.13±0.11
2XMM J075134.5+145759.1	07:51:34.50 +14:57:59.1	07:51:34.44 +14:57:58.6	1.72	> 22.5	-12.78	0.93±0.14	-0.27±0.20
2XMM J080605.8+152734.3	08:06:05.86 +15:27:34.3	08:06:05.85 +15:27:33.2	1.67	22.30±0.13	-12.74	0.88±0.08	-0.01±0.09
2XMM J080622.9+152731.0	08:06:22.97 +15:27:31.0	08:06:22.95 +15:27:31.1	1.73	21.11±0.01	-12.22	-0.84±0.02	-0.09±0.08
2XMM J082053.8+210735.5	08:20:53.86 +21:07:35.5	08:20:53.91 +21:07:34.7	1.60	> 22.5	-12.90	0.98±0.04	0.21±0.06
2XMM J084030.4+130931.8	08:40:30.49 +13:09:31.8	--	1.58	> 22.5	-12.92	0.31±0.11	-0.00±0.11
2XMM J084630.0+345858.1	08:46:30.08 +34:58:58.1	08:46:30.07 +34:58:57.2	1.56	21.07±0.05	-12.37	0.22±0.04	-0.34±0.04
2XMM J090729.4+620827.5	09:07:29.40 +62:08:27.5	09:07:29.36 +62:08:27.2	1.53	20.38±0.05	-12.12	0.99±0.09	-0.16±0.17
2XMM J091946.3+302953.7	09:19:46.40 +30:29:53.7	09:19:46.44 +30:29:52.9	1.53	22.45±0.17	-12.95	0.27±0.06	-0.28±0.06
2XMM J092043.5+303701.9	09:20:43.56 +30:37:01.9	09:20:43.63 +30:37:01.1	1.85	> 22.5	-12.65	0.47±0.06	-0.10±0.06
2XMM J092201.2+301411.9	09:22:01.25 +30:14:11.9	09:22:01.22 +30:14:12.2	1.72	21.56±0.09	-12.40	0.82±0.06	0.15±0.06
2XMM J093846.0+355643.1	09:38:46.07 +35:56:43.1	--	1.79	> 22.5	-12.71	0.20±0.10	-0.28±0.12
2XMM J093911.2+354536.6	09:39:11.30 +35:45:37.0	09:39:11.20 +35:45:36.6	1.65	22.65±0.06	-12.90	0.14±0.12	-0.58±0.13
2XMM J094204.6+480447.3	09:42:04.68 +48:04:47.3	09:42:04.65 +48:04:49.7	1.82	22.13±0.19	-12.54	-0.13±0.08	-0.29±0.11
2XMM J094301.9+385830.8	09:43:01.95 +38:58:30.8	--	1.60	> 22.5	-12.89	-0.11±0.08	-0.34±0.10
2XMM J094352.4+465506.7	09:43:52.42 +46:55:06.7	--	1.56	> 22.5	-12.94	0.24±0.05	-0.21±0.05
2XMM J095753.2+690348.3	09:57:53.21 +69:03:48.3	09:57:53.29 +69:03:48.2	2.65	20.51±0.10	-11.05	0.27±0.01	-0.27±0.01
2XMM J100058.1+014559.0	10:00:58.20 +01:45:59.0	10:00:58.21 +01:45:59.0	1.51	21.82±0.13	-12.72	0.29±0.03	-0.17±0.03
2XMM J101317.2-001908.0	10:13:17.24 -00:19:08.0	10:13:17.34 -00:19:10.1	1.60	21.18±0.07	-12.38	0.47±0.11	-0.18±0.12
2XMM J101659.8+213316.0	10:16:59.81 +21:33:16.0	10:16:59.80 +21:33:15.4	2.02	22.32±0.11	-12.41	0.10±0.04	-0.42±0.05
2XMM J102016.0+082142.9	10:20:16.10 +08:21:42.9	10:20:16.20 +08:21:43.0	1.69	22.06±0.13	-12.63	-0.06±0.09	-0.21±0.10
2XMM J102336.7+005152.2	10:23:36.74 +00:51:52.2	10:23:36.72 +00:51:52.9	1.72	22.38±0.13	-12.73	0.01±0.08	-0.19±0.09
2XMM J103118.4+505336.4	10:31:18.46 +50:53:36.4	10:31:18.52 +50:53:35.9	1.71	16.74±0.004	-10.48	0.03±0.01	-0.50±0.01

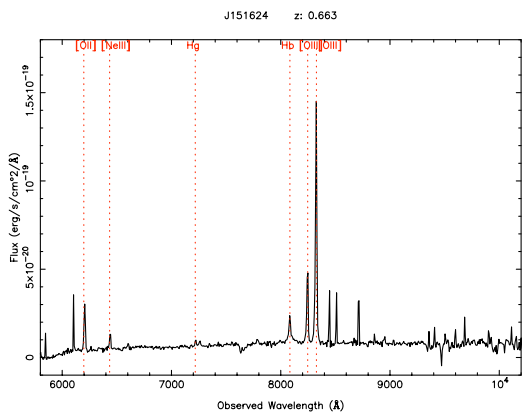
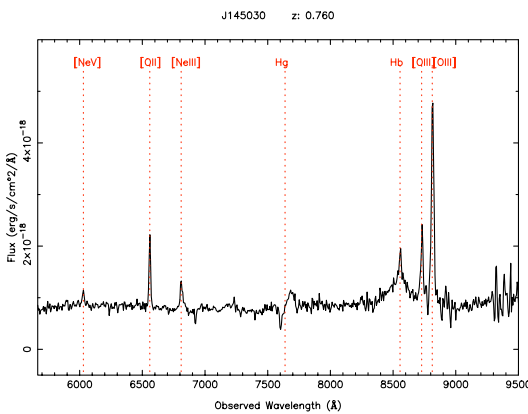
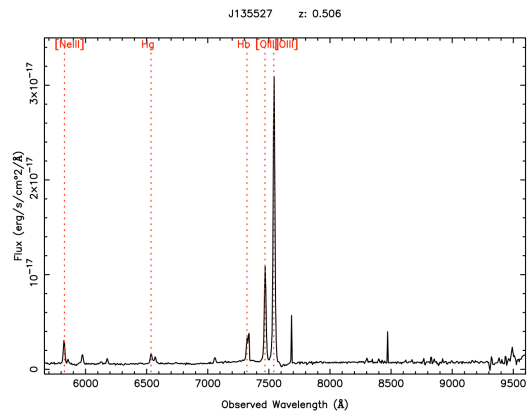
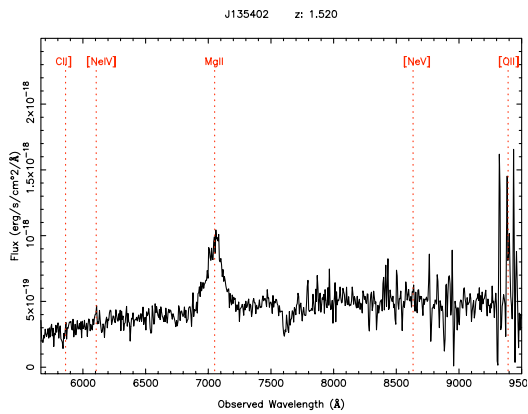
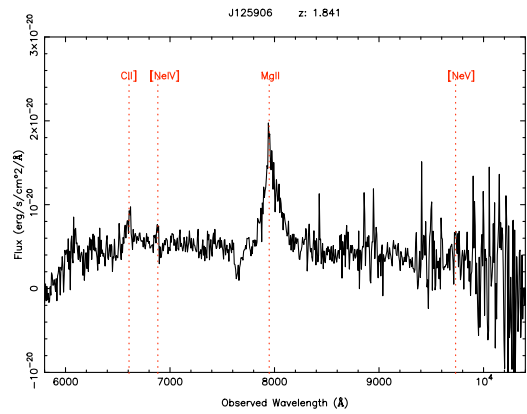
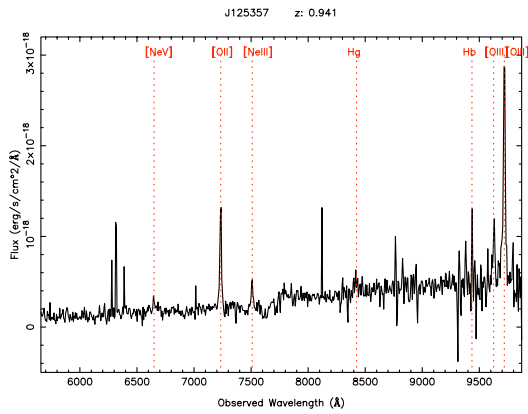
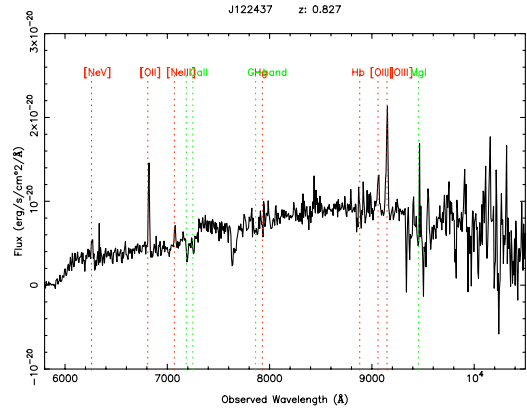
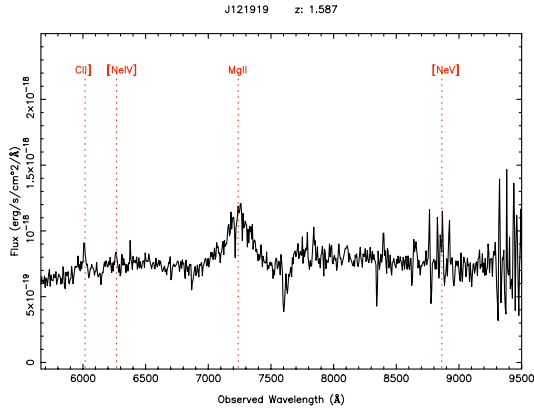
2XMM ID	X-ray RA dec	Optical RA dec	$\log(f_X/f_{\text{opt}})$	r mag	$\log f_{0.2-12}$	HR2	HR3
2XMM J103444.8+392504	10:34:44.88 +39:25:04.5	10:34:45.38 +39:25:04.6	1.64	> 22.5	-12.86	-0.18±0.24	-0.18±0.32
2XMM J103451.0+393836	10:34:51.05 +39:38:36.3	10:34:50.96 +39:38:35.3	1.69	> 22.5	-12.81	0.42±0.08	-0.39±0.09
2XMM J103915.1+205206	10:39:15.19 +20:52:06.7	10:39:15.23 +20:52:06.9	1.54	22.39±0.17	-12.91	0.78±0.36	0.76±0.12
2XMM J103958.3+085946	10:39:58.39 +08:59:47.0	--	1.55	> 22.5	-12.95	0.97±0.07	0.13±0.11
2XMM J104026.8+204544	10:40:26.81 +20:45:44.7	10:40:26.85 +20:45:44.4	1.65	19.77±0.02	-11.76	0.05±0.02	-0.37±0.02
2XMM J104452.1+213727	10:44:52.11 +21:37:27.2	--	1.57	> 22.5	-12.92	0.36±0.02	-0.21±0.02
2XMM J110353.8+445205	11:03:53.83 +44:52:06.0	--	1.81	> 22.5	-12.69	0.55±0.17	-0.32±0.17
2XMM J111121.2+482333	11:11:21.28 +48:23:33.0	11:11:21.37 +48:23:32.8	1.69	21.53±0.08	-12.42	0.22±0.03	-0.32±0.03
2XMM J112305.8+014913	11:23:05.85 +01:49:13.1	11:23:05.85 +01:49:06.3	3.00	25.13±0.10	-12.54	0.39±0.05	-0.23±0.05
2XMM J112604.1+423950	11:26:04.13 +42:39:50.0	11:26:04.32 +42:39:50.3	1.58	22.17±0.19	-12.79	0.28±0.11	-0.06±0.11
2XMM J113954.9+662211	11:39:54.96 +66:22:11.1	--	2.04	> 23.7	-12.94	0.56±0.13	-0.02±0.13
2XMM J114234.7+660403	11:42:34.71 +66:04:03.8	11:42:34.92 +66:04:02.6	1.52	> 22.5	-12.98	0.25±0.21	-0.30±0.22
2XMM J114903.7+285015	11:49:03.75 +28:50:15.2	11:49:03.57 +28:50:13.3	1.67	22.30±0.14	-12.75	0.28±0.24	-0.29±0.24
2XMM J115446.8+232917	11:54:46.88 +23:29:17.8	--	1.73	> 22.5	-12.77	0.32±0.05	-0.27±0.05
2XMM J115530.0+233819	11:55:30.00 +23:38:19.1	11:55:29.97 +23:38:18.9	1.57	> 22.5	-12.93	0.16±0.15	-0.38±0.16
2XMM J121107.5+503610	12:11:07.50 +50:36:10.8	--	1.50	> 22.5	-12.99	0.27±0.05	-0.17±0.05
2XMM J121134.2+390054	12:11:34.23 +39:00:54.6	12:11:34.21 +39:00:53.6	2.22	21.03±0.05	-11.69	0.04±0.02	-0.46±0.02
2XMM J121147.6+391708	12:11:47.61 +39:17:08.4	--	1.60	> 22.5	-12.90	0.14±0.08	-0.36±0.08
2XMM J121218.6+502049	12:12:18.61 +50:20:49.9	--	1.54	> 22.5	-12.96	0.73±0.14	0.35±0.10
2XMM J121622.1+361352	12:16:22.20 +36:13:52.8	--	1.60	> 22.5	-12.90	0.03±0.27	-0.23±0.29
2XMM J121919.0+295320	12:19:19.10 +29:53:20.4	12:19:19.01 +29:53:28.3	1.74	21.86±0.14	-12.50	0.13±0.09	-0.33±0.10
2XMM J122437.8+131327	12:24:37.87 +13:13:27.9	12:24:37.84 +13:13:26.9	1.54	> 22.5	-12.96	-0.15±0.09	-0.10±0.11
2XMM J122628.8+333626	12:26:28.83 +33:36:26.1	12:26:29.06 +33:36:21.7	1.54	22.43±0.16	-12.93	0.040±0.02	-0.56±0.02
2XMM J123016.9+143821	12:30:16.95 +14:38:21.5	12:30:16.91 +14:38:22.8	1.53	22.45±0.28	-12.95	0.23±0.21	-0.31±0.23
2XMM J123020.5+214946	12:30:20.57 +21:49:46.6	12:30:20.81 +21:49:41.2	1.71	22.51±0.50	-12.80	0.65±0.12	-0.12±0.11
2XMM J123204.9+215254	12:32:04.92 +21:52:54.7	12:32:04.23 +21:53:12.3	3.74	23.94±0.10	-11.84	0.84±0.03	0.15±0.03
2XMM J123242.9+000455	12:32:42.98 +00:04:55.7	12:32:42.96 +00:04:55.7	1.66	> 22.5	-12.84	0.30±0.03	-0.22±0.03
2XMM J123349.2+373633	12:33:49.25 +37:36:33.4	12:33:49.26 +37:36:34.2	1.57	> 22.5	-12.93	0.11±0.13	-0.36±0.15
2XMM J123417.8+392437	12:34:17.81 +39:24:37.3	12:34:17.78 +39:24:37.4	1.65	> 22.5	-12.85	0.19±0.04	-0.39±0.04
2XMM J123537.5+373448	12:35:37.60 +37:34:48.1	12:35:37.53 +37:34:50.9	1.63	> 22.5	-12.87	0.97±0.06	0.19±0.10
2XMM J123718.9+113832	12:37:18.98 +11:38:32.1	--	1.66	> 22.5	-12.84	0.53±0.08	-0.17±0.08
2XMM J124158.0+322851	12:41:58.10 +32:28:51.3	--	1.62	> 22.5	-12.88	0.25±0.03	-0.13±0.03
2XMM J125001.5+251756	12:50:01.53 +25:17:56.4	--	1.70	> 22.5	-12.80	0.59±0.10	-0.16±0.10
2XMM J125005.5+254017	12:50:05.60 +25:40:17.4	12:50:05.65 +25:40:18.3	1.53	22.48±0.16	-12.96	0.04±0.10	-0.31±0.12
2XMM J125357.1+154314	12:53:57.16 +15:43:14.0	12:53:57.16 +15:43:12.2	1.62	22.48±0.30	-12.87	0.67±0.04	-0.09±0.04
2XMM J125834.5+281435	12:58:34.58 +28:14:35.5	12:58:34.59 +28:14:34.9	1.54	> 22.5	-12.96	-0.15±0.06	-0.35±0.08

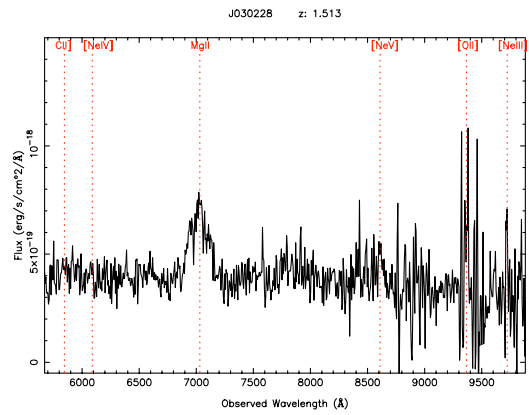
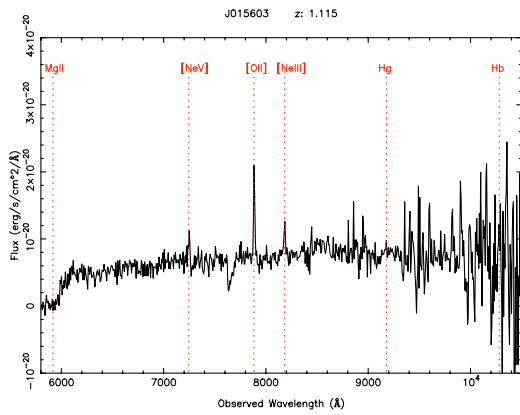
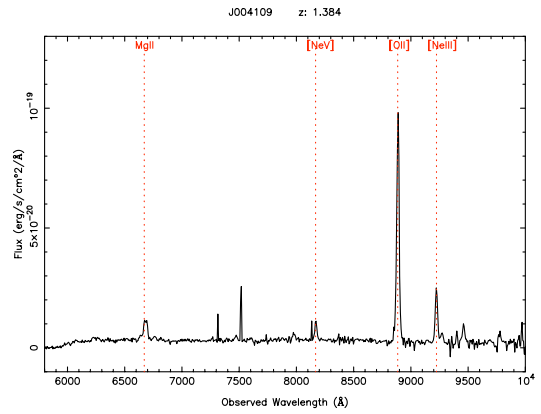
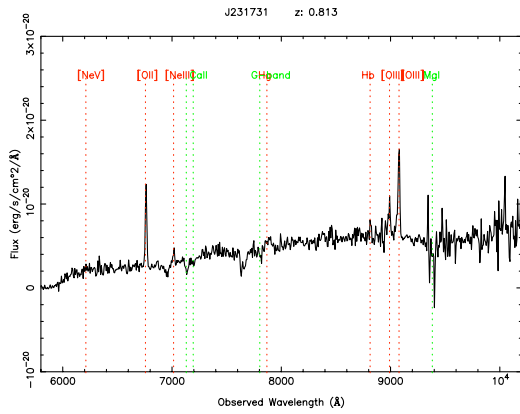
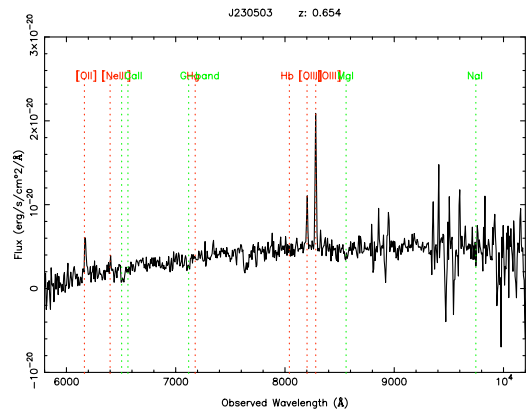
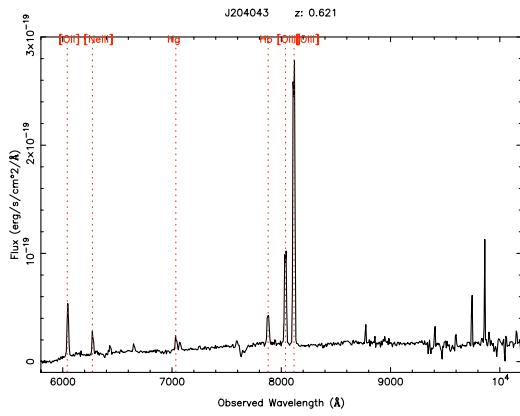
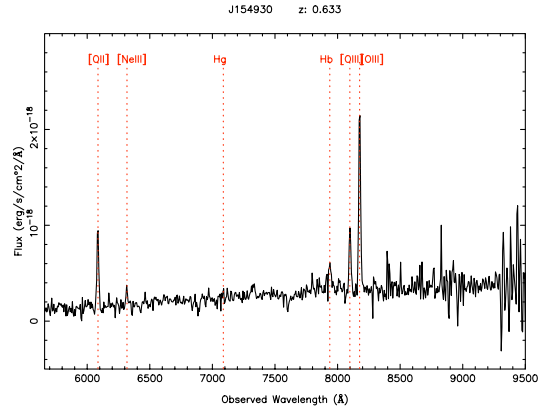
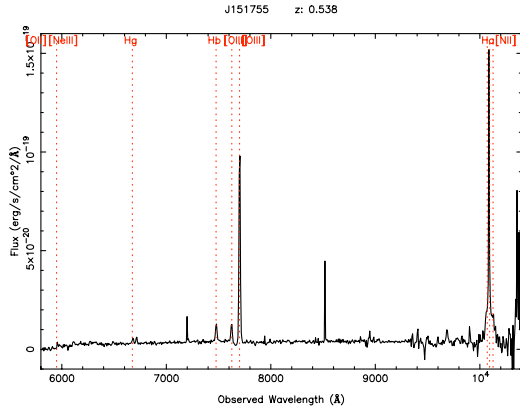
2XMM ID	X-ray RA dec	Optical RA dec	$\log(f_X/f_{\text{opt}})$	r mag	$\log f_{0.2-12}$	HR2	HR3
2XMM J125906.6-015057	12:59:06.66 -01:50:57.5	12:59:06.62 -01:50:58.4	1.58	21.64±0.11	-12.57	0.08±0.03	-0.32±0.03
2XMM J125948.8+163935	12:59:48.87 +16:39:35.6	12:59:48.54 +16:39:37.2	1.58	> 22.5	-12.92	-0.21±0.13	-0.56±0.18
2XMM J130048.9+282715	13:00:48.95 +28:27:15.7	--	1.66	> 22.5	-12.84	0.43±0.02	-0.21±0.02
2XMM J130848.1+212707	13:08:48.15 +21:27:07.0	--	2.98	> 22.5	-11.521	-0.93±0.001	-0.99±0.004
2XMM J130955.6+321122	13:09:55.64 +32:11:22.9	--	1.51	> 22.5	-12.98	0.38±0.05	-0.36±0.06
2XMM J131026.4+323401	13:10:26.49 +32:34:01.2	13:10:26.52 +32:34:00.2	1.59	> 22.5	-12.91	0.11±0.08	-0.29±0.08
2XMM J131109.6+275558	13:11:09.67 +27:55:58.9	--	1.54	> 22.5	-12.96	0.71±0.07	0.06±0.07
2XMM J131207.2+352840	13:12:07.22 +35:28:40.8	--	1.55	> 22.5	-12.95	0.38±0.09	-0.33±0.09
2XMM J131223.4+173659	13:12:23.46 +17:36:59.5	13:12:23.49 +17:36:59.2	1.58	19.76±0.02	-11.82	0.23±0.01	-0.18±0.014
2XMM J132505.8+300111	13:25:05.85 +30:01:11.6	13:25:05.78 +30:01:10.6	1.71	22.58±0.05	-12.82	0.16±0.04	-0.39±0.04
2XMM J132530.0+073859	13:25:30.07 +07:38:59.4	--	1.50	> 22.5	-13.00	0.53±0.12	-0.07±0.10
2XMM J132833.6+114519	13:28:33.62 +11:45:19.6	13:28:33.57 +11:45:20.5	1.76	18.99±0.01	-11.33	-0.11±0.01	-0.48±0.01
2XMM J133423.8+410159	13:34:23.86 +41:01:59.0	13:34:23.86 +41:01:58.9	1.64	22.39±0.20	-12.82	0.89±0.15	0.29±0.13
2XMM J134139.3+402611	13:41:39.32 +40:26:11.9	13:41:38.99 +40:26:14.0	1.57	> 22.5	-12.92	0.76±0.10	-0.11±0.10
2XMM J134150.2+355102	13:41:50.27 +35:51:02.3	13:41:50.25 +35:51:02.1	1.55	22.36±0.18	-12.90	0.03±0.06	-0.55±0.07
2XMM J134413.8+553924	13:44:13.85 +55:39:24.7	13:44:13.90 +55:39:25.8	1.54	> 22.5	-12.96	0.62±0.16	0.06±0.13
2XMM J134939.0+264215	13:49:39.02 +26:42:15.0	--	2.01	> 23.51	-12.90	0.60±0.05	-0.14±0.05
2XMM J135358.3+635737	13:53:58.40 +63:57:37.3	--	1.62	> 22.5	-12.88	0.25±0.08	-0.22±0.08
2XMM J135402.1+401420	13:54:02.16 +40:14:20.1	13:54:02.20 +40:14:20.0	1.53	21.97±0.08	-12.76	0.12±0.05	-0.33±0.05
2XMM J135527.6+181639	13:55:27.64 +18:16:39.5	13:55:27.67 +18:16:38.9	1.73	21.17±0.06	-12.24	0.15±0.03	-0.28±0.03
2XMM J140203.4+541829	14:02:03.43 +54:18:29.1	--	1.53	> 22.5	-12.97	0.26±0.05	-0.21±0.05
2XMM J140414.0+542604	14:04:14.07 +54:26:04.6	14:04:14.34 +54:26:02.7	2.03	> 22.5	-12.47	-0.01±0.01	-0.62±0.01
2XMM J140750.1+283322	14:07:50.14 +28:33:22.5	14:07:50.10 +28:33:24.0	1.55	> 22.5	-12.95	0.14±0.10	-0.32±0.10
2XMM J142236.1+474816	14:22:36.19 +47:48:16.4	14:22:36.03 +47:48:16.2	1.64	> 22.5	-12.86	-0.09±0.25	0.10±0.26
2XMM J142652.7+263125	14:26:52.79 +26:31:25.1	14:26:52.78 +26:31:24.7	1.50	> 22.5	-13.00	0.92±0.07	0.15±0.07
2XMM J142832.6+424021	14:28:32.62 +42:40:21.4	14:28:32.61 +42:40:21.1	1.80	16.18±0.004	-10.17	0.13±0.001	-0.41±0.001
2XMM J143023.7+420436	14:30:23.72 +42:04:36.8	14:30:23.74 +42:04:36.5	2.23	21.01±0.04	-11.67	0.11±0.01	-0.29±0.01
2XMM J143102.7+420149	14:31:02.72 +42:01:49.1	--	1.69	> 22.5	-12.81	0.94±0.06	0.33±0.06
2XMM J143623.8+631726	14:36:23.88 +63:17:26.4	14:36:23.79 +63:17:26.2	2.02	22.4±0.18	-12.45	0.53±0.03	-0.16±0.03
2XMM J144704.8+402220	14:47:04.84 +40:22:20.4	14:47:04.95 +40:22:20.7	1.55	> 22.5	-12.95	0.41±0.15	-0.18±0.16
2XMM J145030.1+270633	14:50:30.11 +27:06:33.6	14:50:30.05 +27:06:33.4	1.50	21.86±0.12	-12.74	0.51±0.06	-0.24±0.06
2XMM J145033.0+190713	14:50:33.08 +19:07:13.6	--	1.56	> 22.5	-12.94	0.48±0.15	0.27±0.10
2XMM J145712.3+221257	14:57:12.35 +22:12:58.0	--	2.00	> 23.42	-12.87	0.56±0.05	-0.19±0.05
2XMM J145717.5+223332	14:57:17.51 +22:33:32.0	14:57:17.56 +22:33:32.0	1.64	21.77±0.10	-12.57	0.07±0.04	-0.34±0.04
2XMM J151624.2-000141	15:16:24.24 -00:01:41.1	15:16:24.28 -00:01:40.2	1.53	22.05±0.12	-12.79	0.58±0.05	-0.28±0.05
2XMM J151755.9+062232	15:17:55.94 +06:22:32.3	15:17:55.87 +06:22:31.8	1.66	21.97±0.13	-12.63	0.50±0.19	0.01±0.16

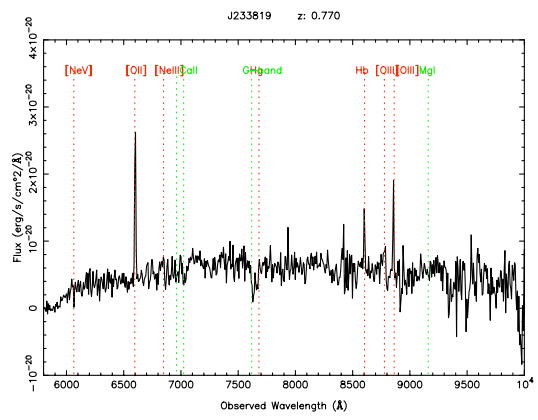
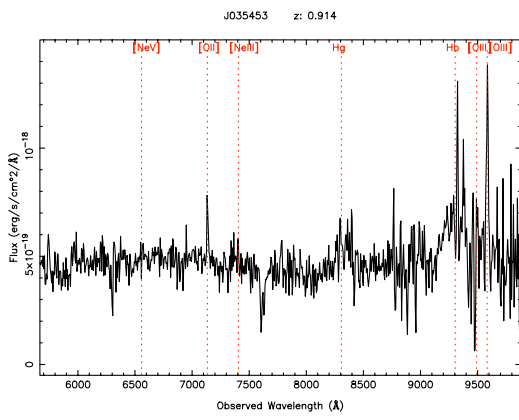
2XMM ID	X-ray RA dec	Optical RA dec	$\log(f_X/f_{\text{opt}})$	r mag	$\log f_{0.2-12}$	HR2	HR3
2XMM J151818.3+424407	15:18:18.33 +42:44:07.6	15:18:18.21 +42:44:02.7	1.50	> 22.5	-13.00	0.50±0.08	-0.15±0.08
2XMM J151839.2+311544	15:18:39.25 +31:15:44.3	15:18:38.77 +31:15:43.9	1.56	> 22.5	-12.93	0.57±0.16	0.11±0.12
2XMM J153756.9+543230	15:37:56.98 +54:32:30.4	--	1.53	> 22.5	-12.97	0.42±0.09	-0.21±0.09
2XMM J154930.6+213422	15:49:30.61 +21:34:22.4	15:49:30.59 +21:34:22.8	1.76	22.38±0.10	-12.69	0.38±0.06	-0.25±0.06
2XMM J154943.2+255638	15:49:43.20 +25:56:38.5	15:49:43.14 +25:56:41.8	1.55	> 22.5	-12.95	0.84±0.12	0.06±0.13
2XMM J155027.4+211926	15:50:27.49 +21:19:26.6	--	1.58	> 22.5	-12.92	0.36±0.06	-0.34±0.06
2XMM J155542.9+111124	15:55:42.97 +11:11:24.5	15:55:43.04 +11:11:24.3	1.69	15.40±0.01	-9.97	0.05±0.003	-0.48±0.003
2XMM J160518.5+324918	16:05:18.51 +32:49:18.0	16:05:19.89 +32:49:27.3	3.56	23.55±0.13	-11.35	-0.87±0.002	-1.00±0.002
2XMM J160532.5+330240	16:05:32.55 +33:02:40.9	--	1.67	> 22.5	-12.83	0.27±0.07	-0.21±0.07
2XMM J160545.9+255145	16:05:45.91 +25:51:45.2	16:05:45.88 +25:51:45.2	1.93	19.70±0.02	-11.44	0.00±0.01	-0.38±0.01
2XMM J160606.1+255241	16:06:06.18 +25:52:41.6	16:06:05.71 +25:52:44.3	1.56	> 22.5	-12.94	0.67±0.08	0.07±0.07
2XMM J160645.9+081523	16:06:45.92 +08:15:23.9	16:06:45.87 +08:15:24.8	1.88	21.62±0.02	-12.27	0.87±0.15	0.82±0.05
2XMM J165648.3+351642	16:56:48.35 +35:16:42.6	16:56:48.76 +35:16:32.7	1.91	22.54±0.15	-12.60	0.81±0.28	0.02±0.38
2XMM J170106.0+593939	17:01:06.04 +59:39:39.5	--	1.91	> 22.5	-12.59	0.20±0.17	-0.47±0.18
2XMM J204043.2-004548	20:40:43.30 -00:45:48.8	20:40:43.48 -00:45:50.0	1.67	21.44±0.04	-12.41	0.71±0.11	-0.13±0.11
2XMM J213311.1+100659	21:33:11.17 +10:06:59.2	21:33:12.15 +10:06:59.9	1.69	22.7± 0.13	-12.89	0.30±0.09	-0.11±0.08
2XMM J213314.8+101140	21:33:14.81 +10:11:40.9	--	1.51	> 22.5	-12.98	0.22 ±0.11	-0.11±0.11
2XMM J230503.4-085005	23:05:03.48 -08:50:05.7	23:05:03.54 -08:50:05.8	1.55	> 22.5	-12.95	1.00±0.26	0.07±0.23
2XMM J231731.6+001032	23:17:31.64 +00:10:32.5	23:17:31.69 +00:10:32.6	1.74	> 22.5	-12.76	0.36±0.11	-0.39±0.11
2XMM J231740.8+001051	23:17:40.88 +00:10:52.0	23:17:40.92 +00:10:52.2	1.53	> 22.5	-12.96	0.98±0.39	0.81±0.14
2XMM J233819.9+001113	23:38:19.91 +00:11:13.4	23:38:19.87 +00:11:11.2	1.66	22.81±0.07	-12.97	0.70±0.13	-0.17±0.13

Figure A1.1: The optical spectra of the identified objects obtained from the Subaru telescope and the ESO-VLT telescope. The red vertical lines indicate the main optical emission lines typical of AGN, while the green vertical lines indicate the absorption lines, which are typical of galaxies. The labels on top of each spectrum indicate the 2XMM ID (shortened to the first six numbers for simplicity; see Table A1.1) and the redshift of the source.









Appendix 2: SXDS source parameters

Table A2.1:

Best-fit parameters of the SXDS sample objects (Chapter 5). In this Table the spectral slope of the main power-law component and the intrinsic hydrogen column density N_{H} are reported; the parameters of any additional components are summarised in various Tables in Chapter 5.

The table is arranged as follows:

Col. 1: SXDS source name; **Cols. 2:** X-ray coordinates (J2000.0); **Col. 3:** Hard band count rate in counts/s; **Col. 4:** X-ray-to-optical flux ratio calculated from the X-ray flux in the 2–10 keV and the R band magnitude; **Col. 5:** SXDS field name; **Col. 6:** Spectroscopic redshift; **Col. 7:** Total (pn+MOS1+MOS2) net counts in the 0.2 – 10 keV energy band; **Col. 8:** Spectral index Γ from the best-fit model of each source (the errors are calculated at 90% confidence level); **Col. 9:** Hydrogen column density in units of 10^{21} cm^{-2} ; **Col. 10:** Reduced χ^2 ; **Col. 11:** Best-fit model (see Chapter 5); the asterisk indicates the presence of a Fe $K\alpha$ line in the spectra; **Col. 12:** Unabsorbed X-ray flux in the 2 – 10 keV rest-frame; **Col. 13:** Logarithm of the unabsorbed X-ray luminosity in the 0.5-2 keV (soft band) rest-frame; **Col. 14:** Logarithm of the unabsorbed X-ray luminosity in the 2 – 10 keV (hard band) rest-frame; **Col. 15:** Optical classification (see Sect. 5.3); the label “NAV” is given to the sources where the redshift is known, but the spectral identification is not available.

SXDS X-ray spectral parameters from the best-fit models

ID	R.A. dec (<i>h</i> : <i>m</i> : <i>s</i>) (<i>d</i> : <i>m</i> : <i>s</i>)	Rate Cts/s	$\log(f_x/f_{opt})$ (2–10 keV)	Field	<i>z</i>	Net Cts	Γ	N_H (10^{21} cm^{-2})	$\chi^2/d.o.f.$	Model	f_{2-10} (10^{-14} egs)	$\log L_{0.5-2}$ (erg/s)	$\log L_{2-10}$ (erg/s)	Class
SXDS 0750	02:18:17.38 – 04:51:12.4	0.0336	0.62	SDS-1	1.081	10665.0	$1.83^{+0.03}_{-0.03}$	<0.10	480.90 / 524	MOD1	21.22	44.76	45.09	BL AGN
SXDS 0764	02:18:20.59 – 05:04:27.3	0.0112	0.59	SDS-1	0.649	4489.0	$1.86^{+0.05}_{-0.05}$	<0.10	288.20 / 250	MOD1	6.53	43.80	44.05	BL AGN
SXDS 0883	02:18:43.01 – 05:04:36.3	0.0062	0.97	SDS-1	0.961	1254.0	$1.794^{+0.15}_{-0.14}$	$3.35^{+1.41}_{-1.21}$	67.32 / 76	MOD1	3.14	43.79	44.12	NL AGN
SXDS 0806	02:18:27.17 – 04:54:56.3	0.0041	-0.21	SDS-1	2.190	1885.0	$2.088^{+0.07}_{-0.07}$	<0.79	105.10 / 110	MOD1	2.34	44.61	44.98	BL AGN
SXDS 0619	02:17:53.74 – 04:57:48.4	0.0040	0.09	SDS-1	1.410	2107.0	$2.001^{+0.08}_{-0.07}$	<0.20	123.80 / 125	MOD1	2.15	44.13	44.43	BL AGN
SXDS 0346	02:17:08.69 – 04:57:42.7	0.0039	0.53	SDS-1	1.434	768.0	$2.04^{+0.23}_{-0.13}$	<1.67	44.68 / 45	MOD1	1.37	43.98	44.26	BL AGN
SXDS 0330	02:17:05.47 – 04:56:55.3	0.0034	2.07	SDS-1	–	368.0	$2.13^{+0.56}_{-0.45}$	$2.32^{+1.60}_{-1.27}$	18.26 / 19	MOD1	1.135	–	–	–
SXDS 0740	02:18:15.43 – 04:56:18.3	0.0032	0.56	SDS-1	1.433	1564.0	$1.81^{+0.09}_{-0.04}$	<0.51	133.30 / 94	MOD1	2.11	43.97	44.36	BL AGN
SXDS 0710	02:18:08.62 – 05:12:23.6	0.0031	0.39	SDS-1	1.036	769.0	$1.934^{+0.13}_{-0.13}$	<0.47	42.96 / 43	MOD1	1.06	43.63	43.82	BL AGN
SXDS 0774	02:18:22.22 – 05:06:15.0	0.0240	0.01	SDS-1	0.048	1571.0	$1.52^{+0.38}_{-0.37}$	$224.40^{+39.50}_{-36.20}$	115.10 / 94	MOD2*	65.30	42.12	42.54	ABS
SXDS 0617	02:17:53.52 – 04:55:42.4	0.0097	0.82	SDS-1	0.550	1137.0	$1.78^{+0.29}_{-0.27}$	$96.40^{+22.30}_{-19.90}$	56.90 / 67	MOD2*	9.40	43.73	44.02	NL AGN
SXDS 0707	02:18:08.26 – 04:58:45.6	0.0327	0.40	SDS-1	0.714	26220.0	$1.95^{+0.05}_{-0.04}$	<0.16	471.00 / 384	MOD3	22.80	44.65	44.72	BL AGN
SXDS 0817	02:18:30.50 – 04:56:22.2	0.0055	-0.54	SDS-1	1.400	3610.0	$2.11^{+0.13}_{-0.14}$	<0.10	185.40 / 197	MOD3	3.30	44.68	44.69	BL AGN
SXDS 0816	02:18:29.83 – 04:55:13.8	0.0044	-1.62	SDS-1	0.000	11073.0	$2.86^{+0.06}_{-0.06}$	0.0	1419.70 / 414	2T	2.35	36.45	35.65	STAR
SXDS 1082	02:19:23.30 – 04:51:48.4	0.0068	-0.02	SDS-2	0.629	2251.0	$2.495^{+0.07}_{-0.07}$	<0.12	162.20 / 128	MOD1	3.40	44.01	43.87	BL AGN
SXDS 0997	02:19:08.30 – 04:55:00.9	0.0050	0.31	SDS-2	1.843	485.0	$1.484^{+0.19}_{-0.14}$	<3.17	12.29 / 26	MOD1	4.61	44.18	44.83	BL AGN
SXDS 1239	02:20:22.06 – 04:57:05.5	0.0044	0.45	SDS-2	1.657	258.0	$1.968^{+0.49}_{-0.23}$	<0.10	10.34 / 12	MOD1	2.75	44.33	44.69	BL AGN
SXDS 1228	02:20:13.06 – 04:51:13.9	0.0041	0.55	SDS-2	0.925	305.0	$1.844^{+0.33}_{-0.33}$	<1.94	14.65 / 16	MOD1	2.03	43.62	43.92	BL AGN
SXDS 1216	02:20:04.85 – 04:55:15.1	0.0038	0.90	SDS-2	1.471	460.0	$1.933^{+0.33}_{-0.29}$	$7.40^{+4.83}_{-3.83}$	15.92 / 24	MOD1	2.87	44.11	44.54	BL AGN
SXDS 1232	02:20:16.82 – 04:56:46.6	0.0034	0.41	SDS-2	0.517	273.0	$1.233^{+0.40}_{-0.24}$	$3.23^{+3.39}_{-2.56}$	11.24 / 13	MOD1	2.66	43.68	43.37	NL AGN
SXDS 1014	02:19:10.92 – 05:01:10.9	0.0034	1.53	SDS-2	–	195.0	$1.83^{+0.61}_{-0.34}$	<2.87	16.64 / 8	MOD1	2.74	–	–	–
SXDS 1118	02:19:31.01 – 04:49:58.6	0.0031	0.34	SDS-2	0.293	242.0	$1.59^{+0.46}_{-0.40}$	$3.12^{+3.78}_{-2.10}$	2.35 / 10	MOD1	2.65	42.40	42.81	NL AGN
SXDS 1242	02:20:27.14 – 04:59:34.0	0.0030	0.39	SDS-2	1.904	151.0	$1.70^{+0.32}_{-0.32}$	<0.10	5.719 / 6	MOD1	3.37	43.78	44.80	BL AGN
SXDS 1136	02:19:34.22 – 05:08:59.7	0.0030	0.17	SDS-2	1.321	607.0	$2.11^{+0.17}_{-0.16}$	<0.58	35.09 / 34	MOD1	1.82	44.13	44.32	BL AGN
SXDS 1156	02:19:39.10 – 05:11:33.4	0.0111	-0.62	SDS-2	0.151	231.0	$2.41^{+0.80}_{-0.80}$	$111.70^{+48.20}_{-37.50}$	16.20 / 17	MOD2	13.70	43.10	42.96	NL AGN
SXDS 1240	02:20:24.77 – 05:02:31.6	0.0284	0.51	SDS-2	0.252	4944.0	$1.90^{+0.15}_{-0.12}$	<2.63	299.60 / 261	MOD3	21.10	43.52	43.61	BL AGN
SXDS 1244	02:20:28.99 – 04:58:01.8	0.0033	0.13	SDS-2	–	90.0	1.9	<1.63	2.85 / 3	MOD1	1.65	–	–	–
SXDS 1184	02:19:48.41 – 04:51:32.3	0.0030	0.73	SDS-2	0.818	136.0	1.9	$29.30^{+20.90}_{-16.30}$	3.23 / 5	MOD1	2.0	43.12	43.79	ABS
SXDS 0999	02:19:08.42 – 04:47:31.5	0.0102	0.02	SDS-3	0.278	520.0	$1.176^{+0.34}_{-0.30}$	$3.49^{+4.30}_{-2.94}$	33.74 / 29	MOD1	10.16	42.65	43.31	NL AGN
SXDS 0771	02:18:21.77 – 04:34:49.8	0.0087	1.70	SDS-3	2.207	394.0	$1.606^{+0.36}_{-0.30}$	$11.20^{+1.44}_{-1.01}$	34.16 / 21	MOD1	6.95	44.54	45.21	NL AGN
SXDS 0973	02:19:03.48 – 04:39:34.4	0.0054	0.12	SDS-3	1.853	733.0	$2.116^{+0.13}_{-0.13}$	<0.86	38.81 / 42	MOD1	3.12	44.65	44.93	BL AGN
SXDS 0970	02:19:02.66 – 04:46:28.0	0.0046	-0.06	SDS-3	1.697	431.0	$2.097^{+0.24}_{-0.18}$	<1.94	19.56 / 22	MOD1	2.70	44.50	44.76	BL AGN
SXDS 0936	02:18:55.10 – 04:43:30.0	0.0051	1.98	SDS-3	–	30.0	–	–	0.0 / 0	–	–	–	–	–

ID	R.A. dec (<i>h</i> : <i>m</i> : <i>s</i>) (<i>d</i> : <i>m</i> : <i>s</i>)	Rate ^a Cts/s	$\log(f_x/f_{opt})$ (2–10 keV)	Field	<i>z</i>	Net Cts ^a	Γ	N_H (10^{21} cm ⁻²)	$\chi^2/d.o.f.$	Model	f_{2-10} (10^{-14} cgs)	$\log L_{0.5-2}$ (erg/s)	$\log L_{2-10}$ (erg/s)	Class
SXDS 0790	02:18:24.38 – 04:39:46.4	0.0039	0.21	SDS-3	1.291	75.0	1.9	<93.60	1.08 / 1	MOD1	2.90	–	44.39	BL AGN
SXDS 0924	02:18:52.70 – 04:32:42.0	0.0033	0.42	SDS-3	1.725	121.0	1.9	<26.70	11.79 / 4	MOD1	1.08	43.95	44.42	BL AGN
SXDS 0369	02:17:14.71 – 04:36:01.8	0.0058	0.16	SDS-4	0.293	760.0	$1.745^{+0.21}_{-0.19}$	$1.63^{+0.87}_{-0.73}$	28.18 / 42	MOD1	2.35	43.49	43.78	NL AGN
SXDS 0275	02:16:56.78 – 04:47:45.3	0.0055	1.10	SDS-4	0.883	184.0	$2.045^{+0.89}_{-0.75}$	$43.30^{+48.90}_{-41.00}$	3.73 / 7	MOD1	4.55	43.02	44.26	NL AGN
SXDS 0511	02:17:34.80 – 04:33:43.2	0.0053	0.64	SDS-4	–	881.0	$1.678^{+0.12}_{-0.10}$	<0.19	45.38 / 52	MOD1	4.33	–	–	–
SXDS 0559	02:17:43.01 – 04:36:23.4	0.0039	-0.11	SDS-4	0.785	195.0	$2.23^{+0.97}_{-0.70}$	$53.00^{+62.70}_{-27.50}$	9.22 / 8	MOD1	2.68	43.83	43.95	NAV
SXDS 0215	02:16:45.46 – 04:48:27.4	0.0038	1.30	SDS-4	1.456	180.0	$1.273^{+0.62}_{-0.50}$	$46.6^{+84.50}_{-40.10}$	4.02 / 7	MOD1	2.32	43.27	44.21	NL AGN
SXDS 0561	02:17:43.27 – 04:33:28.0	0.0034	0.39	SDS-4	1.428	585.0	$1.933^{+0.12}_{-0.14}$	<0.76	35.08 / 33	MOD1	2.07	44.08	44.40	BL AGN
SXDS 0357	02:17:12.02 – 04:46:18.7	0.0033	-0.35	SDS-4	1.100	523.0	$1.843^{+0.20}_{-0.16}$	<0.98	47.85 / 29	MOD1	2.58	43.87	44.19	BL AGN
SXDS 0185	02:16:40.82 – 04:44:05.9	0.0186	-0.25	SDS-4	0.875	4708.0	$1.83^{+0.09}_{-0.10}$	<0.10	251.30 / 247	MOD3	11.80	44.61	44.68	BL AGN
SXDS 0457	02:17:27.24 – 04:48:35.7	0.0108	0.50	SDS-4	0.484	1656.0	$1.92^{+0.13}_{-0.09}$	$30.80^{+10.80}_{-9.60}$	67.90 / 94	MOD2	7.61	43.70	43.84	NAV
SXDS 0611	02:17:52.66 – 04:28:15.9	0.0040	1.77	SDS-4	–	30.0	–	–	0.0 / 0	–	3.27	–	–	–
SXDS 0085	02:16:18.24 – 05:06:08.9	0.0165	0.44	SDS-5	0.478	1954.0	$1.68^{+0.10}_{-0.10}$	$0.42^{+0.37}_{-0.34}$	108.40 / 117	MOD1	12.23	43.63	43.98	NL AGN
SXDS 0015	02:15:43.92 – 05:07:15.8	0.0096	-0.99	SDS-5	0.098	583.0	$1.669^{+0.16}_{-0.12}$	<0.27	28.60 / 32	MOD1	6.87	41.84	42.21	NAV
SXDS 0315	02:17:03.43 – 04:55:34.6	0.0074	0.39	SDS-5	0.571	408.0	$1.17^{+0.32}_{-0.28}$	$8.71^{+6.18}_{-0.41}$	16.96 / 21	MOD1	5.00	42.98	43.67	NL AGN
SXDS 0192	02:16:42.02 – 04:55:59.0	0.0051	0.44	SDS-5	0.600	999.0	$2.016^{+0.15}_{-0.14}$	<0.41	52.82 / 58	MOD1	3.15	43.51	43.68	NL AGN
SXDS 0036	02:15:57.70 – 04:50:09.4	0.0045	-0.37	SDS-5	0.890	817.0	$2.443^{+0.14}_{-0.13}$	<0.25	66.39 / 46	MOD1	2.06	44.11	44.04	BL AGN
SXDS 0088	02:16:18.62 – 05:09:41.0	0.0036	0.77	SDS-5	1.129	165.0	$1.539^{+0.52}_{-0.40}$	<0.10	10.17 / 6	MOD1	2.19	43.40	44.05	NL AGN
SXDS 0019	02:15:46.87 – 05:05:09.1	0.0051	0.08	SDS-5	1.443	480.0	$2.31^{+0.24}_{-0.18}$	<1.26	11.60 / 20	MOD1	2.11	44.46	44.56	BL AGN
SXDS 0166	02:16:36.10 – 05:01:40.3	0.0033	0.30	SDS-5	0.626	326.0	$2.17^{+0.99}_{-0.69}$	<20.70	11.50 / 14	MOD3	2.51	43.80	43.83	BL AGN
SXDS 0128	02:16:26.16 – 05:09:56.7	0.0035	0.71	SDS-5	2.178	136.0	1.9	<0.10	6.97 / 5	MOD1	2.13	44.44	45.05	BL AGN
SXDS 0395	02:17:18.65 – 05:29:21.7	0.0173	0.95	SDS-6	0.633	4647.0	$2.314^{+0.08}_{-0.07}$	$0.96^{+0.26}_{-0.24}$	240.70 / 247	MOD1	10.88	44.37	44.34	ABS
SXDS 0590	02:17:49.03 – 05:23:06.9	0.0131	1.52	SDS-6	0.986	595.0	$1.662^{+0.41}_{-0.37}$	$113.40^{+35.20}_{-19.20}$	41.52 / 33	MOD1*	12.11	44.25	44.69	NL AGN
SXDS 0500	02:17:33.29 – 05:15:51.3	0.0102	0.68	SDS-6	0.603	444.0	$1.559^{+0.43}_{-0.38}$	$46.60^{+22.00}_{-16.80}$	22.10 / 24	MOD1	8.58	43.53	44.08	NL AGN
SXDS 0293	02:16:59.90 – 05:32:03.5	0.0077	-0.45	SDS-6	2.809	1013.0	$2.02^{+0.10}_{-0.10}$	<1.84	60.92 / 59	MOD1	4.39	44.97	45.46	BL AGN
SXDS 0529	02:17:36.55 – 05:21:56.4	0.0043	0.88	SDS-6	1.024	739.0	$1.767^{+0.18}_{-0.12}$	<0.15	36.35 / 42	MOD1	2.82	43.77	44.13	BL AGN
SXDS 0630	02:17:55.70 – 05:20:18.3	0.0039	0.74	SDS-6	–	287.0	$1.266^{+0.54}_{-0.44}$	<6.46	15.05 / 14	MOD1	3.31	–	–	–
SXDS 0338	02:17:06.31 – 05:15:32.9	0.0033	1.15	SDS-6	1.739	586.0	$1.792^{+0.25}_{-0.22}$	$5.73^{+5.20}_{-4.00}$	33.48 / 32	MOD1*	2.05	44.08	44.54	BL AGN
SXDS 0299	02:17:01.20 – 05:33:11.5	0.0032	0.37	SDS-6	0.913	258.0	$2.015^{+0.30}_{-0.25}$	<0.97	14.24 / 11	MOD1	1.51	43.62	43.81	BL AGN
SXDS 0276	02:16:57.07 – 05:32:00.5	0.0046	0.53	SDS-6	0.455	123.0	1.9	<0.10	5.35 / 4	MOD1	3.69	43.20	43.44	BL AGN
SXDS 0472	02:17:29.02 – 05:34:01.8	0.0039	0.71	SDS-6	–	165.0	$1.7^{+0.63}_{-0.33}$	<1.51	11.80 / 7	MOD1	4.34	–	–	–
SXDS 0983	02:19:05.57 – 05:14:42.8	0.0052	0.45	SDS-7	–	210.0	$1.247^{+1.13}_{-0.74}$	$13.00^{+25.70}_{-12.60}$	12.61 / 9	MOD1	3.44	–	–	–
SXDS 0840	02:18:34.61 – 05:25:52.2	0.0033	0.27	SDS-7	1.531	547.0	$1.998^{+0.28}_{-0.21}$	<0.24	39.41 / 29	MOD1	2.05	44.20	44.49	BL AGN
SXDS 0861	02:18:38.90 – 05:32:37.1	0.0065	0.33	SDS-7	0.472	575.0	$2.09^{+0.18}_{-0.16}$	<0.35	35.48 / 29	MOD1	3.89	44.38	43.50	NL AGN

ID	R.A. dec (h : m : s)(d : m : s)	Rate ^a Cts/s	$\log(f_x/f_{opt})$ (2–10 keV)	Field	z	Net Cts ^a	Γ	N_H (10^{21} cm^{-2})	$\chi^2/d.o.f.$	Model	f_{2-10} (10^{-14} cgs)	$\log L_{0.5-2}$ (erg/s)	$\log L_{2-10}$ (erg/s)	Class
SXDS 0838	02:18:34.51 –05:13:56.2	0.0043	0.43	SDS-7	0.514	818.0	$2.07^{+0.13}_{-0.12}$	<0.26	51.40 / 48	MOD1	2.80	43.26	43.45	BL AGN

Bibliography

- Abazajian, K., Adelman-McCarthy, J. K., Agüeros, M. A., et al. 2004, *AJ*, 128, 502
- Abazajian, K., Adelman-McCarthy, J. K., Agüeros, M. A., et al. 2005, *AJ*, 129, 1755
- Abazajian, K., Adelman-McCarthy, J. K., Agüeros, M. A., et al. 2003, *AJ*, 126, 2081
- Abazajian, K. N., Adelman-McCarthy, J. K., Agüeros, M. A., et al. 2009, *ApJS*, 182, 543
- Adelman-McCarthy, J. K., Agüeros, M. A., Allam, S. S., et al. 2008, *ApJS*, 175, 297
- Adelman-McCarthy, J. K., Agüeros, M. A., Allam, S. S., et al. 2007, *ApJS*, 172, 634
- Adelman-McCarthy, J. K., Agüeros, M. A., Allam, S. S., et al. 2006, *ApJS*, 162, 38
- Akiyama, M., Ohta, K., Yamada, T., et al. 2000, *ApJ*, 532, 700
- Akiyama, M., Ueda, Y., & Ohta, K. 2002, *ApJ*, 567, 42
- Alexander, D. M., Aussel, H., Bauer, F. E., et al. 2002, *ApJ*, 568, L85
- Alexander, D. M., Bauer, F. E., Brandt, W. N., et al. 2003, *AJ*, 126, 539
- Alexander, D. M., Brandt, W. N., Hornschemeier, A. E., et al. 2001a, *AJ*, 122, 2156
- Alexander, D. M., La Franca, F., Fiore, F., et al. 2001b, *ApJ*, 554, 18
- Antonucci, R. 1993, *ARA&A*, 31, 473
- Aretxaga, I., Terlevich, R. J., & Boyle, B. J. 1998, *MNRAS*, 296, 643
- Arnaud, K. A. 1996, in *Astronomical Society of the Pacific Conference Series*, Vol. 101, *Astronomical Data Analysis Software and Systems V*, ed. G. H. Jacoby & J. Barnes, 17–+
- Baldi, A., Molendi, S., Comastri, A., et al. 2002, *ApJ*, 564, 190
- Barcons, X., Carrera, F. J., Ceballos, M. T., et al. 2007, *A&A*, 476, 1191
- Barger, A. J., Cowie, L. L., Brandt, W. N., et al. 2002, *AJ*, 124, 1839
- Bassani, L., Dadina, M., Maiolino, R., et al. 1999, *ApJS*, 121, 473

- Bianchi, S., Matt, G., Balestra, I., Guainazzi, M., & Perola, G. C. 2004, *A&A*, 422, 65
- Blundell, K. M., Beasley, A. J., Lacy, M., & Garrington, S. T. 1996, *ApJ*, 468, L91+
- Bongiorno, A., Zamorani, G., Gavignaud, I., et al. 2007, *A&A*, 472, 443
- Brand, K., Dey, A., Desai, V., et al. 2007, *ApJ*, 663, 204
- Brandt, W. N. & Hasinger, G. 2005, *ARA&A*, 43, 827
- Brotherton, M. S., Tran, H. D., Becker, R. H., et al. 2001, *ApJ*, 546, 775
- Brusa, M., Gilli, R., & Comastri, A. 2005, *ApJ*, 621, L5
- Caccianiga, A., Severgnini, P., Braito, V., et al. 2004, *A&A*, 416, 901
- Caccianiga, A., Severgnini, P., Della Ceca, R., et al. 2008, *A&A*, 477, 735
- Casali, M., Adamson, A., Alves de Oliveira, C., et al. 2007, *A&A*, 467, 777
- Chini, R., Kreysa, E., & Biermann, P. L. 1989, *A&A*, 219, 87
- Cirasuolo, M., Magliocchetti, M., & Celotti, A. 2005, *MNRAS*, 357, 1267
- Civano, F., Comastri, A., & Brusa, M. 2005, *MNRAS*, 358, 693
- Comastri, A. 2001, *X-ray Astronomy: Stellar Endpoints, AGN, and the Diffuse X-ray Background*, 599, 73
- Comastri, A. 2004, in *Multiwavelength AGN Surveys*, ed. R. Mújica & R. Maiolino, 323–+
- Comastri, A. & Fiore, F. 2004, *Ap&SS*, 294, 63
- Comastri, A., Setti, G., Zamorani, G., & Hasinger, G. 1995, *A&A*, 296, 1
- Corral, A., Page, M. J., Carrera, F. J., et al. 2008, *ArXiv e-prints*
- Cowie, L. L., Barger, A. J., Bautz, M. W., Brandt, W. N., & Garmire, G. P. 2003, *ApJ*, 584, L57
- Crummy, J., Fabian, A. C., Gallo, L., & Ross, R. R. 2006, *MNRAS*, 365, 1067
- Currie, M., Wright, G., Bridger, A., & Economou, F. 1999, in *Astronomical Society of the Pacific Conference Series, Vol. 172, Astronomical Data Analysis Software and Systems VIII*, ed. D. M. Mehringer, R. L. Plante, & D. A. Roberts, 175–+
- Cutri, R. M., Nelson, B. O., Francis, P. J., & Smith, P. S. 2002, in *Astronomical Society of the Pacific Conference Series, Vol. 284, IAU Colloq. 184: AGN Surveys*, ed. R. F. Green, E. Y. Khachikian, & D. B. Sanders, 127–+
- de Ruiter, H. R., Arp, H. C., & Willis, A. G. 1977, *A&AS*, 28, 211
- Del Moro, A., Watson, M. G., Mateos, S., et al. 2009, *A&A*, 493, 445
- Della Ceca, R., Caccianiga, A., Severgnini, P., et al. 2008, *A&A*, 487, 119

den Herder, J. W., Brinkman, A. C., Kahn, S. M., et al. 2001, *A&A*, 365, L7

Di Matteo, T., Springel, V., & Hernquist, L. 2005, *Nature*, 433, 604

Dickey, J. M. & Lockman, F. J. 1990, *ARA&A*, 28, 215

Done, C. & Nayakshin, S. 2007, *MNRAS*, 377, L59

Dunlop, J. S., McLure, R. J., Kukula, M. J., et al. 2003, *MNRAS*, 340, 1095

Dwelly, T. & Page, M. J. 2006, *MNRAS*, 372, 1755

Ebrero, J., Carrera, F. J., Page, M. J., et al. 2009, *A&A*, 493, 55

Elitzur, M. 2008, *New Astronomy Review*, 52, 274

Elston, R., Rieke, G. H., & Rieke, M. J. 1988, *ApJ*, 331, L77

Elvis, M. 2000, *ApJ*, 545, 63

Elvis, M., Maccacaro, T., Wilson, A. S., et al. 1978, *MNRAS*, 183, 129

Elvis, M., Risaliti, G., Nicastro, F., et al. 2004, *ApJ*, 615, L25

Elvis, M., Wilkes, B. J., McDowell, J. C., et al. 1994, *ApJS*, 95, 1

Fabian, A. C. 2006, *Astronomische Nachrichten*, 327, 943

Fabian, A. C. & Iwasawa, K. 1999, *MNRAS*, 303, L34

Fabian, A. C., Iwasawa, K., Reynolds, C. S., & Young, A. J. 2000, *PASP*, 112, 1145

Fabian, A. C., Vaughan, S., Nandra, K., et al. 2002, *MNRAS*, 335, L1

Fazio, G. G., Hora, J. L., Allen, L. E., et al. 2004, *ApJS*, 154, 10

Ferrarese, L. & Merritt, D. 2000, *ApJ*, 539, L9

Fiore, F., Brusa, M., Cocchia, F., et al. 2003, *A&A*, 409, 79

Fiore, F., Giommi, P., Vignali, C., et al. 2001, *MNRAS*, 327, 771

Foucaud, S., Almaini, O., Smail, I., et al. 2007, *MNRAS*, 376, L20

Franceschini, A., Manners, J., Polletta, M. d. C., et al. 2005, *AJ*, 129, 2074

Fukugita, M., Ichikawa, T., Gunn, J. E., et al. 1996, *AJ*, 111, 1748

Furusawa, H., Kosugi, G., Akiyama, M., et al. 2008, *ApJS*, 176, 1

Gabriel, C., Denby, M., Fyfe, D. J., et al. 2004, in *Astronomical Society of the Pacific Conference Series*, Vol. 314, *Astronomical Data Analysis Software and Systems (ADASS) XIII*, ed. F. Ochsenbein, M. G. Allen, & D. Egret, 759–+

Gandhi, P., Fabian, A. C., & Crawford, C. S. 2006, *MNRAS*, 369, 1566

Gebhardt, K., Bender, R., Bower, G., et al. 2000, *ApJ*, 539, L13

- Giacconi, R., Murray, S., Gursky, H., et al. 1974, *ApJS*, 27, 37
- Gilli, R., Comastri, A., & Hasinger, G. 2007, *A&A*, 463, 79
- Gilli, R., Salvati, M., & Hasinger, G. 2001, *A&A*, 366, 407
- Granato, G. L., De Zotti, G., Silva, L., Bressan, A., & Danese, L. 2004, *ApJ*, 600, 580
- Granato, G. L., Silva, L., Monaco, P., et al. 2001, *MNRAS*, 324, 757
- Guainazzi, M., Matt, G., & Perola, G. C. 2005, *A&A*, 444, 119
- Gunn, J. E., Carr, M., Rockosi, C., et al. 1998, *AJ*, 116, 3040
- Gunn, J. E., Siegmund, W. A., Mannery, E. J., et al. 2006, *AJ*, 131, 2332
- Hasinger, G. 2003, in *American Institute of Physics Conference Series*, Vol. 666, *The Emergence of Cosmic Structure*, ed. S. H. Holt & C. S. Reynolds, 227–236
- Hasinger, G. 2004, *Nuclear Physics B Proceedings Supplements*, 132, 86
- Hasinger, G. 2008, *A&A*, 490, 905
- Hasinger, G., Altieri, B., Arnaud, M., et al. 2001, *A&A*, 365, L45
- Hasinger, G., Cappelluti, N., Brunner, H., et al. 2007, *ApJS*, 172, 29
- Hasinger, G., Miyaji, T., & Schmidt, M. 2005, *A&A*, 441, 417
- Hatziminaoglou, E., Pérez-Fournon, I., Polletta, M., et al. 2005, *AJ*, 129, 1198
- Hawkins, M. R. S. 2004, *A&A*, 424, 519
- Heckman, T. M. 1980, *A&A*, 88, 365
- Hewett, P. C., Warren, S. J., Leggett, S. K., & Hodgkin, S. T. 2006, *MNRAS*, 367, 454
- Hodgkin, S. T., Irwin, M. J., Hewett, P. C., & Warren, S. J. 2009, *MNRAS*, 394, 675
- Høg, E., Fabricius, C., Makarov, V. V., et al. 2000, *A&A*, 355, L27
- Hopkins, P. F., Hernquist, L., Cox, T. J., et al. 2006, *ApJS*, 163, 1
- Ichikawa, T., Suzuki, R., Tokoku, C., et al. 2006, in *Presented at the Society of Photo-Optical Instrumentation Engineers (SPIE) Conference*, Vol. 6269, *Ground-based and Airborne Instrumentation for Astronomy*. Edited by McLean, Ian S.; Iye, Masanori. *Proceedings of the SPIE*, Volume 6269, pp. 626916 (2006).
- Ivezić, Ž., Lupton, R. H., Schlegel, D., et al. 2004, *Astronomische Nachrichten*, 325, 583
- Jansen, F., Lumb, D., Altieri, B., et al. 2001, *A&A*, 365, L1
- Kallman, T. & Mushotzky, R. 1985, *ApJ*, 292, 49
- Kellermann, K. I., Sramek, R., Schmidt, M., Shaffer, D. B., & Green, R. 1989, *AJ*, 98, 1195

- Koekemoer, A. M., Alexander, D. M., Bauer, F. E., et al. 2004, *ApJ*, 600, L123
- Kormendy, J. & Gebhardt, K. 2001, in *American Institute of Physics Conference Series*, Vol. 586, 20th Texas Symposium on relativistic astrophysics, ed. J. C. Wheeler & H. Martel, 363–381
- Kormendy, J. & Richstone, D. 1995, *ARA&A*, 33, 581
- Kouzuma, S. & Yamaoka, H. 2009, *ArXiv e-prints*
- Krumpe, M., Lamer, G., Corral, A., et al. 2008, *A&A*, 483, 415
- Kuhn, O. P. 2004, *MNRAS*, 348, 647
- Kuraszkiewicz, J., Wilkes, B. J., Schmidt, G., et al. 2009, *ApJ*, 692, 1143
- La Franca, F., Fiore, F., Comastri, A., et al. 2005, *ApJ*, 635, 864
- Lanzuisi, G., Piconcelli, E., Fiore, F., et al. 2009, *A&A*, 498, 67
- Laor, A. & Behar, E. 2007, *Memorie della Societa Astronomica Italiana*, 78, 397
- Lawrence, A. 1991, *MNRAS*, 252, 586
- Lawrence, A. 2007, in *IAU Symposium*, Vol. 238, *IAU Symposium*, ed. V. Karas & G. Matt, 117–122
- Lawrence, A. & Elvis, M. 1982, *ApJ*, 256, 410
- Lawrence, A., Warren, S. J., Almaini, O., et al. 2007, *MNRAS*, 379, 1599
- Li, Y., Hernquist, L., Robertson, B., et al. 2007, *ApJ*, 665, 187
- Lonsdale, C., Polletta, M. d. C., Surace, J., et al. 2004, *ApJS*, 154, 54
- López-Santiago, J., Micela, G., Sciortino, S., et al. 2007, *A&A*, 463, 165
- Lupton, R., Gunn, J. E., Ivezić, Z., Knapp, G. R., & Kent, S. 2001, in *Astronomical Society of the Pacific Conference Series*, Vol. 238, *Astronomical Data Analysis Software and Systems X*, ed. F. R. Harnden Jr., F. A. Primini, & H. E. Payne, 269–+
- Lynden-Bell, D. 1969, *Nature*, 223, 690
- Maccacaro, T., Gioia, I. M., Wolter, A., Zamorani, G., & Stocke, J. T. 1988, *ApJ*, 326, 680
- Maccacaro, T., Perola, G. C., & Elvis, M. 1982, *ApJ*, 257, 47
- MacKenty, J. W., Maíz-Apellániz, J., Pickens, C. E., Norman, C. A., & Walborn, N. R. 2000, *AJ*, 120, 3007
- Magdziarz, P. & Zdziarski, A. A. 1995, *MNRAS*, 273, 837
- Magorrian, J., Tremaine, S., Richstone, D., et al. 1998, *AJ*, 115, 2285
- Mainieri, V., Bergeron, J., Hasinger, G., et al. 2002, *A&A*, 393, 425

- Mainieri, V., Hasinger, G., Cappelluti, N., et al. 2007, *ApJS*, 172, 368
- Maiolino, R. 2002, in *Astronomical Society of the Pacific Conference Series*, Vol. 258, *Issues in Unification of Active Galactic Nuclei*, ed. R. Maiolino, A. Marconi, & N. Nagar, 15–+
- Maiolino, R., Marconi, A., & Oliva, E. 2001a, *A&A*, 365, 37
- Maiolino, R., Marconi, A., Salvati, M., et al. 2001b, *A&A*, 365, 28
- Maiolino, R., Shemmer, O., Imanishi, M., et al. 2007, *A&A*, 468, 979
- Malkan, M. A. & Sargent, W. L. W. 1982, *ApJ*, 254, 22
- Marconi, A. & Hunt, L. K. 2003, *ApJ*, 589, L21
- Martínez-Sansigre, A., Rawlings, S., Lacy, M., et al. 2006, *MNRAS*, 370, 1479
- Mason, K. O., Breeveld, A., Much, R., et al. 2001, *A&A*, 365, L36
- Mateos, S., Barcons, X., Carrera, F. J., et al. 2005a, *A&A*, 433, 855
- Mateos, S., Barcons, X., Carrera, F. J., et al. 2005b, *A&A*, 444, 79
- Mateos, S., Saxton, R. D., Read, A. M., & Sembay, S. 2009, *A&A*, 496, 879
- Mateos, S., Warwick, R. S., Carrera, F. J., et al. 2008, *A&A*, 492, 51
- Matt, G., Guainazzi, M., & Maiolino, R. 2003, *MNRAS*, 342, 422
- Matt, G., Perola, G. C., & Piro, L. 1991, *A&A*, 247, 25
- McLeod, K. K. & Rieke, G. H. 1995, *ApJ*, 454, L77+
- McLure, R. J. & Dunlop, J. S. 2002, *MNRAS*, 331, 795
- Mignoli, M., Pozzetti, L., Comastri, A., et al. 2004, *A&A*, 418, 827
- Miller, J. M. 2007, *ARA&A*, 45, 441
- Miyazaki, S., Komiyama, Y., Sekiguchi, M., et al. 2002, *PASJ*, 54, 833
- Monet, D. G., Levine, S. E., Canzian, B., et al. 2003, *AJ*, 125, 984
- Morrison, R. & McCammon, D. 1983, *ApJ*, 270, 119
- Mortier, A. M. J., Serjeant, S., Dunlop, J. S., et al. 2005, *MNRAS*, 363, 563
- Mushotzky, R. F., Cowie, L. L., Barger, A. J., & Arnaud, K. A. 2000, *Nature*, 404, 459
- Nandra, K. 2006, *MNRAS*, 368, L62
- Nandra, K., Laird, E. S., Adelberger, K., et al. 2005, *MNRAS*, 356, 568
- Nandra, K., O’Neill, P. M., George, I. M., & Reeves, J. N. 2007, *MNRAS*, 382, 194
- Nandra, K. & Pounds, K. A. 1994, *MNRAS*, 268, 405

- Nenkova, M., Sirocky, M. M., Ivezić, Ž., & Elitzur, M. 2008a, *ApJ*, 685, 147
- Nenkova, M., Sirocky, M. M., Nikutta, R., Ivezić, Ž., & Elitzur, M. 2008b, *ApJ*, 685, 160
- Netzer, H., Shemmer, O., Maiolino, R., et al. 2004, *ApJ*, 614, 558
- Newberg, H. J., Richards, G. T., Richmond, M., & Fan, X. 1999, *ApJS*, 123, 377
- Oke, J. B. & Gunn, J. E. 1983, *ApJ*, 266, 713
- Orr, M. J. L. & Browne, I. W. A. 1982, *MNRAS*, 200, 1067
- Page, M. J., Loaring, N. S., Dwelly, T., et al. 2006, *MNRAS*, 369, 156
- Page, M. J., Mittaz, J. P. D., & Carrera, F. J. 2001, *MNRAS*, 325, 575
- Panessa, F. & Bassani, L. 2002, *A&A*, 394, 435
- Panessa, F., Bassani, L., Cappi, M., et al. 2006, *A&A*, 455, 173
- Panessa, F., Carrera, F. J., Bianchi, S., et al. 2009, *MNRAS*, 398, 1951
- Pei, Y. C. 1992, *ApJ*, 395, 130
- Perola, G. C., Puccetti, S., Fiore, F., et al. 2004, *A&A*, 421, 491
- Piconcelli, E., Vignali, C., Bianchi, S., et al. 2010, *ApJ*, 710, 992
- Pier, J. R., Munn, J. A., Hindsley, R. B., et al. 2003, *AJ*, 125, 1559
- Pineau, F., Derriere, S., Michel, L., & Motch, C. 2008, in *Astronomical Society of the Pacific Conference Series*, Vol. 394, *Astronomical Data Analysis Software and Systems XVII*, ed. R. W. Argyle, P. S. Bunclark, & J. R. Lewis, 369–+
- Polletta, M., Tajer, M., Maraschi, L., et al. 2007, *ApJ*, 663, 81
- Polletta, M., Weedman, D., Hönig, S., et al. 2008, *ApJ*, 675, 960
- Polletta, M. d. C., Wilkes, B. J., Siana, B., et al. 2006, *ApJ*, 642, 673
- Predehl, P. & Schmitt, J. H. M. M. 1995, *A&A*, 293, 889
- Reeves, J. N., Nandra, K., George, I. M., et al. 2004, *ApJ*, 602, 648
- Reeves, J. N. & Turner, M. J. L. 2000, *MNRAS*, 316, 234
- Reynolds, C. S., Ward, M. J., Fabian, A. C., & Celotti, A. 1997, *MNRAS*, 291, 403
- Rieke, G. H., Young, E. T., Engelbracht, C. W., et al. 2004, *ApJS*, 154, 25
- Rigby, J. R., Rieke, G. H., Donley, J. L., Alonso-Herrero, A., & Pérez-González, P. G. 2006, *ApJ*, 645, 115
- Risaliti, G. 2009, *ArXiv e-prints*
- Risaliti, G. & Elvis, M. 2004, in *Astrophysics and Space Science Library*, Vol. 308, *Supermassive Black Holes in the Distant Universe*, ed. A. J. Barger, 187–+

- Risaliti, G., Elvis, M., Fabbiano, G., Baldi, A., & Zezas, A. 2005, *ApJ*, 623, L93
- Risaliti, G., Elvis, M., Fabbiano, G., et al. 2007, *ApJ*, 659, L111
- Risaliti, G., Marconi, A., Maiolino, R., Salvati, M., & Severgnini, P. 2001, *A&A*, 371, 37
- Roche, P. F., Lucas, P. W., Mackay, C. D., et al. 2003, in Presented at the Society of Photo-Optical Instrumentation Engineers (SPIE) Conference, Vol. 4841, Society of Photo-Optical Instrumentation Engineers (SPIE) Conference Series, ed. M. Iye & A. F. M. Moorwood, 901–912
- Rosati, P., della Ceca, R., Norman, C., & Giacconi, R. 1998, *ApJ*, 492, L21+
- Rosati, P., Tozzi, P., Giacconi, R., et al. 2002, *ApJ*, 566, 667
- Sanders, D. B. 1999, in IAU Symposium, Vol. 194, Activity in Galaxies and Related Phenomena, ed. Y. Terzian, E. Khachikian, & D. Weedman, 25–+
- Sanders, D. B., Phinney, E. S., Neugebauer, G., Soifer, B. T., & Matthews, K. 1989, *ApJ*, 347, 29
- Scoville, N., Aussel, H., Brusa, M., et al. 2007, *ApJS*, 172, 1
- Setti, G. & Woltjer, L. 1989, *A&A*, 224, L21
- Severgnini, P., Caccianiga, A., Braitto, V., et al. 2006, *A&A*, 451, 859
- Severgnini, P., Caccianiga, A., Braitto, V., et al. 2003, *A&A*, 406, 483
- Severgnini, P., Della Ceca, R., Braitto, V., et al. 2005, *A&A*, 431, 87
- Shakura, N. I. & Sunyaev, R. A. 1973, *A&A*, 24, 337
- Shang, Z., Brotherton, M. S., Green, R. F., et al. 2005, *ApJ*, 619, 41
- Shields, G. A. 1978, *Nature*, 272, 706
- Silva, L., Granato, G. L., Bressan, A., & Danese, L. 1998, *ApJ*, 509, 103
- Simons, D. A. & Tokunaga, A. 2002, *PASP*, 114, 169
- Simpson, C. 2005, *MNRAS*, 360, 565
- Simpson, C., Martínez-Sansigre, A., Rawlings, S., et al. 2006, *MNRAS*, 372, 741
- Somerville, R. S., Lee, K., Ferguson, H. C., et al. 2004, *ApJ*, 600, L171
- Steffen, A. T., Barger, A. J., Cowie, L. L., Mushotzky, R. F., & Yang, Y. 2003, *ApJ*, 596, L23
- Streblyanska, A., Hasinger, G., Finoguenov, A., et al. 2005, *A&A*, 432, 395
- Strüder, L., Briel, U., Dennerl, K., et al. 2001, *A&A*, 365, L18
- Sturm, E., Schweitzer, M., Lutz, D., et al. 2005, *ApJ*, 629, L21

- Sulentic, J. W., Marziani, P., Zwitter, T., Calvani, M., & Dultzin-Hacyan, D. 1998, *ApJ*, 501, 54
- Sulentic, J. W., Stirpe, G. M., Marziani, P., et al. 2004, *A&A*, 423, 121
- Sutherland, W. & Saunders, W. 1992, *MNRAS*, 259, 413
- Telfer, R. C., Zheng, W., Kriss, G. A., & Davidsen, A. F. 2002, *ApJ*, 565, 773
- Tozzi, P., Gilli, R., Mainieri, V., et al. 2006, *A&A*, 451, 457
- Treister, E. & Urry, C. M. 2006, *ApJ*, 652, L79
- Turner, M. J. L., Abbey, A., Arnaud, M., et al. 2001, *A&A*, 365, L27
- Turner, T. J., George, I. M., Nandra, K., & Mushotzky, R. F. 1998, *ApJ*, 493, 91
- Turner, T. J., Kraemer, S. B., George, I. M., Reeves, J. N., & Bottorff, M. C. 2005, *ApJ*, 618, 155
- Turner, T. J. & Miller, L. 2009, *A&A Rev.*, 17, 47
- Ueda, Y., Akiyama, M., Ohta, K., & Miyaji, T. 2003, *ApJ*, 598, 886
- Ueda, Y., Watson, M. G., Stewart, I. M., et al. 2008, *ApJS*, 179, 124
- Urrutia, T., Lacy, M., & Becker, R. H. 2008, *ApJ*, 674, 80
- Urry, C. M. & Padovani, P. 1995, *PASP*, 107, 803
- Vanden Berk, D. E., Richards, G. T., Bauer, A., et al. 2001, *AJ*, 122, 549
- Vanden Berk, D. E., Shen, J., Yip, C.-W., et al. 2006, *AJ*, 131, 84
- Veilleux, S. & Osterbrock, D. E. 1987, *ApJS*, 63, 295
- Véron-Cetty, M. & Véron, P. 2001, *A&A*, 374, 92
- Wang, J. X., Jiang, P., Zheng, Z. Y., et al. 2007, *ApJ*, 657, 95
- Ward, M., Elvis, M., Fabbiano, G., et al. 1987, *ApJ*, 315, 74
- Ward, M. J., Done, C., Fabian, A. C., Tennant, A. F., & Shafer, R. A. 1988, *ApJ*, 324, 767
- Watson, M. G., Schröder, A. C., Fyfe, D., et al. 2009, *A&A*, 493, 339
- Wilkes, B. 2004, in *Astronomical Society of the Pacific Conference Series*, Vol. 311, *AGN Physics with the Sloan Digital Sky Survey*, ed. G. T. Richards & P. B. Hall, 37–4
- Wilkes, B. J., Pounds, K. A., & Schmidt, G. D. 2008, *ApJ*, 680, 110
- Willott, C. J., Simpson, C., Almaini, O., et al. 2004, *ApJ*, 610, 140
- Woltjer, L. 1959, *ApJ*, 130, 38
- Worsley, M. A., Fabian, A. C., Barcons, X., et al. 2004, *MNRAS*, 352, L28

- Worsley, M. A., Fabian, A. C., Bauer, F. E., et al. 2005, MNRAS, 357, 1281
- Yaqoob, T., Murphy, K. D., Miller, L., & Turner, T. J. 2010, MNRAS, 401, 411
- Yaqoob, T. & Padmanabhan, U. 2004, ApJ, 604, 63
- Yuan, M. J. & Wills, B. J. 2003, ApJ, 593, L11
- Zacharias, N., Urban, S. E., Zacharias, M. I., et al. 2000, AJ, 120, 2131
- Zakamska, N. L., Strauss, M. A., Heckman, T. M., Ivezić, Ž., & Krolik, J. H. 2004, AJ, 128, 1002
- Zakamska, N. L., Strauss, M. A., Krolik, J. H., et al. 2003, AJ, 126, 2125
- Zdziarski, A. A., Fabian, A. C., Nandra, K., et al. 1994, MNRAS, 269, L55+
- Zel'Dovich, Y. B. 1964, Soviet Physics Doklady, 9, 195